NATIONAL AERONAUTICS AND SPACE ADMINISTRATION

Space Programs Summary 37-66, Vol. II

The Deep Space Network

For the Period September 1 to October 31, 1970

JET PROPULSION LABORATORY
CALIFORNIA INSTITUTE OF TECHNOLOGY
PASADENA, CALIFORNIA

November 30, 1970

JET PROPULSION LABORATORY *California Institute of Technology • 4800 Oak Grove Drive, Pasadena, California 91103*

ANNOUNCEMENT

CANCELLATION OF THE SPACE PROGRAMS SUMMARY (SPS)

With the completion of the SPS 37-66 series, the Space Programs Summary (SPS) is cancelled as a periodical publication of the Jet Propulsion Laboratory. The SPS is being replaced by a new publication, the JPL Quarterly Technical Review (QTR).

The QTR will be comprised of brief technical articles describing selected JPL work and a bibliography of recent JPL publications.

Current recipients of the SPS will automatically receive the new QTR.

Telephone 354-4321

Twx 213-449-2451

NATIONAL AERONAUTICS AND SPACE ADMINISTRATION

Space Programs Summary 37-66, Vol. II

The Deep Space Network

For the Period September 1 to October 31, 1970

JET PROPULSION LABORATORY
CALIFORNIA INSTITUTE OF TECHNOLOGY
PASADENA, CALIFORNIA

November 30, 1970

SPACE PROGRAMS SUMMARY 37-66, VOL. II

Prepared Under Contract No NAS 7-100
National Aeronautics and Space Administration

Preface

The Space Programs Summary is a multivolume, bimonthly publication that presents a review of technical information resulting from current engineering and scientific work performed, or managed, by the Jet Propulsion Laboratory for the National Aeronautics and Space Administration. The Space Programs Summary is currently composed of four volumes:

Vol. I. *Flight Projects* (Unclassified)

Vol. II. *The Deep Space Network* (Unclassified)

Vol. III. *Supporting Research and Advanced Development* (Unclassified)

Vol. IV. *Flight Projects and Supporting Research and Advanced Development* (Confidential)

Foreword

Volume II of the Space Programs Summary reports the results of work performed by the Deep Space Network (DSN). Information is presented, as appropriate, in the following categories:

Introduction
- Description of the DSN
- Description of DSN Systems

Mission Support
- Interplanetary Flight Projects
- Planetary Flight Projects
- Manned Space Flight Project
- Advanced Flight Projects

Advanced Engineering
- Tracking and Navigational Accuracy Analysis
- Communications Systems Research
- Communications Elements Research
- Supporting Research and Technology

Development and Implementation
- Space Flight Operations Facility Development
- Ground Communications Facility Development
- Deep Space Instrumentation Facility Development
- DSN Project and System Development

Operations and Facilities
- DSN Operations
- Space Flight Operations Facility Operations
- Ground Communications Facility Operations
- Deep Space Instrumentation Facility Operations
- Facility Engineering

In each issue, the section entitled "Description of DSN Systems" reports the current configuration of one of the six DSN systems (tracking, telemetry, command, monitoring, simulation, and operations control). The fundamental research carried out in support of the DSN is reported in Vol. III.

Contents

Contents (contd)

Contents (contd)

Contents (contd)

I. Description of the DSN

INTRODUCTION

The Deep Space Network (DSN), established by the NASA Office of Tracking and Data Acquisition under the system management and technical direction of JPL, is designed for two-way communications with unmanned spacecraft traveling approximately 10,000 mi from earth to planetary distances. It supports, or has supported, the following NASA deep space exploration projects: *Ranger*, *Surveyor*, *Mariner* Venus 1962, *Mariner* Mars 1964, *Mariner* Venus 67, *Mariner* Mars 1969, *Mariner* Mars 1971 (JPL); *Lunar Orbiter* and *Viking* (Langley Research Center); *Pioneer* (Ames Research Center); *Helios* (West Germany); and *Apollo* (Manned Spacecraft Center), to supplement the Manned Space Flight Network (MSFN).

The DSN is distinct from other NASA networks such as the MSFN, which has primary responsibility for tracking the manned spacecraft of the *Apollo* Project, and the Space Tracking and Data Acquisition Network (STADAN), which tracks earth-orbiting scientific and communications satellites. With no future unmanned lunar spacecraft presently planned, the primary objective of the DSN is to continue its support of planetary and interplanetary flight projects.

To support flight projects, the DSN simultaneously performs advanced engineering on components and systems, integrates proven equipment and methods into the network,[1] and provides direct support of each project through that project's Tracking and Data System. This management element and the project's Mission Operations personnel are responsible for the design and operation of the data, software, and operations systems required for the conduct of flight operations. The organization and procedures necessary to carry out these activities are described in SPS 37-50, Vol. II, pp. 15–17.

By tracking the spacecraft, the DSN is involved in the following data types:

(1) *Metric:* generate angles, one- and two-way doppler, and range.

(2) *Telemetry:* receive, record, and retransmit engineering and scientific data.

(3) *Command:* send coded signals to the spacecraft to activate equipment to initiate spacecraft functions.

[1]When a new piece of equipment or new method has been accepted for integration into the network, it is classed as Goldstone duplicate standard (GSDS), thus standardizing the design and operation of identical items throughout the network.

The DSN operation is characterized by six DSN systems: (1) tracking, (2) telemetry, (3) command, (4) monitoring, (5) simulation, and (6) operations control.

The DSN can be characterized as being comprised of three facilities: the Deep Space Instrumentation Facility (DSIF), the Ground Communications Facility (GCF), and the Space Flight Operations Facility (SFOF).

1. Deep Space Instrumentation Facility

a. Tracking and data acquisition facilities. A worldwide set of deep space stations (DSSs) with large antennas, low-noise phase-lock receiving systems, and high-power transmitters provide radio communications with spacecraft. The DSSs and the deep space communications complexes (DSCCs) they comprise are given in Table 1.

Radio contact with a spacecraft usually begins when the spacecraft is on the launch vehicle at Cape Kennedy, and it is maintained throughout the mission. The early part of the trajectory is covered by selected network stations of the Air Force Eastern Test Range (AFETR) and the MSFN of the Goddard Space Flight Center.[2] Normally, two-way communications are established between the spacecraft and the DSN within 30 min after the spacecraft has been injected into lunar, planetary, or interplanetary flight. A compatibility test station at Cape Kennedy (discussed later) monitors the spacecraft continuously during the launch phase until it passes over the local horizon. The deep space phase begins with acquisition by either DSS 51, 41, or 42. These and the remaining DSSs given in Table 1 provide radio communications to the end of the flight.

To enable continuous radio contact with spacecraft, the DSSs are located approximately 120 deg apart in longitude; thus, a spacecraft in deep space flight is always within the field-of-view of at least one DSS, and for several hours each day may be seen by two DSSs. Furthermore, since most spacecraft on deep space missions travel within 30 deg of the equatorial plane, the DSSs are located within latitudes of 45 deg north or south of the equator. All DSSs operate at S-band frequencies: 2110–2120 MHz for earth-to-spacecraft transmission and 2290–2300 MHz for spacecraft-to-earth transmission.

[2]The 30-ft-diam-antenna station established by the DSN on Ascension Island during 1965 to act in conjunction with the MSFN orbital support 30-ft-diam-antenna station was transferred to the MSFN in July 1968.

To provide sufficient tracking capability to enable useful data returns from around the planets and from the edge of the solar system, a 210-ft-diam-antenna network will be required. Two additional 210-ft-diam-antenna DSSs are under construction at Madrid and Canberra, which will operate in conjunction with DSS 14 to provide this capability. These stations are scheduled to be operational by early 1973.

b. Compatibility test facilities. In 1959, a mobile L-band compatibility test station was established at Cape Kennedy to verify flight-spacecraft–DSN compatibility prior to the launch of the *Ranger* and *Mariner* Venus 1962 spacecraft. Experience revealed the need for a permanent facility at Cape Kennedy for this function. An S-band compatibility test station with a 4-ft-diam antenna became operational in 1965. In addition to supporting the preflight compatibility tests, this station monitors the spacecraft continuously during the launch phase until it passes over the local horizon.

Spacecraft telecommunications compatibility in the design and prototype development phases was formerly verified by tests at the Goldstone DSCC. To provide a more economical means for conducting such work and because of the increasing use of multiple-mission telemetry and command equipment by the DSN, a compatibility test area (CTA) was established at JPL in 1968. In all essential characteristics, the configuration of this facility is identical to that of the 85- and 210-ft-diam-antenna stations

The JPL CTA is used during spacecraft system tests to establish the compatibility with the DSN of the proof test model and development models of spacecraft, and the Cape Kennedy compatibility test station is used for final flight spacecraft compatibility validation testing prior to launch.

2. Ground Communications Facility

The GCF, using, in part, facilities of the worldwide NASA Communications Network (NASCOM),[3] provides voice, high-speed data, and teletype communications between the SFOF and all DSSs, except those of the Goldstone DSCC. Communications between the Goldstone DSCC and the SFOF are provided by a microwave link leased from a common carrier. Early missions were

[3]Managed and directed by the Goddard Space Flight Center

Table 1. Tracking and data acquisition stations of the DSN

DSCC	Location	DSS	DSS serial designation	Antenna		Year of initial operation
				Diameter, ft	Type of mounting	
Goldstone	California	Pioneer	11	85	Polar	1958
		Echo	12	85	Polar	1962
		(Venus)[a]	13	85	Az–El	1962
		Mars	14	210	Az–El	1966
—	Australia	Woomera[b]	41	85	Polar	1960
Tidbinbilla	Australia	Weemala (formerly Tidbinbilla)[b]	42	85	Polar	1965
		Ballima[b] (formerly Booroomba)	43	210	Az–El	Under construction
—	South Africa	Johannesburg[b]	51	85	Polar	1961
Madrid	Spain	Robledo[b]	61	85	Polar	1965
		Cebreros[b]	62	85	Polar	1967
		Robledo	63	210	Az–El	Under construction

[a]A research-and-development facility used to demonstrate the feasibility of new equipment and methods to be integrated into the operational network. Besides the 85-ft-diam az–el-mounted antenna, DSS 13 has a 30-ft-diam az–el-mounted antenna that is used for testing the design of new equipment and support of ground-based radio science.

[b]Normally staffed and operated by government agencies of the respective countries (except for a temporary staff of the Madrid DSCC), with some assistance of U.S. support personnel.

supported with voice and teletype circuits only, but increased data rates necessitated the use of wide-band circuits from all DSSs.

3. Space Flight Operations Facility

Network and mission control functions are performed at the SFOF at JPL. (Prior to 1964, these functions were performed in temporary facilities at JPL.) The SFOF receives data from all DSSs and processes that information required by the flight project to conduct mission operations. The following services are provided: (1) real-time processing and display of metric data; (2) real-time and non-real-time processing and display of telemetry data; (3) simulation of flight operations; (4) near-real-time evaluation of DSN performance; (5) operations control, and status and operational data display; and (6) general support such as internal communications by telephone, intercom, public address, closed-circuit TV, documentation, and reproduction of data packages. Master data records of science data received from spacecraft are generated. Technical areas are provided for flight project personnel who analyze spacecraft performance, trajectories, and generation of commands.

The SFOF is equipped to support many spacecraft in flight and those under test in preparation for flight. Over a 24-h period in 1967, as many as eight in-flight spacecraft or operational-readiness tests for flight were supported by the SFOF.

II. Interplanetary Flight Projects

MISSION SUPPORT

A. *Pioneer* Mission Support, *A. J. Siegmeth*

1. Introduction

The DSN continues to support the second-generation *Pioneer VI, VII, VIII,* and *IX* missions. The four still-active spacecraft were launched on December 16, 1965, August 17, 1966, December 13, 1967, and November 8, 1968. Tracking and data acquisition (TDA) support services for these missions were presented in SPS 37-50, 37-51, 37-56, 37-59, 37-61, and 37-63, Vol. II. SPS 37-61, Vol. II, also contains an introduction to the third-generation *Pioneer F* and *G* missions.

The major events of DSN support of the active interplanetary *Pioneers* during 1970 are covered in this article, and a summary is given of the planetary support planning activities for the *Pioneer F* and *G* missions. These missions, to be launched in 1972 and 1974, will provide the first closeup reconnaissance of Jupiter.

2. *Pioneer VI, VII, VIII,* and *IX* Missions

a. Support Instrumentation Requirements Document (SIRD). The latest revision of the *Pioneer VI, VII, VIII,* and *IX* SIRD was prepared in November 1969. This document describes the required support of the cruise phase of the still-active second-generation *Pioneer* missions. These requirements will be reviewed at least on a 2-yr cycle basis and new SIRD revisions will follow.

In accordance with the SIRD, the following TDA coverage is required:

Pioneer VI	4- to 8-h daily coverage from DSS 14, or from the 85-ft-diam antenna stations when the Earth–spacecraft range decreases within the threshold capabilities of these stations
Pioneer VII	4- to 8-h daily coverage from DSS 14; absolute minimum: 3 h/day
Pioneer VIII	Continuous coverage from the 85-ft-diam antenna network; absolute minimum: two tracks/day
Pioneer IX	Same as *Pioneer VII*

b. NASA Support Plan (NSP). The planned DSN support for the *Pioneer VI, VII, VIII,* and *IX* missions is described in the NSP that was approved in August 1969; also included is the support of the ill-fated *Pioneer E* mission, which was terminated on August 27, 1969 (SPS 37-61, Vol. II, pp. 8–16). This NSP, as are all similar support plans, is subject to constraints caused by limitation of resources and relative priorities of planetary and interplanetary flight projects.

The DSN recently completed a revised *Pioneer VI, VII, VIII,* and *IX* NSP which is delineating the support plan for the extended missions.

c. DSN Operations Plan, Vol. I, DSN Operations Support. In September 1970, the DSN published Vol. I of the DSN Operations Plan for *Pioneers VI* through *IX*. This plan complements the NSP. Applicable equipment, software capabilities, tracking time allocation, management, and organizational responsibilities are delineated.

In keeping with the NASA Office of Tracking and Data Acquisition policy, the DSN continued support of the extended mission phases of the flight projects on an annual basis. Therefore, this Operations Plan covers the 1971 fiscal year starting on July 1, 1970 and ending on June 30, 1971.

d. Project support configuration.

Telemetry. Telemetry is processed by mission-dependent equipment and software. Decommutated, sampled, and processed engineering and science data streams are sent via TTY in real time to Ames Research Center. The FR 1400 analog magnetic tape containing all received telemetry is sent in non-real time to Ames Research Center in a data package along with the JPL validation report. The *Pioneer* Project uses the POLDOPS program to generate the digital experimenter tapes.

Radio metric link. Data are sent by the DSS to the SFOF in real time and logged on computers for later processing to maintain orbital parameters. A save tape is generated from these data and one digital magnetic tape and three printed listings are made by the DSN and sent to the Project.

Predicts. Predicts are generated by the DSN as required, using trajectory information, and are transmitted to the various DSSs for *Pioneer* tracking. Predicts for the 150-ft-diam uplink antenna at Stanford University that supports the radio propagation experiment are also generated, as required, and sent via Ames Research Center.

e. DSN operational control. DSN operational control for *Pioneers VI* through *IX* is provided by the DSN mission-independent operations organization. In this organization, the DSN Operation Chief is responsible for the overall direction of DSN operations and is specifically responsible for proper operation of the DSN resources committed to the *Pioneer* Project. The Operations Chief acts as the single point of contact between the *Pioneer* Project and the DSN. In this capacity, he is responsible to the DSN Operations Manager.

f. DSN actual support. The monthly tracking and data acquisition support hours provided for *Pioneers VI, VII, VIII,* and *IX* are depicted in Fig. 1. This support was constrained by the available resources, the budget, the requirements of *Mariners VI* and *VII*, and the requirements of other users of the network.

To assure an efficient data return from all four active *Pioneer* spacecraft, special efforts were made to maximize the capabilities of the network, and to enhance the support from the 85-ft-diam antenna stations. Specifically, DSN provided the following support configurations for each *Pioneer* mission.

Pioneer VI. The use of the advanced S-band polar ultra (SPU) cone (SPS 37-63, Vol. II, p. 9) at DSS 12 allowed extended downlink tracking from this 85-ft-diam antenna station. The received signal level was approximately −170.5 dBmW. By September, the standard 85-ft-diam stations were tracking this spacecraft routinely

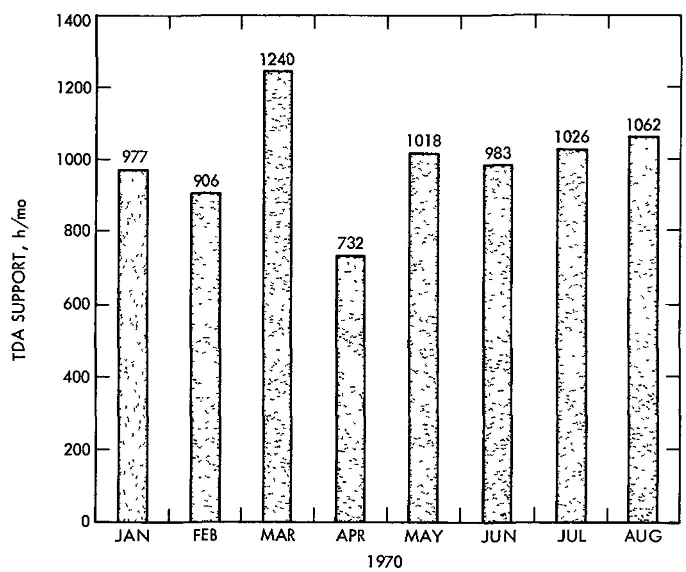

Fig. 1. *Pioneer VI, VII, VIII,* and *IX* missions—TDA support

at an average downlink signal power of -164 dBmW. The *Pioneer VI* support operation will be confined to downlink tracking only, approximately until an earth–spacecraft range of 0.7 AU. Until this time, commands can only be sent to the *Pioneer VI* spacecraft via DSS 14. This spacecraft operates with a spacecraft receiver connected to the low-gain antenna.

Pioneer VII. The DSN has routinely tracked the *Pioneer VII* spacecraft from DSS 14 in a two-way mode; the average tracking time has been between 3 and 4 h per week. Because emphasis was given to special experiments of *Pioneers VI, VIII,* and *IX, Pioneer VII* coverage was below average.

Pioneer VIII. The DSN was successful in regularly tracking the *Pioneer VIII* spacecraft from 85-ft-diam stations, thus obtaining a large data return. The spiral/radio coverage involving *Pioneers VI* and *VIII* started in August 1970. At this time, the *Pioneer VI* and *VIII* spacecraft were aligned versus the Sun in a straight line; later, they were in a spiral configuration. The experimenters obtained simultaneous measurements from both spacecraft on fields and particles emanating from the Sun. The correlation between measurements obtained from *Pioneers VI* and *VIII* has resulted in a better understanding of the propagation characteristics of the solar plasma and particles.

Pioneer VIII was supported by two 85-ft-diam antenna stations operating in a signal-combining telemetry mode similar to that described in SPS 37-63, Vol. II, p. 10. The culmination of this support was a signal-combining test involving DSSs 61 and 62. DSS 61 processed telemetry data using the mission-dependent *Pioneer* GOE, and DSS 62 processed telemetry data using the mission-independent Multimission Telemetry System (MMT). At DSS 62, the processed telemetry signals originating from the GOE and MMT were combined; and after signal-combining, the telemetry was further processed by the station's second telemetry and command processor. The results were as follows:

Configuration	Average bit error rate, %	Signal-to-noise ratio, dB
DSS 61 (GOE)	0.215	5.8
DSS 62 (MMT)	0.114	6.4
DSS 61/62 (combined)	0.0014	9.3

The signal-combining configuration provided a 3.5-dB improvement over the DSS 61 configuration, and a 2.9-dB improvement over the DSS 62 configuration.

Pioneer IX. The DSN regularly supported the *Pioneer IX* spacecraft from DSS 12, where the SPU cone was installed, and from DSS 14. Whenever the DSS 12 signal level dropped below -172.5 dBmW, tracking data acquisition was transferred to DSS 14. The support at DSS 12 continued until the middle of July when the station was taken out of operational status for upgrade work necessary for *Mariner* Mars 1971 support.

Support coverage for the *Pioneer IX* solar occultation experiment started on August 15, 1970. This experiment is one of the major objectives of the *Pioneer IX* mission and, therefore, the support of this spacecraft had high priority. The center point of the *Pioneer IX* solar occultation experiment will be on December 18, 1970. The DSN plans to furnish almost daily support from DSS 14 for this project, and special arrangements were made to support the Faraday rotation and the two frequency uplink Standford University experiments.

g. DSN performance. The performance of the DSN Telemetry System during the support of *Pioneers VI, VII, VIII,* and *IX* is depicted in Fig. 2. From the average signal-to-noise ratio of the detected telemetry subcarrier signal shown, it can be seen that the telecommunications link was used efficiently during most of the *Pioneer* support activities. The subcarrier energy per bit versus the unit bandwidth spectral noise density was in the vicinity of the required *Pioneer* threshold, defined by the Project at 6.8 dB for a bit-error rate of 1 error in 1000 detected bits.

During the reporting period, the four *Pioneers* operated at a telemetry bit rate of 8 and 16 bps, depending on the received subcarrier signal-to-noise ratio. *Pioneer IX* also operated in the convolutional coded mode, which allowed signal-to-noise ratios of 0.6 dB. The effective coding gain was 3.2 dB.

The performance of the DSN tracking system during the support of the four *Pioneers* is shown in Fig. 3. The total number of tracking hours is indicated at the top of each left column, and the DSN exceeded the 95% committed two-way doppler data during most of the support activities. The average doppler noise started below the normal limit line, and only a few tracking passes exhibited excessive noise in the data. The tracking data

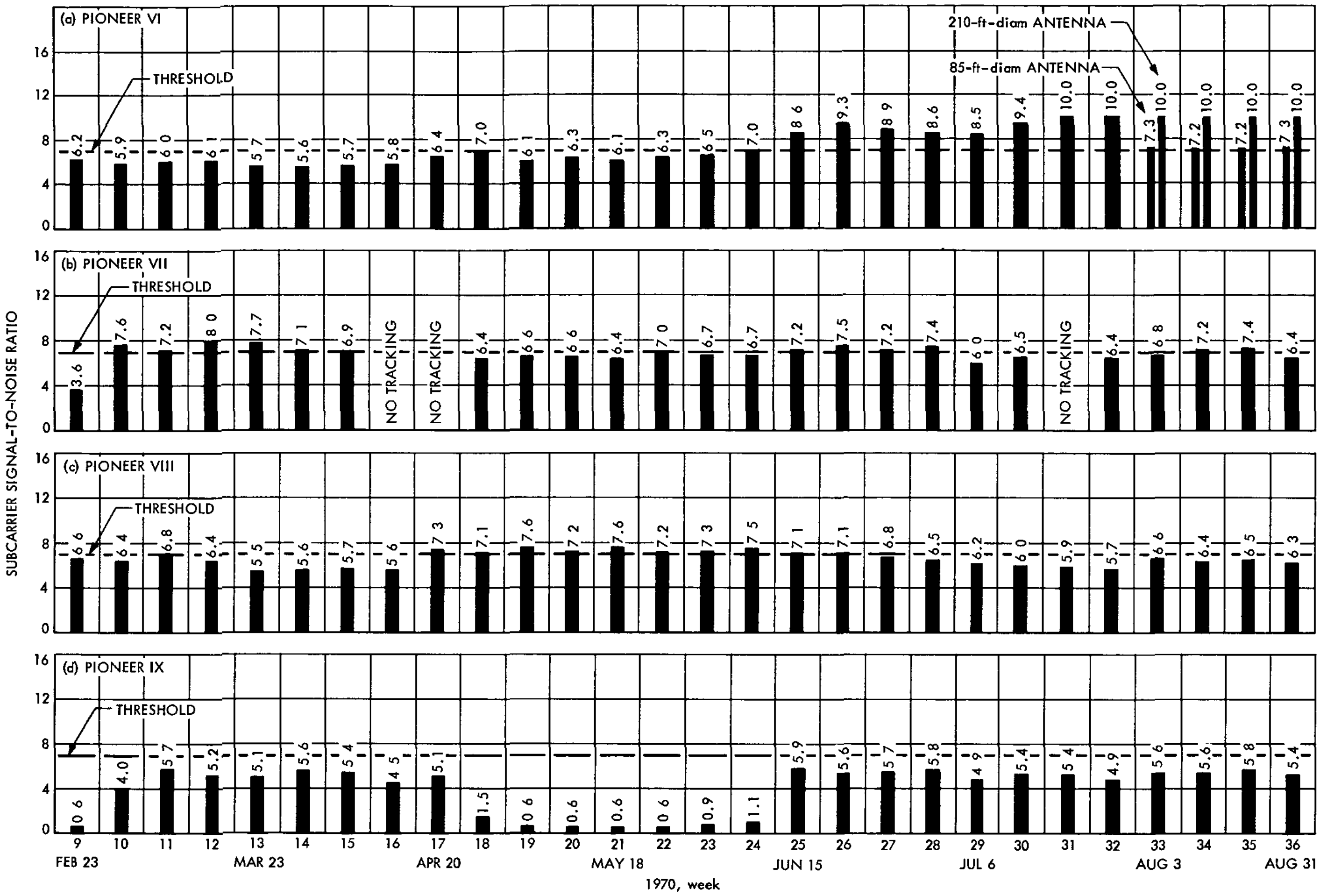

ALL VALUES ARE AVERAGE VALUES
PIONEER SIGNAL-TO-NOISE THRESHOLD = 6.8 dB FOR A BIT ERROR RATE OF 1

Fig. 2. *Pioneer VI, VII, VIII, and IX missions*—support performance of the DSN Telemetry System

were used for the update of the solar orbits of the four *Pioneer* missions.

3. *Pioneer F* and *G* Missions

a. Mission objectives.

Primary. To conduct, during the 1972 and 1973 Jovian opportunities, exploratory investigations beyond the orbit of Mars of the interplanetary medium, the nature of the Asteroid Belt, and the environmental and atmospheric characteristics of the planet Jupiter.

Secondary. To advance the technology and operational capability for long-duration flights to the outer planets.

b. Launch dates. Within the constraints of the launch vehicles available for the *Pioneer F* and *G* missions, the launch opportunities occur approximately once every 13 months. Based on the expected performance of the launch vehicles selected for the missions and the weight of the spaceflight system, the opportunities will be as follows:

(1) *Pioneer F:* February 28, 1972 to March 16, 1972.

(2) *Pioneer G:* April 3, 1973 to April 20, 1973.

Pioneer F and *G* launches will occur within these opportunities, with preference given to the early portions of each launch opportunity because the trip time from Earth to Jupiter is shorter for such launch times than for those occurring toward the end of the opportunity.

c. Trajectory. The powered flight trajectory for *Pioneers F* and *G* will be direct ascent. The interplanetary trajectory will be near the ecliptic plane, will pass through the Asteroid Belt, and will encounter Jupiter between approximately 600 and 900 days after launch.

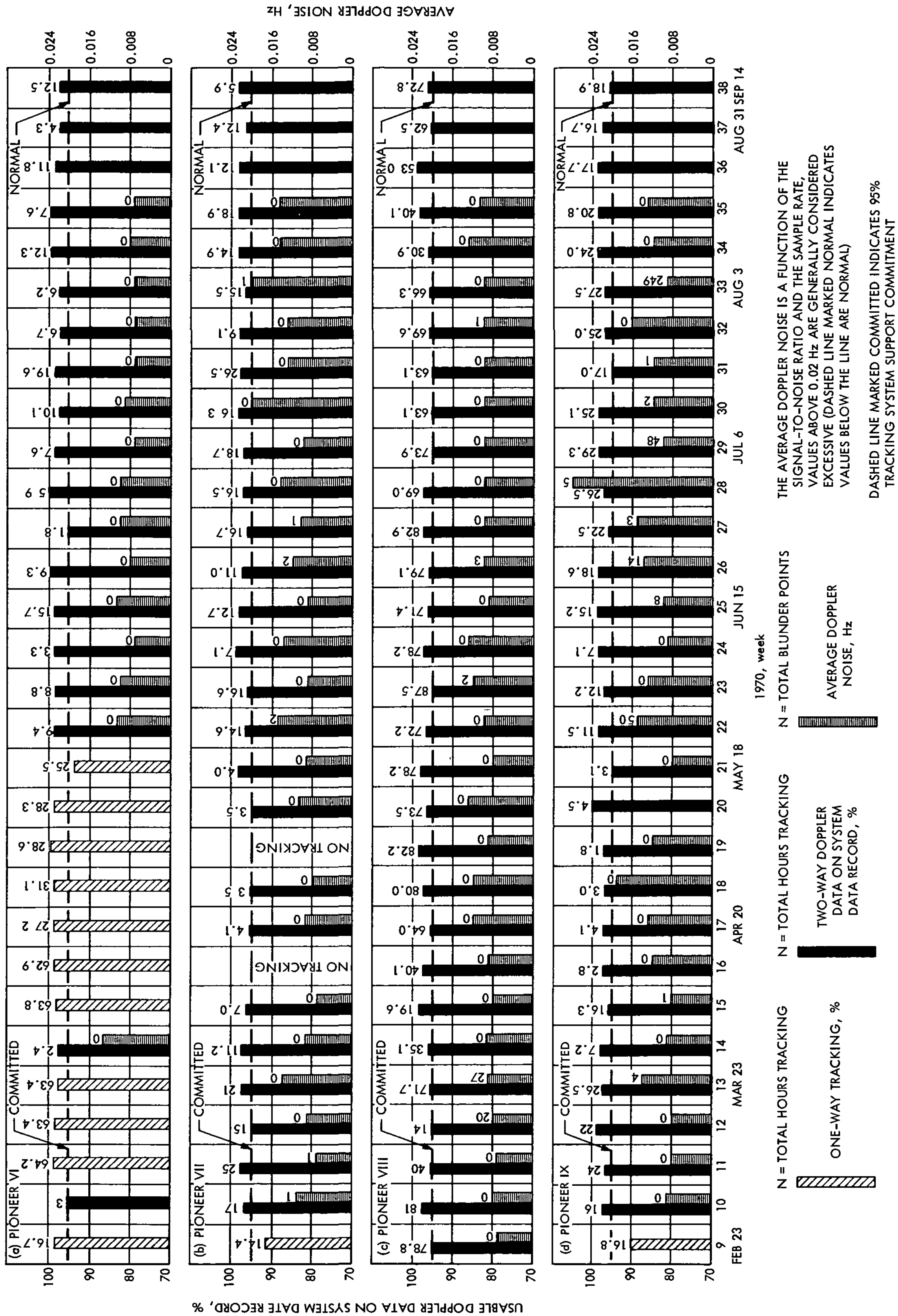

Fig. 3. Pioneer VI, VII, VIII, and IX missions—support performance of the DSN Tracking System

Pioneer F will pass by Jupiter near its equatorial plane at about 3 Jupiter radii from the planet center at closest approach and thereafter will continue away from the Sun on a trajectory that will permit the spacecraft eventually to escape from the solar system. The encounter trajectory for *Pioneer G* has not been selected.

d. Spaceflight system. The spaceflight system comprises the spacecraft [including the radioisotope thermoelectric generator (RTG)] and the scientific instruments. Equipment compartments house the spacecraft and most of the scientific instruments and a high-gain antenna with a parabolic reflector mounted above the compartments. Electric power is supplied by four RTGs that are mounted in pairs on two deployable trusses which extend radially from the RTG equipment compartment. A long deployable boom extending from the equipment compartment on a side opposite the RTG trusses supports the magnetometer sensor. Significant characteristics of the spaceflight system are as follows:

(1) *Weight:* 550 lb.

(2) *Size:* When appendages are stowed, the system fits within a cylinder having a diameter of 9 ft and a length of 8 ft. When the appendages are deployed, the RTG trusses extend 5.7 ft and the magnetometer boom extends 15.8 ft radially beyond the limits of the cylindrical envelope.

Spacecraft. Significant characteristics of the spacecraft are as follows:

(1) *Weight:* 490 lb.

(2) *Size:* Same as spaceflight system.

(3) *Attitude:* The spacecraft attitude is stabilized by spinning at approximately 5 rpm. The attitude is controlled by hydrazine-fueled thrusters which are periodically activated by ground commands to maintain the spin axis and high-gain antenna axis pointed toward Earth.

(4) *Electric power:* Supplied by four RTG units each capable of generating 30 W of dc power at 4.2 V at the time of encounter with Jupiter.

(5) *Communications:* Operates at S-band frequencies and is capable of communicating with Earth (using the DSN 210-ft-diam antennas) at distances up to approximately 15 AU.

(6) *Data rate:* Continuous transmission with capability of transmitting at all integer powers of 2 between 16 and 2048 bps.

(7) *Thermal control:* Active louvers beneath equipment compartment, thermal paints, insulation blankets, and radioisotope heaters.

(8) *Command system:* Operates at S-band frequencies with capability of implementing over 256 qualitative commands.

(9) *Propulsion system:* Hydrazine thrusters commandable from the ground and having sufficient fuel capability for up to 200-m/s velocity change in any selectable direction.

Scientific instruments. Pioneers F and *G* carry eleven scientific instruments with an approximate total weight of 60 lb.

e. Launch vehicle. The launch vehicles will be:

(1) *Pioneer F: Atlas* SLV-3C/*Centaur* D/TE-364-4.

(2) *Pioneer G: Atlas* SLV-3C/*Centaur* D-1A/TE-364-4.

f. Tracking and data acquisition. The support of the near-Earth phase of the mission will be performed by AFETR and MSFN facilities. The tracking and data acquisition support of the deep space phase of the mission will be performed by the DSN, using one 85-ft-diam antenna subnet. The 210-ft-diam antenna subnet will also be used to support the critical phases of the mission to enhance the data return from the spacecraft.

g. Management. The principal elements of the *Pioneer* Project, the organizations responsible for their management, and the principal organization responsible for their implementation are shown in Table 1.

h. Special features. The following is a summary of specific spacecraft capabilities. Their impact on the configuration and support of the tracking and data acquisition system is separately noted.

(1) The spin-stabilized third-generation *Pioneer F* and *G* spacecraft will serve as the first explorers of the Asteroid Belt and the near-Jovian environment and will be equipped with fields, particles, infrared, ultraviolet, and visible-light imaging instrumentation. Almost continuous tracking and data acquisition support will be required.

(2) Isotope heat sources (RTG) will generate onboard electric power. The elimination of solar panels will make the spacecraft attitude independent of

the Sun's location. There are no solar constraints on the high-gain antenna.

(3) For temperature control, onboard isotope heater elements will be used. The less the load on the power system, the more power is available for the telecommunication subsystem.

(4) Spacecraft attitude will be constrained by a narrow-beam, 9-ft-diam, rotating, high-gain, S-band spacecraft antenna. The 3.5-deg halfpower beamwidth of the antenna has to be pointed to the Earth. To point the high-gain antenna to Earth, the signatures of the telecommunications link will be used to determine the orientation of the spin axis.

(5) A unified hydrazene-type thruster system will be used for spin rate, spin-axis attitude, and spacecraft velocity corrections. This capability will allow accurate adjustment of the spacecraft's antenna toward Earth.

(6) Most engineering/housekeeping and instrument calibration functions will be controlled from Earth-based resources to assure the highest mission utilization efficiency. Spacecraft data processed by the

Table 1. Principal elements of the *Pioneer F* and G projects

Element	Management organization	Implementing organization
Program	OSSA Planetary Programs	OSSA Planetary Programs
Project	NASA ARC	ARC *Pioneer* Project Office
Spaceflight system		
Spacecraft		
RTG	AEC Space Nuclear Systems	Teledyne Isotopes
All other components	ARC *Pioneer* Project Office	TRW Systems Group, TRW, Inc.
Instruments	ARC *Pioneer* Project Office	
Helium vector magnetometer		Jet Propulsion Laboratory
Plasma analyzer		Time Zero Corporation
Charge particle instrument		University of Chicago
Geiger tube telescope		University of Iowa
Cosmic ray telescope		NASA Goddard Space Flight Center
Trapped radiation telescope		University of California, San Diego
Ultraviolet photometer		University of Southern California
Imaging photopolarimeter		Santa Barbara Research Center
Infrared radiometer		Santa Barbara Research Center
Asteroid/meteroid detector		General Electric Company
Meteroid detector		NASA Langley Research Center
Launch vehicle	NASA Lewis Research Center	General Dynamics, Convair Division
	NASA Goddard Space Flight Center	McDonnell-Douglas Astronautics Company
Launch operations	NASA Kennedy Space Center	General Dynamics, Convair Division
Mission operations	ARC *Pioneer* Project Office	ARC *Pioneer* Project Office
Tracking and data acquisition	Jet Propulsion Laboratory	Deep Space Network
Data processing	ARC *Pioneer* Project Office	Non-personal Services Support Contractor
Data reduction and analysis	ARC *Pioneer* Project Office	
Magnetic fields		Jet Propulsion Laboratory
Plasma		ARC Space Science Division
Charge particle composition		University of Chicago
Jovian charged particles		University of Iowa
Cosmic ray energy spectra		NASA Goddard Space Flight Center
Jovian trapped radiation		University of California, San Diego
Ultraviolet photometry		University of Southern California
Imaging photopolarimetry		University of Arizona
		Dudley Observatory
Jovian infrared thermal structure		California Institute of Technology
Asteroid/meteroid astronomy		General Electric Company
Meteroid detection		NASA Langley Research Center
S-band occultation		Jet Propulsion Laboratory
Celestial mechanics		Jet Propulsion Laboratory

AEC = Atomic Energy Commission; ARC = Ames Research Center; OSSA = Office of Space Science and Applications.

DSN for the Project will include the information necessary to control the flight equipment efficiently.

(7) A coded telemetry system with a capability of transmitting at all integer powers of 2 between 16 and 2048 bps will be adaptable to the increasing telecommunications range. The DSN expects to provide near-optimum data return.

(8) A convolutional coded telemetry data rate of 512 bps or higher is predicted during Jovian encounter. The DSN plans to provide the 210-ft-diam antenna subnet to make this data rate possible. The tracking of high doppler rates constrains the spacecraft and DSN equipment.

(9) Signatures of the telecommunications signals will be used for spin-axis attitude control. The DSN plans to make special arrangements to provide this support.

(10) Spacecraft CONSCAN capable of pointing the high-gain spacecraft antenna to Earth will use the DSN S-band uplink as a beacon signal. The DSN has to provide a stable, uplink signal.

(11) Earth-based resources will be used to navigate from Earth to Jupiter. The DSN plans to provide precision two-way tracking data for the Project for navigation.

(12) An *Atlas/Centaur* / advanced solid third stage, direct-ascent launch vehicle will inject the spacecraft at Antigua. The doppler-rate ground injection is within the capabilities of the first-acquisition stations.

(13) Extended mission phases will require telecommunications support up to 15 AU. Early studies indicated that the spacecraft's high-gain antenna configuration, combined with the DSN 210-ft-diam antenna subnet, has the capability to meet this requirement.

i. Support planning. The DSN has continued the planning and implementation of the required configuration necessary for the tracking and data acquisition support of the *Pioneer F* and *G* missions. In January 1970, a comprehensive presentation was given to the *Pioneer* Project on the Mark III Data System Development Plan, with special emphasis on the 1972–1976 time period. Requirements on the DSN Telemetry, Command, Tracking, Simulation, Monitoring, and Operations Control Systems were established. Volume III of the DSN Operations Plan for the *Pioneer F* Project, entitled DSN Systems Description, was published. This document defines the configuration and data flow of each of the six DSN systems planned to support *Pioneer F*.

Design of the spacecraft's telecommunication subsystem was reviewed. Whenever a possible design interface incompatibility was identified, DSN forwarded this information to the Project Manager. Special efforts were extended to identify, describe, and specify the Flight Project/DSN interfaces. In March 1970, the Deep Space Network/Flight Project Interface Design Handbook was published as a part of the DSN Standard Practice Document. This handbook covers DSIF and SFOF interfaces with flight projects for the period 1970–1973. Material in this handbook was used to revise, validate, and update the *Pioneer* Project document, entitled *Pioneer F* and *G* Spacecraft/DSIF Interface Specification, which controls the design of the spacecraft.

The first and second quarterly Tracking and Data System Progress Reports were issued in March and May 1970. These documents covered the near-Earth and deep-space phase tracking and data acquisition support status. *Pioneer* Quarterly Reviews were held at Ames Research Center in March and August 1970. Status of support plans was presented and interface problem areas were delineated.

To support project-dependent software development, the DSN furnished to Project all systems, hardware, and software documents which had a direct or indirect impact on the functional configuration, design, implementation, and testing of the Flight Project/DSN interface. Special emphasis was given to documents describing the computers at the SFOF Central Processing System. The DSN also furnished technical information, specifications, and guidelines to define the performance and operational characteristics of DSN interfacing hardware and software.

In October, the *Pioneer* Project published a revision of the *Pioneer F* and *G* Support Instrumentation Requirements Document. The DSN began preparation to draft the *Pioneer F* and *G NASA* Support Plan, which will describe the planned resources necessary to meet the Project's support requirements.

III. Tracking and Navigational Accuracy Analysis

ADVANCED ENGINEERING

A. Introduction, *T. W. Hamilton and D. W. Trask*

The DSN Inherent Accuracy Project was formally established by the DSN Executive Committee in July 1965. The objectives of the project are:

(1) Determination (and verification) of the inherent accuracy of the DSN as a radio navigation instrument for lunar and planetary missions.

(2) Formulation of designs and plans for refining this accuracy to its practical limits.

Achievement of these goals is the joint responsibility of the Telecommunications and Mission Analysis Divisions of JPL. To this end, regular monthly meetings are held to coordinate and initiate relevant activities. The project leader and his assistant (from the Mission Analysis and Telecommunications Divisions, respectively) report to the DSN Executive Committee, and are authorized to task project members to (1) conduct analyses of proposed experiments, (2) prepare reports on current work, and (3) write descriptions of proposed experiments. The project is further authorized to deal directly with those flight projects using the DSN regarding data-gathering procedures that bear on inherent accuracy.

The various data types and tracking modes provided by the DSIF in support of lunar and planetary missions are discussed in SPS 37-39, Vol. III, pp. 6–8. Technical work directly related to the Inherent Accuracy Project is presented in SPS 37-38, Vol. III, and in subsequent *Deep Space Network* SPS volumes, and is continued in the following sections of this volume.

For most upcoming planetary missions, such as *Mariner* Mars 1971, the tightest bounds on the allowable errors for a number of parameters arise from the navigational accuracy requirements during encounter support. In particular, encounter navigational accuracy is most sensitive to error sources that cause a diurnal signature on the radio tracking data (SPS 37-39, Vol. III, pp. 18–24). These sources of error are of two classes: (1) those parameters that define the locations of the DSS in inertial space, and (2) those phenomena that directly affect the DSS tracking data. The first category includes the locations of the DSS with respect to earth's crust; Universal Time (UT1);

polar motion (the motion of the earth's crust with respect to the spin axis); precession and nutation (orientation of the earth's spin axis with respect to inertial space); and the ephemerides of the earth, moon, and target body. Of these, uncertainties in the first three are currently the major limitations to the encounter support of navigational accuracy.

The dominant sources of error in the second category are those affecting the tracking data directly. These include frequency system instability, electrical phase path variations (through both the spacecraft and the DSS), and the transmission media (the troposphere and the charged particles in the ionosphere and space plasma).

To meet the navigational goals under consideration for some planetary projects, the uncertainties in DSS longitude and the distance off the earth's spin axis must be known on the order of 1 m. To accomplish this, polar motion which affects DSS locations by amounts ranging up to and exceeding 20 m must be taken into account as discussed in SPS 37-45, Vol. III, pp. 10–14. Polar motion data is determined optically and disseminated by both the International Polar Motion Service (IPMS) and the Bureau International de l'Heure (BIH). However, disagreements between these two sources exceed the 1-m level. A promising method for resolving these disagreements is furnished by doppler tracking of artificial satellites and has been investigated by the United States Naval Weapons Laboratory. A comparison between the doppler and optical determinations is reported in *Section B*. While the doppler determinations are only of moderate precision compared to the optical determinations, they already constitute an important measure of polar motion because of the relative independence of errors which affect the optical determinations.

With the advent of technical studies on the feasibility of planetary orbiter missions, such as the *Mariner* Mars 1971 orbiter mission and the *Viking* 1973 Mars orbiter/lander mission, JPL has become increasingly aware of the difficulties of determining accurately the orbit of a spacecraft placed as an artificial satellite at a distant planet from DSN metric radio tracking data, as discussed in SPS 37-60, Vol. II, pp. 97–103. The orbit determination process works to minimize the sum of squares of the differences between computed and actual observables. Among the error sources which contribute to these differences are charged particles in the ionosphere, the space plasma, and tropospheric refraction which directly affect the actual observable. There are also errors in tracking station locations, solar radiation pressure and drag effects, and the Mars ephemeris which lead to the errors in the computed observables. It is difficult to separate the above effects from the effects of the Mars harmonics, in that the orbit determination process may absorb the effect of any of the neglected error sources and of the solution for the estimated parameters, making it difficult to solve accurately for the spacecraft state and the Mars harmonics. *Section C*, which analyzes the processing of DSN metric tracking data during planetary orbiter missions, shows that an improved performance (reduced sensitivity to the above error sources and reduced computed running time) over methods currently used during real-time operations can be realized by using sequential estimation techniques with process noise.

B. The Use of Sequential Estimation With Process Noise for Processing DSN Tracking Data During Planetary Orbiter Missions, *R. K. Russell*

1. Problems Inherent in the Least-Squares Method and the Reasons for Using Sequential Estimation

Much experience with orbiter state estimation and prediction based on the "batch" least-squares method has been accumulated. This method is called "batch" processing since all the data is processed simultaneously to obtain an estimate of the state at one given time. During the *Lunar Orbiter* missions, severe problems were experienced with the "batch" filter operating in a real-time operations mode. Since these problems arose due to gravitational perturbations, there is the distinct possibility similar problems will exist for the *Mariner* Mars 1971 orbiter phase.

The existence of gravitational anomalies (i.e., mascons) on Mars similar to those on the moon could impose a requirement to estimate a large number of the harmonics in the Legendre expansion representation of the gravity field. Estimation of a large number of harmonics results in problems of numerical accuracy and consumption of time in data processing. As a result, only a relatively low order of harmonics may be included in the estimation list.

However, estimation of a small number of harmonics (such as fourth order and less) may not be sufficient to adequately describe gravitational anomalies. This may result in relatively poor state estimation and prediction capabilities. In addition, estimation of an inadequate harmonic set may actually cause the inclusion of certain data such as that near periapsis to actually degrade the state estimate. From this arises the problem of ascertaining the data span to provide the best state estimate.

Finally, the differential correction method works to minimize the sum of squares of the differences between computed and actual observables. There are many error sources which contribute to these differences. Charged particles in the ionosphere and transmission refraction in the troposphere directly affect the actual observables. Errors in tracking station locations, solar radiation pressure and drag effects, and the Mars ephemeris lead to errors in the computed observables. It is extremely difficult to separate the effects of all these error sources from the effects of the Mars harmonics. The differential correction method will absorb the effect of any of the neglected error sources into the solution for the estimated parameters, making it difficult to solve accurately for the spacecraft state and the Mars harmonics.

All these problems pose severe requirements on data processing and human response, which in a real-time operation may be difficult to meet.

As a result it would seem to be reasonable to look for a data processing method which could circumvent some of the problems associated with the batch filter operating in the presence of gravitational perturbations. The sequential data filter, incorporating process noise, appears to be such a method. The inclusion of an appropriately chosen process noise may obviate the need to solve for harmonics in real-time while providing a more accurate state estimate than that of the batch filter. In addition this filter seems to eliminate the problem of "optimum data spans" as additional data does not degrade the state estimate.

2. Theory of the Sequential Data Processing Method

Sequential estimation, as embodied in a double precision computer study program, the Sequential Orbit Determination (SOD) Program (SPS 37-62, Vol. II, pp. 97–104), is performed as follows:

(1) The simulated state $(\bar{x}_a, \bar{v}_a)$ and estimated state $(\bar{x}, \bar{v})$ of the spacecraft are mapped between points of time in target-centered, cartesian, plane-of-the-sky coordinates. The vector equations are:

$$\left.\begin{aligned} \dot{\bar{v}}_a &= -\frac{\mu_a}{r^3}\bar{x}_a + \bar{a} \\ \dot{\bar{x}}_a &= \bar{v}_a \end{aligned}\right\} \text{simulated state}$$

$$\left.\begin{aligned} \dot{\bar{v}} &= -\frac{\mu}{r^3}\bar{x} \\ \dot{\bar{x}} &= \bar{v} \end{aligned}\right\} \text{estimated state}$$

where a is a perturbative acceleration due to gravitational harmonics, and μ is the mass constant of Mars. (Note the simulated state is mapped with the simulated μ_a, while the estimated state is mapped with the estimated μ.)

The actual mapping of the simulated state is performed as follows:

$$(\bar{x}_{a_{i+1}},\bar{v}_{a_{i+1}}) = \Phi(\bar{x}_{a_i},\bar{v}_{a_i},\mu_a) + (\bar{0},\bar{a},\Delta t)$$

where i denotes the ith timepoint, Φ is an exact two-body mapping of the state, and $\Delta t = t_{i+1} - t_i$. The last term is an approximation to the perturbation in the simulated state at t_{i+1} due to accelerations over the interval Δt.

The mapping of the estimated state obeys the equation

$$(\bar{x}_{i+1}\bar{v}_{i+1}) = \Phi(\bar{x}_i,\bar{v}_i,\mu)$$

(2) The tracking observables ρ_a (range rate) and ρ_a (range) are generated directly from the simulated state. The observables are assumed corrupted by independent, gaussian noise increments, and the observable vector z_a becomes

$$z_a = \begin{bmatrix} \dot{\rho}_a \\ \rho_a \end{bmatrix} + \begin{bmatrix} \eta_1 \\ \eta_2 \end{bmatrix}$$

η_1 and η_2 are simulated by a random number generator which yields the following statistics:

$$E[\eta_1] = E[\eta_2] = 0$$

$$E[\eta_1(t_i)\eta_1(t_j)] = \sigma^2_{\eta_1}\,\delta_{ij}$$

$$E[\eta_2(t_i)\eta_2(t_j)] = \sigma^2_{\eta_2}\,\delta_{ij}$$

$$E[\eta_1(t_i)\eta_2(t_j)] = 0$$

The estimated tracking observables $\dot{\rho}$ and ρ are computed directly from the estimated state.

(3) The filter covariance, Γ_p, of errors in the estimated state and gravitational mass, μ, is mapped by the following equation:

$$\frac{d\Gamma_p}{dt} = F\Gamma_p + \Gamma_p F^T + Q$$

where

$$F = \frac{\partial\left(-\frac{\mu}{r^3}\bar{x}, \bar{v}, \mu\right)}{\partial(\bar{v}, \bar{x}, \mu)}$$

and Q is a symmetric matrix representative of the covariance of any assumed "white noise" type of accelerations on the probe (including both gravitational and nongravitational accelerations).

We define:

Γ_a to be the covariance of errors in the estimated state due only to data noise.

Γ_c to be the covariance of errors in the estimated state due to data noise and errors in a set, $\bar{y}$, of gravitational harmonics. ($\bar{y}$ are "consider parameters.")

The actual mapping is performed as follows:

$$\Gamma_{a_{i+1}} = U_{i+1,i}\,\Gamma_{a_i}\,U^T_{i+1,i}$$

where

$$U_{i+1,i} = \left(\frac{\partial\bar{x}_{i+1}}{\partial\bar{x}_i}\right)$$

and

$$\Gamma_{p_{i+1}} = \Gamma_{a_{i+1}} + Q$$

$$\Gamma_{c_{i+1}} = \Gamma_{a_{i+1}} + S_{i+1}\tilde{\Gamma}_y S^T_{i+1}$$

where

$$S_{i+1} = \left(\frac{\partial\bar{x}_{i+1}}{\partial\bar{y}}\right)$$

Γ_y is the *a priori* covariance of errors in the set y of harmonics. S is called the sensitivity matrix (SPS 37-56, Vol. II, pp. 85–87) and

$$S_{i+1} = U_{i+1,i}S_i + V_{i+1}$$

where

$$V_{i+1} = \left.\frac{\partial\bar{x}_{i+1}}{\partial\bar{y}}\right|_{x_i\ \text{constant}}$$

(4) A new state estimate is formed at each point of observation, which can be as often as desired. The new estimate x_+ is computed from the old estimate x_- by the equation

$$\bar{x}_+ = \bar{x}_- + K[z_a - z]$$

where z is the estimated observable vector

$$z = \begin{bmatrix} \dot{\rho} \\ \rho \end{bmatrix}$$

and K, the gain matrix, is given by

$$K = \Gamma_p^- H^T [H \Gamma_p^- H^T + R]^{-1}$$

with

$$\Gamma_p^- = E[(\bar{x}_a - \bar{x}_-)(\bar{x}_a - \bar{x}_-)^T]$$

$$H = \frac{\partial z}{\partial \bar{x}_-}$$

$$R = \begin{bmatrix} \sigma_{\eta_1}^2 & 0 \\ 0 & \sigma_{\eta_2}^2 \end{bmatrix}$$

The various covariances of errors in the estimated state incorporating the new observational data are formed as follows:

$$\Gamma_a^+ = (I - KH)\Gamma_a^-(I - KH)^T + KRK^T$$
$$\Gamma_p^+ = (I - KH)\Gamma_p^-(I - KH)^T + KRK^T$$
$$\Gamma_c^+ = \Gamma_a^+ + S^+\tilde{\Gamma}_y S^{+T}$$

where

$$S^+ = (I - KH)S^-$$

These then are the equations governing the functioning of the sequential filter in SOD. It remains, however, to more adequately delineate the matrix Q, which is designed to be representative of the covariance of the perturbative gravitational accelerations experienced by the spacecraft.

3. Methods for Degrading the Information Content of the Data to Compensate for Gravitational Anomalies

It can be seen from the equations presented in *Subsection* 2 that the gain matrix K, is a strong function of the mapped covariance, Γ_p, which contains the matrix Q. An increase in Q will have the effect of increasing the weight of the new data with respect to the old.

As a result of this, Q can be varied to properly deweight old data in portions of orbit where gravitational anomalies significantly perturb the orbit.

In SOD, Q is assumed to be a 7×7 matrix formed as

$$Q = \left[\begin{array}{c|ccc|c} 0_{3\times 3} & & 0 & & 0 \\ \hline & q & 0 & 0 & \\ 0 & 0 & q & 0 & 0 \\ & 0 & 0 & q & \\ \hline 0 & & 0 & & 0 \end{array}\right]$$

where

$$q = \tau \Delta t \sigma_\eta^2$$

with

$\Delta t = t_{i+1} - t_i =$ mapping interval

$\tau =$ assumed correlation time of the perturbative acceleration

$\sigma_\eta =$ standard deviation of perturbative acceleration (process noise)

Q, therefore, represents a corruption of the velocity information due to a perturbative acceleration acting over the time interval Δt.

4. Selection of the Process Noise Model

Inasmuch as the Legendre expansion of a general gravitational field yields a power series in (R_M/R) (R being the distance to the center of the coordinate system and R_M being the mean radius of the gravitational body), it would appear natural to choose the standard deviation of the process noise σ_η to be of the form

$$\sigma_\eta = k\left(\frac{R_M}{R}\right)^n$$

where k and n are constant parameters to be chosen on the basis of simulation exercises.

If the center of the coordinate system is defined to be the center of mass of the perturbing body, then the first-order harmonics in the Legendre expansion are identically zero. As a result, only second-order harmonics and above contribute to the perturbative field, creating perturbative accelerations which vary with the radial distance by $1/R^4$ or higher powers.

A study to find acceptable values of k and n was made. For this purpose the *Mariner* Mars 1971 Mission A orbit with periapsis height of 1250 km was used. Harmonics through fourth order were considered (excepting first order). Position, velocity, and μ were estimated. *A priori* uncertainty in position and velocity were chosen so as not to affect the estimation (i.e., 1000 km on x, y, z and 10 m/s on $\dot{x}$, $\dot{y}$, $\dot{z}$). *A priori* uncertainty on μ was assumed to be 0.1 km^3/s^2. Five-min data compression was used. Range rate data with a noise standard deviation of 1 mm/s commenced 40 min after the initial periapsis P_0.

The orbit characteristics are:

$a = 12650.6$ km = semi-major axis

$e = 0.632952$ = eccentricity

$T = 0$ second = time of periapsis passage

$\Omega = 310°0$ = longitude of ascending node (relative to Earth equatorial 1950.0 coordinate)

$\omega = 309°9$ = argument of periapsis (relative to Earth equatorial 1950.0 coordinate)

$i = 61°0$ = inclination (relative to Earth equatorial 1950.0 coordinate)

The uncertainties in gravitational harmonics of Mars are shown in Table 1. These have been computed by extrapolation from the Earth harmonics assuming:

(1) Structural material of Mars is similar to that of Earth.

(2) The time constant of return to equilibrium is the same as the Earth.

Table 1. One-sigma uncertainties for Mars harmonic coefficients based on dimensional analysis

Zonal harmonics	One-sigma uncertainty	Tesseral harmonics	One-sigma uncertainty
J_2	0.22×10^{-4}	C_{21}, S_{21} C_{22}, S_{22}	0.233×10^{-4} 0.111×10^{-4}
J_3	0.202×10^{-4}	C_{31}, S_{31} C_{32}, S_{32} C_{33}, S_{33}	0.828×10^{-5} 0.260×10^{-5} 0.107×10^{-5}
J_4	0.13×10^{-4}	C_{41}, S_{41} C_{42}, S_{42} C_{43}, S_{43} C_{44}, S_{44}	0.410×10^{-5} 0.960×10^{-6} 0.258×10^{-6} 0.910×10^{-7}

The criterion of acceptability was chosen to be:

Which values of k and n minimized the rss position standard deviation

$$|\sigma_x| = \sqrt{\sigma_x^2 + \sigma_y^2 + \sigma_z^2}$$

formed at the second or third periapsis (P_1 or P_2) as a result of range rate data taken to P_1 (12^h) or P_2 (24^h)? (Note that $|\sigma_x|$ was taken from the consider covariance matrix Γ_c.)

The results are shown in Fig. 1 for $|\sigma_x|$ at P_1 and in Fig. 2 for $|\sigma_x|$ at P_2. The results reveal three acceptable forms of process noise standard deviation. They

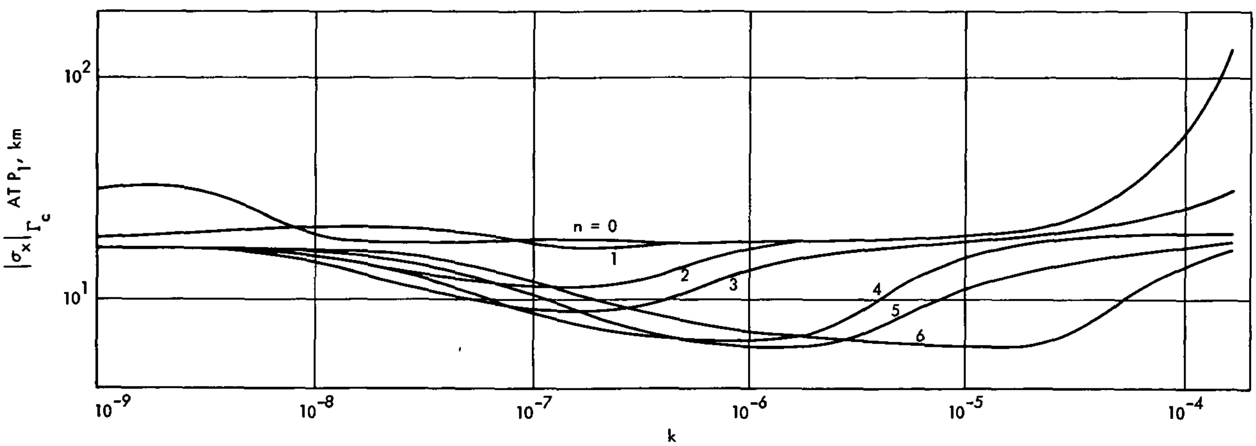

Fig. 1. Sensitivity of $|\sigma_x|_{\Gamma_c}$ at P_1 to k, n

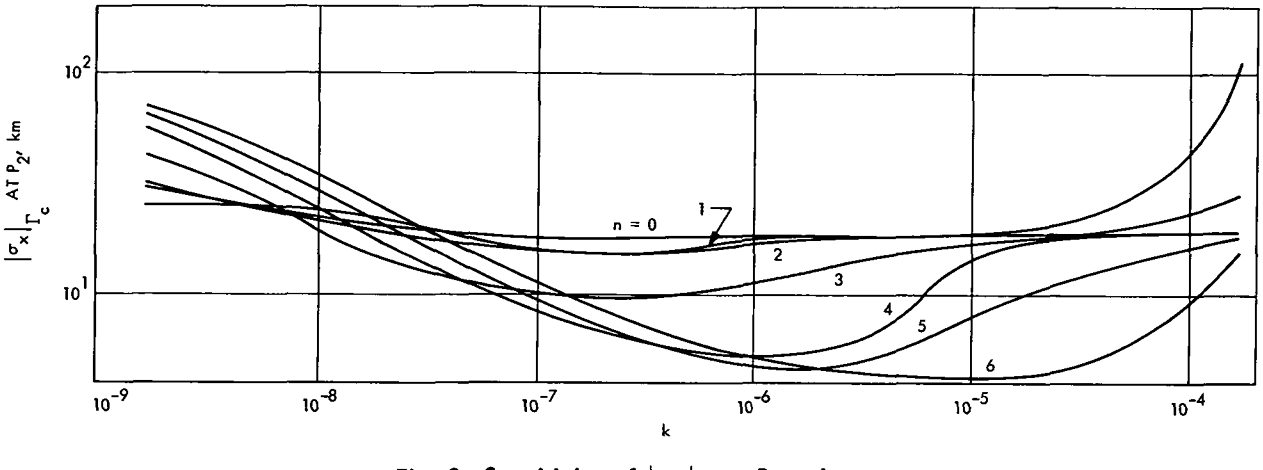

Fig. 2. Sensitivity of $|\sigma_x|_{\Gamma_c}$ at P_2 to k, n

comprise the values 4, 5, and 6 for n. The forms chosen for further study are:

(a) $\sigma_\eta = 1.67 \times 10^{-5} \times \left(\frac{R_M}{R}\right)^6$

(b) $\sigma_\eta = 1.67 \times 10^{-6} \times \left(\frac{R_M}{R}\right)^5$

(c) $\sigma_\eta = 1.67 \times 10^{-6} \times \left(\frac{R_M}{R}\right)^4$

Figure 1 shows an improvement in $|\sigma_x|$ at P_1 of roughly a factor of 3 over the batch filter for a similar data span for these three process noise forms.

5. Presentation of Orbit Determination Accuracy Studies Using Acceptable Process Noise Models

Using the Mission A orbit with $h_p = 1250$ and $i = 80°$ (relative to Mars equator) and the study assumptions outlined in *Subsection 4* (except no data compression was used), $|\sigma_x|$ was computed from Γ_c at 2-hour intervals to 24 hours for all three process noise models. Figure 3 displays these results in the form of a filter time history plot using process noise model (a) shown above. The solid lines indicate range rate data taken throughout the 24-hour interval. Dashed lines indicate data processing was terminated at P_1.

All three process noise models yield very similar results. It can be seen that mapping from P_1 to P_2 causes a severe degradation in the state estimate at P_2.

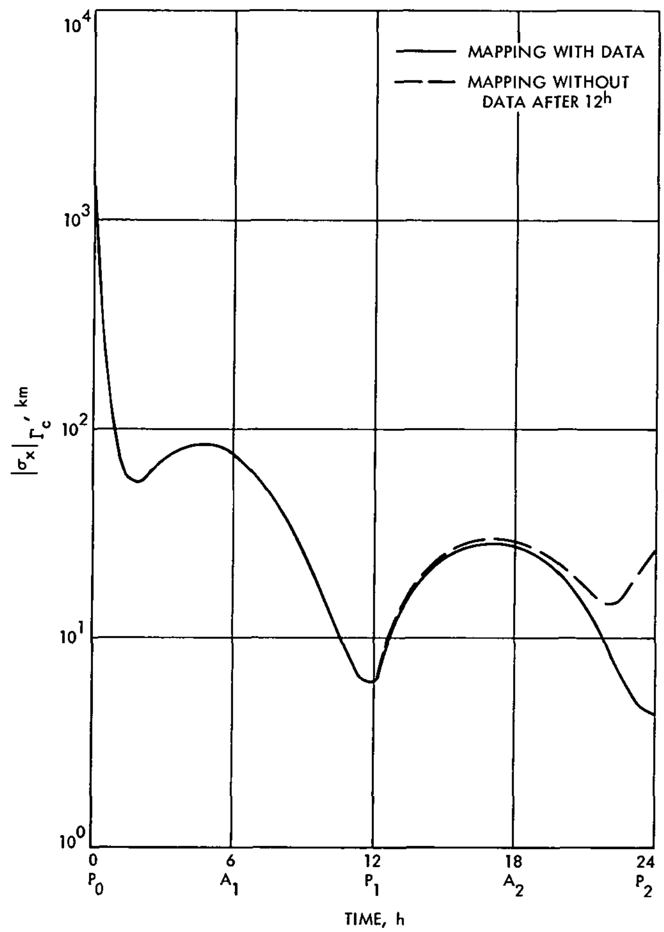

Fig. 3. $|\sigma_x|_{\Gamma_c}$ vs maptime (with and without data) for $\sigma_\eta = 1.67 \times 10^{-5} (R_M/R)^6$

Using what appears to be the most acceptable process noise models, the sequential filter yields the following results:

$|\sigma_x|_{\Gamma_c} = 6\text{–}7$ km at P_1 (12^h) with data to 12^h

$|\sigma_x|_{\Gamma_c} = 4.4\text{–}5.7$ km at P_2 (24^h) with data to 24^h

$|\sigma_x|_{\Gamma_c} = 26\text{–}27$ km at P_2 (24^h) with data to 12^h

An additional requirement on the process noise model should be that the behavior of the computed filter covariance Γ_p should be reflective of the consider covariance Γ_c and the $|\sigma_x|$ formed from Γ_p should not be overly optimistic (i.e., $|\sigma_x|_{\Gamma_p} \geq |\sigma_x|_{\Gamma_c}$). It is therefore desirable to have $|\sigma_x|_{\Gamma_p} \approx |\sigma_x|_{\Gamma_c}$.

Figures 4, 5, and 6 show the filter time history of the rss position standard deviation computed from both Γ_c and Γ_p for data taken and processed up to 24 hours for the three listed process noise models. Figure 5 reveals that $\sigma_\eta = 1.67 \times 10^{-6}\ (R_M/R)^5$ yields slightly optimistic values for $|\sigma_x|_{\Gamma_p}$. This, however, can be corrected by increasing the size of k, which will compromise the estimation capability of this model only slightly (see Figs. 1 and 2). Figures 7, 8, and 9 show $|\sigma_x|$ based on Γ_c and Γ_p for data to 12^h and mapping to 24^h.

These figures reveal an intrinsic problem with the concept of process noise as a model for gravitational perturbations, namely that the physical law of gravitation being a conservative field is not embodied in the theory. As a result mapping over lengthy intervals tends to increase $|\sigma_x|_{\Gamma_p}$ well beyond $|\sigma_x|_{\Gamma_c}$. Part of this difficulty can be removed by a more judicious choice of k in the process noise model. However, it should be anticipated that $|\sigma_x|_{\Gamma_p}$ will gradually tend to diverge as a result of lengthy mapping without data.

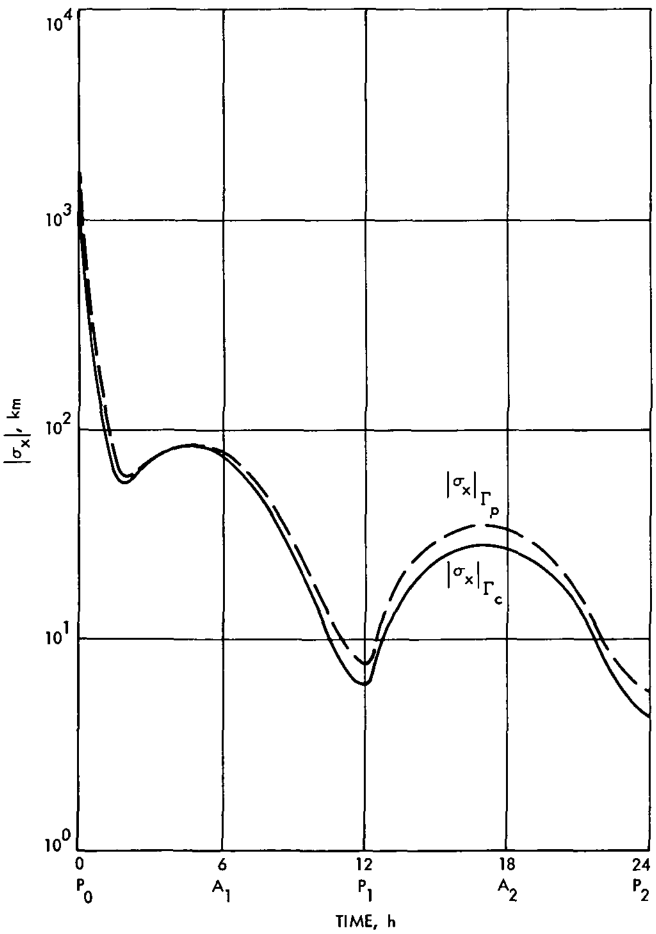

Fig. 4. $|\sigma_x|_{\Gamma_c}$ and $|\sigma_x|_{\Gamma_p}$ vs maptime (with data) for $\sigma_\eta = 1.67 \times 10^{-5}\ (R_M/R)^6$

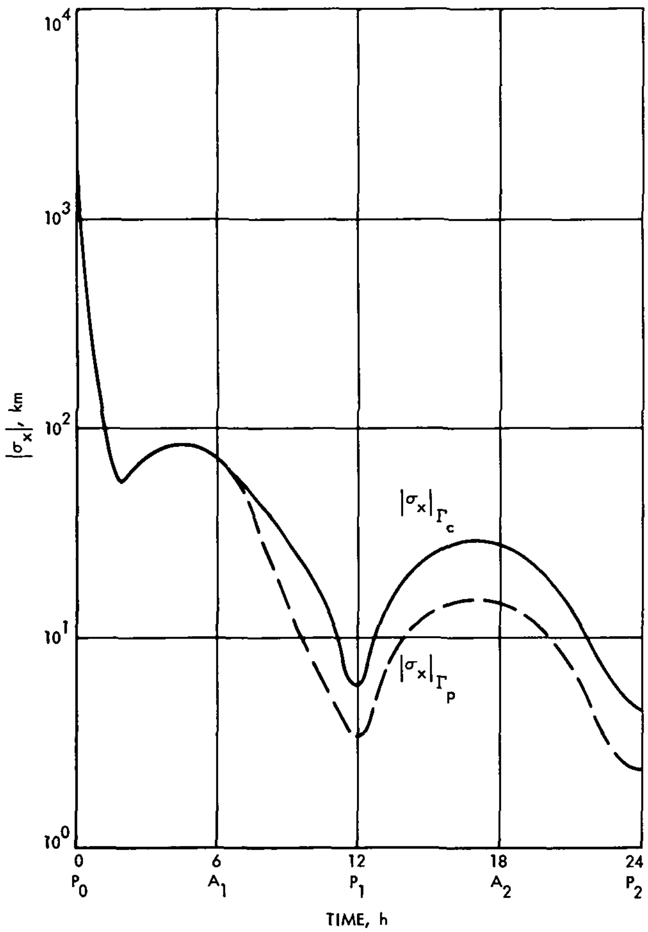

Fig. 5. $|\sigma_x|_{\Gamma_c}$ and $|\sigma_x|_{\Gamma_p}$ vs maptime (with data) for $\sigma_\eta = 1.67 \times 10^{-6}\ (R_M/R)^5$

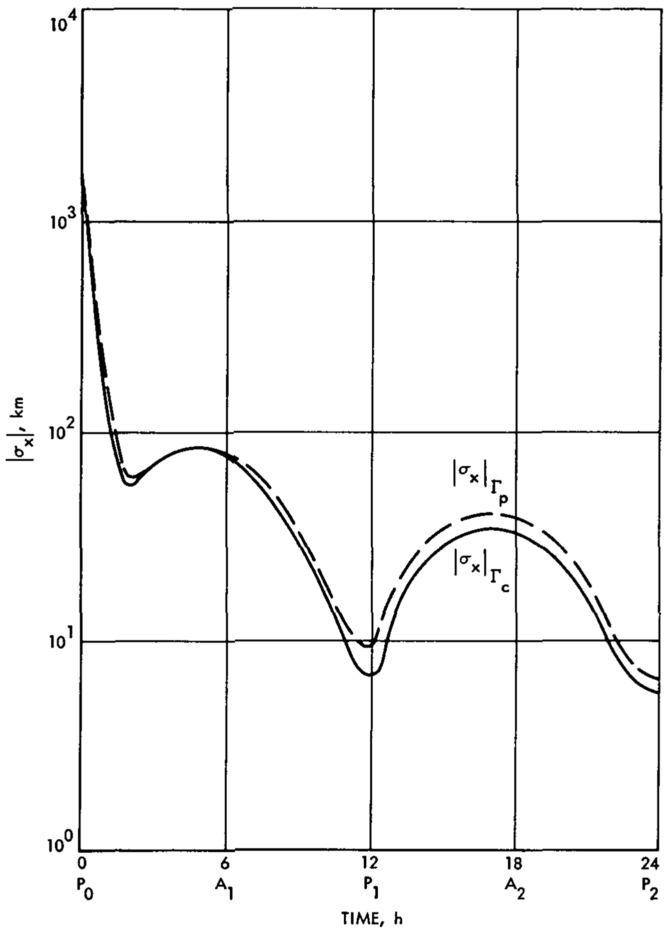

Fig. 6. $|\sigma_x|_{\Gamma_c}$ **and** $|\sigma_x|_{\Gamma_p}$ **vs maptime (with data) for** $\sigma\eta = 1.67 \times 10^{-6} (R_M/R)^4$

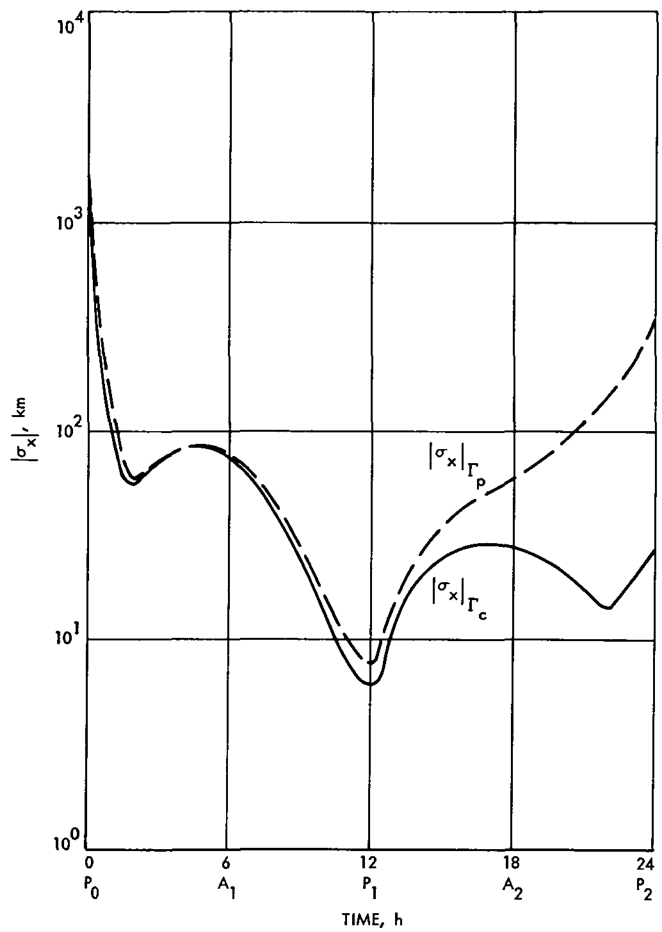

Fig. 7. $|\sigma_x|_{\Gamma_c}$ **and** $|\sigma_x|_{\Gamma_p}$ **vs maptime (without data after** 12^h**) for** $\sigma\eta = 1.67 \times 10^{-5} (R_M/R)^6$

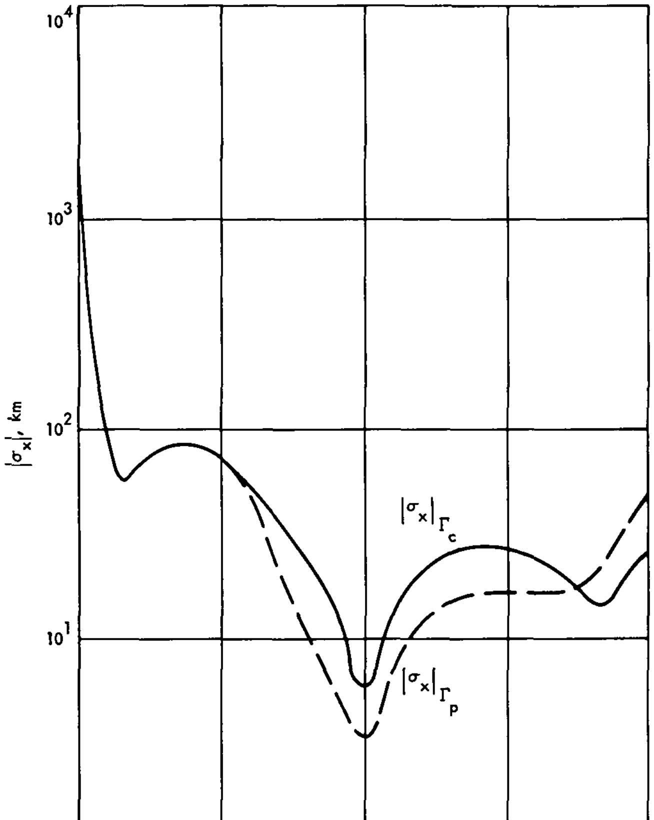

Fig. 8. $|\sigma_x|_{\Gamma_c}$ **and** $|\sigma_x|_{\Gamma_p}$ **vs maptime (without data after 12^h) for** $\sigma\eta = 1.67 \times 10^{-6} (R_M/R)^5$

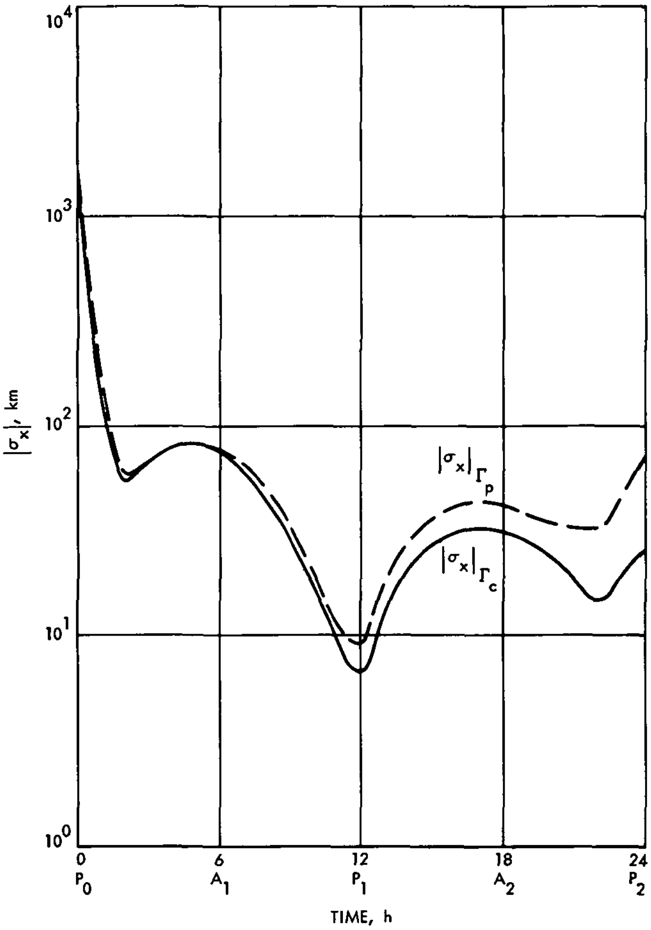

Fig. 9. $|\sigma_x|_{\Gamma_c}$ **and** $|\sigma_x|_{\Gamma_p}$ **vs maptime (without data after 12^h) for** $\sigma\eta = 1.67 \times 10^{-6} (R_M/R)^4$

6. Comparison of the Sequential and Least Squares Data Processors

Figures 10 and 11 show the comparison of SOD and a least-squares data processor called SNAP for Mission A with $h_p = 1500$ km and 1250 km, respectively. Shown in these figures is rss position uncertainty $|\sigma_x|$ at P_1 formed with data to 8^h, 9^h, 10^h, 11^h, and 12^h.

It appears that there exists a great improvement in $|\sigma_x|_{P_1}$ for the batch filter when not estimating harmonics as a result of terminating data at 11^h. However, the sequential filter continues to show improvement in $|\sigma_x|_{P_1}$ as data goes to 12^h, in effect eliminating the problem of optimal data spans.

In addition it should be mentioned that the sequential filter, with a satisfactory process noise, does show an improvement over the batch filter (not estimating harmonics and using an optimal data span) in estimation capability.

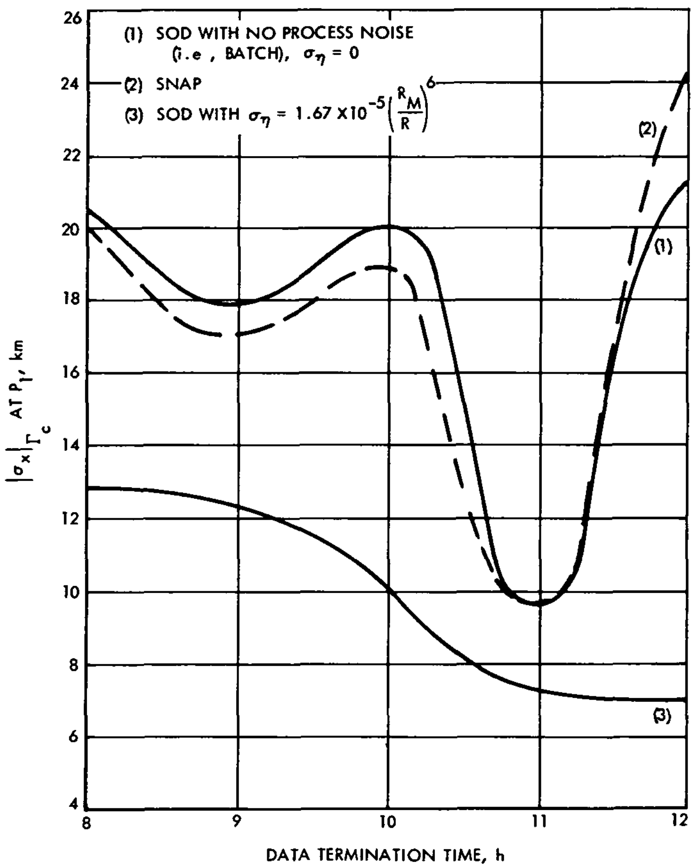

Fig. 10. $|\sigma_x|_{\Gamma_c}$ at P_1 vs hours of data (h_p = 1500)

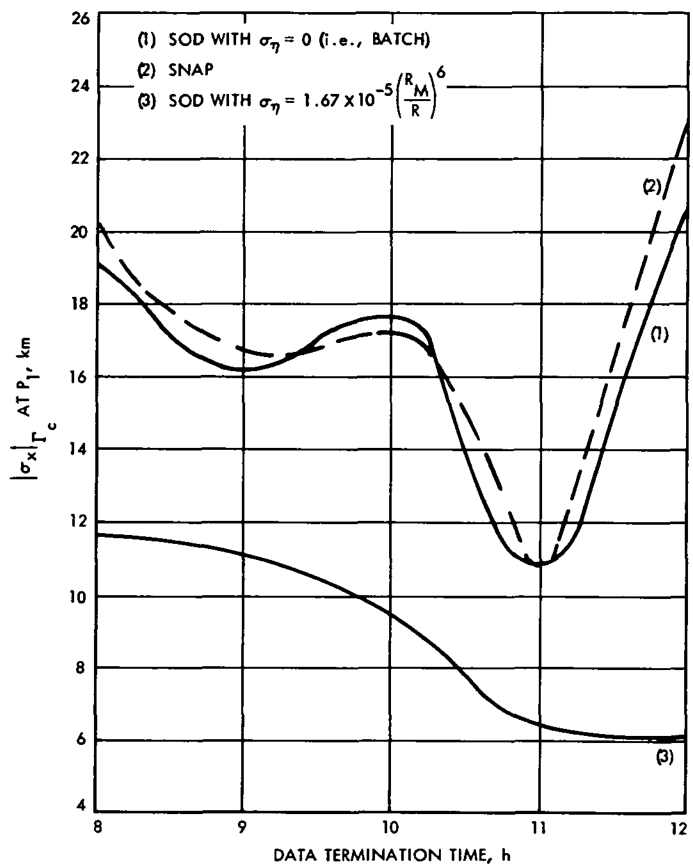

Fig. 11. $|\sigma_x|_{\Gamma_c}$ at P_1 vs hours of data (h_p = 1250)

C. Polar Motion: Doppler Determinations Using Satellites Compared to Optical Results, *C. C. Chao and H. F. Fliegel*[1]

1. Introduction

Critical to the success of JPL deep space missions is accurate knowledge of time and polar motion. To meet the navigational goals under consideration for some planetary projects, the uncertainties in DSS longitude and the distance off the earth's spin axis must be known on the order of 1 m. We find that the disagreements between optical sources of polar motion are of this order. A promising method for resolving these disagreements is furnished by doppler tracking of artificial satellites.

Anderle (Ref. 1) has determined the position of the terrestrial poles daily over a 2-yr period using doppler tracking data on navigational satellites. In this study, the precision and the absolute accuracy attainable by this promising new method is compared with that of the principal astronomical sources: the International Latitude Service, the Bureau International de L'Heure, and the International Polar Motion Service.

2. Sources of Polar Motion Data

There are three major optical sources of polar motion data. The first of these sources is the chain of five International Latitude Service (ILS) stations, all situated at approximately the same latitude and observing almost all stars in common. This source is most nearly immune to the systematic errors that plague astrometric measurements; it is therefore quite valuable even though the random error from night to night is large. The second source is the Bureau International de L'Heure (BIH) solution for time and polar motion, formed from an ever-increasing number of zenith tubes, astrolabes, and photoelectric transits throughout the world. The third source is the International Polar Motion Service (IPMS) average of 26 participating observatories. For convenience these three sources are designated A for ILS, *B* for BIH, and *C* for IPMS. They are strongly correlated. All the ILS stations are used by both IPMS and BIH, and 23 of the 26 stations are used by BIH.

The doppler data of Anderle (Ref. 1), designated *D*, were taken by 13 base stations and several mobile stations mostly on the American continent. Least-squares solutions were made for the six orbital parameters, a drag scaling factor, the coordinates of the mobile stations, and instrumental bias factors, from batches of data each spanning 48 h. These workers found no bias between computations based on different satellites, but reported a 2.0-m bias in the *Y* direction between doppler values and IPMS.

3. Accuracy of Optical Versus Doppler Polar Motion Data

We want to know the standard deviations of *A*, *B*, and *C* separately, with respect to the true pole (wherever that may be). We can measure only the differences between the sources. Subtracting out the constant average difference between the sources (which presumably represents a bias in one or both sources) and calculating the sum of the squares of the differences so adjusted, we obtain the standard deviation between sources:

$$\sigma_{IJ}^2 = \frac{\sum_1^n \Delta_{IJ}^2}{n-1} \tag{1}$$

where n is the number of observations, and

$$\sum_1^n \Delta_{IJ}^2 \equiv \sum_1^n (I-J)^2 - \frac{\left[\sum_1^n (I-J)\right]^2}{n} \tag{2}$$

where I and J represent the coordinates of the pole (in either the X or the Y direction) given by any two sources at a given time. In principle, we can calculate the standard deviations of each source from the true pole if we know the correlation coefficients:

$$\sigma_{IJ}^2 = \sigma_I^2 + \sigma_J^2 - 2\rho_{IJ}\sigma_I\sigma_J \tag{3}$$

where σ_{IJ}^2 is what we measure, σ_I and σ_J are what we want to deduce, and ρ_{IJ} is the normalized correlation coefficient of I,J such that $-1 \leq \rho_{IJ} \leq +1$. There are three such equations, and three unknowns if the correlation coefficients can be estimated.

Let us assume that the only correlation between the sources is caused by the stations shared between them. The unnormalized covariance is

$$\text{cov}\,(I,J) \equiv \rho(I,J)\,\sigma_I\sigma_J = E(I \cdot J) - E(I) \cdot E(J) \tag{4}$$

[1]The authors gratefully acknowledge P. Gottlieb, Systems Analysis Section, and J. G. Williams, Tracking and Orbit Determination Section, for their many helpful suggestions.

where $E(I \cdot J)$ is the expected value of $I \cdot J$, and $E(I)$, $E(J)$ are the expected values of I and of J, respectively. In our case, BIH, for example, is an average of stations belonging to ILS (A) and those not belonging to ILS ($\bar{A}$); and we may write

$$B = k_1 A + k_2 \bar{A} \tag{5}$$

where k_1 and k_2 are the relative weights of A and of $\bar{A}$ in the BIH solution. From Eq. (4), we note that cov is a linear operator. Therefore, we may write

$$\begin{aligned} \text{cov}\,(B,A) &= \text{cov}\,(k_1 A + k_2 \bar{A}, A) \\ &= k_1 \,\text{cov}\,(A,A) \end{aligned} \tag{6}$$

because cov $(A,\bar{A})$ is zero by hypothesis. From Eq. (4), remembering that $E(A)$ is zero because we removed all biases (hopefully) by means of Eq. (2), we have

$$\text{cov}\,(A,A) = \sigma_A^2 \tag{7}$$

and therefore

$$\begin{aligned} \sigma_{AB}^2 &= \sigma_A^2 + \sigma_B^2 - 2k_{1,AB}\,\sigma_A^2 \\ &= (1 - 2k_{1,AB})\,\sigma_A^2 + \sigma_B^2 \end{aligned} \tag{8}$$

The same logic applies to σ_{AC}. In practice, the computation of k_1 must be done separately for X and for Y.

To estimate the values of k_1, we proceed as follows. The observational equation for the coordinates of the pole (X,Y) with respect to the Conventional International Origin from latitude information alone is (Ref. 2)

$$X \cos L_{0,i} + Y \sin L_{0,i} = \phi_i - \phi_{0,i} \tag{9}$$

where $(L_{0,i}, \phi_{0,i})$ are the nominal values for the longitude and latitude, respectively, of the ith observatory, and ϕ_i is the true latitude measured by the ith observatory on a given night. It can be shown that, if the BIH observatories are well distributed in longitude so that

$$\sum^{\text{BIH}} \cos L_{0,i} \sin L_{0,i} \doteq 0 \tag{10}$$

then values of k_1 and k_2 satisfying Eq. (5) exist and are given by the equations

$$k_1 = \frac{\sum^{\text{ILS}} \omega_i \cos^2 L_{0,i}}{\sum^{\text{BIH}} \omega_i \cos^2 L_{0,i}} \tag{11}$$

and

$$k_2 = 1 - k_1 \tag{12}$$

where

ω_i = weight ascribed to the ith observatory by BIH

$\sum^{\text{ILS}}$ = sum taken over ILS observatories only

$\sum^{\text{BIH}}$ = sum over all BIH observatories

The values of ρ_{IJ} derived in this analysis are given in Table 1. The biases between the various sources were solved numerically, and are given in Table 2. Solutions of Eq. (3) were obtained numerically, and are given in Table 3. The goodness of the solutions is indicated by the values of Table 4. The data used spanned 3 yr from 1967.0 to 1970.0. The precision of the IPMS determinations is significantly greater than that of BIH. Both BIH and IPMS are about equally precise in X and in Y, but the ILS is probably more precise in Y (along the axis of Gaithersburg, Maryland, and Mizusawa, Japan) than in X.

Once the standard deviations of BIH with respect to the true pole have been derived, the corresponding values for the doppler data can be determined. They are given by

$$\sigma_D^2 = \sigma_{B-D}^2 - \sigma_B^2 \tag{13}$$

Table 1. Correlation coefficients between sources of polar motion data

	X	Y
ρ_{AB}	0.137	0.114
ρ_{AC}	0.219	0.166
ρ_{BC}	0.624	0.688

A: ILS mean of 5 stations.
B: BIH mean of 40 stations.
C: IPMS mean of 26 stations.

in X and Y, where σ^2_{B-D} can be directly measured, and σ^2_D is the unknown to be computed. The data used spanned 2 yr, from 1968.0 to 1969.9 (see Figs. 1 and 2). Solutions are in Table 3.

Table 2. Biases between various types of polar motion data, in meters

	X	Y
Δ_{A-B}	+1.45	−0.83
Δ_{C-A}	+0.22	0.00
Δ_{B-C}	−1.67	+0.83
Δ_{D-B}	+1.08	−1.57

A: ILS mean of 5 stations.
B: BIH mean of 40 stations.
C: IPMS mean of 26 stations.
D: USNWL doppler data.

Table 3. Standard deviations of various types of polar motion data, in meters

	X		Y	
	Nominal solution	Uncertainty	Nominal solution	Uncertainty
σ_A	0.83	±0.09	0.65	±0.15
σ_B	0.69	±0.12	0.54	±0.19
σ_C	0.42	±0.09	0.43	±0.15
σ_D	1.36	±0.15	1.25	±0.20

A: ILS mean of 5 stations.
B: BIH mean of 40 stations.
C: IPMS mean of 26 stations.
D: USNWL doppler data.

Table 4. Standard deviations measured between various types of polar motion data, in meters

	X		Y	
	Measured	Implied by nominal solution	Measured	Implied by nominal solution
σ_{AB}	0.91 ± 0.14	0.91	0.89 ± 0.13	0.76
σ_{AC}	0.85 ± 0.08	0.85	0.61 ± 0.11	0.72
σ_{BC}	0.35 ± 0.10	0.40	0.46 ± 0.11	0.36
σ_{BD}	1.39	1.39	1.47	1.47

A: ILS mean of 5 stations.
B: BIH mean of 40 stations.
C: IPMS mean of 26 stations.
D: USNWL doppler data.

As Anderle reports (Ref. 1), the optical determinations are formally more precise than the doppler determinations, i.e., the former show smaller scatter. However, for JPL purposes we are concerned with the total error, not just the random error. Notice that the biases between ILS and BIH are comparable to those between BIH and the doppler data. Disparity between results obtained from different combinations of ILS data is already of concern to optical astronomers (Ref. 3). Furthermore, two facts suggest that there is at least some systematic error in BIH data. First, the doppler data, which is presumably independent of systematic errors affecting optical sources, is in better agreement with the smoothed results of ILS than with BIH. (See Figs. 1 and 2, and the values of the biases in Table 2.) Second, the agreement of ILS and IPMS against BIH is higher than one could explain from the number of ILS stations used in the IPMS 26-station average. Data from 1967.0 to 1968.9 show that the correlation coefficient between (IPMS–BIH) and (ILS–BIH) is 0.62 in X and 0.78 in Y. Finally, the standard deviations in Table 3 should not be regarded as complete measures of the total error, since the frequency of residuals is somewhat abnormal. Figure 3 displays the standard deviations of normal points formed from doppler and from BIH data as they diminish with the number of days of data forming each normal point. The curves so formed are compared with the inverse square root function which would be displayed by normally distributed residuals. The flatness of the curves reflects

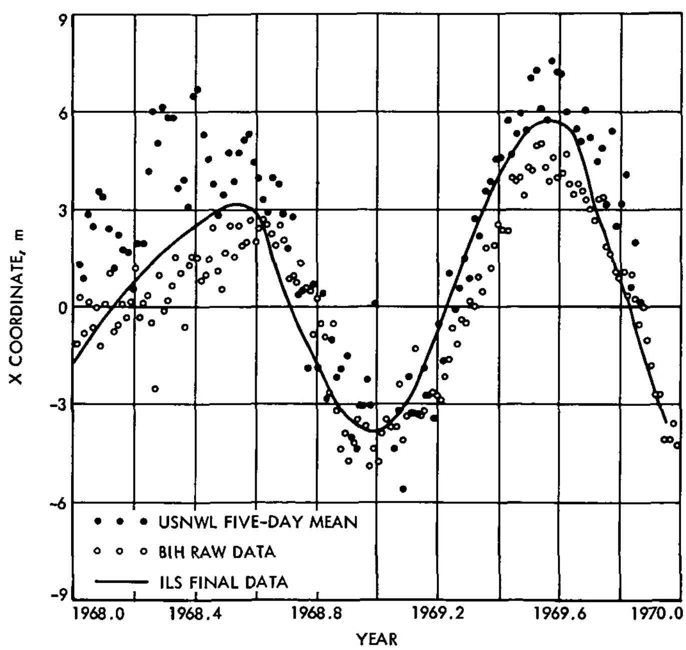

Fig. 1. Determination of X by BIH, ILS, and USNWL

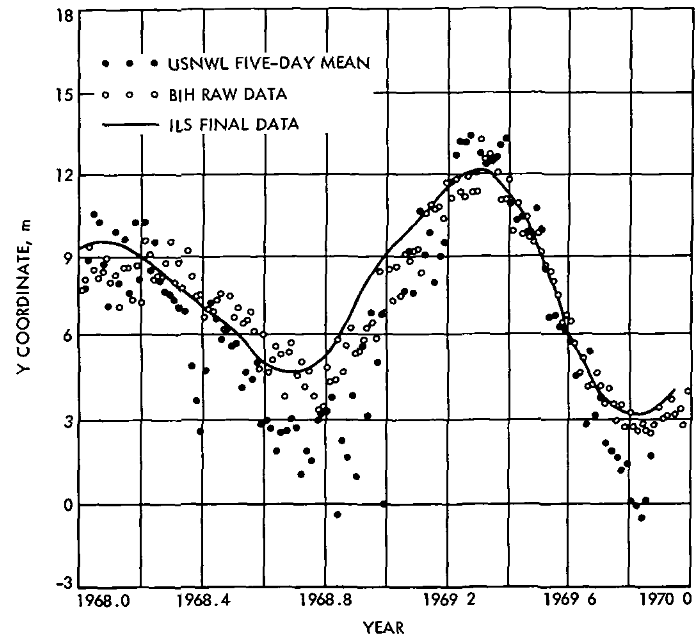

Fig. 2. Determination of Y by BIH, ILS, and USNWL

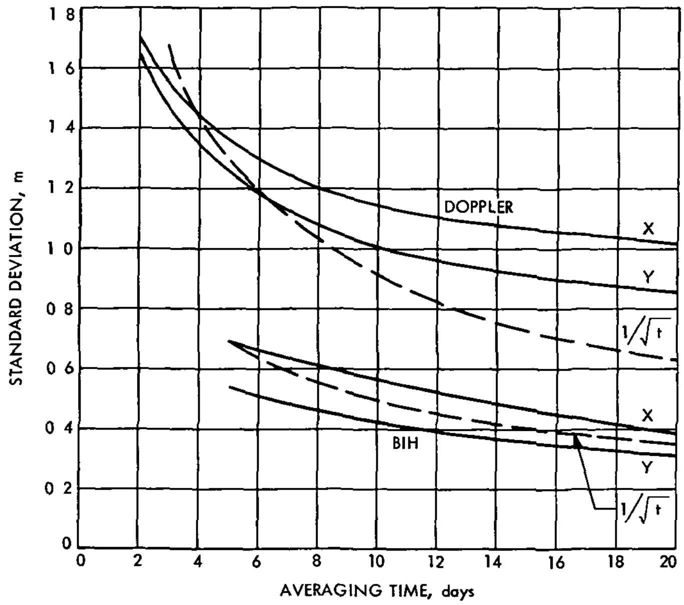

Fig. 3. Standard deviation of normal point versus number of days of data in normal point

the correlation of residuals over many days. We maintain that the doppler data are of value primarily because they are independent of the catalog errors, problems of optical refraction, and the like, which afflict optical data.

4. Conclusions

(1) If we regard only the scatter in the data (the random, as opposed to the systematic, error), then the precision of the IPMS 26-station determinations is higher than that of BIH, which in turn is considerably higher than that of the U. S. Naval Weapons Laboratory (USNWL) doppler data.

(2) However, the 3-yr mean biases given in Table 2 are generally larger than the standard deviations. In other words, the systematic errors in the optical data are more important than the random errors.

(3) The USNWL doppler data are in better agreement with ILS and with IPMS than with BIH. This suggests, although it does not prove, that an important source of the systematic error is in BIH data.

(4) We believe that the doppler data, although now only of moderate precision, is already an important measure of polar motion because of its relative independence of optical sources of error.

References

1. Anderle, R. J., *Polar Motion Determinations by U S. Naval Doppler Satellite Observations,* Technical Report TR-2432, U.S. Naval Weapons Laboratory, Dahlgren, Va., 1970.

2. Guinot, B., Feissel, M , and Laclare, F., *BIH Rapport Annuel Pour 1969,* p. 7, Paris, 1970

3. Yumi, S., and Wako, Y., "Secular Motion of the Pole," *Publications of the International Latitude Observatory of Mizusawa,* Vol. V, No. 2, p. 74, 1966.

IV. Communications Systems Research

ADVANCED ENGINEERING

A. Group Delay Measurements of Block IIIC Receiver–Exciter Modules, *R. L. Sydnor and G. Thompson*

1. Introduction

In evaluating the range accuracy of the fast-acquisition ranging system, the group-delay stability of the DSIF receiver–exciter system was measured (SPS 37-62, Vol. II, pp. 55–61). To satisfy the requirements of the Mark III Data System Development Plan for orbiter missions, ranging accuracy must be better than 1.5 m for an 8-h tracking period. This implies that the total group-delay instability of the receiver–exciter system must be less than 10 ns. At the present time, it is not yet verified that the Block IIIC receiver–exciter system can meet this specification.

A measurement program was started to determine the major sources of instability in the DSIF receiver–exciter system. The objective of the program is to measure the variations of the group delay as a function of temperature, signal level, antenna pointing angle, etc. This article explains the technique used to measure group delay and tabulates the measurement results to date.

2. Measurement Technique

The measurement of group delay can be illustrated by considering the amplifier test system shown in Fig. 1. The sinusoidally amplitude-modulated signal is amplified by the module under test. The phase stability of the subcarrier after amplification is monitored as a function of temperature, shock, signal level, etc.

The measurement principle is the same as for other modules such as phase modulators, mixers, or frequency multipliers. The actual measurement circuit will differ somewhat because of the function of the module.

3. Preliminary Results

The group-delay stability of several modules as a function of temperature is tabulated in Table 1. From the data, it would appear that broadband amplifiers cause no group-delay problems. However, the present exciter

Table 1. Group delay versus temperature

Module	Group delay from 0–50°C, ns
10-MHz distribution amplifier	0.55
Prototype 10-MHz amplifier	0.55
×3 and phase modulator	6.90
Prototype ×3 and phase modulator	79.0

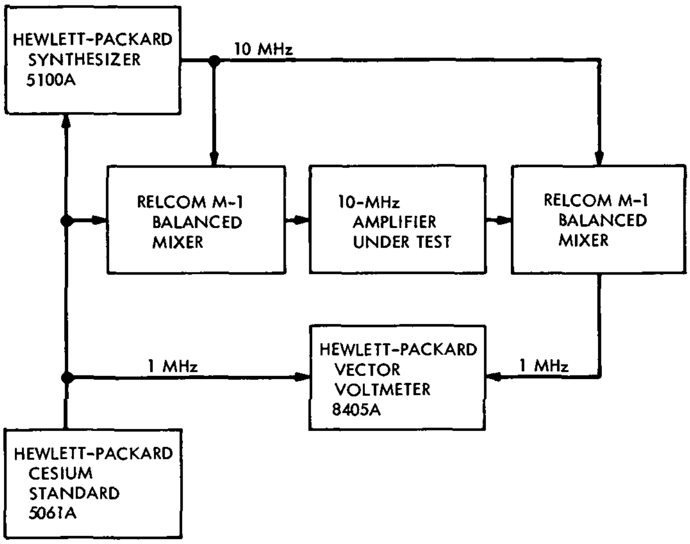

Fig. 1. Measurement of group delay in an amplifier

phase modulator has a 6.9-ns shift from 0 to 50°C and the new prototype phase modulator has a 79-ns shift in its present version. The change in group delay versus temperature is nonlinear, as shown in Fig. 2. In the neighborhood of 25°C, group delay is less sensitive than at lower temperatures. Since the system tests of group delay reported in SPS 37-62, Vol. II, pp. 55–61, were run under conditions of small temperature changes, it would not appear that the phase modulator alone could account for the total group-delay instability.

The variation of group delay as a function of automatic gain control voltage on the 50-MHz IF amplifier was measured. At low signal levels, the group delay varies about 3 ns, which is within the error budget of 10 ns.

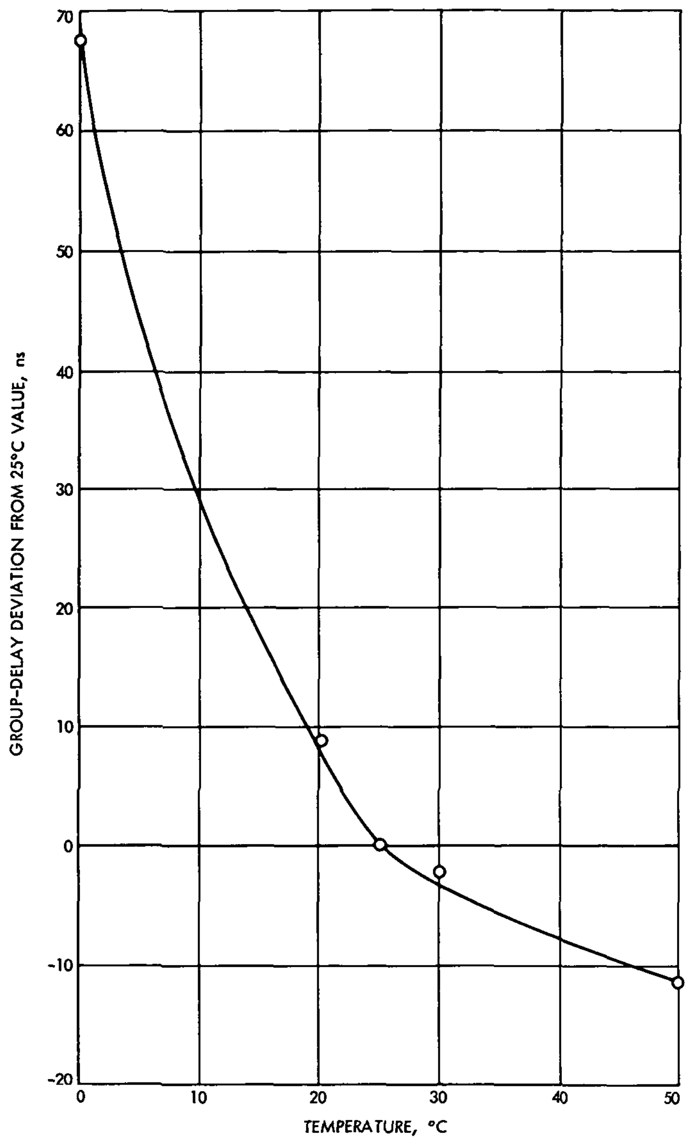

Fig. 2. Temperature profile for prototype phase modulator

These measurements show that the exciter phase modulator is critical to good group-delay stability. Further measurements are in progress on other system components such as the front-end maser and frequency multipliers. The major contributors to group-delay instability will be pin-pointed so that new designs can be implemented to upgrade system performance.

B. Integrated-Circuit Packaging System,

T. O. Anderson and D. Bodkin

1. Introduction

This article describes a model of an integrated-circuit packaging system. The basic design technique used was first developed in the construction of a video data compressor reported in SPS 37-61, Vol. III, pp. 43–54. The advanced model of this packaging scheme has been adopted, with minor modifications, for the prototype of the telemetry data decoder assembly for *Pioneer F* to be used throughout the DSIF.

General considerations and problems arising in packaging of high-speed digital integrated circuits are discussed. They are listed in the order in which their solutions are dependent upon each other. A packaging system is described which takes into account these considerations. The most salient features of the system are pointed out.

2. Design Constraints

High speed of operation dictates close proximity of all functional components. The size of such a system, even considering medium-scale integrated circuits (ICs) requires a larger packaging area than previously used mounting boards of 4- × 5-in. average size. For larger mounting boards, where several ports of 16 to 32-bit parallel computer words must be considered, the number of input/output (I/O) connections increases considerably. If one considers an in-line I/O connector, then it necessarily must be quite long. For 19-in. cabinet packaging, an approximately 6- × 16-in. board appears to be a good engineering compromise. Such a board will hold approximately 200 ICs. This in turn means that the power distribution and heat dissipation must be carefully considered.

In most IC board packaging systems, the structure that holds the boards obstructs the general air flow; or a specific air flow cannot easily be applied where needed.

Guidance during engagement and disengagement, i.e., the seating and fastening of a large board with a multi-pin connector, is perhaps the most important consideration, especially under the constraints of not obstructing the air flow. The guidance and locking mechanism must also not intrude upon the boards' IC mounting area, and should, if possible, not require special tools.

The mounting boards should further be designed to endure rough handling in the field; and, as in any IC mounting board system, it should be designed so as to easily facilitate an extender board.

3. System Description

Figures 1 and 2 show the model assembly. Figure 3 is a cut-away view of the IC mounting board.

For maximum strength the mounting board is made of steel, which is tin-plated for protection. Bent edges along the long side of the board prevent warping and provide strength against torsion. The board holds two sections of 15 columns of 5 each of 16-pin IC mounting sockets on a 0.1-in. grid for machine wire wrap connections. It also holds two 90-pin right angle I/O connectors on the same grid for machine wire wrap connections to the IC sockets. The long-side edge flanges are sufficiently wide and bent in the direction to protect the wire wrap pins. Also, the I/O connector is recessed on the card beyond the edge so that its blades are protected during bench handling. The wiring is further protected by a transparent lucite plate. The ICs are protected against physical damage during bench handling by a natural three-point system that consists of the two I/O connectors and the fastening jack-screw block.

Thin printed circuit laminates are used for power and ground distribution. The planes are close together on one side, but electrically isolated from the chassis. Both the planes have a minimum cutout for minimum inductive

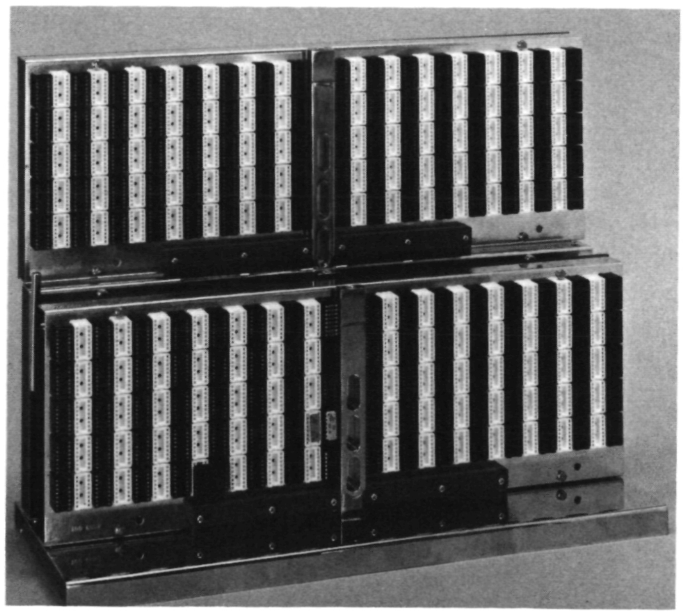

Fig. 1. Model assembly, including two mounting boards and one extender board (component side)

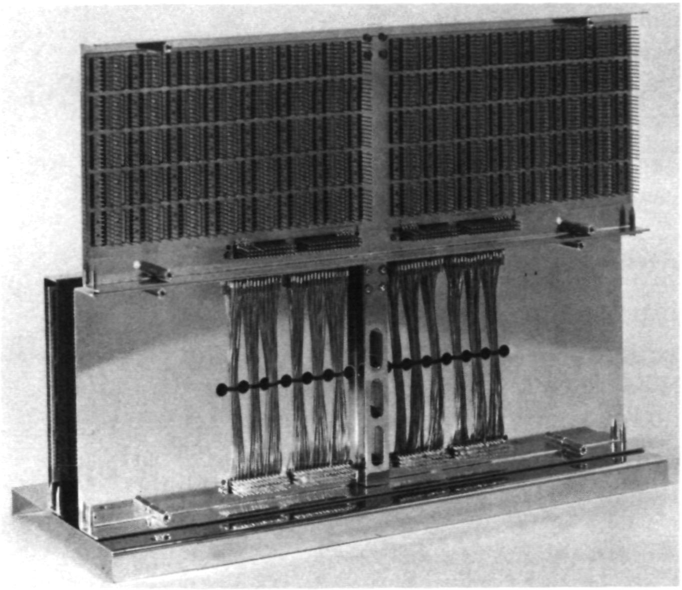

Fig. 2. Model assembly, including two mounting boards and one extender board (wiring side)

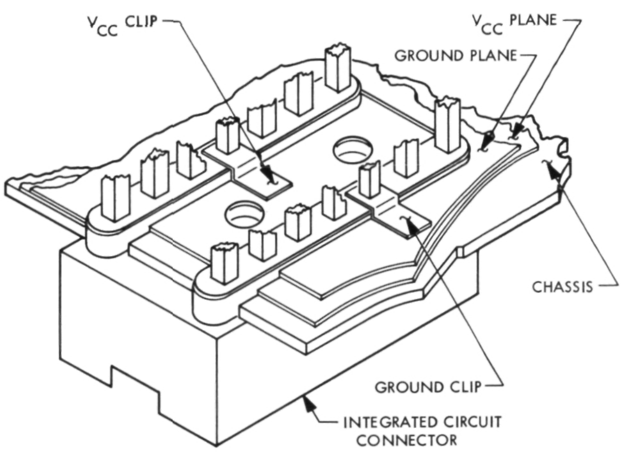

Fig. 3. Cut-away view of IC mounting board

currents and resistive voltage drops. The close proximity of the planes constitutes a desirable high-frequency filter capacitance (25 pF/in.^{2}). The connection between power planes and IC connector pins is made with small sheet metal clips. The IC socket power plane is continued on the I/O connector "back-panel." The power planes are then surrounding the back-panel I/O connectors and the same clips are used. Cutouts are made so that any number of clips not used for signals can be used along the long side of the connector.

The power planes are further divided by etching into several sections for different voltages, all accessible to the connector pins.

4. Guide System

In most card mounting systems, the guide system usually obstructs the air flow. This packaging scheme will not obstruct the air flow; also, provision is made to direct specific air flow to areas where most needed. In a system which has multi-pin I/O connectors which require high total contact pressure, a screw is a practical instrument to engage and disengage the board. A single screw only is mounted in a block secured to the top of the board along the center line. This screw mates with a threaded hole in a single guide post. The board is initially guided by the post and one connector on each side of it. To guide the board for final connector engagement, two holes at the outside of the lower flange of the board match pins in the chassis. The guide post is centered between the two connectors and is as long as possible so as to place the canting tolerance as far from the center of rotation as possible. The canting angle is thus reduced to a minimum and the card remains parallel during engagement and disengagement. Also, by placing the jack screw at the top, it becomes easily accessible by regular tools. Once the connectors are properly engaged, and the screw tightened, the card is rigidly secured. The block secured to the card seats on the guide post at the instant the connector is fully engaged so as to prevent crushing of the connector by further tightening of the screw.

5. Power and Ground Planes

Laminates that are metalized on one side provide the power and ground distribution planes. The top plane is normally the signal-ground plane, which is isolated from the chassis, and the second plane is the power plane. Simple sheet metal clips connect the appropriate connector pins to the appropriate planes.

A cutout of the ground plane between two rows of pins for each socket frees the power plane for convenient connection of the clip. The small cutout leaves the ground plane as continuous as possible in order to keep inductive ground currents low. High-frequency noise components are filtered by the capacity between the power and ground distribution planes.

6. Cooling System

The guide post system lends itself to any general air flow cooling scheme. Also, an additional directed air flow cooling scheme is being considered. The back plane is then one side of a shallow air-tight box. Fans are coupled to the box. Small parallel holes, one for each column of IC sockets, provide for air jets directed precisely toward the heat generating components.

7. Extender Board

The extender board is an important integral part of any IC mounting board system and must be considered throughout the design of the regular mounting board. Its engagement with the chassis connector must be identical to a regular board and its top must be identical to the arrangement in the chassis. In this design, it is of interest to note that the guide post is extended through the entire height of the extender board. When mounted, this arrangement is then very sturdy.

C. Estimating the Parameter of an Exponential Distribution Using Quantiles, *I. Eisenberger*

1. Introduction

The one-parameter exponential distribution is particularly important in the field of reliability because the distribution of time to failure for many types of DSIF equipment obeys this law for a long period of time between an initial so called "burn-in" period and the time when wearout becomes a significant failure factor. The density function for this distribution is given by

$$g(t) = \lambda e^{-\lambda t}, \qquad t > 0$$

The parameter λ is usually unknown and can be estimated as the reciprocal of the mean of n sample values; that is,

$$\frac{1}{\widehat{\lambda}} = \widehat{m} = \frac{1}{n}\sum_{i=1}^{n} t_i$$

where $m = E(t) = 1/\lambda$.

The problem of estimating m using sample quantiles has been considered previously by J. Ogawa, who derived asymptotically optimum linear estimators of the form

$$\widehat{m} = \sum_{i=1}^{k} \alpha_i \, z(p_i)$$

for $k = 1,2,\cdots,15$, where $z(p_i)$ denotes the sample quantile of order p_i. The estimators, asymptotically, are unbiased and have minimum variance. They are given in Ref. 1, pp. 374–375, along with their relative efficiencies and spacings.

Since the optimum quantile estimators are derived on the basis of the asymptotic distribution of the quantiles, and since n is never infinite, the question naturally arises as to the effect of a finite sample size on the bias and efficiency of the estimators. The purpose of this article is to determine this effect for $n = 50$, 100, and 200. For $n = 50$, this will be done for $k = 1,2,\cdots,7$ and for $n = 100$ and 200, for $k = 1,2,\cdots,10$. It will be seen that even for moderate sample sizes such as $n = 50$, the estimators are quite useful.

2. The Asymptotic Distribution of Sample Quantiles

To define a quantile, consider a sample of n independent sample values, $x_1, x_2, \cdots, x_n$, taken from a distribution of a continuous type, with distribution function $G(x)$ and density function $g(x)$. The quantile of order p of the distribution or population, denoted by $\zeta^*(p)$, is defined as the root of the equation $G(\zeta) = p$; that is,

$$p = \int_{-\infty}^{\zeta^*(p)} g(x)\, dx$$

The corresponding sample quantile $z(p)$ is defined as follows. If the sample values are arranged in non-decreasing order of magnitude,

$$x_{(1)} \leq x_{(2)} \leq \cdots \leq x_{(n)}$$

Then $x_{(i)}$ is called the ith order statistic and

$$z(p) = x_{[np]+1}$$

where $[np]$ denotes the greatest integer $\leq np$.

If $g(x)$ is differentiable in some neighborhood of each quantile value considered, it has been shown (Ref. 2) that the joint distribution of any number of quantiles is asymptotically normal as $n \rightarrow \infty$ and that, asymptotically,

$$E(z(p)) = \zeta^*(p)$$

$$\text{Var}(z(p)) = \frac{p(1-p)}{ng^2(\zeta^*(p))}$$

$$\rho_{12} = \left[\frac{p_1(1-p_2)}{p_2(1-p_1)}\right]^{1/2}$$

where ρ_{12} is the correlation between $z(p_1)$ and $z(p_2)$, $p_1 < p_2$.

Thus, for the case where

$$g(t) = \lambda e^{-\lambda t}$$

$$G(t) = 1 - e^{-\lambda t}$$

one has

$$p = \lambda \int_0^{\zeta^*(p)} e^{-\lambda t}\, dt = \int_0^{\lambda\zeta^*(p)} e^{-t}\, dt = \int_0^{\zeta(p)} e^{-t}\, dt$$

where $\zeta(p)$ is the population quantile of order p of the standardized density function $f(t) = e^{-t}$. Since

$$g(\zeta^*(p)) = \frac{1}{\lambda} f(\zeta(p))$$

it follows that

$$E(z(p)) = \zeta^*(p) = \frac{1}{\lambda}\ \zeta(p)$$

$$\text{Var}\,(z(p)) = \frac{p(1-p)}{ng^2(\zeta^*(p))} = \frac{\lambda^2 p(1-p)}{nf^2(\zeta(p))} = \frac{\lambda^2(1-e^{-\zeta(p)})}{n\, e^{-\zeta(p)}}$$

so that the asymptotic moments of the sample quantiles can be expressed in terms of the population quantiles of the standardized density.

3. The Exact Distribution and Moments of the Sample Quantiles

Let x_μ denote the sample quantile of order p such that $\mu = [np]$. It is shown in Ref. 2 that the density function $g_1(x_\mu)$ associated with x_μ is given by

$$g_1(x_\mu) = \binom{n}{\mu}(n-\mu)\,[G(x_\mu)]^\mu\,[1-G(x_\mu)]^{n-\mu-1}\,g(x)$$

$$= \lambda\binom{n}{\mu}(n-\mu)(1-e^{-\lambda x_\mu})^\mu\, e^{-\lambda(n-\mu)x_\mu}, \qquad x_\mu > 0$$

To determine the mean and variance of x_μ, one must evaluate $E(x_\mu)$ and $E(x_\mu^2)$. Beginning with the former, one has

$$E(x_\mu) = \int_0^\infty g_1(x_\mu)\, dx_\mu$$

Integrating by parts results in the following recursive relationship:

$$E(x_\mu) = \frac{1}{\lambda(n-\mu)} + E(x_{\mu-1}) \tag{1}$$

For $\mu = 0$, that is, when p is sufficiently small so that $np < 1$, one obtains

$$E(x_0) = \lambda n \int_0^\infty x_\mu e^{-\lambda n x_\mu}\, dx_\mu = \frac{1}{\lambda n} \tag{2}$$

From Eqs. (1) and (2), it follows readily that

$$E(x_\mu) = \frac{1}{\lambda}\sum_{k=0}^{\mu}\frac{1}{n-k}$$

Integration by parts of

$$E(x_\mu^2) = \int_0^\infty x_\mu^2\, g_1(x_\mu)\, dx_\mu$$

results in the recursive relationship

$$E(x_\mu^2) = \frac{2E(x_\mu)}{\lambda(n-\mu)} + E(x_{\mu-1}^2) \tag{3}$$

From Eq. (3) and the fact that

$$E(x_0^2) = \frac{2}{n^2\lambda^2}$$

one finally obtains

$$E(x_\mu^2) = \frac{2}{\lambda^2}\left[\sum_{k=1}^{\mu}\sum_{j=0}^{k}\frac{1}{(n-k)(n-j)} + \frac{1}{n^2}\right]$$

$$\text{Var}\,(x_\mu) = E(x_\mu^2) - [E(x_\mu)]^2$$

Now let x_{μ_1} and y_{μ_2} denote the quantiles of orders p_1 and p_2, respectively, such that $\mu_1 = [np_1]$ and $\mu_2 = [np_2]$, $\mu_2 > \mu_1$. The joint density function $h(x_{\mu_1}, y_{\mu_2})$ of x_{μ_1} and y_{μ_2} has been derived previously by the author (SPS 37-65, Vol. II, pp. 47–50) and is given by

$$h(x_{\mu_1}, y_{\mu_2}) = K[G(x_{\mu_1})]^{\mu_1} [1 - G(y_{\mu_2})]^{n-\mu_2-1} [G(y_{\mu_2}) - G(x_{\mu_1})]^{\mu_2-\mu_1-1} g(x_{\mu_1})\, g(y_{\mu_2})$$

$$= \lambda^2 K [1 - \exp(-\lambda x_{\mu_1})]^{\mu_1} [\exp(-\lambda x_{\mu_1}) \exp(-\lambda y_{\mu_2})]^{\mu_2-\mu_1-1} \exp[-\lambda(n - \mu_2) y_{\mu_2}] \exp(-\lambda x_{\mu_1}),$$

$$0 \leq x_{\mu_1} < \infty, \qquad x_{\mu_1} < y_{\mu_2} < \infty$$

where

$$K = 2\binom{n}{\mu_1}\binom{n-\mu_1}{\mu_2-\mu_1-1}\binom{\mu_2-\mu_1-1}{2}$$

To determine the covariance between x_{μ_1} and y_{μ_2}, one must evaluate $E(x_{\mu_1} y_{\mu_2})$. Accordingly, one has, integrating again by parts,

$$E(x_{\mu_1} y_{\mu_2}) = \int_0^\infty \int_{x_{\mu_1}}^\infty x_{\mu_1} y_{\mu_2} h(x_{\mu_1}, y_{\mu_2})\, dy_{\mu_2}\, dx_{\mu_1}$$

$$= \frac{1}{\lambda(n-\mu_2)} E(x_{\mu_1}) + E(x_{\mu_1} y_{\mu_{2-1}}) \qquad (4)$$

From Eq. (4) and the fact that

$$E(x_{\mu_1} y_{\mu_1+1}) = E(x^2_{\mu_1}) + \frac{1}{\lambda(n-\mu_1-1)} E(x_{\mu_1})$$

one obtains

$$E(x_{\mu_1} y_{\mu_2}) = E(x^2_{\mu_1}) + E(x_{\mu_1}) \sum_{j=1}^{\mu_2-\mu_1} \frac{1}{\lambda(n-\mu_1-j)}$$

$$\mathrm{Cov}(x_{\mu_1}, y_{\mu_2}) = E(x_{\mu_1} y_{\mu_2}) - E(x_{\mu_1})E(y_{\mu_2})$$

$$= E(x^2_{\mu_1}) + \frac{1}{\lambda} E(x_{\mu_1})$$

$$\times \left[\sum_{j=1}^{\mu_2-\mu_1} \frac{1}{n-\mu_1-j} - \sum_{j=0}^{\mu_2} \frac{1}{n-j}\right]$$

$$= E(x^2_{\mu_1}) - \frac{1}{\lambda} E(x_{\mu_1}) \sum_{j=0}^{\mu_1} \frac{1}{n-j}$$

$$= E(x^2_{\mu_1}) - E^2(x_{\mu_1}) = \mathrm{Var}(x_{\mu_1})$$

Thus, we obtain the surprising result that not only is the covariance between x_{μ_1} and y_{μ_2} independent of μ_2 for $\mu_2 > \mu_1$, it is identical with the variance of x_{μ_1}. It should be noted that this result does not apply to the *correlation* between x_{μ_1} and y_{μ_2}. Since the correlation ρ_{12} is defined as

$$\rho_{12} = \frac{\mathrm{cov}(x_{\mu_1}, y_{\mu_2})}{[\mathrm{Var}(x_{\mu_1})\mathrm{Var}(y_{\mu_2})]^{1/2}} = \left[\frac{\mathrm{Var}(x_{\mu_1})}{\mathrm{Var}(y_{\mu_2})}\right]^{1/2}$$

and since the fact that

$$\mathrm{Var}(x_{\mu+1}) - \mathrm{Var}(x_\mu) = \frac{1}{\lambda^2(n-\mu-1)^2}$$

means that the variance of the sample quantiles is an increasing function of μ, the correlation between x_{μ_1} and y_{μ_2}, for fixed μ_1, is a decreasing function of μ_2, as it should be.

4. The Asymptotic Quantile Estimators $\widehat{m}(k)$

Let z_i denote the sample quantile of order p_i such that $p_i < p_j$ if $i < j$; let ζ_i denote the corresponding population quantile of the standardized density, and let $\widehat{m}(k)$ denote the asymptotic quantile estimator of the mean $m = 1/\lambda$ of an exponential distribution, using k sample quantiles. Then, since $\widehat{m}(k)$ is of the form

$$\widehat{m}(k) = \sum_{i=1}^{k} \alpha_i z_i$$

one has, asymptotically

$$E(\widehat{m}(k)) = \sum_{i=1}^{k} \alpha_i E(z_i) = m \sum_{i=1}^{k} \alpha_i \zeta_i$$

$$\mathrm{Var}(\widehat{m}(k)) = \sum_{i=1}^{k} \sum_{j=1}^{k} \alpha_i \alpha_j \mathrm{Cov}(z_i, z_j)$$

In effect, Ogawa chose the orders of the quantiles and the α_i so as to simultaneously satisfy the conditions

$$\sum_{i=1}^{k} \alpha_i \zeta_i = 1, \qquad \mathrm{Var}(\widehat{m}(k)) = \text{minimum}$$

Table 1. Asymptotically optimum orders p_i, the corresponding coefficients α_i, and spacings ζ_i of the sample quantiles z_i used in estimating the mean $m = 1/\lambda$ of an exponential distribution with density $g(t) = \lambda e^{-\lambda t}$, $t > 0$

$$\widehat{m}(k) = \sum_{i=1}^{k} \alpha_i z_i$$

k	1	2	3	4	5	6	7	8	9	10
p_1	0.7968	0.6386	0.5296	0.4514	0.3931	0.3478	0.3121	0.2827	0.2583	0.2381
α_1	0.6275	0.5232	0.4477	0.3907	0.3463	0.3108	0.2819	0.2579	0.2375	0.2201
ζ_1	1.5936	1.0177	0.7541	0.6003	0.4994	0.4274	0.3741	0.3323	0.2988	0.2719
p_2		0.9266	0.8300	0.7419	0.6670	0.6042	0.5513	0.5066	0.4680	0.4349
α_2		0.1790	0.2266	0.2361	0.2320	0.2228	0.2119	0.2009	0.1905	0.1804
ζ_2		2.6113	1.7718	1.3544	1.0997	0.9268	0.8015	0.7064	0.6311	0.5707
p_3			0.9655	0.9067	0.8434	0.7828	0.7277	0.6782	0.6340	0.5946
α_3			0.0775	0.1195	0.1402	0.1492	0.1519	0.1511	0.1483	0.1446
ζ_3			3.3654	2.3721	1.8538	1.5271	1.3009	1.1338	1.0052	0.9030
p_4				0.9810	0.9434	0.8978	0.8506	0.8047	0.7613	0.7212
α_4				0.0409	0.0709	0.0902	0.1017	0.1082	0.1116	0.1127
ζ_4				3.9657	2.8715	2.2812	1.9012	1.6332	1.4326	1.2771
p_5					0.9885	0.9631	0.9297	0.8928	0.8551	0.8181
α_5					0.0234	0.0456	0.0615	0.0725	0.0799	0.0847
ζ_5					4.4651	3.2989	2.6553	2.2335	1.9320	1.7045
p_6						0.9925	0.9746	0.9496	0.9205	0.8896
α_6						0.0156	0.0311	0.0438	0.0536	0.0607
ζ_6						4.8925	3.6730	2.9876	2.5323	2.2039
p_7							0.9948	0.9818	0.9626	0.9394
α_7							0.0107	0.0222	0.0324	0.0407
ζ_7							5.2666	4.0053	3.2864	2.8042
p_8								0.9963	0.9865	0.9715
α_8								0.0076	0.0164	0.0246
ζ_8								5.5989	4.3041	3.5583
p_9									0.9973	0.9897
α_9									0.0056	0.0124
ζ_9									5.8977	4.5760
p_{10}										0.9979
α_{10}										0.0042
ζ_{10}										6.1696
Eff	0.6476	0.8203	0.8910	0.9269	0.9476	0.9606	0.9693	0.9754	0.9798	0.9832

Table 2. The expected value and efficiencies of the quantile estimators $\widehat{m}(k)$

k	$n = 50$		$n = 100$		$n = 200$	
	$\lambda E(\widehat{m}(k))$	Eff $(\widehat{m}(k))$	$\lambda E(\widehat{m}(k))$	Eff $(\widehat{m}(k))$	$\lambda E(\widehat{m}(k))$	Eff $(\widehat{m}(k))$
1	0.9853	0.6740	0.9975	0.6542	1.0037	0.6445
2	1.0025	0.8249	0.9943	0.8340	1.0023	0.8185
3	1.0173	0.8712	1.0048	0.8872	1.0079	0.8793
4	1.0398	0.8643	1.0160	0.9020	1.0074	0.9154
5	1.0233	0.9174	1.0003	0.9508	0.9980	0.9539
6	1.0129	0.9448	1.0088	0.9505	0.9991	0.9652
7	0.9939	0.9875	1.0042	0.9676	0.9955	0.9792
8			1.0014	0.9771	1.0017	0.9754
9			1.0037	0.9759	1.0056	0.9723
10			0.9922	0.9993	0.9952	0.9952

Ogawa's results are given in Table 1 for $k = 1,2,\cdots,10$. The relative efficiencies of the estimators are also given in the last row of the table, where the relative efficiency is defined as the ratio of the variance of the mean of all the sample values to $\mathrm{Var}(\widehat{m}(k))$. Thus,

$$\mathrm{Eff}(\widehat{m}(k)) = \frac{1}{n\lambda^2 \mathrm{Var}(\widehat{m}(k))}$$

Using the results obtained in *Subsection 3*, the exact expected value and efficiencies of $\widehat{m}(k)$ were computed for $k = 1,2,\cdots,7$ when $n = 50$, and for $k = 1,2,\cdots,10$ when $n = 50$ and $n = 100$. The results are given in Table 2. For $n = 50$, no results are given for more than seven quantiles because when more than seven quantiles are used, the optimum orders p_{k-1} and p_k are such that $\mu_k = \mu_{k-1}$ when $n = 50$. This can readily be seen from Table 1. This is the reason the condition $\mu_2 > \mu_1$ was used in deriving the exact joint distribution of two sample quantiles, rather than the condition $p_2 > p_1$.

5. Unbiased Estimators for $n = 50$, 100, and 200

Estimators will be constructed using k sample quantiles, for $k = 1,2,\cdots,7$ and $n = 50$, 100, and 200, of the form

$$\widehat{m}(k) = \sum_{i=1}^{k} \alpha_i z_i$$

with the α_i chosen so that the estimators are unbiased and have minimum variance. The orders of the quantiles will be identical with those given in Table 1 for the optimum asymptotic estimators. As a result, the estimators to be derived will be either optimum or very nearly optimum. The efficiencies will also be determined.

For any choice of k sample quantiles such that $\mu_i = [np_i] \neq \mu_j = [np_j]$ when $i \neq j$, the estimators will be unbiased if

$$\sum_{i=1}^{k} \alpha_i E_i = 1$$

or, say,

$$\alpha_1 = \frac{1 - \sum_{i=2}^{k} \alpha_i E_i}{E_1} \tag{5}$$

where

$$E_i = \sum_{j=0}^{\mu_i} \frac{1}{n-j}$$

The variance of $\widehat{m}(k)$ is given by

$$\mathrm{Var}(\widehat{m}(k)) = \alpha_k^2 \,\mathrm{Var}(z_k) + \sum_{i=1}^{k-1} \mathrm{Var}(z_i)\left(\alpha_i^2 + 2\sum_{j=i+1}^{k} \alpha_i\alpha_j\right) \tag{6}$$

Now, if one substitutes in Eq. (6) the expression for α_1 given in Eq. (5) and then sets the partial derivatives with respect to α_j, $j = 2,3,\cdots,k$, equal to zero, the solutions of the resulting $k-1$ linear equations, together

Table 3. The coefficients α_i and spacings E_i of the sample quantiles z_i used in the minimum variance, unbiased estimators of the mean $m = 1/\lambda$ of an exponential distribution (the orders of the z_i are optimum with respect to their asymptotic distribution)

k	α_1	E_1	α_2	E_2	α_3	E_3	α_4	E_4	α_5	E_5	α_6	E_6	α_7	E_7	Eff
$n = 50$															
1	0.6378	1.5702													0.6543
2	0.5328	1.0041	0.1744	2.6659											0.8293
3	0.4450	0.7649	0.2284	1.7813	0.0722	3.4992									0.9020
4	0.3965	0.6077	0.2314	1.3960	0.1225	2.4159	0.0312	4.4992							0.9393
5	0.3483	0.5042	0.2337	1.1185	0.1391	1.9063	0.0619	2.9992	0.0250	4.4992					0.9614
6	0.3148	0.4407	0.2227	0.9515	0.1360	1.5702	0.0973	2.2159	0.0364	3.4992	0.0206	4.4992			0.9710
7	0.2822	0.3810	0.2122	0.8084	0.1492	1.3191	0.0999	1.9063	0.0557	2.6659	0.0267	3.4992	0.0204	4.4992	0.9805
$n = 100$															
1	0.6291	1.5896													0.6509
2	0.5227	1.0128	0.1814	2.5945											0.8246
3	0.4550	0.7494	0.2211	1.8066	0.0774	3.3540									0.8959
4	0.3912	0.6119	0.2300	1.3714	0.1242	2.3584	0.0364	4.1874							0.9321
5	0.3441	0.5075	0.2324	1.0986	0.1405	1.8691	0.0639	2.9040	0.0291	4.1874					0.9524
6	0.3120	0.4281	0.2235	0.9338	0.1445	1.5420	0.0921	2.2584	0.0461	3.3540	0.0139	5.1874			0.9676
7	0.2836	0.3833	0.2063	0.8147	0.1538	1.2959	0.0961	1.9358	0.0623	2.5945	0.0305	3.6874	0.0123	5.1874	0.9761
$n = 200$															
1	0.6252	1.5995													0.6492
2	0.5250	1.0172	0.1774	2.6265											0.8224
3	0.4513	0.7522	0.2271	1.7892	0.0742	3.4280									0.8933
4	0.3905	0.6049	0.2355	1.3592	0.1201	2.3829	0.0389	4.0447							0.9294
5	0.3468	0.5009	0.2306	1.1036	0.1392	1.8508	0.0701	2.8582	0.0260	4.3780					0.9501
6	0.3098	0.4294	0.2226	0.9251	0.1492	1.5280	0.0896	2.2803	0.0457	3.2852	0.0162	4.8780			0.9635
7	0.2829	0.3772	0.2107	0.8066	0.1529	1.3026	0.0989	1.9164	0.0599	2.6265	0.0301	3.5947	0.0142	4.8780	0.9717

with Eq. (5), give the required values of the coefficients α_i in order that $\widehat{m}(k)$ be unbiased and have minimum variance for the given choice of quantiles.

The results of carrying out the above procedure, using the asymptotically optimum quantiles, are given in Table 3, in which are recorded the α_i and the spacings E_i. The efficiencies of the estimators are also given in the last column of the table, and are, as usual, quite high. This makes these estimators ideal ones for an automated DSIF logistics program.

References

1. Sarhan, A. E., and Greenberg, B. G., *Contributions to Order Statistics.* John Wiley & Sons, Inc., New York, 1962.
2. Cramér, H., *Mathematical Methods of Statistics.* Princeton University Press, Princeton, N. J., 1946.

D. DSIF Integrated-Circuit Layout and Isoperimetric Problems, *L. Harper*

1. Introduction

Recently, while writing a survey paper on what I called "Combinatorial Coding Theory," I was approached by Warren Lushbaugh, a JPL engineer. "I'm designing a Viterbi decoder," he said.[1] "The wiring diagram is a deBruijn graph of order four (Fig. 1). How should I place these sixteen components on a linear chassis so that the total length of the wire used to connect them is minimized?" (The direction of edges are irrelevant for this problem, and looped edges may be eliminated. Double edges are relevant, however.) After several minutes of discussion, I realized that this problem was a special case of my so-called combinatorial coding problem and that it was a case for which a technique had been developed (Ref. 1). This technique and the solution of Lushbaugh's problem are described below.

[1] SPS 37-58, Vol. III, pp. 50–55.

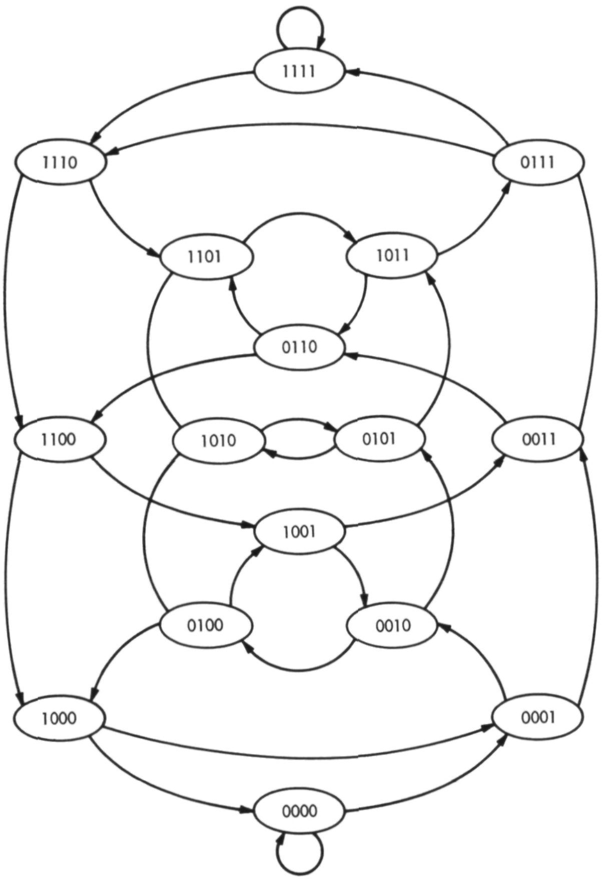

Fig. 1. deBruijn graph of order four

2. Lushbaugh's Problem

If a graph G has N vertices, then a one-to-one function $\phi : V \rightarrow \{1, \cdots, N\}$ (V being the set of vertices) is called a code. This function was called a "numbering" by Harper in 1964 (Ref. 1), and a "code" by Harper in 1970 (Ref. 2). Neither of these is particularly appropriate in the present context; however, we shall use the term "code," with the warning to the reader that what it denotes is quite different from the algebraic coding theorist's idea of a code. If E is the set of edges in G, and e a member of E having endpoints v,w, then define

$$\Delta_e(\phi) = | \phi(v) - \phi(w) |$$

Lushbaugh's problem is equivalent to finding a code on the degree-four deBruijn graph ($N = 16$) minimizing

$$\sum_{e \in E} \Delta_e(\phi)$$

Let $S \subseteq V$ and define $\theta(S)$ to be the number of edges "cut" by S, i.e., the number of edges with one end in S and the other in S^c (S complement). Also, define

$$S_\ell(\phi) \equiv \{v \in V : \phi(v) \leq \ell\}$$

Then, we have

Lemma.

$$\sum_{e \in E} \Delta_e(\phi) = \sum_{\ell=1}^{N} \theta(S_\ell(\phi))$$

Proof. This identity is not new, but it is basic to what follows and its proof is so simple that we shall include it.

Edge e, with endpoints v,w, contributes

$$\Delta_e(\phi) = | \phi(v) - \phi(w) |$$

to the left-hand side. On the right-hand side, if $j = \phi(w)$ and $k = \phi(v)$, $j < k$, then e contributes 1 to each of the terms $\theta_j, \theta_{j+1} \cdots, \theta_{k-1}$ for a total of $k - j = | \phi(v) - \phi(w) |$ QED

Theorem.

$$\min_{\phi} \sum_{e \in E} \Delta_e(\phi) = \min \sum_{\ell=1}^{N} \theta(S_\ell(\phi))$$

$$\geq \sum_{\ell=1}^{N} \min_{\phi} \theta(S_\ell(\phi))$$

$$= \sum_{\ell=1}^{N} \min_{S_\ell} \theta(S_\ell)$$

The term θ can be viewed as a "boundary functional" and the problem of minimizing θ over all sets of ℓ vertices then becomes an isoperimetric problem, the number of vertices in a set being interpreted as "area." If this isoperimetric problem can be solved, we then have a lower bound on

$$\min_{\phi} \sum_{e \in E} \Delta_e(\phi)$$

And if there exists an increasing family of sets $S_1 \subseteq S_2 \cdots \subseteq S_N$, each a solution of the isoperimetric problem, the lower bound is achieved, with $\phi^{-1}(\ell) \equiv S_\ell - S_{\ell-1}$ *defining an optimal code.*

This approach to the problem also suggests a heuristic for finding a good code: Assign the numbers to the vertices in order, minimizing $\theta(S_{\ell+1}(\phi))$ at each step, given $S_\ell(\phi)$ from the step before. Following this heuristic in the case of the given deBruijn graph, we produced the code ϕ_0 (Fig. 2). Using this code to identify the vertices, we assert that Table 1 contains all solution sets for the isoperimetric problem.

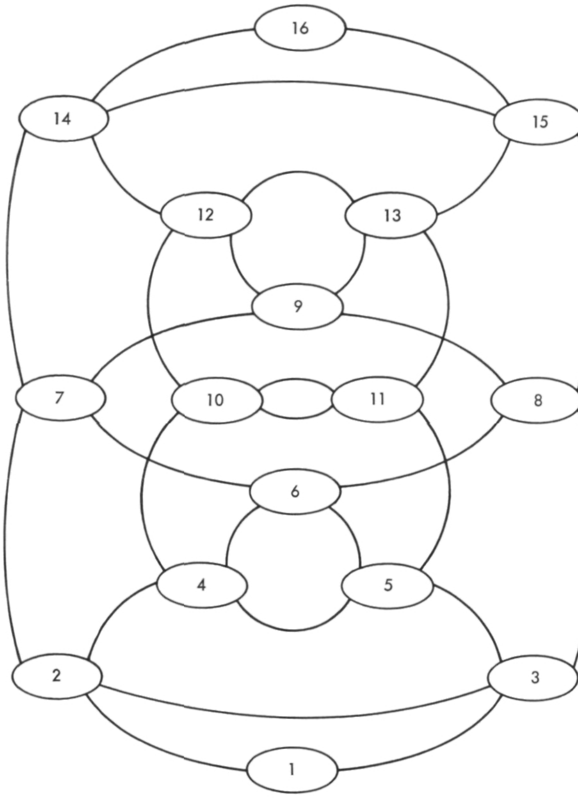

Fig. 2. $\phi_0, \sum \Delta_e(\phi_0) = 76$

Because of the identity $\theta(S) = \theta(S^c)$, it was only necessary to determine the solution sets for $\ell = 1,\cdots,8$. According to our theorem then,

$$\min_{\phi} \sum_{e \in E} \Delta_e(\phi) \geq 74$$

but for the heuristically derived code ϕ_0,

$$\sum_{e \in E} \Delta_e(\phi_0) = 76$$

Inspection of the list of solution sets shows, however, that there is no monotone-increasing sequence of solution sets, and since $\theta(S_\ell)$ must be even on a graph whose local degrees are all even,

$$\min_{\phi} \sum_{e \in E} \Delta_e(\phi) \geq 76$$

and ϕ_0 is optimal.

3. Generalizations to Two Dimensions

A successful mathematical idea will often suggest new problems. Although the analysis presented above is exactly the same as in Harper (Ref. 1) for the graph of the n-cube, the change of setting, from a coding problem to an integrated-circuit (IC) card layout problem, suggested new variants. Let us suppose that we wished to lay out our wiring diagram on a rectangular IC card, rather than just a linear one. For sixteen components, the dimensions of such a board could conveniently be 2×8 or 4×4. And suppose that all wires must run only horizontally and vertically, so that the total length of wire needed to connect components at locations (a,b) and (c,d) on the board would be $|a - c| + |b - d|$. Thus, if component v is placed at location $(\phi_1(v), \phi_2(v))$ on the rectangular board, the total length of wire needed to complete the wiring will be

$$\sum_{(v,w) \in E} (|\phi_1(v) - \phi_1(w)| + |\phi_2(v) - \phi_2(w)|)$$

Also, the pair of functions (ϕ_1,ϕ_2) must take the value (i,j) exactly once, assuming (i,j) is the coordinate of a place on the board. This implies that ϕ_1 and ϕ_2, considered as functions on the probability space V with normalized counting measure, are stochastically independent. Thus, we have the relations

$$\frac{|\{\phi_1 \leq k, \phi_2 \leq \ell\}|}{N} = \frac{|\{\phi_1 \leq k\}|}{N} \frac{|\{\phi_2 \leq \ell\}|}{N}$$

$$= \frac{|S_k(\phi_1)|\,|S_\ell(\phi_2)|}{N^2}$$

Table 1. Solution sets for the isoperimetric problems

ℓ	Solution sets	min $\theta(S_\ell)$
1	{1}, {16}	2
2	{1,2}, {1,3}, {16,15}, {11,14}, {10,11}, {1,16}	4
3	{1,2,3}, {11,15,14}	4
4	{1,2,3,4}, {1,2,3,5}, {16,15,14,13}, {11,15,14,12}, {1,2,3,16}, {16,15,14,1}, {4,5,10,11}, {13,12,11,10}	6
5	{1,2,3,4,5}, {16,15,14,13,12}, {4,5,6,10,11}, {13,12,11,10,9}	6
6	{1,2,3,4,5,6}, {16,15,14,13,12,9}	6
7	{1,2,3,4,5,10,11}, {16,15,14,13,12,11,10}, {1,2,3,4,5,6,7}, {1,2,3,4,5,6,8}, {16,15,14,13,12,9,8}, {16,15,14,13,12,9,7}	6
8	{1,2,3,4,5,6,7,8}, {16,15,14,13,12,9,8,7}, {1,2,3,4,5,6,10,11}, {16,15,14,13,12,11,10,9}	6
9	{1,2,3,4,5,6,7,8,9}, {16,15,14,13,12,9,8,7,6}, {1,2,3,4,5,6,7,10,11}, {1,2,3,4,5,6,8,10,11}, {16,15,14,13,12,11,10,9,8}, {16,15,14,13,12,11,10,9,7}	6
10	{1,2,3,4,5,6,7,8,10,11}, {15,14,13,12,11,10,9,8,7}	6
11	{1,2,3,4,5,6,7,8,9,10,11}, {16,15,14,13,12,11,10,9,8,7,6}, {1,2,3,4,5,6,7,8,14,15,16}, {16,15,14,13,12,11,10,9,8,7,3,2,1}	6
12	{1,2,3,4,5,6,7,8,9,10,11,12}, {16,15,14,13,12,11,10,9,8,7,6,5}, {1,2,3,4,5,6,7,8,9,10,11,12}, {16,15,14,13,12,11,10,9,8,7,6,4}, {2,3,4,5,6,7,8,9,10,11,12,13}, {15,14,13,12,11,10,9,8,7,6,5,4}	6
13	{1,2,3,4,5,6,7,8,9,10,11,12,13}, {16,15,14,13,12,11,10,9,8,7,6,5,4}	4
14	{1,2,3,4,5,6,7,8,9,10,11,12,13,14}, {1,2,3,4,5,6,7,8,9,10,11,12,13,15}, {16,15,14,13,12,11,10,9,8,7,6,5,4,3}, {16,15,14,13,12,11,10,9,8,7,6,5,4,2}, {1,2,3,4,5,6,7,8,9,12,13,14,15,16}, {2,3,4,5,6,7,8,9,10,11,12,13,14,15}	2
15	{1,2,3,4,5,6,7,8,9,10,11,12,13,14,15}, {16,15,14,13,12,11,10,9,8,7,6,5,4,3,2}	2

and

$$|S_k(\phi_1)| = kJ, \qquad 1 \le k \le I$$
$$|S_\ell(\phi_2)| = \ell I, \qquad 1 \le \ell \le J$$

The functional we wish to minimize is

$$\sum_{(v,w)\in E} |\phi_1(v) - \phi_1(w)| + |\phi_2(v) - \phi_2(w)| =$$

$$\sum_{k=1}^{I} \theta(S_k(\phi_1)) + \sum_{\ell=1}^{J} \theta(S_\ell(\phi_2))$$

This formulation suggests a heuristic for defining good codes: Increase the values of k and ℓ alternately, i.e., select $0 < k_1 < k_2 < \cdots$ and $0 < \ell_1 < \ell_2 \cdots$ to be minimal so that

$$k_1|J| \le \ell_1|I| \le k_2|J| \le \cdots$$

At each step, add numbers to S_{k_i} or S_{ℓ_i} so that the independence conditions are obeyed and $\theta(S_{k_{i+1}})$ or $\theta(S_{\ell_{i+1}})$ is minimized, given S_{k_i} and S_{ℓ_i}.

For instance, if we wish to place our deBruijn graph wiring diagram with sixteen components on a 4×4 card, then $I = J = 4$ so that k and ℓ will be increasing by one each time. After a short series of run-throughs, a code was produced (Fig. 3). The total length of wire used in the corresponding layout would be 44. Comparison of Table 2 with Table 1 makes the near-optimality and probable optimality of this code quite apparent.

Another apparently good idea for coding the deBruijn graph into the square was to take the linear card (*Subsection 1*) and compress it into the square, for instance by "snake-in-the-box" mapping (Fig. 4), and compose these with the optimal code (*Subsection 1*). The total length of wire required, however, is 56. Another natural candidate for optimality was Fig. 5, which utilizes the

Table 2. Heuristic solutions of the isoperimetric problem for stochastically independent sets

k	$\theta(S_k(\phi_1))$	ℓ	$\theta(S_\ell(\phi_2))$
1	6	1	6
2	6	2	10
3	8	3	8

[1] ϕ_1 and ϕ_2 are obtained from Fig. 3.

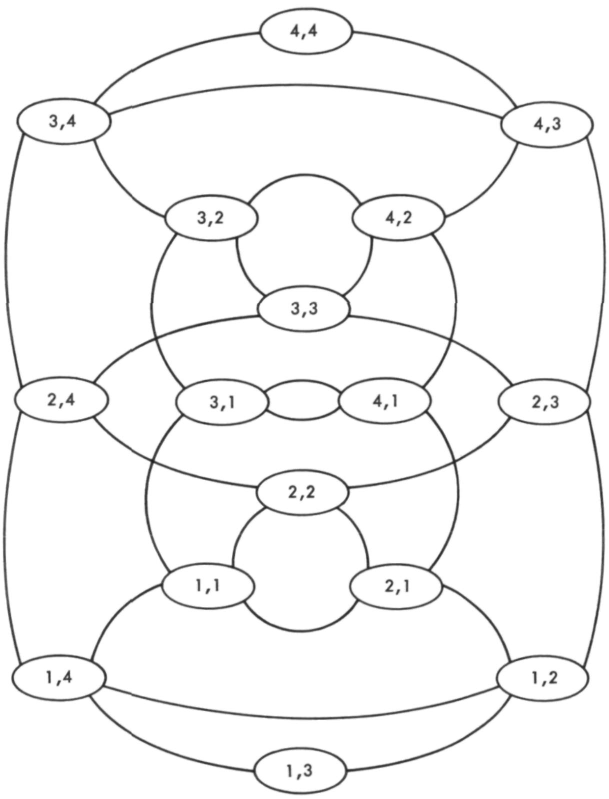

Fig. 3. Application of heuristic,
$$\sum_{e \in E} \Delta_e(\phi_1) + \Delta_e(\phi_2) = 44$$

similarity between the deBruijn graph and the square chassis. But again the total length is 56. Such examples cannot prove anything, of course, unless done to exhaustion. As this would require evaluating at least 653,837,184,000 different codes, the advantage of a good heuristic is apparent.

The aim in this subsection was only to present a quick and dirty technique for finding a better code than naive approaches yield. In practical situations, a good candidate for optimality is often just as good as a mathematically certified optimal code. The questions of whether

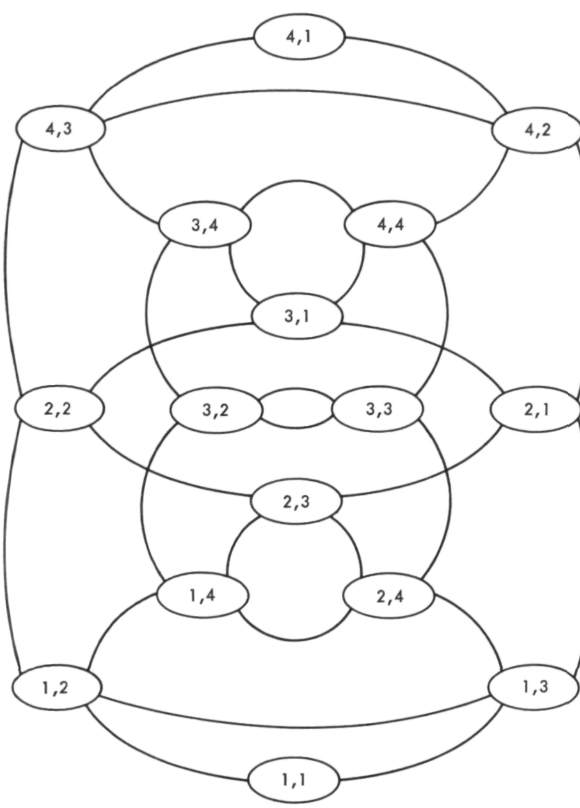

Fig. 4. Snake-in-the-box composed with ϕ_0 of Fig. 2,
$$\sum_{e \in E} \Delta_e(\phi_1) + \Delta_e(\phi_2) = 56$$

our best coding of the given deBruijn graph into the square is best possible, or whether solutions can be found for all n, are left untouched.

4. Maximum Wire-Length Criteria

Another problem considered by Warren Lushbaugh was that of minimizing the maximal length of any wire in laying out the same deBruijn graph on a linear chassis. Harper (Ref. 3) contains a variant of the theory for minimizing total length which is directly applicable.

For $S \subseteq V$, let $\Phi(S)$ be the number of nearest neighbors of members of S which are not themselves in S. Then,

Lemma. *For all codes* $\phi : V \to \{1, \cdots, N\}$,

$$\max_{e \in E} \Delta_e(\phi) \geq \max_{1 \leq \ell \leq N} \Phi(S_\ell(\phi))$$

Proof. $S_\ell(\phi)$ is connected to $\Phi(S_\ell(\phi))$ members of $(S_\ell(\phi))^c$. No matter how the integers $\ell + 1, \ell + 2, \cdots, \ell + \Phi(S_\ell(\phi))$ are placed on these vertices, a difference of at least $\Phi(S_\ell(\phi))$ must occur on one of those connecting edges.

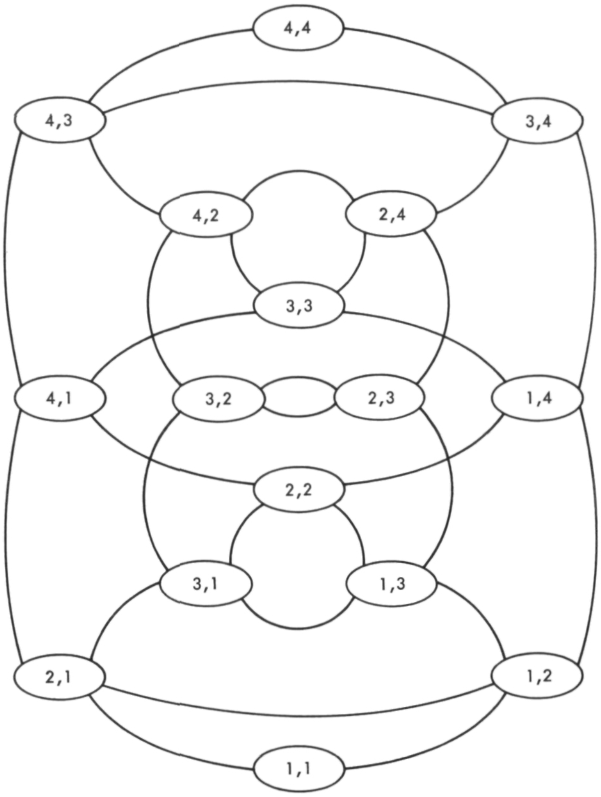

Fig. 5. Code utilizing similarity between square chassis and deBruijn graph, $\sum_{e \in E} \Delta_e(\phi_1) + \Delta_e(\phi_2) = 56$

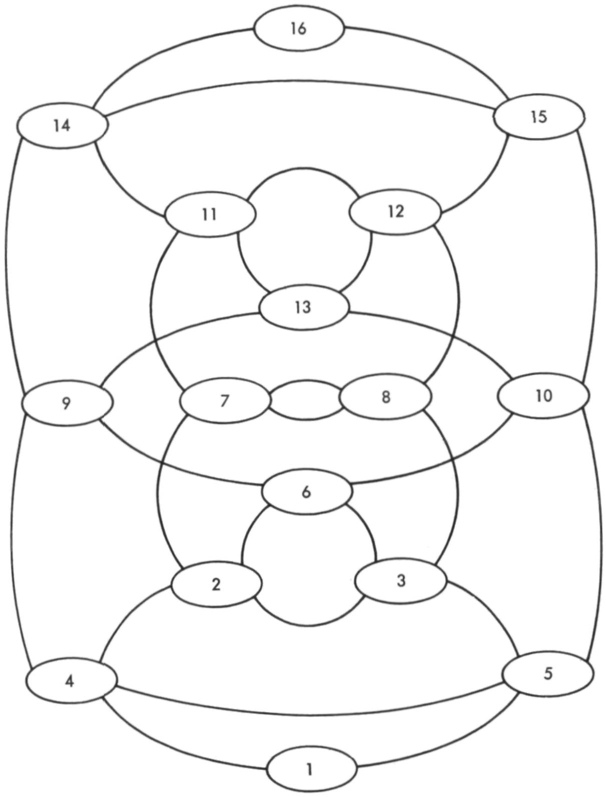

Fig. 6. Heuristic code starting from S_8

THEOREM. *For all codes* $\phi: V \to \{1,\cdots,N\}$,

$$\min_{\phi} \max_{e \in E} \Delta_e(\phi) \geq \max_{1 \leq \ell \leq N} \min_{S_\ell} \Phi(S_\ell)$$

where S_ℓ *ranges over all sets of* ℓ *vertices.*

The term Φ may be considered another boundary functional, so again we have an isoperimetric problem on G.

Proof. Apply the above lemma, then interchange min and max.

It is easily seen that min $\Phi(S_3) = 5$ so that

$$\min_{\phi} \max_{e \in E} \Delta_e(\phi) \geq 5$$

by the theorem. The code of Fig. 6 achieves this bound and with only six edges having the maximal difference. This is probably best possible. The code was constructed by noting that for the set $S_8(\phi)$, $\Phi(S_8(\phi)) = 4$ and that the vertices numbered 2 and 3 had no connections with elements of $(S_8(\phi))^c$.

5. Variants, Extensions, and Unsolved Problems

The isoperimetric problems considered in *Subsections 1* and *2* are, as far as the present author knows, unsolved except for a small number of special cases. The isoperimetric problems may be stated as integer geometric programming problems:

$$\text{minimize } \theta = \sum_{(v,w) \in V} x_v(1 - x_w)$$

$$\text{subject to } \sum_{v \in V} x_v = \ell, \qquad x_v = 0 \text{ or } 1$$

We can rewrite

$$\theta = \sum_{v,w \in V} r_{vw} x_v (1 - x_w)$$

where $R = (r_{vw})$ is the incidence matrix of G. Define

$$r'_{vw} = \begin{cases} r_{vw} & \text{if } w \neq v \\ \left(\max_t \sum_{u \in V} r_{tw}\right) - \sum_{\substack{u \in V \\ u \neq v}} r_{vu} & \text{if } w = v \end{cases}$$

and

$$\theta' = \sum_{v,\, w \in V} r'_{vw}\, x_v(1 - x_w)$$

Then, minimizing θ under the given conditions is equivalent to minimizing θ'.

$$\theta' = \sum_{v \in V} x_v \sum_{w \in V} r'_{vw} - \sum_{v,\, w \in W} r'_{vw}\, x_v x_w$$

$$= \ell \left(\max_{t} \sum_{u \in V} x_{tw} \right) - \sum_{v, w \in V} r'_{vw}\, x_v x_w$$

Therefore, minimizing θ is equivalent to maximizing a positive semidefinite quadratic (rather than linear) form under the given conditions.

The isoperimetric problem for Φ can also be expressed as an integer geometric program:

$$\Phi = \sum_{v \in V} x_v \left(1 - \prod_{(v,w)\, tE} x_w \right)$$

with the same conditions,

$$\sum_{v \in V} x_v = \ell, \qquad x_v = 0 \text{ or } 1$$

There is only one paper on positive semidefinite integer quadratic programs, by Kunzi and Oettli (Ref. 4), and none, according to a recent survey of integer programming by Balinski (Ref. 5), on more general nonlinear integer programs.

The heuristic solutions given may start from any set, $S_\ell \subseteq V$, and proceed in both directions. For instance, S_ℓ may be a known solution of the corresponding isoperimetric problem. The code of Fig. 6 was, in fact, of exactly this type, starting from S_8.

The problems of minimizing total wire length or maximal wire length have been solved herein only for the deBruijn graph of order four. Even for order five, it would seem that new ideas are required to demonstrate an optimal code. However, when this Viterbi decoder is demonstrated, it is probable that a better, i.e., higher-order decoder, will be designed, and the solutions of higher-order problems would be of considerable interest.

References

1. Harper, L. H., "Optimal Assignments of Numbers to Vertices," *J. SIAM*, Vol. 12, No. 1, pp. 131–135, Mar. 1964.
2. Harper, L. H., "Combinatorial Coding Theory," presented at the Proceedings of the University of North Carolina Conference on Combinatorial Theory and its Applications, Chapel Hill, N. C., May 1970.
3. Harper, L. H., "Optimal Numberings and Isoperimetric Problems on Graphs," *J. of Combinatorial Theory*, Vol. 1, No. 3, pp. 385–393, Nov. 1966.
4. Kunzi, H. P., and Oettli, W., "Integer Quadratic Programming," *Recent Advances in Mathematical Programming*, pp. 303–308. Edited by R. L. Graves and P. Wolfe. McGraw-Hill Book Co., Inc., New York, 1963.
5. Balinski, M. L., "Integer Programming; Methods, Uses, Computation," *Mathematics of the Decision Sciences, Part 1*, pp. 179–256. Edited by G. B. Dantzig and A. F. Veinott. American Mathematical Society, Providence, R. I., 1968.

E. An Asymptotic Formula for the Mean Cycle-Slip Time of Second-Order Phase-Locked Loop With Frequency Offset,

R. C. Tausworthe

1. Introduction

A number of authors (e.g., Refs. 1 and 2) have derived a formula for the mean time to first cycle slip of a phase-locked loop by considering an associated two-dimensional differential equation describing the time-dependent loop error statistics. Lindsey (Ref. 2) gives a recursive formula for higher moments of this slip time, extended to loops of a specified type, but of arbitrary order. Lindsey's formula, however, contains in it an unknown function, a conditional expectation, that for loops of degree greater than unity, has never been evaluated. The author (Ref. 3) was able to approximate this function in a way that gave extremely good agreement with experimental data, so that, formally at least, the cycle-slip statistics were considered solved.

Evaluation of the formula, however, to give actual numerical answers has, until now, presented quite a problem. Theoretical manipulations, such as series expansions or an asymptotic formula, have not been forthcoming. Direct evaluation by numerical integration involved differences of exponentially large quantities, and required very careful programming in multiprecision arithmetic with very small error tolerances to obtain reasonable answers at even moderate loop signal-to-noise ratios (SNRs).[1] Consequently, such evaluations were very slow and costly to obtain, and of use only at lower loop SNRs.

This article presents a method by which a much-reduced precision program is required to obtain the mean first-cycle slip time of an arbitrary second-order loop with lead compensation whose input may have a frequency offset term. It also presents a simple approximate formula that is asymptotically tight at higher loop SNRs. As a limiting case, the asymptotic formula agrees, for a first-order loop at zero offset, with the known formula given in Viterbi (Ref. 1).

2. The Mean Cycle-Slip Time Formula

To introduce the notation to be used, we start with the usual representation (Ref. 1) of the phase-error process $\phi = \phi(t)$ for a second-order loop,

$$\dot{\phi} = \Omega_0 - AKF(p)\left[\sin\phi + \frac{n(t)}{A}\right] \tag{1}$$

in which Ω_0 represents the (assumed constant) frequency offset between the incoming sinusoid and the voltage-controlled oscillator at rest; A, the rms signal amplitude; $n(t)$, a baseband white Gaussian noise with one-sided spectral density N_0; K, the loop gain; $p = d/dt$, the Heaviside operator; and $F(s)$, the loop filter transfer function. In terms of its time-constant ratio, $F = \tau_2/\tau_1$, the loop filter is assumed to take the form

$$F(s) = \frac{1+\tau_2 s}{1+\tau_1 s} = F + \frac{(1-F)}{1+\tau_1 s} \tag{2}$$

When $F = 1$, the first-order loop thus results.

A vector representation $\boldsymbol{\phi} = (\phi_1, \phi_2)$ of the process of particular use in this case is

$$\left.\begin{aligned} \phi_1 &= \phi \\ \phi_2 &= \frac{AK(1-F)}{1+\tau_1 p}\left\{\sin\phi + \frac{n(t)}{A}\right\} \end{aligned}\right\} \tag{3}$$

[1]Lindsey, W. C., University of Southern California, personal communication of work yet unpublished.

The time-derivative $\dot{\boldsymbol{\phi}}$ of $\boldsymbol{\phi}$ is described then by

$$\left.\begin{aligned} \dot{\phi}_1 &= \Omega_0 - AKF\left[\sin\phi + \frac{n(t)}{A}\right] - \phi_2 \\ \dot{\phi}_2 &= \frac{AK(1-F)}{\tau_1}\left[\sin\phi + \frac{n(t)}{A}\right] - \frac{1}{\tau_1}\phi_2 \end{aligned}\right\} \tag{4}$$

This last equation shows quite clearly that the representation of the process by $\boldsymbol{\phi}$ is a vector Markov process, because incremental changes in $\boldsymbol{\phi}$ are dependent only upon present values of the system state and disturbing function.

Based on this model, an evaluation of Lindsey's (Ref. 2) general formula for the mean time to first cycle slip yields the expression to be studied:

$$T = \frac{4}{N_0(KF)^2}\int_{-2\pi}^{2\pi}\int_{x}^{2\pi}[u(y-\phi_0) - D]\,e(x,y)\,dy\,dx \tag{5}$$

The function $u(\cdot)$ is the ordinary unit-step, and $\phi_0 = \phi(0)$. The constant D is given by

$$D = \frac{\displaystyle\int_{\phi_0}^{2\pi} e(0,y)\,dy}{\displaystyle\int_{-2\pi}^{2\pi} e(0,y)\,dy} \tag{6}$$

and the function $e(x,y)$ is

$$e(x,y) = \exp\left[\frac{4}{N_0(KF)^2}\int_{y}^{x} E(\dot{\phi}\mid\phi)\,d\phi\right] \tag{7}$$

We shall find it convenient in what follows to define

$$\left.\begin{aligned} \hat{\rho} &= \frac{4A}{N_0 KF} \\ h(x) &= \frac{1}{AKF}\int^{x} E(\dot{\phi}\mid\phi)\,d\phi \end{aligned}\right\} \tag{8}$$

it being understood that the indefinite integral is to be evaluated only at its upper limit.

As the reader may appreciate, the formal evaluation of $E(\dot{\phi}\mid\phi)$ is not possible without knowing the probability density of the error process; however, as mentioned earlier, approximation is possible. Lindsey (Ref. 4), for example, tried the Orthogonality Principle, but the resulting values for T did not agree well with observed data.

3. Approximation of $E(\dot{\phi} \mid \phi)$

Another method, due to the author, approximates the conditional expectation $E(\dot{\phi} \mid \phi)$ to a high experimental accuracy. Since it is presented elsewhere (Ref. 3), its exposure here will be cursory: the form of $\dot{\phi}$ given in Expression (4) suggests

$$E(\dot{\phi} \mid \phi) = \Omega_0 - AKF \sin \phi + B(\phi) \tag{9}$$

where $B(\phi)$ is a function to be determined, say as a series, $B(\phi) = b_0 + b_1\phi + \cdots$. Experimental evidence (SPS 37-43, Vol. III, pp. 76–80; SPS 37-58, Vol. II, pp. 29–32), in fact, strongly indicates that the first two terms of $B(\phi)$ are in dominance. Values for $E(\dot{\phi})$ and $E(\phi\dot{\phi})$ can be computed in two ways: first directly from Eq. (9); and second, by using the usual linear loop theory valid at low angular disturbances. According to linear theory, once the initial transients have died (i.e., the loop has reached steady state),

$$\phi = \frac{\Omega_0}{AK} - \frac{L(p)n(t)}{A \cos \phi_{ss}} \tag{10}$$

Here $L(s)$ represents the well-known loop transfer function linearized about the steady-state phase error point ϕ_{ss}. Since we tacitly have agreed by Eq. (10) to start observing the slip beginning at steady-state lock, we take $\phi_0 = \phi_{ss}$.

Equating the two types of evaluations for $E(\dot{\phi})$ and $E(\phi\dot{\phi})$ yields a solution for b_0 and b_1, and provides the following approximate form of $E(\dot{\phi} \mid \phi)$:

$$\begin{aligned} E(\dot{\phi} \mid \phi) &= AKF\left[\frac{\Omega_0}{AK} - \sin\phi + \frac{(1-F)\cos\phi_0}{1 + r\cos\phi_0}(\phi - \phi_0)\right] \\ &= AKF[\alpha - \sin\phi + \beta\phi] \end{aligned} \tag{11}$$

Parameters introduced in this equation are

$$\left.\begin{aligned} r &= AKF\tau_2 \\ \Omega &= \frac{\Omega_0}{AK} \\ \alpha &= \Omega - \beta\phi_0 \\ \beta &= \frac{(1-F)\cos\phi_0}{1 + r\cos\phi_0} \end{aligned}\right\} \tag{12}$$

The parameter r is very closely related to the loop damping factor, as $\zeta = r^{1/2}(1 + F/r)/2$.

The exponential integrand $e(\phi,y)$ of Eq. (5) is thus

$$\left.\begin{aligned} e(\phi,y) &= \exp[\hat{\rho}h(\phi) - \hat{\rho}h(y)] \\ h(x) &= ax + \cos x + \frac{1}{2}\beta x^2 \end{aligned}\right\} \tag{13}$$

At this point, the values of T are formally attainable. However, because of the exponential character of Expression (13), the integration required to evaluate T must be sufficiently precise not to allow significant error when its positive and negative parts are combined.

4. Integration of T

The problem of evaluating T numerically arises from the negative component of T. Due to the exponential character of $e(\phi,y)$ as a function of $\hat{\rho}$, the dominant contributions to T occur in neighborhoods of the relative maxima of $e(\phi,y)$, and thereby, at the relative maxima of $h(\phi) - h(y)$. At such a point, call it $P^* = (\phi^*,y^*)$, the coordinates ϕ^* and y^* are maxima and minima of $h(x)$, respectively, on the region $-2\pi \leq \phi \leq y \leq 2\pi$. These are illustrated in Fig. 1, denoted ϕ_0, ϕ_1, ϕ_2, and ϕ_3; the maximum nearest the origin and both minima are solutions to $h'(\phi_i) = 0$, viz,

$$\alpha + \beta\phi_i = \sin\phi_i \tag{14}$$

shown in Fig. 2. It is of interest to point out at such points that $E(\dot{\phi} \mid \phi) = 0$; hence, these are precisely the lock point ϕ_0 and the first-slip saddle-points ϕ_1 and ϕ_2.

The remaining maximum of interest ϕ_3 may either be a solution to $h'(\phi) = 0$, if one exists (when $\alpha \geq 2\pi\beta$), or $\phi_3 = -2\pi$ otherwise.

There are only three relative maximum points within the bounds of integration, shown in Fig. 3. These are

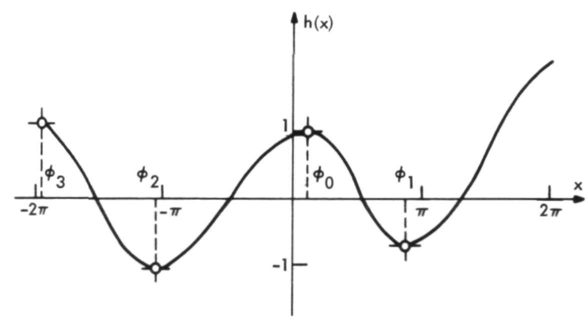

Fig. 1. Exponent function $h(x)$

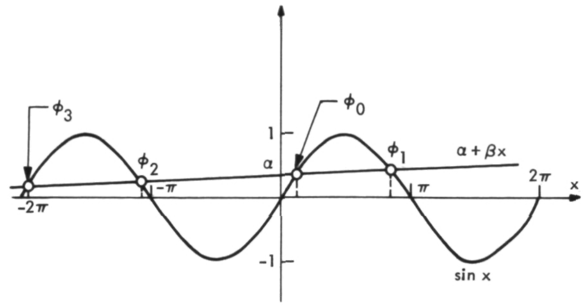

Fig. 2. Solution method for maxima and minima of $h(x)$

$P_1 = (\phi_0,\phi_1)$, $P_2 = (\phi_3,\phi_1)$, and $P_3 = (\phi_3,\phi_2)$. As $\hat{\rho}$ becomes large, the integrals about each point also become very large, leading to potentially large errors when differenced.

We now develop a way to remove P_2 and P_3 from the region of integration. The formula for T can alternately be written (Fig. 3)

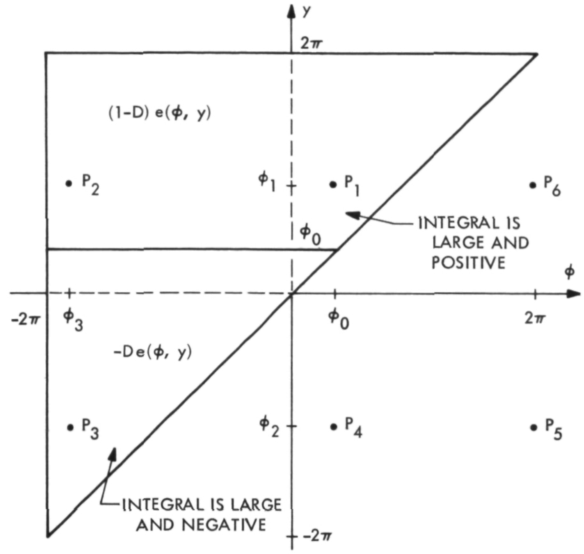

Fig. 3. Region of integration for T, showing subregions with positive and negative integrands (points of relative maximum $e(\phi,y)$ also shown)

$$T = \frac{\hat{\rho}}{AKF}\left\{ -D \int_{-2\pi}^{\phi_0} \int_{-2\pi}^{y} e(\phi,y)\, d\phi\, dy + (1-D) \int_{\phi_0}^{2\pi} \int_{-2\pi}^{y} e(\phi,y)\, d\phi\, dy \right\} \tag{15}$$

The latter integral over $(-2\pi,y)$ can be broken into two parts, $(-2\pi,\phi_0)$ and (ϕ_0,y). When the integrals Eq. (6) for D and $1-D$ are inserted, Eq. (15) can be manipulated to give

$$T = \frac{\hat{\rho}}{AKF}\left\{ D \int_{-2\pi}^{\phi_0} \int_{y}^{\phi_0} e(\phi,y)\, d\phi\, dy + (1-D) \int_{\phi_0}^{2\pi} \int_{\phi_0}^{y} e(\phi,y)\, d\phi\, dy \right\} \tag{16}$$

This rearrangement of the integration has dismissed the negative portion of T altogether, so that Eq. (16) can be evaluated straightforwardly by numerical integration routines having only moderate precision.

5. Asymptotic Evaluation of T

The Taylor series of $h(x)$ about the maximum points remaining inside the integration boundaries, P_1 and P_4 (Fig. 4), allow the integrand, say in the neighborhood of P_1 to be written as

$$e(\phi,y) = e(\phi_0,\phi_1) \exp\left\{\frac{1}{2}\hat{\rho}h''(\phi_0)(\phi-\phi_0)^2 + \cdots\right\} \times \exp\left\{-\frac{1}{2}\hat{\rho}h''(\phi_1)(y-\phi_1)^2 + \cdots\right\} \tag{17}$$

A similar expression arises at P_4. Since $h''(x) = (\beta - \cos x)$ is negative at ϕ_0 and positive at ϕ_1, integration of $e(\phi,y)$ about P_1 is very nearly related to the normal probability integral. When $\hat{\rho}$ is even moderately large, the quadratic nature of Eq. (17) extends far enough that the y-integral limits in Eq. (16) can be replaced by $(-\infty,+\infty)$ with only a small error. The limits on ϕ can similarly be replaced by $(-\infty,0)$ and $(0,\infty)$ in the two regions. The result is an asymptotic formula for T, which we denote as $\hat{T}$:

$$\hat{T} = \frac{\pi}{AKF(\cos\phi_0 - \beta)^{1/2}} \times \left[\frac{D\, e(\phi_0,\phi_2)}{(\beta - \cos\phi_2)^{1/2}} + \frac{(1-D)\, e(\phi_0,\phi_1)}{(\beta-\cos\phi_1)^{1/2}}\right] \tag{18}$$

The validity of this formula depends only on the one condition that ρ is large enough that any deviations from the quadratic character postulated in Eq. (17)

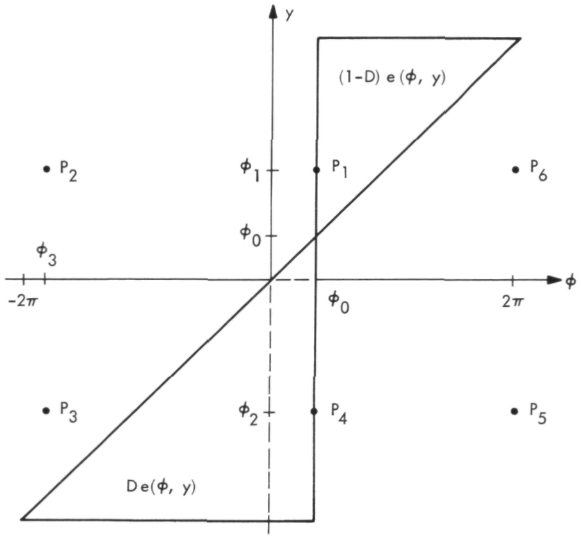

Fig. 4. Transformed integration formula for T, having positive integrand only (integration encompasses the maxima at P_1 and P_4, which lie on the boundary)

occur when $e(\phi,y) \ll e(\phi_0,\phi_{1,2})$ and thus cause negligible errors.

The same technique can be applied to the computation of D. We find, for example,

$$\int_{\phi_0}^{2\pi} e(0,y) \approx e(0,\phi_1) \int_{-\infty}^{+\infty} \exp\left[-\frac{\widehat{\rho}}{2} h''(\phi_1)(y-\phi_1)^2\right] dy$$
$$= e(0,\phi_1)\left[\frac{2\pi}{\widehat{\rho} h''(\phi_1)}\right]^{1/2} \tag{19}$$

so that the asymptotic value of D is

$$\widehat{D} = \frac{e(0,\phi_1)[\beta - \cos\phi_2]^{1/2}}{e(0,\phi_1)[\beta - \cos\phi_2]^{1/2} + e(0,\phi_2)[\beta - \cos\phi_1]^{1/2}} \tag{20}$$

Insertion of this $\widehat{D}$ into Eq. (18) gives the final asymptotic formula for $\widehat{T}$. It is convenient to introduce at this point the parameters

$$\left.\begin{aligned} \rho &= \frac{A^2}{N_0 b_L} = \widehat{\rho}\left(\frac{r+F}{r+1}\right) \\ b_L &= \frac{r(r+1)}{4\tau_2(r+F)} \end{aligned}\right\} \tag{21}$$

The parameter b_L is the loop baseband single-sided noise bandwidth, as referred to $\Omega_0 = 0$, and ρ represents the baseband SNR inside this bandwidth. The actual passband around the carrier is twice this wide because of the zero-beat heterodyning effect of the loop. Hence, we may take

$$w_L = 2b_L \tag{22}$$

as the loop carrier-bandwidth. The expressions for $\widehat{T}$ are

$$\begin{aligned} \widehat{T} w_L &= \left(\frac{r+1}{r+F}\right) \frac{\pi(1-\widehat{D})\, e(\phi_0,\phi_1)}{[(\cos\phi_0 - \beta)(\beta - \cos\phi_1)]^{1/2}} \\ &= \left(\frac{r+1}{r+F}\right) \frac{\pi\widehat{D}\, e(\phi_0,\phi_2)}{[(\cos\phi_0 - \beta)(\beta - \cos\phi_2)]^{1/2}} \end{aligned} \tag{23}$$

The angles ϕ_0, ϕ_1, and ϕ_2 are all solutions to $h'(\phi) = \alpha + \beta_0 - \sin\phi = 0$ and are independent of $\widehat{\rho}$.

6. Evaluation for the First-Order Loop with Frequency Offset

The first-order loop results in our theory by setting $F = 1$. Then we have $\beta = 0$, $\alpha = \Omega$, and $\widehat{\rho} = \rho$. Further, the solutions to $h'(\phi) = 0$ are

$$\left.\begin{aligned} \phi_0 &= \arcsin\Omega \\ \phi_1 &= \pi - \phi_0 \\ \phi_2 &= -\pi - \phi_0 \end{aligned}\right\} \tag{24}$$

These values inserted into Eq. (23) yield

$$\begin{aligned} \widehat{T} w_L &= \frac{\pi \exp[2\rho(\Omega\phi_0 + \cos\phi_0)]}{2\cos\phi_0 \cosh(\pi\Omega\rho)} \\ &= \frac{\pi}{2} e^{2\rho} \text{ for } \phi_0 = 0 \end{aligned} \tag{25}$$

The limiting case, $\phi_0 = 0$, is the correct asymptotic result contained in Viterbi (Ref. 1).

7. Evaluation and Comparison of Results

To calibrate the effectiveness of the asymptotic formula and the accuracy of the improved integral formula, test cases were run on a digital computer. The results were also compared with previous experimental data (SPS 37-43, Vol. III; SPS 37-58, Vol. II; Refs. 5–7) for further verification that the approximation $E(\dot{\phi} \mid \phi)$ was accurate. Computations show, as illustrated in Fig. 5, that the asymptotic formula is accurate for the range of parameters considered within 35%, for ρ as low as $\rho = 0.5$, and increases in accuracy to about 10% at $\rho = 5$.

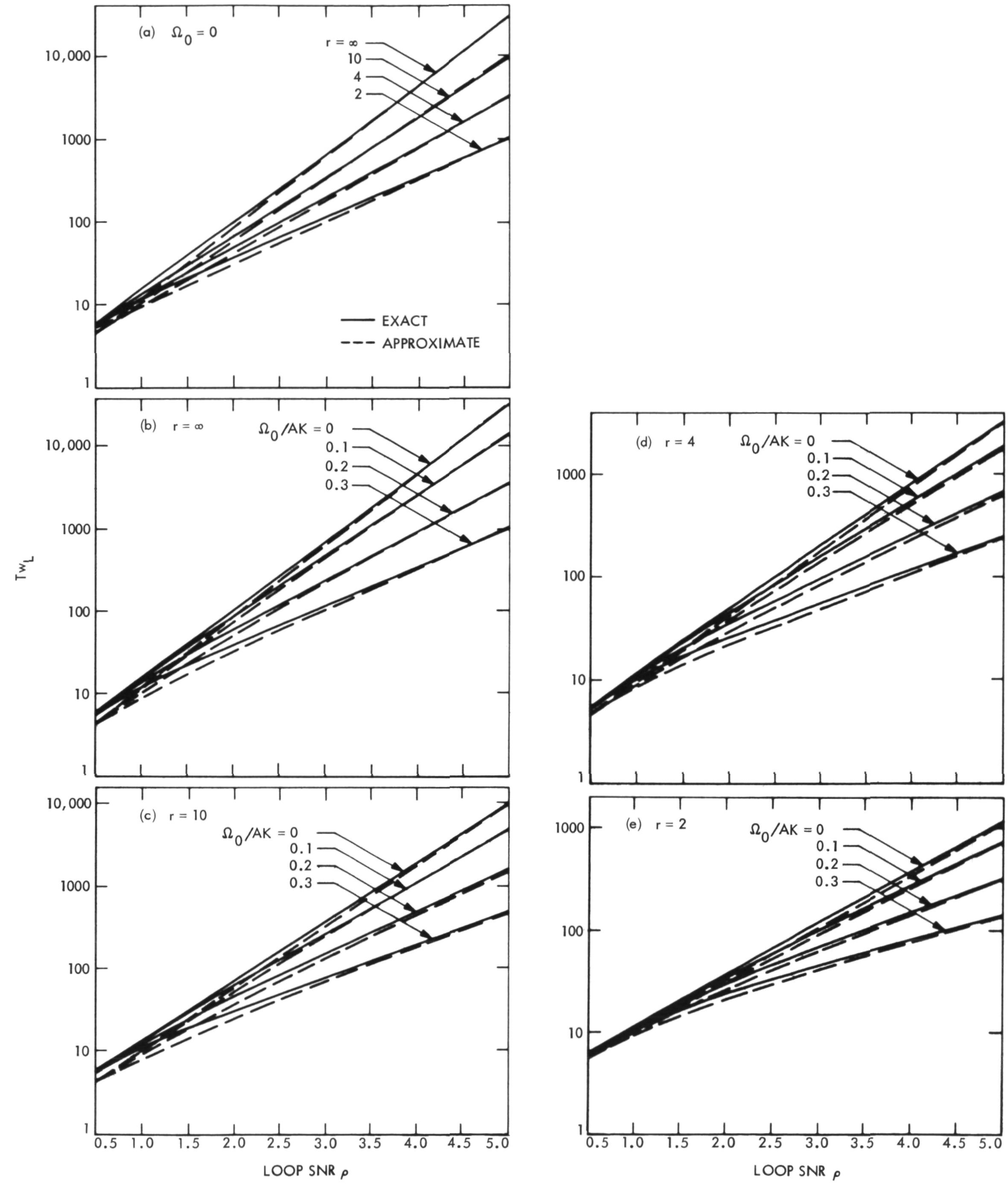

Fig. 5. Comparison of integral and asymptotic formulas for mean slip-time T_{w_L} as a function of loop SNR ρ for various loop damping and detuning parameters r, Ω_0/AK

The curves in Fig. 5 clearly illustrate the asymptotic exponential character of both T and $\widehat{T}$. This exponent ξ can be found from the asymptotic behavior of $\widehat{T}$ and fit to a convenient form, such as

$$\left.\begin{aligned}
\xi &= \left(\frac{r+1}{r+F}\right)[h(\phi_0) - h(\phi_1)] \\
\phi_0 &= \arcsin \Omega \\
\phi_1 &= \pi - 2.6414/r + 1.8318/r^2 \\
&\quad -\Omega(1.0156 - 1.1295/r + 1.0/r^2) \\
\phi_2 &= -\pi + 2.6414/r - 1.8318/r^2 \\
&\quad -\Omega(1.0156 - 1.5266/r + 1.6825/r^2)
\end{aligned}\right\} \tag{26}$$

A somewhat more accurate asymptotic form for $\widehat{T}$ than Eq. (23) is suggested by extrapolating the known exact slip-time formula for the first-order loop with $\Omega_0 = 0$, viz,

$$Tw_L = \pi^2 \rho I_0^2(\rho) \tag{27}$$

to include the effects of Ω_0 and r. Such a form is

$$\widehat{T}w_L = \left\{\pi^2 \left(\frac{r+1}{r+F}\right) \frac{\xi(1-\widehat{D})}{[(\cos\phi_0 - \beta)(\beta - \cos\phi_1)]^{1/2}}\right\} \times \rho I_0^2\left(\frac{1}{2}\xi\rho\right) \tag{28}$$

Evaluations of this last formula show errors no larger than about 15% for $r \geq 2$, $\Omega_0/AK \leq 0.3$, and $\rho \geq 1$. For the first-order loop, the result is exact at $\Omega_0 = 0$, and within 9% for $\rho \geq 1$ and $\Omega_0/AK \leq 0.3$; for $\rho \geq 5$, it lies within 4%. For the second-order loop, $r \geq 2$ and $\Omega_0 = 0$, the results are within 11% at $\rho = 1$, and taper to 3% at $\rho = 5$. For all $\Omega_0/AK \leq 0.3$, $r \geq 2$, the formula is correct to 10% for $\rho \geq 5$.

References

1. Viterbi, A. J., *Principles of Coherent Communications,* pp. 96–103. McGraw-Hill Book Co., Inc., New York, 1966.
2. Lindsey, W. C., "Nonlinear Analysis of Generalized Tracking Systems," *Proc. IEEE,* Vol. 57, No. 10, pp. 1705–1722, Oct. 1969.
3. Tausworthe, R. C., "Cycle Slipping in Phase-Locked Loops," *IEEE Trans. Commun. Tech.,* Vol. COM-15, No. 3, pp. 417–421, Jun. 1967.
4. Lindsey, W. C., "Nonlinear Analysis and Synthesis of Generalized Tracking Systems, Part II," Report USCEE-342. Electronic Sciences Laboratory, University Southern California, Los Angeles, Calif., Apr. 1969.
5. Sanneman, R. W., and Rowbotham, J. R., "Unlock Characteristics of the Optimum Type II Phase-Locked Loop," *IEEE Trans. Aerospace and Nav. Elec.,* Vol. ANE-11, pp. 15–24, Mar. 1964.
6. Smith, B. M., "The Phase-Locked Loop with Filter: Frequency of Slipping Cycles," *Proc. IEEE,* Vol. 54, No. 2, pp. 296–297, 1966.
7. Charles, F. J., and Lindsey, W. C., "Some Analytical and Experimental Phase-Locked Loop Results for Low Signal-to-Noise Ratios," *Proc. IEEE,* Vol. 54, No. 9, pp. 1152–1166, Sep. 1966.

V. Communications Elements Research

ADVANCED ENGINEERING

A. Low Noise Receivers: Microwave Maser Development, *R. C. Clauss*

1. Introduction

Isolators used with comb-type traveling wave masers (TWMs) have been described previously in several SPSs. Improvements in the isolator performance have been one of the objectives of maser development for several years. This work has improved TWM performance by reducing losses in the comb structure.

A cryogenic switching circulator for use at X-band has been developed for JPL by E and M Laboratories of Westlake Village, Calif. A versatile liquid nitrogen-cooled dewar system has been used for hard vacuum testing of the circulator.

2. Resonance Isolator

Single crystal and polycrystalline yttrium iron garnet (YIG) have been used as a resonance isolator material in JPL-built TWMs. The performance characteristics of these masers can be found in Ref. 1 and the following SPSs:

SPS 37-42, Vol. III, pp. 42–46
SPS 37-44, Vol. III, pp. 69–72
SPS 37-46, Vol. III, pp. 67–72
SPS 37-47, Vol. II, pp. 71–73
SPS 37-48, Vol. II, pp. 48–50
SPS 37-57, Vol. II, pp. 87–90
SPS 37-58, Vol. II, pp. 50–52
SPS 37-61, Vol. II, pp. 86–89

Table 1 reviews the TWM and isolator forward loss data from 1965 to the present. TWM loss is lowest at center frequency; values are also listed for the low-frequency end of the tuning range or bandpass. The S-band masers listed give maximum amplification near the low-frequency cutoff (a characteristic of the particular design and maser material). The problems associated with resonance isolator performance are most severe at the low-frequency cutoff and are reflected by the data in Table 1.

Table 1. TWM isolator performance comparison

TWM type	Date completed	Isolator forward loss, dB		Total TWM forward loss, dB	
		Low frequency	Center frequency	Low frequency	Center frequency
S-Band, Tunable, 2275–2415 MHz	Dec 1965	24	5	31	10
S-Band, Tunable, 2275–2415 MHz	Jun 1966	23	3	30	9
S-Band, Tunable, 2230–2430 MHz	May 1967	13	4	18	8
S-Band, Tunable, 2230–2420 MHz	Aug 1968	10	2	19	7
S-Band, Tunable, 2240–2430 MHz	Jun 1969	8	2	12	5
S-Band, 2nd Gen, 2270–2300 MHz	Aug 1968	8	6	12	10
S-Band, 2nd Gen, 2270–2300 MHz	Jan 1970	4	2	7	5
S-Band, 2nd Gen, 2270–2300 MHz	Jul 1970	4	2	9	6
X-Band, Tunable, 8380–8520 MHz	Sep 1966	10	2.5	28	18.5
X-Band, Tunable, 7600–8900 MHz	Dec 1969	11	6	16	11

The isolator forward loss reduction at S-band from 1967 to the present resulted from improved techniques for material evaluation, selection, fabrication, and assembly. The improved techniques were necessary to produce single crystal YIG isolators for S-band TWMs in the quantity needed for installation in the Deep Space Network. Data listed for July 1970 (Table 1) were obtained during evaluation of the first two masers produced by the R. F. Systems Development Section.

The X-band masers listed in Table 1 use polycrystalline YIG isolators. Isolator performance of the 7600 to 8900-MHz maser has been compromised to cover a wide tuning range and to simplify fabrication problems caused by the small size of the comb structure and ferrite elements.

3. Cryogenic Switching Circulator

A small circulator ($1\frac{1}{4} \times 1\frac{1}{8} \times 1\frac{5}{8}$ in.) that operates at cryogenic temperatures has been built for JPL by E and M Laboratories. The circulator uses an electromagnet and the field strength can be adjusted for optimum performance as a function of temperature. It can be used to provide isolation for a cryogenic amplifier or used as a microwave switch. Switching time is 250 μs. Circulator magnet current for optimum isolation is shown as a function of temperature in Fig. 1. The voltage standing-wave ratio (VSWR) and isolation data are shown in Table 2. The insertion loss is 0.2 dB between all ports at frequencies between 7700 and 8600 MHz.

The circulator is shown mounted on the cold plate of a cryogenic test dewar in Fig. 2. The assembly is shown upside down, with the radiation shield and vacuum housing removed. The charcoal cryopumps (getters) maintain a dewar vacuum of less than 1 micron when the cold plate is at or below liquid nitrogen temperature (78°K). Liquid helium has been used to test the circulator at temperatures below 78°K. The assembled test dewar is shown in Fig. 3.

Table 2. Test data for C39T15 circulator

Frequency, MHz	VSWR			Isolation, dB		
	Port 1	Port 2	Port 3	Port 1 to 3	Port 2 to 1	Port 3 to 2
7700	1.13	1.10	1.11	25	24	24
8150	1.06	1.04	1.03	28	30	>30
8600	1.15	1.11	1.12	26	25	26

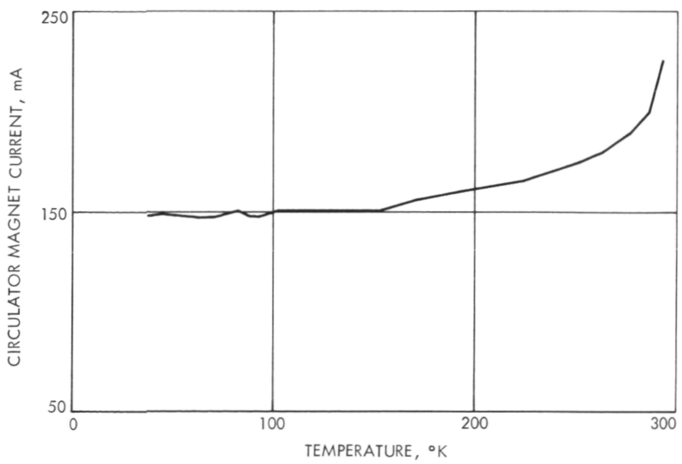

Fig. 1. Optimum current for isolation at temperatures below 300°K

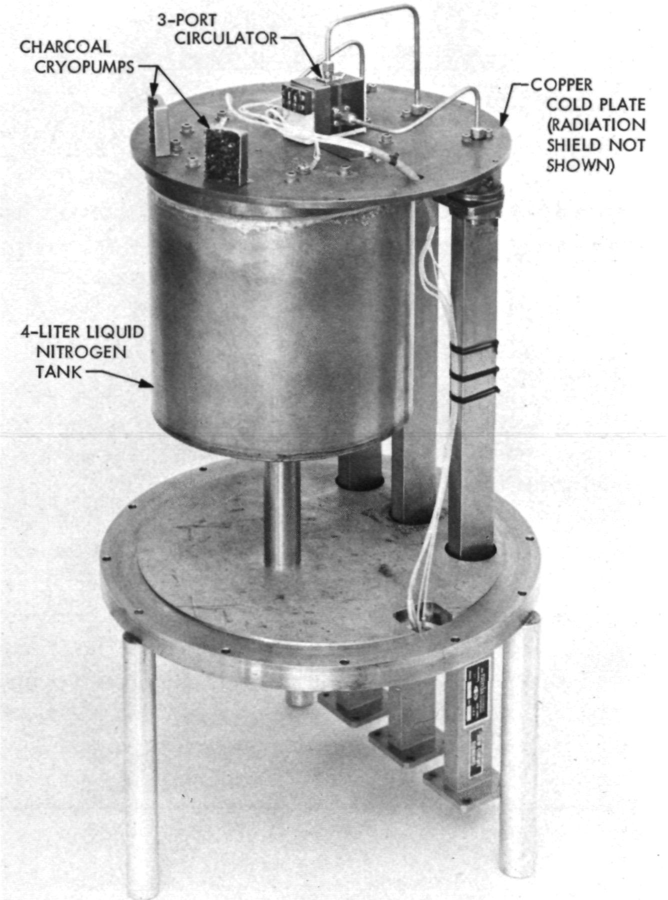

Fig. 2. Switching circulator mounted in test dewar

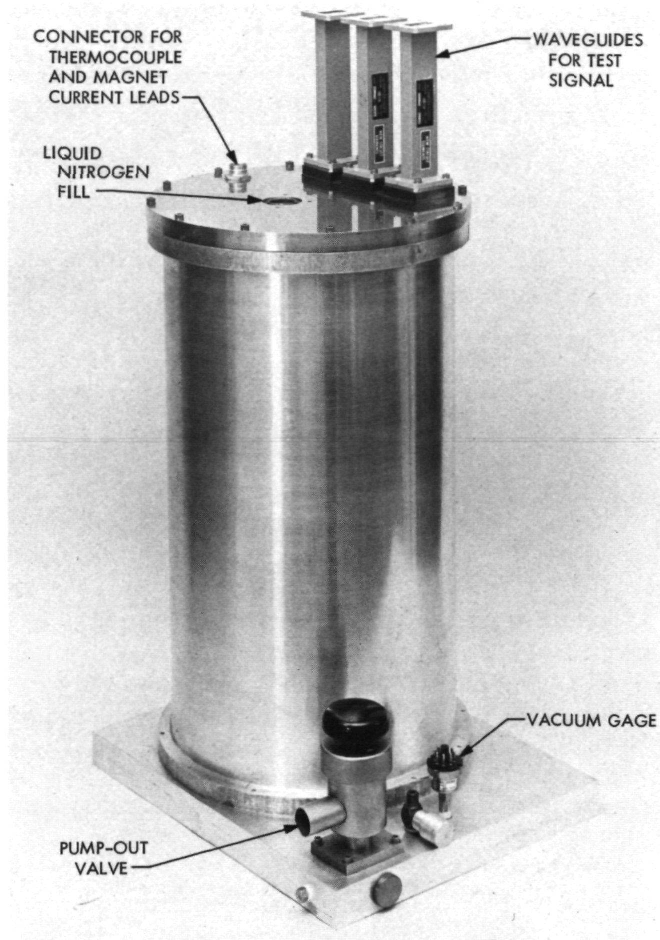

Fig. 3. Cryogenic test dewar

Direct current through the circulator magnet coil (150 mA) causes a 7-mW heat load at liquid nitrogen temperature. Magnet core losses occur when switching the circulator at 60 Hz; this increases the heating rate to 40 mW.

4. Conclusion

Resonance isolators for S-band TWMs have been optimized to the extent that at the maser center frequency only a small reduction in forward loss is possible. Considerable room for improvement still exists at frequencies away from the center of the bandpass. At frequencies above S-band, improvements in gain, bandwidth, and noise temperature can be achieved by use of more efficient isolation techniques. Initial development of new ferrite devices can be accomplished at liquid nitrogen temperature where the complexity and cost of operation are much less than is required for liquid helium temperature testing.

Reference

1. Clauss, R. C., *A Traveling Wave Maser for Deep Space Communication at 2295 and 2388 MHz,* Technical Report 32-1072. Jet Propulsion Laboratory, Pasadena, Calif., Feb. 15, 1967.

B. Improved RF Calibration Techniques: A Study of the RF Properties of the 210-ft-diam Antenna Mesh Material, *T. Y. Otoshi and R. B. Lyon*

1. Introduction

To reduce wind loading on large ground antennas for deep space communications, the reflector surface is usually perforated. A compromise must be made between porosity and acceptable degradation of RF performance because the amount of RF energy that leaks through the reflector surface is a function of porosity (as well as hole size and hole pattern). On the outer 60% radius of the 210-ft-diam antenna at DSS 14, perforated panels having 51% porosity and 3/16-in.-diam holes are used as the reflective surface material. In a previous experimental study of porosity versus RF leakage (SPS 37-20, Vol. IV, pp. 135–137), a test sample of this particular antenna mesh material was not included.

This article presents the results of reflectivity and transmission loss measurements on waveguide test samples having the same physical properties as the mesh material on the 210-ft antenna. The waveguide measurement method and its limitations are discussed.

2. Experimental Method

A waveguide method was used previously at JPL for investigating the relationship between porosity and RF leakage through perforated flat plates (see SPS 37-19, Vol. III, pp. 46–48, and SPS 37-20, Vol. IV, pp. 135–137). Recently, a precision waveguide technique was also developed for investigating the reflectivity properties of various types of flexible mesh materials for use as reflector surfaces of unfurlable spacecraft antennas (SPS 37-61, Vol. III, pp. 99–106).

Figure 1 shows a block diagram of the tuned-reflectometer system employed for precision reflectivity loss measurements. The system operates on the dual-channel principle and utilizes either one of the two types of insertion loss test sets developed at JPL (Refs. 1 and 2). Comparisons of the reflected power from the mesh sample and that from a reference short-circuit are made on the insertion loss test set. A major error on mesh reflectivity loss measurements is usually caused by the residual internal reflection coefficient Γ_{2i} as seen looking back into the reflectometer system at the measurement plane. This reflection coefficient can be made small by

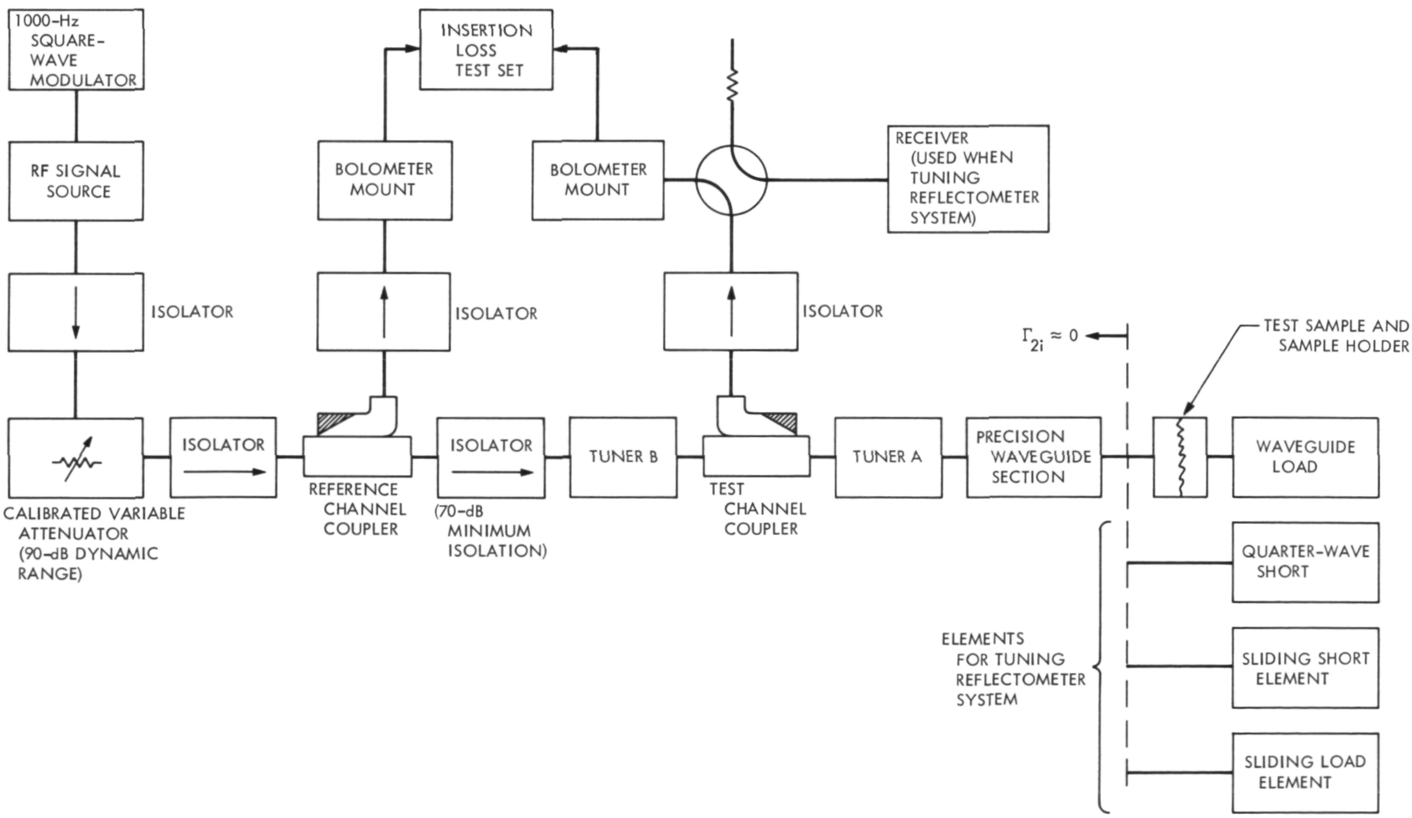

Fig. 1. Block diagram of waveguide system for mesh reflectivity measurements

sliding a short-circuit and adjusting tuner B so that the reflectometer output variations become negligibly small (Ref. 3). In general, it is difficult to reduce the peak-to-peak output variation to less than 0.02 dB. However, it can be shown from an error analysis that although the peak-to-peak output variation of 0.02 dB can result in a maximum error of ±0.01 dB, the error on mesh reflectivity loss measurements will be reduced to less than ±0.003 dB if a flat plate short is used to establish the measurement reference plane and if the mesh sample is then placed at the same reference plane. In practice, the procedure would be to insert a flat plate short into the mesh sample holder and then use the sample holder–short combination to establish the measurement reference plane. To achieve the improved accuracy using this procedure, it is also required that (1) the mesh sample reflectivity loss be less than 0.2 dB, (2) the mesh reflection coefficient phase angle be within ±10 deg of 180 deg which is the phase angle of the flat plate short, and (3) the directivity of the test channel coupler be tuned to at least 70 dB.

Transmission loss shall be defined in this article as the insertion loss when measured in a matched system. Transmission loss and phase angles at fixed frequencies were measured with a Hewlett-Packard (HP) 8140A Network Analyzer. For transmission loss measurements over a broad band of frequencies, the HP 8542A Automatic Network Analyzer was employed. Control test samples were used to cross-check the results obtained with the Network Analyzer to those obtained with RF and ac substitution systems.

To obtain meaningful results with the waveguide method, it is necessary that the waveguide mesh sample have a periodic structure. The free-space situation being simulated by the waveguide method is a plane wave impinging upon an infinitely large sample of the mesh material at an oblique angle of incidence θ_i (see Fig. 2). When the waveguide supports only the TE_{10} mode, the E-field is polarized perpendicular to the plane of incidence. The angle of incidence is determined by the waveguide cutoff frequency f_c and the operating frequency f by the relationship

$$\theta_i = \sin^{-1}\left(\frac{f_c}{f}\right) \tag{1}$$

Simulation of this free-space configuration is accurate (1) if the mesh pattern is imaged to the waveguide walls, and (2) if there are many basic cells (at least two rows and two columns of holes) of the periodic structure

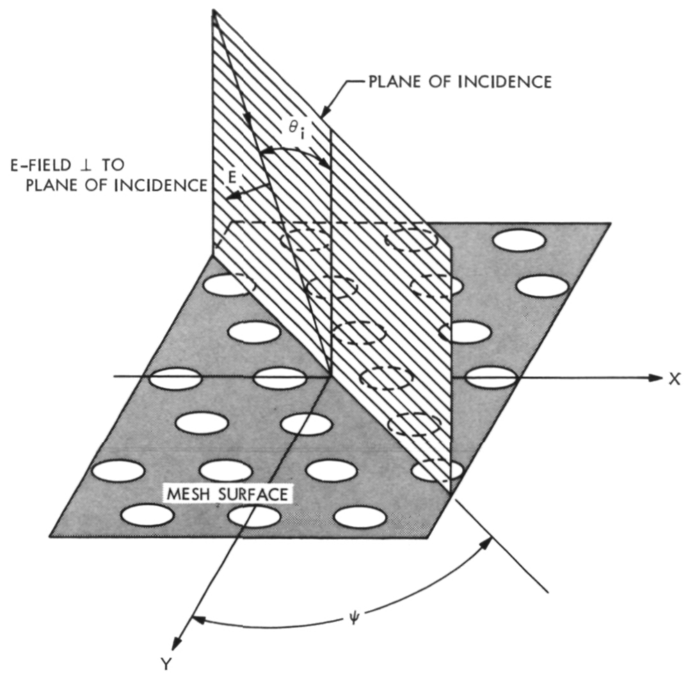

Fig. 2. Free-space test configuration being simulated by the waveguide method

filling the waveguide cross-sectional area. As the number of cells in the waveguide sample is increased, it becomes less critical that the imaging requirement be met.

3. Waveguide Test Samples

Figure 3 shows waveguide test samples having the same physical properties as the 210-ft antenna mesh material. The test samples were made from a 0.090-in.-thick 6061-T4 aluminum sheet having 51% porosity, $\frac{3}{16}$-in.-diam holes, and $\frac{1}{4}$-in. spacing between holes. Successive rows of holes are offset so that adjacent holes are equal distance apart. The waveguide test samples for WR 430 and WR 112 sample holders were cut from 4- by 12-ft perforated sheets that were fabricated by the Diamond Perforated Metal Company in Gardena, Calif. Different test samples were cut so that tests could be made with the hole row patterns oriented in directions that were parallel, 45 deg, and perpendicular to the linearly polarized electric field established by the rectangular waveguide TE_{10} mode. It should be emphasized that although the mesh pattern orientation can be changed as described, simulation of the free-space configuration by the waveguide method is limited to the case where the E-field is perpendicular to the plane of incidence. This fact might be seen better from Fig. 2. It can be seen that making $\psi = 90$ deg will not result in a parallel polarization test configuration.

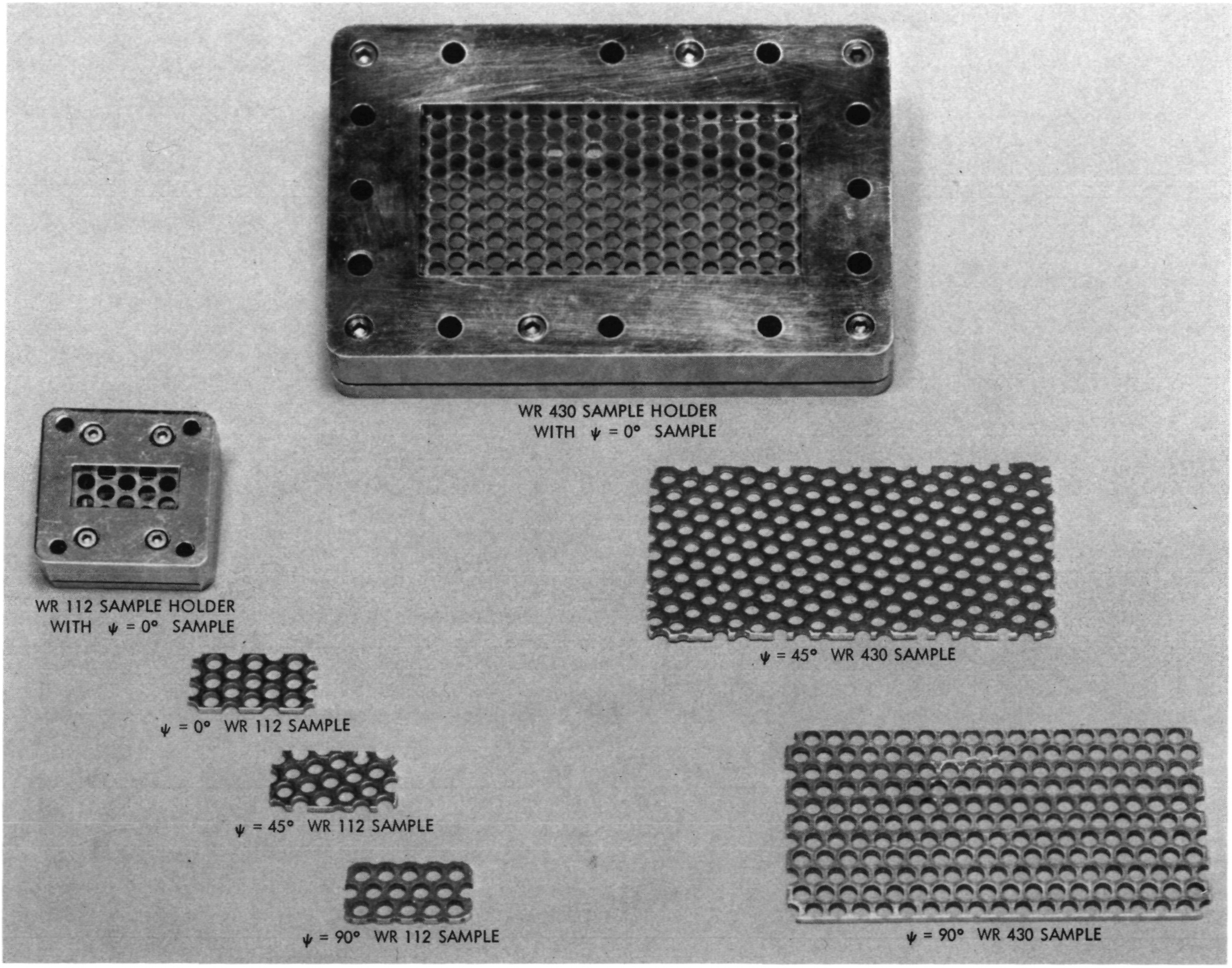

Fig. 3. WR 112 and WR 430 waveguide sample holders and test samples of the 210-ft antenna mesh

4. Experimental Results

Table 1 is a summary of measured reflectivity and transmission losses of the 210-ft antenna mesh samples. The results indicate that for an obliquely incident plane wave (E-field perpendicular to the plane of incidence), the reflectivity losses are approximately 0.001 dB and 0.008 dB at 2295 MHz and 8448 MHz, respectively. The average measured transmission losses are 43.1 dB at 2295 MHz and 30.5 dB at 8448 MHz. Although Table 1 is not complete, it appears that the mesh properties are essentially independent of hole pattern orientation. The overall accuracies for the data in Table 1 are estimated to be better than (1) ± 0.005 dB for reflectivity losses, (2) ± 0.5 dB for transmission losses, and (3) ± 2.0 deg for phase angles. The symbol $s_{\bar{x}}$ is the calculated standard error based on N which denotes the number of measurements.

At a given test frequency the waveguide result is applicable only to a particular angle of incidence. Assuming that a highly reflective mesh behaves in the same manner as a very thin metallic sheet, an estimate of the reflectivity and transmission losses for perpendicular polarization at another incidence θ_i' can be determined from the approximate relationships

$$RL(\theta_i') \simeq [RL(\theta_i)] \left[\frac{\cos \theta_i'}{\cos \theta_i} \right] \tag{2}$$

$$TL(\theta_i') \simeq TL(\theta_i) - 20 \log_{10} \left(\frac{\cos \theta_i'}{\cos \theta_i} \right) \tag{3}$$

where

$RL(\theta_i)$ = reflectivity loss measured in waveguide, dB

$TL(\theta_i)$ = transmission loss measured in waveguide, dB

θ_i = equivalent free-space angle of incidence determined from Eq. (1)

For example, using the 8448-MHz data in Table 1, substitutions of $\theta_i = 38.5$ deg, $RL(\theta_i) = 0.008$ dB, $TL(\theta_i) = 30.5$ dB, $\theta_i' = 0$ deg into Eqs. (2) and (3) result in 0.010 dB and 28.4 dB, respectively, for the reflectivity and transmission losses at normal incidence.

Table 1. Summary of reflectivity and transmission losses of 210-ft antenna mesh for E-field normal to the plane of incidence

Frequency, MHz	Free-space incidence angle θ_i, deg	Hole pattern orientation angle ψ, deg	Reflectivity loss,[a] dB		Phase of reflection coefficient, deg		Transmission loss, dB	Phase of transmission coefficient, deg
			Smooth side	Rough side[b]	Smooth side	Rough side[b]		
2295	36.7	0	0.0010 $\pm 0.0001\ s_{\bar{x}}$ ($N = 13$)	—	177.5	—	43.0 $\pm 0.02\ s_{\bar{x}}$ ($N = 5$)	87.5 $\pm 0.6\ s_{\bar{x}}$ ($N = 5$)
		45	—	—	177.3	—	42.9	89.5
		90	—	—	177.4	—	43.3	89.4
8448	38.5	0	—	—	172.6	173.3	31.0 $\pm 0.04\ s_{\bar{x}}$ ($N = 8$)	82.6
		45	0.0083 $\pm 0.0003\ s_{\bar{x}}$ ($N = 5$)	0.0079 $\pm 0.0004\ s_{\bar{x}}$ ($N = 6$)	173.0	172.4	30.2 $\pm 0.02\ s_{\bar{x}}$ ($N = 8$)	82.1
		90	0.0083 $\pm 0.0002\ s_{\bar{x}}$ ($N = 6$)	0.0089 $\pm 0.0004\ s_{\bar{x}}$ ($N = 6$)	172.4	171.9	30.3 $\pm 0.02\ s_{\bar{x}}$ ($N = 8$)	82.2

[a]Corrections were made for a 0.0005-dB loss of a copper flat plate reference short used at 2295 MHz and 0.0017-dB loss of a brass flat plate reference short used at 8448 MHz.

[b]The rough side of the mesh surface is the back side which contains minute residual burrs formed during the hole punching process.

The calculated transmission loss of 28.4-dB value is in reasonably good agreement with a normal incidence value of 27.6 dB obtained from a free-space measurement made on a 22-in. square sample of the 210-ft antenna mesh material. The free-space value is based on an average of readings obtained at 10 different spacings between the mesh sample and the transmitting and receiving horns. The free-space measurements were performed[1] in an anechoic chamber at the Mesa facility.

Figure 4 is a plot of the measured transmission losses of 210-ft antenna mesh waveguide samples over a frequency range of 2.25 to 2.50 GHz. Figure 5 is a similar plot applicable to the frequency range 8.0 to 10.0 GHz. It can be seen that no significant differences were observed in the broadband data for the mesh pattern oriented in various directions with respect to the linearly polarized E-field. The estimated accuracy of the broadband transmission loss data is ± 0.5 dB.

The experimental results given in this article are presently being correlated with those reported previously in SPS 37-20, Vol. IV. Although the present transmission losses are in the general neighborhood of expected values, a correction formula is needed to account for differences in plate thicknesses. This formula has not been derived as yet.

[1]By G. Voyles, JPL Communications Elements Research Section.

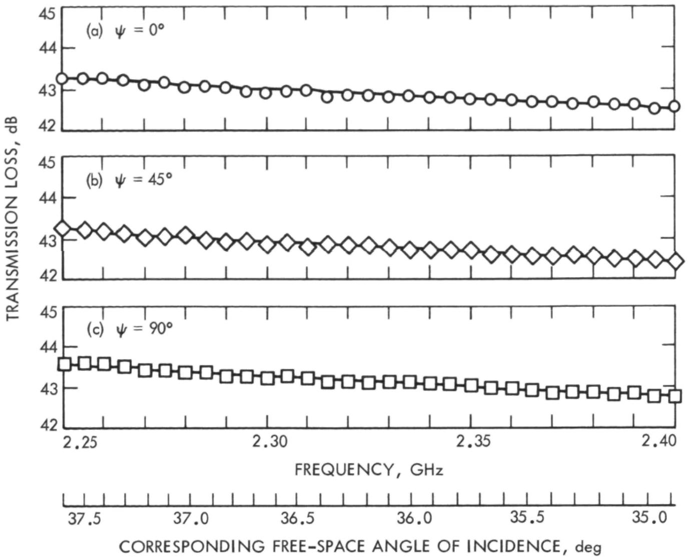

Fig. 4. Transmission losses of 210-ft antenna mesh at S-band frequencies

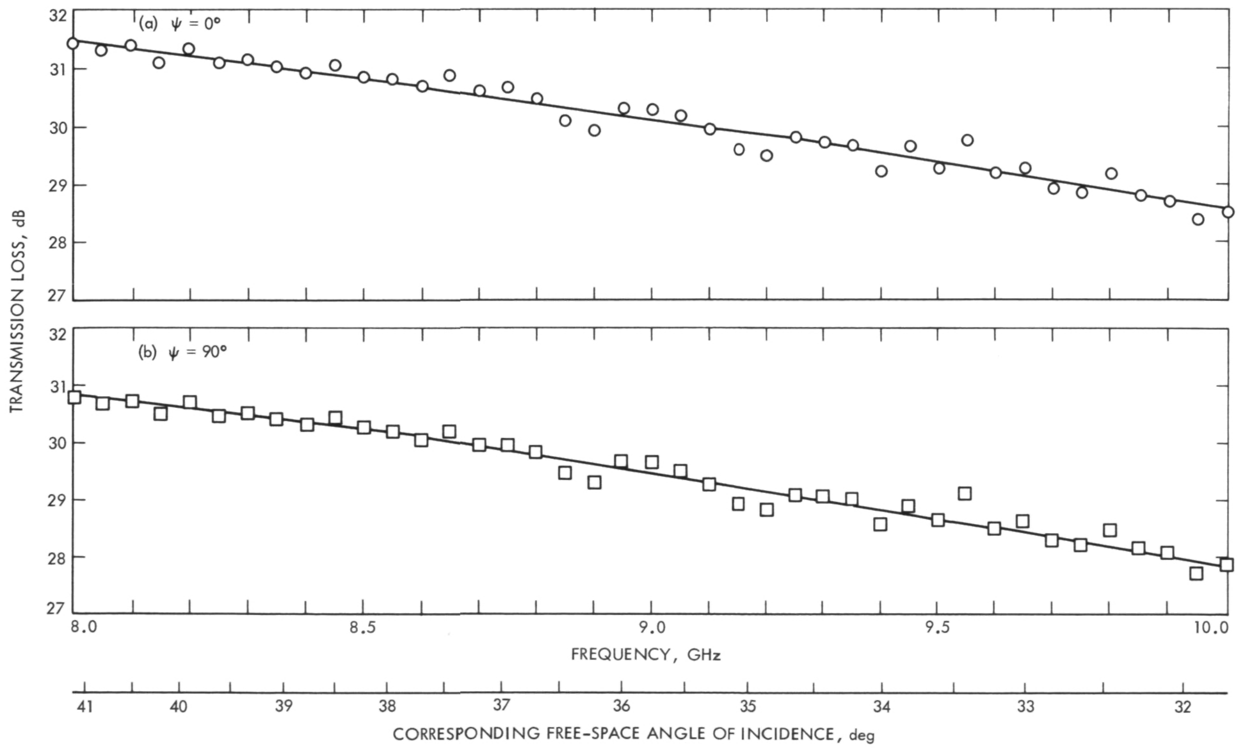

Fig. 5. Transmission losses of 210-ft antenna mesh at X-band frequencies

5. Summary and Conclusions

A procedure for accurately measuring small reflectivity losses has been described. As a future application, the described measurement system and experimental procedure might be employed for the measurement of the small loss contributed by the heat absorption white paint on reflector surfaces.

Reflectivity and transmission losses of the 210-ft antenna mesh were measured, respectively, to be (1) 0.001 dB and 43.1 dB at 2295 MHz for a 36.7-deg angle of incidence, and (2) 0.008 dB and 30.5 dB at 8448 MHz for a 38.5-deg angle of incidence. It should be reemphasized that these data are applicable only to the free-space configuration where the E-field is linearly polarized perpendicularly to the plane of incidence. At present, no experimental or analytical data has been obtained on the mesh for the parallel polarization case.

References

1. Finnie, C. J., Schuster, D., and Otoshi, T. Y., *AC Ratio Transformer Technique for Precision Insertion Loss Measurements,* Technical Report 32-690. Jet Propulsion Laboratory, Pasadena, Calif., Nov. 30, 1964.
2. Stelzried, C. T., Reid, M. S., and Petty, S. M., "A Precision DC Potentiometer Microwave Insertion Loss Test Set," *IEEE Trans. Instrum. Meas.,* Vol. IM-15, pp. 98–104, Sept. 1966.
3. Anson, W. J., "A Guide to the Use of the Modified Reflectometer Technique of VSWR Measurement," *J. Res. NBS, Sec. C,* Vol. 65C, No. 4, pp. 217–223, Oct.–Dec. 1961.

C. Improved RF Calibration Techniques: System Operating Noise Temperature Calibrations of Low Noise Cones, *M. S. Reid*

The system operating noise temperature performance of the low noise cones in the Goldstone Deep Space Communications Complex (GDSCC) is reported. The operating noise temperature calibrations were performed with the ambient termination technique (SPS 37-42, Vol. III, p. 25). The cones on which this technique was used during this reporting period are:

(1) S-band polarization ultra (SPU) cone at DSS 12.

(2) S-band research operational (SRO) cone at DSS 13.

(3) S-band Cassegrain ultra (SCU) cone at DSS 14.

The averaged operating noise temperature calibrations for the various cones, and other calibration data, are presented in Table 1 for the period June 1, through September 30, 1970.

The calibration data were reduced with JPL computer program number 5841000, CTS20B. Measurement errors of each data point average are recorded under the appropriate number in Table 1. The indicated errors are the standard deviation of the individual measurements and of the means, respectively. They do not include instrumentation systematic errors. The averages were computed using only data with:

(1) Antenna at zenith.

(2) Clear weather.

(3) No RF spur in the receiver passband.

(4) Probable error in computed operating noise temperature due to measurement dispersion less than 0.1°K.

The DSIF waveguide switches at DSS 12 were replaced on day 167 (June 16, 1970) with improved versions of the switches. These switch changes are reported by Reilly and McCrea in *Section F* of this chapter. Data taken before and after the switches were changed are shown separately in Table 1. In Fig. 1a, the system operating noise temperatures, T_{op}, at DSS 12 are plotted as a function of day number for the low noise path, and in Fig. 1b for the diplexed path.

Table 1. Averaged operating noise temperature calibrations for the low noise cones at GDSCC

Station	DSS 12				DSS 13		DSS 14	
Cone	SPU				SRO		SCU	
Configuration	Low noise path before switch change	Low noise path after switch change	Diplexed before switch change	Diplexed after switch change				
Frequency, MHz	2295	2295	2295	2295	2388	2295	2388	2295
Maser serial number	96S5	96S5	96S5	96S5	96S2	96S2	96S4	96S4
Maser temperature, K	3.7	3.7	3.7	3.7	5.2	5.2	4.2	4.2
Maser gain, dB	57.0 ±0.19/0.06 10 measurements	57.0 ±0.81/0.15 11 measurements	57.0 ±0.23/0.06 19 measurements	56.9 ±1.00/0.19 11 measurements	37.2 ±2.02/0.23 79 measurements	50.1 ±1.97/0.30 27 measurements	33.7 ±0.31/0.18 3 measurements	47.7 ±0.47/0.15 10 measurements
Follow-up noise temperature contribution, K	0.40 ±0.17/0.06 9 measurements	0.55 ±0.22/0.09 10 measurements	0.47 ±0.03/0.01 19 measurements	0.54 ±0.21/0.09 12 measurements	1.35 ±1.59/0.20 64 measurements	0.19 ±0.22/0.04 33 measurements	0.53 ±1.50/0.88 3 measurements	0.93 ±0.38/0.12 10 measurements
System operating noise temperature, K	17.36 ±0.31/0.10 9 measurements	17.36 ±0.66/0.19 11 measurements	25.44 ±0.34/0.08 19 measurements	24.70 ±0.77/0.21 13 measurements	16.03 ±0.81/0.10 64 measurements	17.06 ±0.95/0.16 33 measurements	24.02 ±2.69/1.56 3 measurements	17.33 ±0.45/0.14 10 measurements

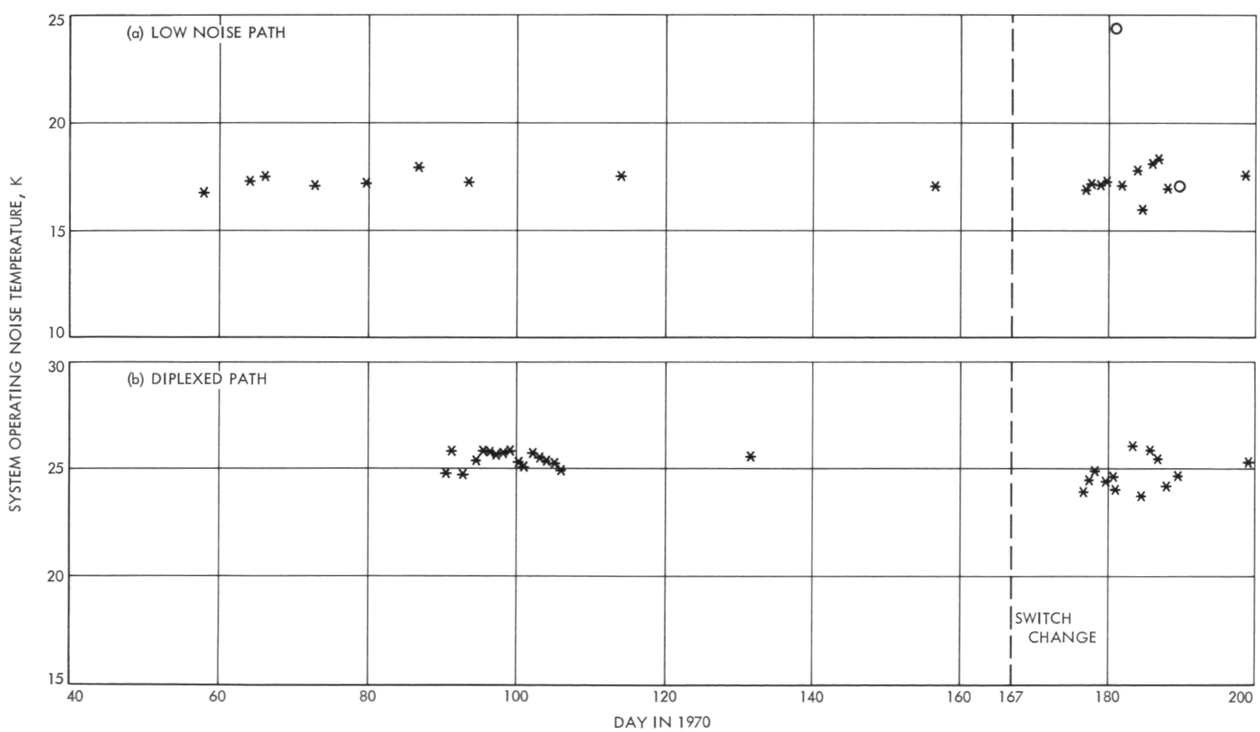

Fig. 1. System operating noise temperature at DSS 12 (SPU cone)

Table 2. Initial checkout data on the PDS cone on the roof of Building 238 using ambient termination technique

Maser serial number	96S3			
Frequency, MHz	2388		2295	
Maser temperature, K	5.1		4.1	
Configuration	Low noise path	Diplexed path	Low noise path	Diplexed path
Maser gain, dB	44.0 1 measurement	44.2 1 measurement	54.1 ±0.35/0.20 3 measurements	53.9 1 measurement
Follow-up noise temperature contribution, K	1.44 1 measurement	1.07 1 measurement	0.12 ±0.03/0.02 3 measurements	0.15 1 measurement
System operating noise temperature, K	17.01 ±0.01 1 measurement	22.20 ±0.01 1 measurement	15.16 ±0.14/0.08 3 measurements	19.33 ±0.03 1 measurement

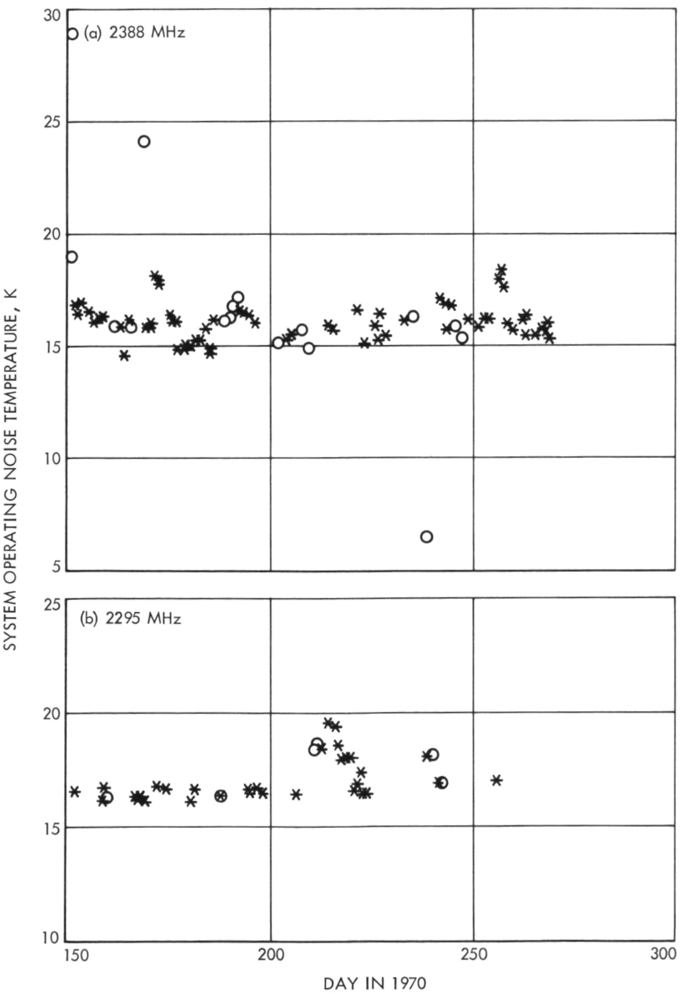

Fig. 2. System operating noise temperature at DSS 13 (SRO cone)

The system operating noise temperatures of the SRO cone at DSS 13 are shown in Figs. 2a and 2b for operating frequencies of 2388 and 2295 MHz, respectively.

The system operating noise temperatures of the SCU cone at DSS 14 are shown in Fig. 3. Data at 2388 MHz are shown enclosed in rectangles; the remainder are data at 2295 MHz.

In all figures, data that satisfy the four conditions stated above are plotted as asterisks, while data that fail one or more conditions are plotted as circles.

Profile data were taken at DSS 14 with the SCU cone in the tricone configuration on the 64-m antenna. Figure 4 shows system operating noise temperature (K) as a function of elevation angle (deg). The operating frequency was 2295 MHz and the azimuth angle was 270 deg. Five other profiles at differing azimuth angles showed minimal differences with that of Fig. 4. This profile should be compared with the one in Fig. 21, SPS 37-60, Vol. II, p. 40, which shows system operating noise temperature as a function of elevation angle for the same cone, at the same frequency, on the same antenna, but in the unicone configuration. It may be seen that the two profiles are essentially the same.

Table 2 shows data taken on the roof of building 238 at JPL during the initial checks on the polarization diversity S-band (PDS) cone. These calibration data were taken with the ambient termination technique and were

Table 3. Initial checkout data on the PDS cone on the roof of Building 238 using liquid helium-cooled termination technique

Configuration	Low noise path	Diplexed path	Low noise path	Diplexed path
Frequency, MHz	2388	2388	2295	2295
Maser serial number	96S3	96S3	96S3	96S3
Horn temperature, K	10.26 ±0.30 8 measurements	15.29 ±0.31 8 measurements	10.55 ±0.30 8 measurements	14.48 ±0.31 8 measurements
System operating noise temperature, K	16.91 ±0.02 8 measurements	21.94 ±0.03 8 measurements	15.67 ±0.02 8 measurements	19.61 ±0.03 8 measurements
Maser noise temperature, K	5.22 8 measurements		5.02 8 measurements	
Receiver noise temperature, K	6.65 ±0.34 8 measurements		5.13 ±0.33 8 measurements	
Follow-up noise temperature contribution, K	1.43 8 measurements		0.11 8 measurements	

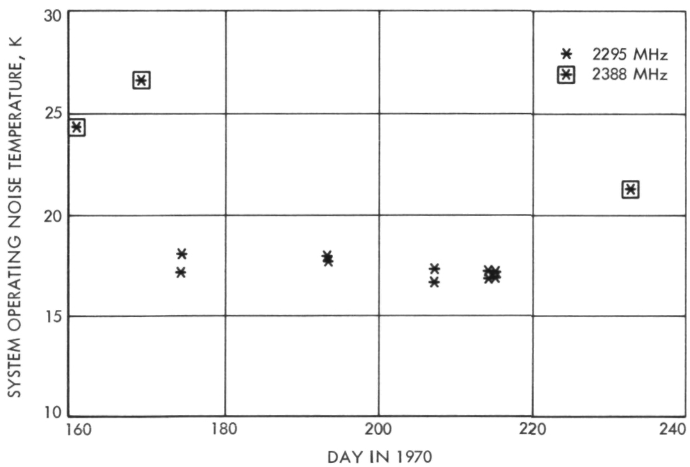

Fig. 3. System operating noise temperature at DSS 14 (SCU cone)

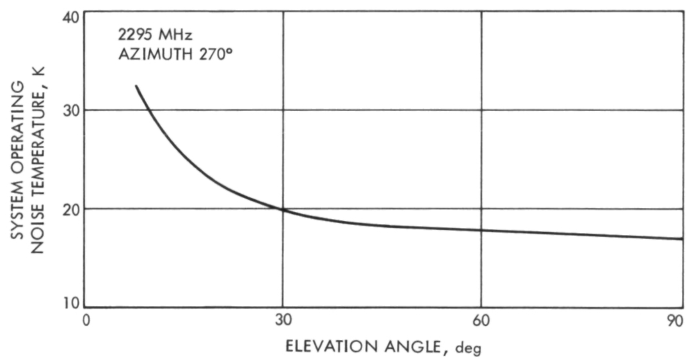

Fig. 4. System operating noise temperature at DSS 14 as a function of elevation angle (SCU cone)

reduced with JPL computer program number 5841000, CTS20B. The indicated errors are the standard deviation of the individual measurements and of the means, respectively, for the low noise path at 2295 MHz. For the other sets they are simply the errors associated with the individual data points.

Further calibration data of the PDS cone taken on the roof of building 238 are presented in Table 3. These calibration data were taken with a liquid helium-cooled termination and were reduced with JPL computer program number 5799000, TYO30A. The indicated errors are, in all cases, standard deviations.

It will be seen that in Table 3 the measured noise temperature of the maser is 5.02 K at 2295 MHz, whereas in Table 2 a maser noise temperature of 4.1 K at 2295 MHz has been used. The latter is a theoretical value. As the masers at the GDSCC are usually evaluated with precision cryogenic loads only when the maser is first constructed, the theoretical values are used in the continuing program of system operating noise temperature monitoring and refinement. The best method for the present GDSCC is probably to use the ambient load technique on a systematic basis and to use a precision cryogenic load for infrequent, periodic calibrations in the field. This has been discussed theoretically and experimentally in Ref. 1 (see also SPS 37-36, Vol. IV, pp. 268–277, and SPS 37-39, Vol. III, pp. 81–83).

Reference

1. Stelzried, C. T., Reid, M. S., and Nixon, D. L., *Precision Power Measurements of Spacecraft CW Signal With Microwave Noise Standards,* Technical Report 32-1066. Jet Propulsion Laboratory, Pasadena, Calif., Feb. 15, 1968.

D. Improved RF Calibration Techniques: PDS Cone Waveguide/Polarimeter Calibrations,

P. D. Batelaan, B. Seidel, and R. B. Lyon

1. Introduction

This article presents a summary of critical waveguide losses and reflection coefficients that were measured for the polarization diversity S-band (PDS) cone on the ground. Subsequent evaluation of individual sources of noise that contribute to operating noise temperature requires accurate knowledge of dissipative and mismatch losses introduced by the various cone components.

A special capability of the PDS cone is that it can be used as an accurate polarimeter and will be used to track the polarization of the signal from the *Pioneer* spacecraft as the signal propagates through the solar corona. To verify polarimeter capabilities of the cone, a test was made measuring the relative amplitude and phase of the two outputs of the orthomode transducer as a function of orientation of the quarter-wave plates. Figure 1 is a simplified block diagram of the cone as it was configured at the time of these measurements.[1] Figure 2 shows the TWM reference flange, port ①.

2. Waveguide Calibration Results

The insertion loss of the PDS traveling wave maser (TWM) to cryogenic load port path, port ① to ③, was measured with a precision laboratory AC Insertion Loss Set (Ref. 1) at two frequencies. The results are

$$0.0264 \pm 0.0006 \; pe_T \text{ dB at } 2295 \text{ MHz}$$

and

$$0.0284 \pm 0.0007 \; pe_T \text{ dB at } 2388 \text{ MHz}$$

where pe_T is the total probable error. The reflection coefficient measurements were made with a high-precision tuned reflectometer. Table 1 shows the results of these measurements.

3. Polarimeter Verification Results

The polarimeter capabilities of the cone were verified by injecting a linearly polarized signal into the feed horn probes and measuring the relative outputs of the two orthomode ports, amplitude and phase, as a function of quarter-wave plate position. The measured values are in excellent agreement with theory. Graphs are presented in Figs. 3 and 4.

Reference

1. Finnie, C. J., Schuster, D., and Otoshi, T. Y., *AC Ratio Transformer Technique for Precision Insertion Loss Measurements,* Technical Report 32-690. Jet Propulsion Laboratory, Pasadena, Calif., Nov. 30, 1964.

[1]The reader is cautioned that some changes are scheduled to be made in certain waveguide parts.

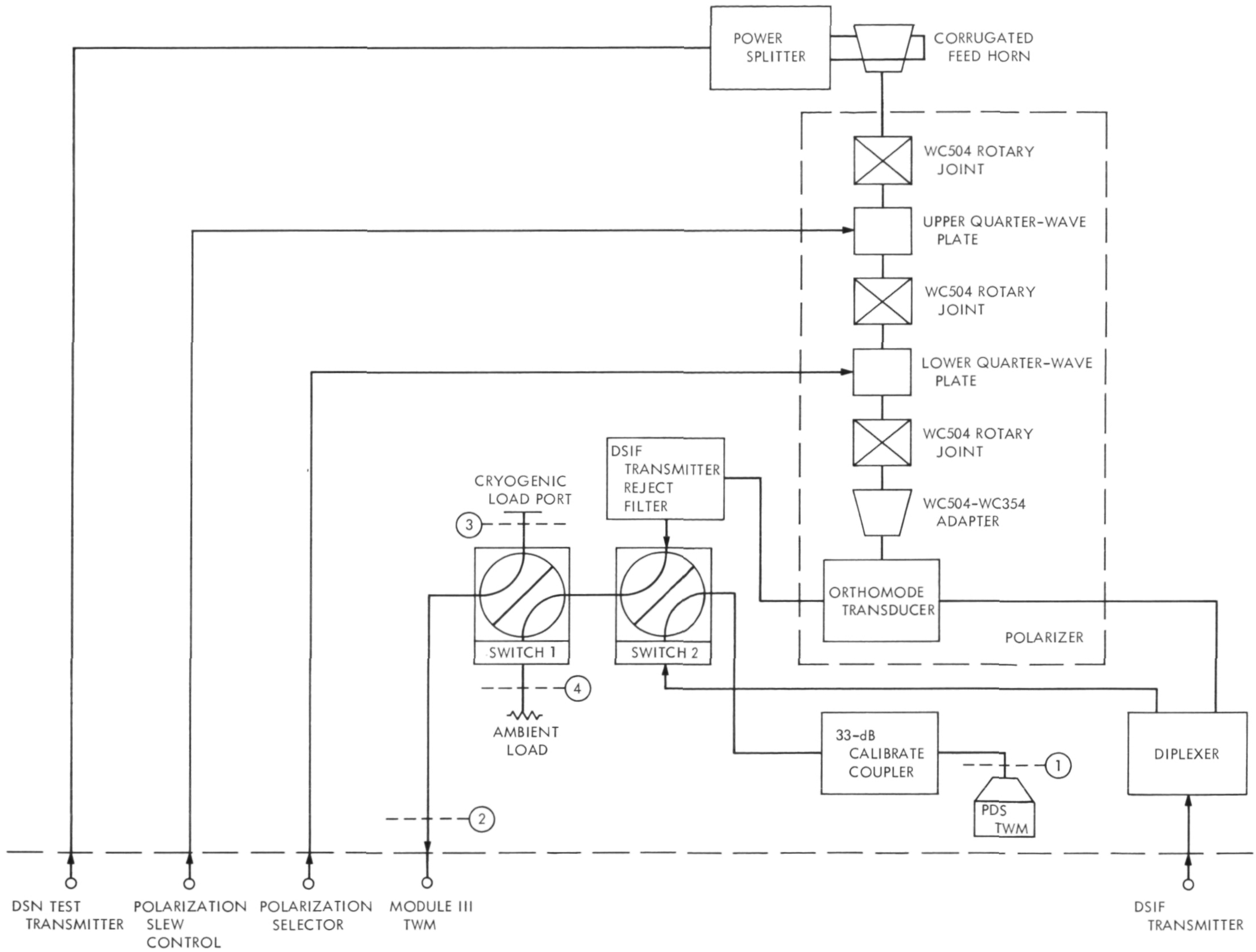

Fig. 1. Simplified PDS cone block diagram

Table 1. Voltage reflection coefficients

Path	2295 MHz	2388 MHz
PDS TWM to cryogenic load (tuned to 2295 MHz), port ① to port ③	0.0020	0.0282
Cryogenic load to PDS TWM, port ③ to port ①	0.0019	0.0260
PDS TWM to ambient load (broadband tuned), port ① to port ④	0.0275	0.0195
PDS TWM to antenna (through transmitter reject filter), port ① to antenna		
Right-hand circular polarization	0.0193	0.1084
Left-hand circular polarization	0.0193	0.1084
Rotating linear, max	0.0234	0.1778
Rotating linear, min	0.0182	0.0861
PDS TWM to antenna (through diplexer), port ① to antenna		
Right-hand circular polarization	0.0372	0.0324
Left-hand circular polarization	0.0372	0.0327
Rotating linear, max	0.0407	0.0661
Rotating linear, min	0.0351	0.0191

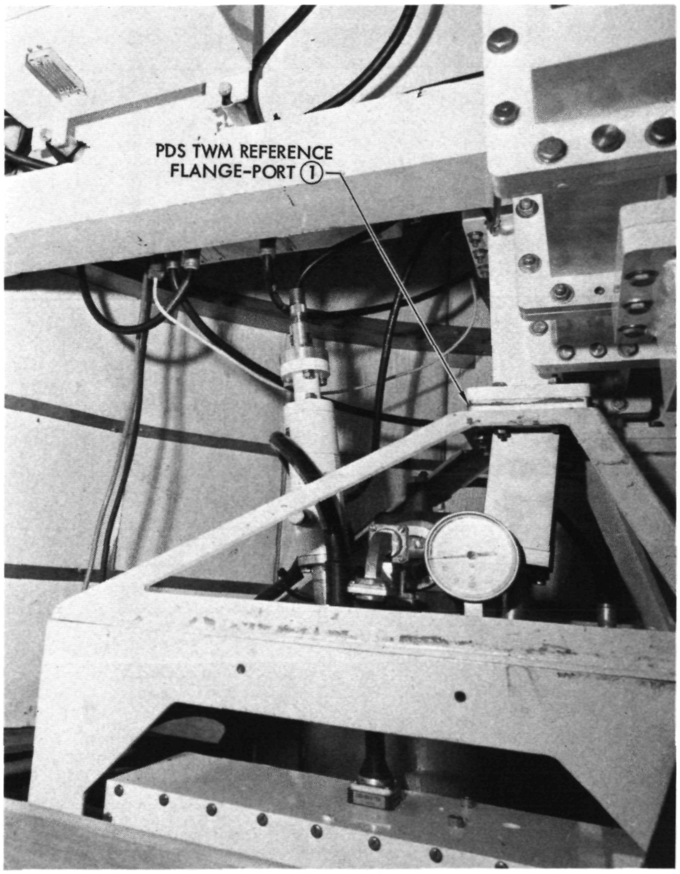

Fig. 2. PDS cone showing TWM reference flange (port ①)

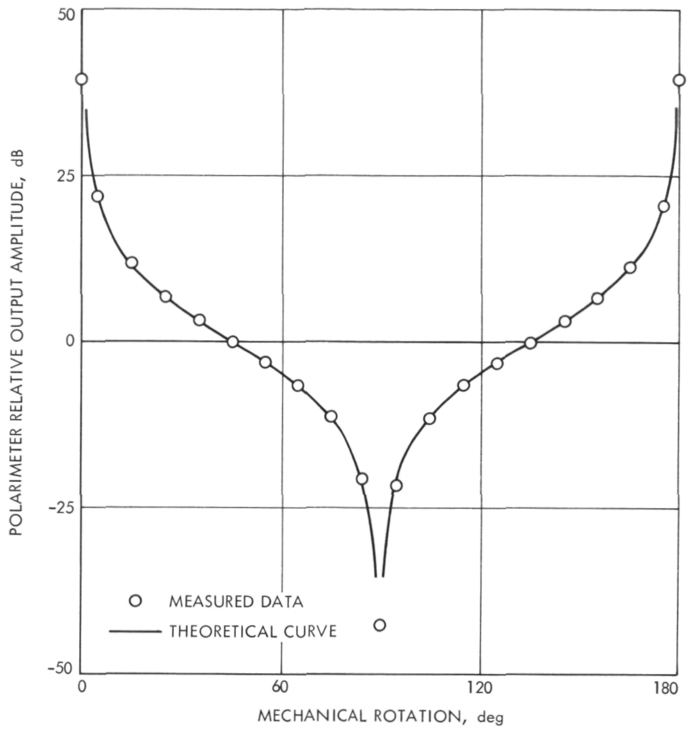

Fig. 3. Polarimeter relative output amplitude vs quarter-wave plate position

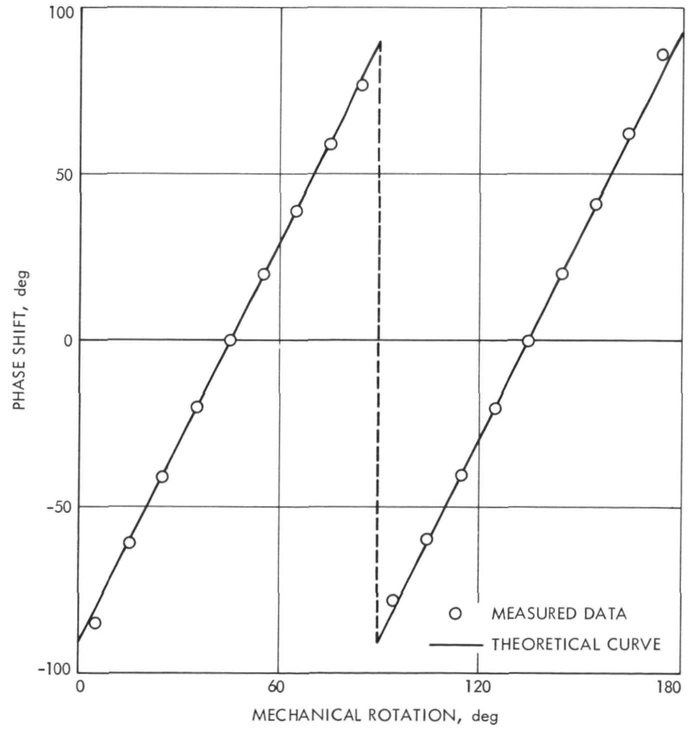

Fig. 4. Polarimeter relative output phase vs quarter-wave plate position

E. High-Power Feed Component Development,

F. E. McCrea, H. F. Reilly, Jr., and D. E. Neff

1. Introduction

Since the introduction of high-powered S-band transmitters (approximately 500 kW, CW) at the Venus (DSS 13) and Mars (DSS 14) Deep Space Stations, three S-band feed systems have been in use. The S-band radar operational (SRO) feed was implemented first to serve in a simple cycled radar mode. The S-band megawatt transmit (SMT) feed followed and allowed the first time-shared (diplexed) operations at high power. Based upon the qualified success of these straightforward systems, the polarization diversity S-band (PDS) feed was developed and recently installed at DSS 14.

All of these systems include similar components in various states of development. This article discusses the basic design of these components, the evaluation efforts to prove them suitable, and the present state of development. The items discussed include WC504 rotary joints, stepped transitions and quarter-wave plate polarizer, and an orthomode transducer.

2. WC504 Components

Figure 1 shows a cross section of the 5.040-in.-diam TE_{11} mode rotary joint. Folded, half-wave choked construction is used to minimize currents at the ball bearings. A minimum insertion length of 3,000 in. was achieved with this design. Precision insertion loss and reflectometer tests show a loss of 0.0018 $\pm$0.0004 dB and a reflection coefficient of 0.00025 $\pm$0.0001 dB at 2295 MHz for 6061 aluminum alloy construction. No cooling other than conduction into adjacent pieces is supplied in this item. Figure 2 is a photograph of an assembled unit showing the 0.010-in. circumferential gap.

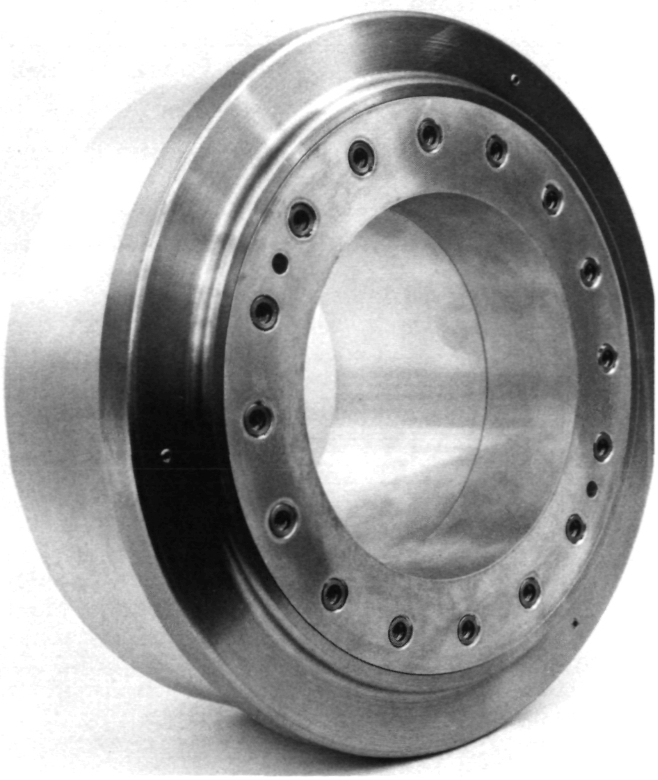

Fig. 2. Assembled WC504 waveguide rotary joint

Serious questions concerning the application of such a component in a high-power, low-noise ($<25°K$) diplexed system arise since the simultaneous transmitted and received currents differ by more than 25 orders of magnitude (>250 dB). The balance of the components used in the earlier feeds, the stepped transitions (Ref. 1) made from a seamless copper block with cooling passages (Fig. 3) and the quarter-wave plate polarizer made from a seamless aluminum block with cooling passages (Fig. 4), was expected to cause no difficulties.

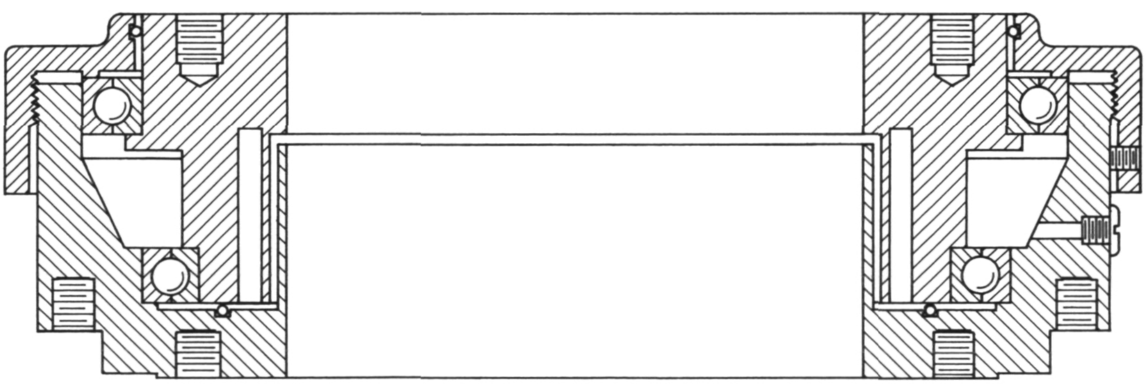

Fig. 1. Cross section of WC504 waveguide rotary joint

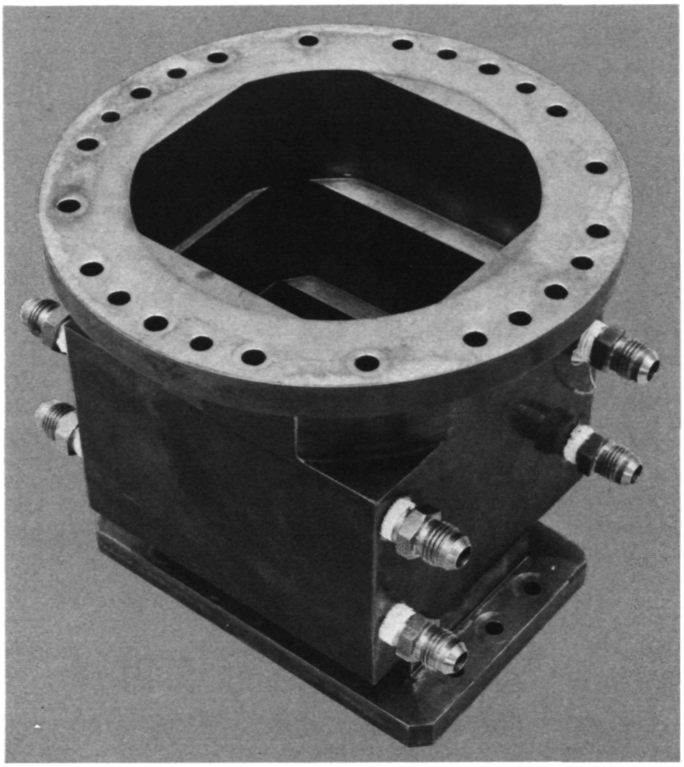

Fig. 3. Seamless waveguide stepped transition

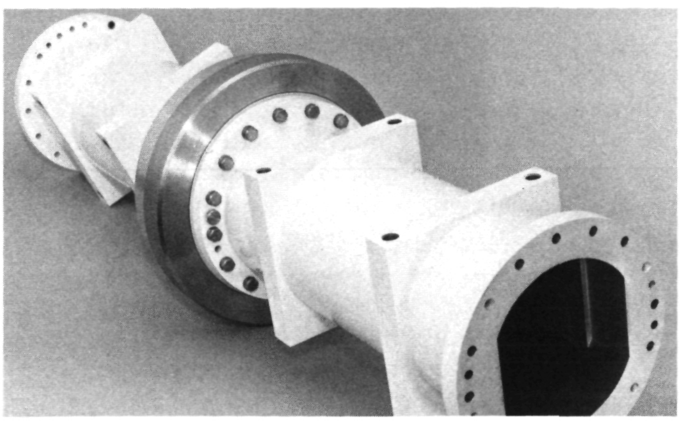

Fig. 4. Seamless waveguide quarter-wave plates with rotary joint

It was decided to test the above items in one setup by use of the Goldstone Microwave Test Facility (MTF) 500-kW resonant ring (SPS 37-40, Vol. III, pp. 24–26) in a diplexed configuration. For this test, the quarter-wave plate was simulated by a simple WC504 waveguide, approximately 12 in. long, to avoid polarization transformation problems in the resonant ring. A block diagram of the test setup is shown in Fig. 5. A photograph of the five pieces under test is shown in Fig. 6. A lever

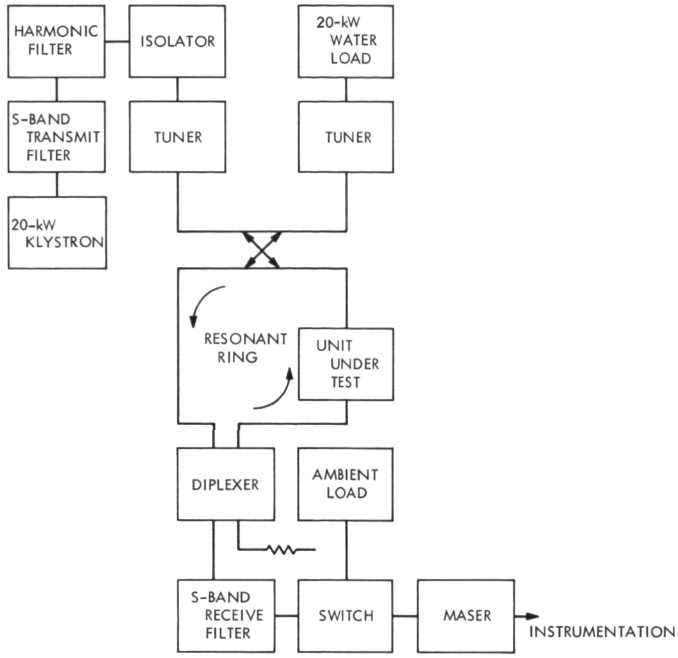

Fig. 5. Block diagram of resonant ring diplexing test setup

and scale were attached to the rotating section to determine starting and running torques of the rotary joints (9 and 8 ft-lb, respectively, at room temperature).

The first test was done without any water cooling to determine just where and what the problem areas would be. In all tests the ring was brought up in 100-kW steps and the components allowed to temperature stabilize. The maser was monitored for noise bursts; the starting and running torque was also monitored at these steps. At 200 kW the joints ceased to rotate. The torque required to rotate the test piece had risen to above 30 ft-lb.

Upon disassembly and careful inspection, it was determined that the cause was the expansion of the aluminum rotating section against the stationary bearing preload load ring. The loading ring inner diameter was bored an additional 0.015 in. on both joints. It was also noted that the component with the greatest temperature rise was the 12-in. section of aluminum WC504 waveguide at 161°F.

Test 2 was conducted with water-cooled transitions and greater clearance in the loading ring. At 300 kW the joints again failed to rotate. Disassembly showed that the lower bearing inner race had come in contact with the aluminum housing; this was due to the expansion of the round guide section which overloaded the lower bearing, forcing it to gall against the aluminum housing. It was also noted at this time that the bearing lubricant had not withstood the temperature at 169°F. It appeared to have run and splattered about the inside. These malfunctions were corrected by machining 0.010 in. from the race area and water cooling the round guide, and by using a high-temperature grease.

In test 3 all components except the rotary joints were water-cooled. The ring was resonant at 2099 MHz, and the maximum output in this configuration was 420 kW. The maximum temperature recorded was 145°F after one hour. The starting and running torque was 6 and 4 ft-lb, respectively. Some noise bursting was detected but this was attributed to the resonant ring rectangular waveguides because during the rotation of the test piece, no bursting could be induced. At no time during this or successive runs and disassemblies were visible signs of arcing evident.

Later tests of the same basic design rotary joints, but incorporating improved dust and gas seals rather than the original O-rings, were conducted at a level of 600 kW. This level was possible since no diplexer was used. The reduced insertion loss of the total ring allowed a higher multiplication to be achieved. During these tests, back-power and arcing were closely monitored in lieu of the sensitive receiver technique used earlier. Because of component heating, it was possible to maintain ring resonance for only a few minutes at 600 kW; nevertheless, no visible signs of breakdown were found.

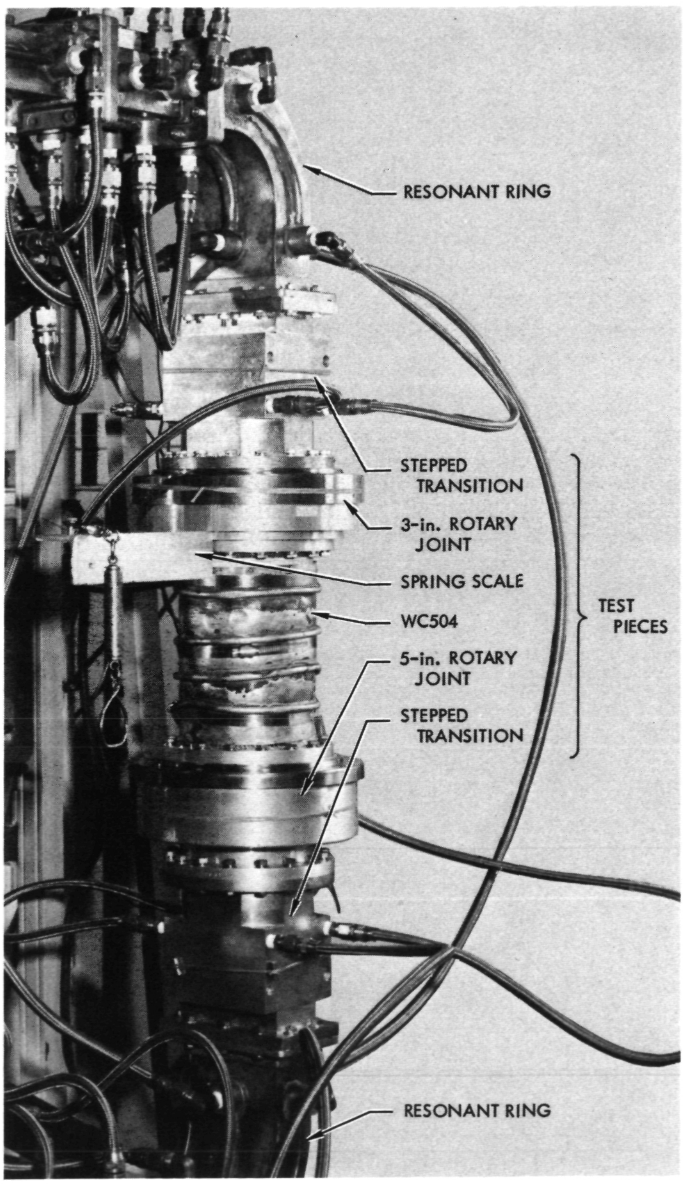

Fig. 6. Resonant ring test pieces, rotary units

3. Orthomode

Figure 7 shows the original design of the orthomode transducer used in the S-band multifrequency (SMF) feed system at 20-kW (SPS 37-38, Vol. IV, pp. 192–199). Although every effort to eliminate joints within this unit was made at the initial design (1965), the available techniques for fabrication at that time dictated some joints be used.[1] Water-cooling passages were added to available 6061 aluminum alloy parts and the most questionable joints were heliarc welded to preclude arcing. Since the orthomode effectively forms an H-plane waveguide bend, while the Goldstone MTF resonant ring is an E-plane arrangement, a rather inefficient assembly resulted, from an insertion-loss standpoint (Fig. 8). Approximately 30 ft of various waveguides were used,

[1]Construction was restricted to techniques excluding dip brazing since frequent flux contamination problems have been experienced with brazed parts.

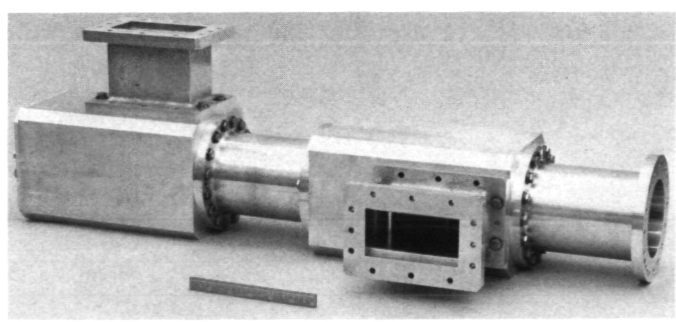

Fig. 7. Aluminum alloy 20-kW orthomode transducer

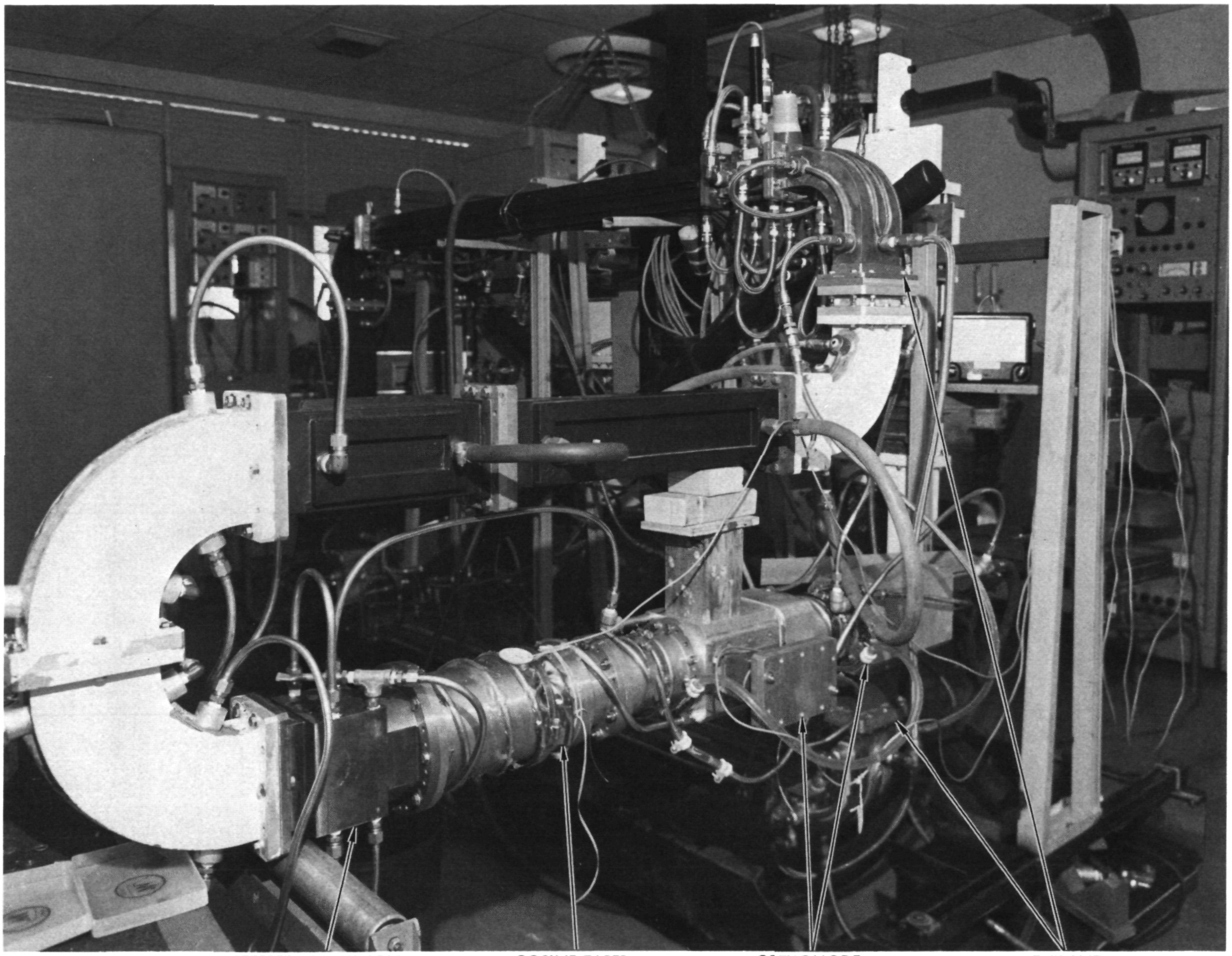

Fig. 8. Resonant ring test pieces, orthomode units

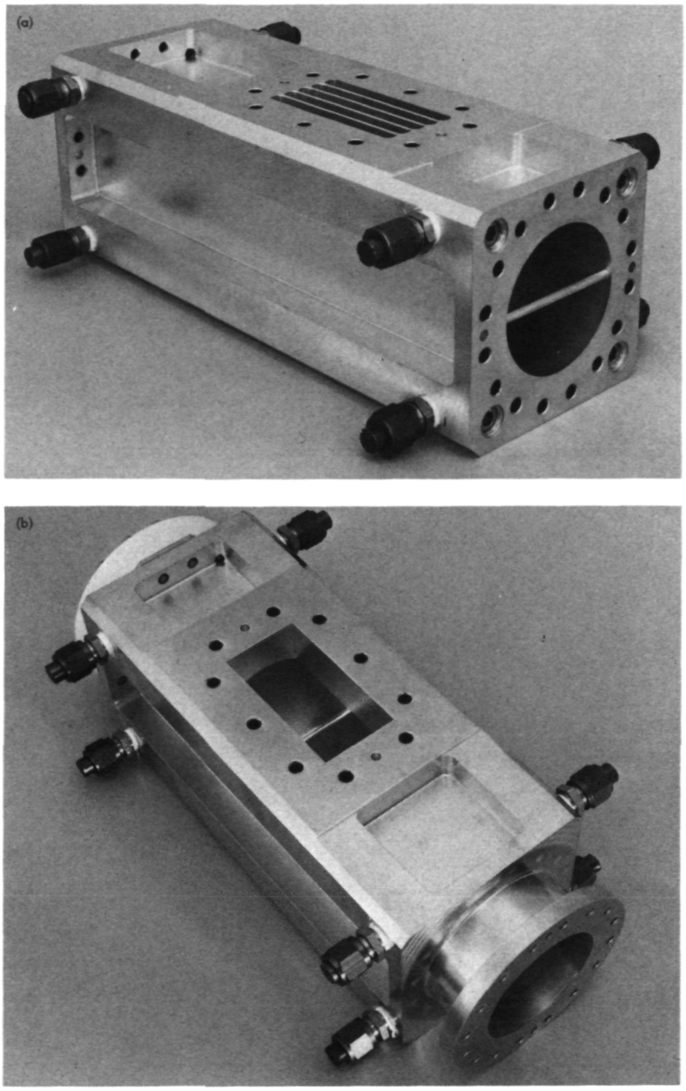

Fig. 9. Seamless copper 500-kW orthomode transducer

occupying a sizable area of floor space; a multiplication to only 260 kW was achieved. Because no difficulty was experienced at 260 kW, and 400 kW is only 25% greater field strength, the fundamental design was considered verified.

An improved orthomode, constructed from solid OFHC (oxygen-free high conductivity) copper blocks with no internal joints, was designed following these tests. Figures 9a and 9b show the two units which comprise the total orthomode. The combination of reduced insertion loss and improved coolant passage design should result in a conservative, thermally stable unit at 400–500 kW.

4. Conclusions

Through extended use experience in some cases, and resonant ring tests in others, a degree of confidence in high-power, low-noise, diplexed, feed component design has been obtained. It appears feasible to implement complex polarization diversity feeds for 500-kW/25°K systems at S-band. An example of a complex diversity system is the PDS feed, consisting of an orthomode, two quarter-wave plates and three rotary joints. Certain practices appear necessary for successful hardware; we have endeavored to begin with inherently broadband components, with careful attention to cleanliness, minimizing or eliminating joints wherever possible, careful flange treatment, and conservative cooling provisions to minimize dimensional creep with resulting mismatch changes.

Reference

1. Bathker, D. A., "A Stepped Mode Transducer Using Homogeneous Waveguides," *IEEE Transactions on Microwave Theory and Techniques,* Vol. MTT-15, No. 2, pp. 128–129, Feb. 1967.

F. S-Band Polar Ultra Cone Improvement,

H. F. Reilly, Jr., and F. E. McCrea

1. Introduction

The S-band polar ultra (SPU) cone was installed at DSS 12 (Echo) on January 28, 1970. Low-noise listen-only and diplexed operations were supported with total operating noise temperatures (T_{op}) of 17.4 and 25.4°K, respectively, until June 16, 1970. At that time improved DSIF waveguide switches were installed. The purpose of this change was (1) to further reduce the T_{op} noise, (2) to improve the transmitter traveling wave maser (TWM) isolation, and (3) to correlate laboratory-measured insertion loss values with field-measured noise temperatures on an operating antenna-mounted feedcone system.

2. Recent Work

The S-band polar ultra cone, described in SPS 37-62, Vol. II, pp. 91–94, uses two 2-position WR430 waveguide switches. As described previously, the initial switches used had been improved over the standard units, namely to insertion losses of 0.016 and 0.018 dB; isolations of 62 to 98 dB across 2.0 to 2.4 GHz, with 75 dB at 2110 MHz; and average voltage standing-wave ratio (VSWR) of 1.049.

Further work has resulted in switches with insertion losses of 0.0049 and 0.0052 dB (dissipative losses of 0.0034 and 0.0037 dB); isolations of 95 dB minimum across 2.0 to 2.4 GHz, with greater than 110 dB at 2110 MHz; and average VSWR of 1.039.

It is noted that improvements in rotor to stator choking in waveguide switches has thus far always resulted in improvements in all three parameters: insertion loss, isolation, and mismatch.

The improved switches were expected to reduce the SPU T_{op} for the low-noise listen mode by 0.74°K (one-switch path) and 2.35°K (three-switch paths) for the diplex mode. The switch paths can be seen in Fig. 39 of SPS 37-62, Vol. II, p. 91. Measured results reported by Reid (*Section C* of this chapter) show, after proper allowance is given to possible followup temperature contribution changes, that 0.15 and 0.81°K improvements were obtained after June 16, 1970, under operational conditions.

3. Conclusions

The improvement expected in T_{op} reduction was apparently not fully achieved. Possible factors not carefully considered here are (1) measurement tolerance, particularly the T_{op} tolerances, and (2) component and overall system reflection coefficients. Even so, the approximate 0.8°K improvement to a 25°K operating system results in a signal-to-noise ratio improvement of 0.14 dB.

Isolation improvement from 75 to greater than 110 dB very effectively reduces the nearly 1 mW of transmitter leakage into the TWM, which was of primary concern, as discussed in the previous reporting.

VI. Supporting Research and Technology

ADVANCED ENGINEERING

A. Simulation Center Hardware Development—Programmed Input/Output Serial Data Generators and Receivers, *A. M. Willems*

1. Introduction

As a result of the functional requirements specified by the DSN and the *Mariner* Mars 1971 project, it was found necessary to expand the input/output (I/O) capabilities of the DSN Simulation Center (Simcen). One area of expansion was the serial data I/O interface of the system. This article describes the two serial data generators and three serial data receivers which were designed, built, and interfaced to the EMR 6050 simulation computer programmed I/O channel. These devices were briefly described in SPS 37-65, Vol. II, pp. 94–97, which outlined overall Simcen expansion.

2. Serial Data Generator

This device is designed to receive, under program control, a parallel-bit data word from the EMR 6050 computer A register and output this word as a serial-bit data stream to an external device. The size of the data word is program-selectable and may vary from 1 to 24 bits. The rate at which the serial data are transmitted is also program-selectable. One of seven different internal clock rates or one external clock rate may be selected. The maximum clock rate allowable is 50 kbits/s.

Serial data are output in two general modes of operation. This mode selection is under program control. In the continuous data mode, a pulse-code-modulated-type serial data stream is transmitted, uninterrupted, at the selected rate for any duration. In this mode, the generator may transmit spacecraft-type data at spacecraft rates for testing and/or recording, as required. Data and clock outputs and external clock input are accessible through the I/O system patchboard. A block diagram of the serial data generator interface is shown in Fig. 1.

In the block synchronous mode, the generator is designed to be compatible, in signal characteristics and timing, with the 4.8-kbit high-speed data system block multiplexer. This is required so that the serial data will be transmitted in a block format controlled by the block multiplexer. The data are then compatible with the NASCOM high-speed data system which is utilized by the GCF at JPL. These block-formatted simulation data are sent to the Deep Space Station or to the SFOF. A test feature was incorporated into the design which en-

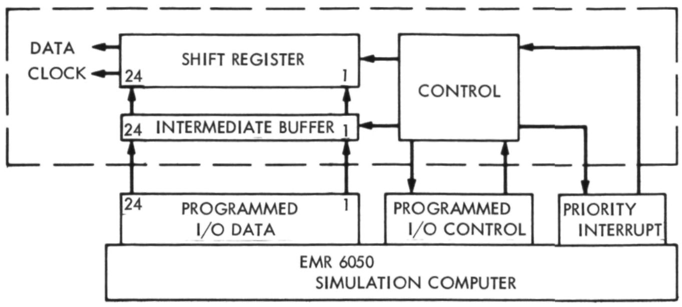

Fig. 1. Serial data generator block diagram

ables the operator to effectively take the device off line and manually select mode controls and data content normally controlled by the computer.

3. Serial Data Receiver

This device receives serial-bit data and synchronous clock from an external source and, under program control, transfers these data as a 24 parallel-bit word to the EMR 6050 computer A register. The receiver has two modes of operation, which are selectable by program control. In the all data mode, the device will receive any serial-type data of the appropriate signal characteristics and bit rate of up to 50 kbits/s. These data are accumulated until a 24-bit word has been assembled. This word is then transferred to the computer. This process can continue indefinitely without interruption or loss of data. Data and clock inputs are accessible on the system patchboard.

In the block synchronous mode, the device is designed to be compatible with the NASCOM high-speed data system decoder output signals and format. In this mode, the receiver "examines" the data input content and will transfer a parallel data word to the computer only after detection of the proper block synchronization code and user-data-type code. The synchronization code assures a uniform data input format and the user-data-type code is examined to allow only those data blocks which are *not* filler-type data. This synchronization process must be performed at the beginning of each block. The types of high-speed data to be received are command data blocks and standard- and limits-type data blocks. A test feature was added to the device to allow off-line manual control of those functions normally under computer control. A block diagram of the serial data receiver is shown in Fig. 2.

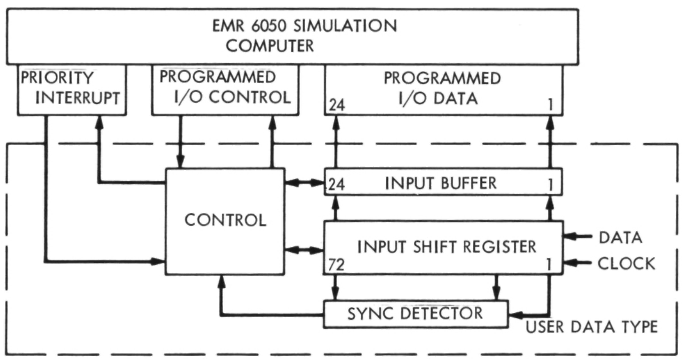

Fig. 2. Serial data receiver block diagram

B. Mark IIIA IBM 360/75 Computer Configuration, *R. A. Stiver*

1. Introduction

The Mark IIIA era of space flight missions will be supported by a modernized data processing system (planned for operation through 1974).[1] Described herein are the hardware subsystems which are contained within the data processing system. NASA has provided two

[1]A broad description is given of the Mark IIIA SFOF by H. S. Simon in *Chapter VII-A*.

IBM 360 Model 75 digital computers to form the nucleus of the new system. Expansion of the processing capability and development of specialized interface equipment were provided by JPL to meet requirements of the DSN Systems: Tracking, Telemetry, Command, and Monitor and Operations Control.

The computer equipment was available in March 1969, and a preliminary design was approved in October 1969. The target date for initial test support for the *Mariner* Mars 1971 project was set at October 1970, leaving one year to complete the system design, procure and install the additional equipment, and develop the required software.

The critical time constraint levied several design compromises. The existing Marshall Space Flight Center Real-Time Operating System of computer programs was chosen as a foundation for the Jet Propulsion Laboratory Operating System. This software is an expansion of the standard IBM-supplied Operating System, which can serve general-purpose use in addition to space flight real-time data processing.

Delivery time and software program compatibility constraints dictated a choice of "off-the-shelf" user devices and computer interfaces. Modification of existing communication terminal equipment was undertaken to comply with compatibility requirements and to insure a smooth transition from Mark II to Mark IIIA capability.

2. Description

The configuration consists of two identical IBM 360 Model 75 digital computers with a typical complement of peripheral and bulk storage equipment (Fig. 1). In addition, an extensive array of communication channels and user devices are included to provide a functional interface between the spacecraft data streams and the experimenters. This array of equipment is comprised of three organizational subsystems: memory and auxiliary storage, computation, and real-time input/output interface. The principal interface is with the user terminal and display subsystem equipment, which is shown in Fig. 1 for reference.

3. Memory and Auxiliary Storage Subsystem

The memory and auxiliary storage subsystem contains the computer main memory, the large capacity storage, which functions as a buffer memory, and the disk and tape files.

The main memory is comprised of four units of random-access magnetic core memory, operating in an interleaved mode which provides an effective cycle time of 400 ns for each doubleword transferred. A doubleword consists of 64 data bits and 8 parity check bits. The main memory contains 1 million 8-bit bytes, which is the maximum expansion available for an IBM 360 Model 75.

The large capacity storage is also a random-access magnetic core memory, with a doubleword cycle time of 8 μs. Two million 8-bit bytes are provided in the current configuration. The large capacity storage functions as a dynamic buffer, providing program and data file access to the main memory with much faster transfer rates than conventional bulk memory.

Mass storage is provided by two direct-access storage units (disks), totaling 460 million 8-bit bytes, and eight magnetic tape units. Both 7- and 9-track tapes are provided to maintain compatibility with other facilities.

4. Computation Subsystem

The computation subsystem contains the central processing unit, the selector and multiplexer channels, and a group of peripheral input/output devices dedicated to computation support and system control.

The central processing unit is the primary control element in the system. In addition to instruction execution and computation functions, it also contains the bus control unit, which performs routing and timing of all data transfer activity on the memory/channel bus. Over this path, many data transfer operations take place concurrently with a composite rate of 20 million 8-bit bytes/s. Additional features include: the universal instruction set, storage protection, the external time and interval timer assembly, and a large capacity storage attachment that enables the large capacity storage to function as an extension of the main memory.

The selector channel contains two standard selector channels which interface to the two direct-access storage units, and a storage channel adapter which functions as a fully buffered channel between the main memory and the large capacity storage. The buffer memory function of the large capacity storage is provided by the storage channel adapter.

The multiplexer channel serves to interface the peripheral support equipment to the system. In addition, the two display control units and the digital television assembly of the user terminal and display subsystem are

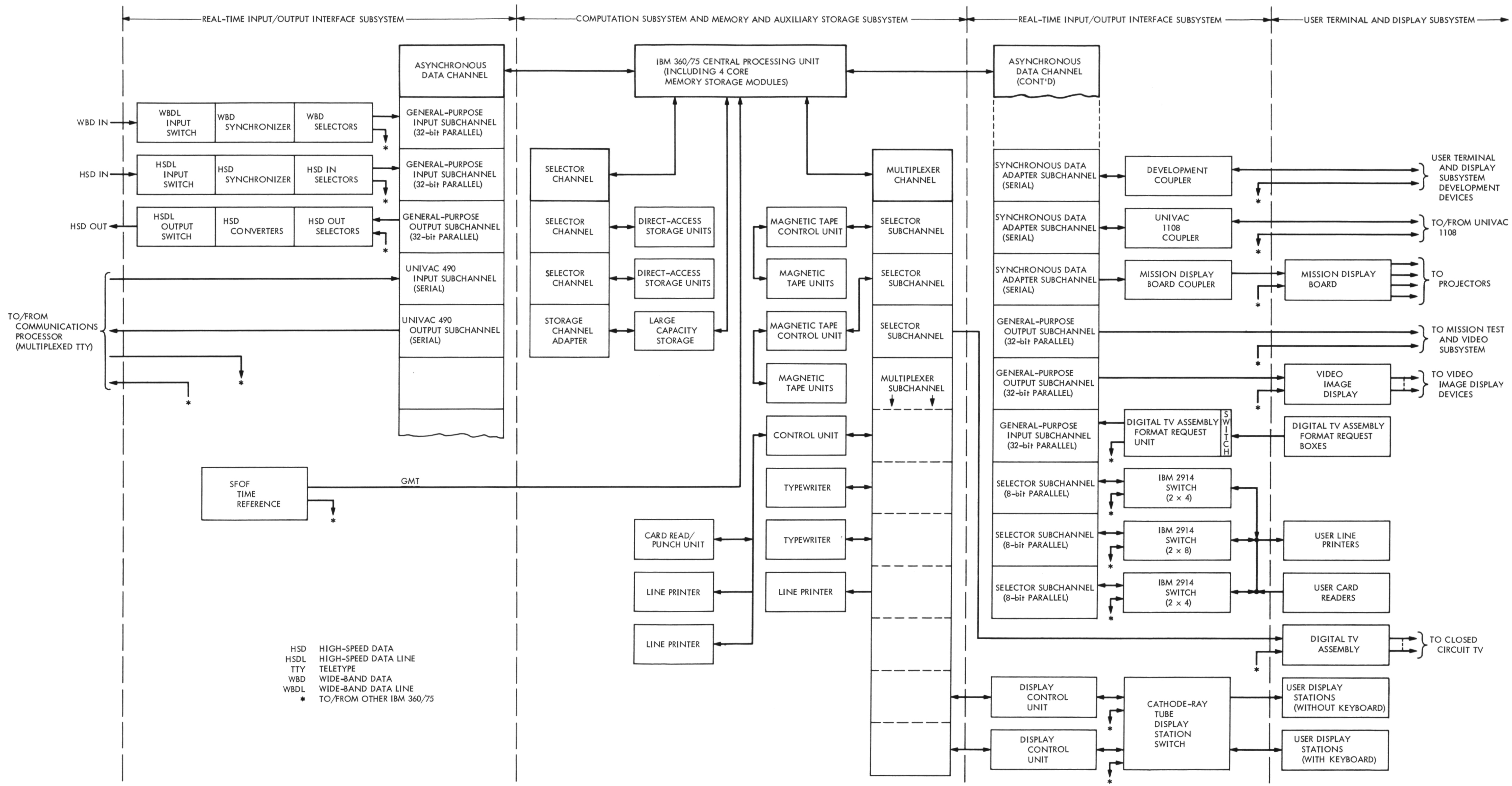

Fig. 1. Mark IIIA IBM 360/75 computer configuration

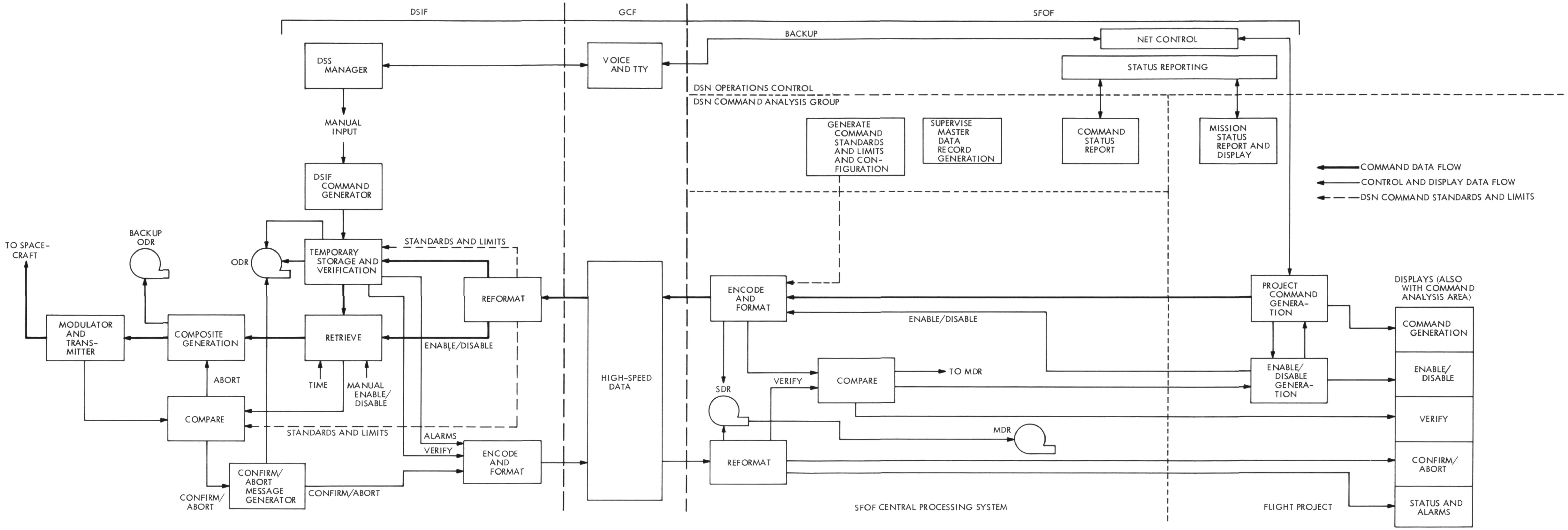

Fig. 1. DSN Command System functional diagram

"PAGE MISSING FROM AVAILABLE VERSION"

also interfaced via the multiplexer channel. The two magnetic tape control units are each connected to a selector subchannel while all of the support devices, including three line printers, two typewriters, and a card read/punch unit, are connected to the multiplexer bus.

5. Real-Time Input/Output Interface Subsystem

The real-time input/output interface subsystem consists of the asynchronous data channel with 24 subchannels, standard IBM control and switch units for attachment of user devices,[2] and special interface and switch units for connection to display equipment, communication lines, and other computer systems. Most of the computer-controlled user equipment and all communication links are interfaced to the asynchronous data channel.

Wideband and high-speed serial-input lines are interfaced to 32-bit word-oriented subchannels via synchronizer units that provide detection and editing functions which minimize central processing unit intervention. Each synchronizer has a dual-output buffer that enables data transfer to either or both 360/75 computers. Wideband rates are 50,000 bits/s, while high-speed rates are 4800 bits/s.

High-speed serial-output lines are driven from converters that operate conversely to the synchronizers. Each converter has a dual-input buffer but only one 360/75 may be enabled at a time.

Multiplexed teletype data are exchanged with a communications processor computer in the GCF over a serial circuit operating at 40,800 bits/s. Special subchannels were available and incorporated for this interface.

[2]See *Chapter VI-C* by N. Habbal.

Three serial data adapter Type II subchannels are incorporated to communicate with peripheral operations in standard format such as USASCII. These include a development activity for future implementation, the Scientific Computing Facility, which executes high-precision orbit determination programs, and the mission display board, which graphically presents data and status to operations control personnel.

The digital television assembly format request unit is a controller/selector which reads data from format request boxes into the selected 360/75 computer. Special hardwired status information can also be entered via this unit.

Three selector subchannels provide a standard IBM interface for line printers and card readers. IBM 2914 switch units are included to provide access to either 360/75 computer from each user device. The cathode-ray tube display switch (2260) functions in the same manner.

Switching of the user devices, communication lines, and adjacent subsystems between the two computers is implemented external to the equipment controllers in order to provide operational simplicity, direct interchangeability, and ease of isolation in troubleshooting. This approach also enables partial functions of the system to be tested and modified on the alternate computer while normal support proceeds without interruption. The dual-input capability from communication lines enables backup processing, which provides increased reliability for critical periods of mission support.

C. SFOF IBM 360/75 User Device Switching Assemblies, *N. Habbal*

1. Introduction

Supporting the DSN are two IBM 360/75 computer installations located in the SFOF. Either the A or the B computer may be assigned to real-time data processing support of flight operations while the other computer may be assigned to support non-operational tasks. Associated with the computers are a large number of user devices such as card readers, printers, cathode-ray tube (CRT) displays, etc. These devices comprise a portion of the real-time input/output interface subsystem (RTIOS) and the user terminal and display subsystem. This article pertains to the switching assemblies of the RTIOS.

Requirements for reliability, maintainability, flexibility, and economy dictated that user devices in the SFOF be able to input and/or output to/from either computer A or B. This posed some design problems requiring considerable trade-off analysis. It would be possible to switch devices on a group basis or an individual basis. Groupings could be by flight project, by specified user areas, or some other grouping. Because of the large number of variable tasks and system configurations, it was determined that maximum flexibility would accrue from individual device switching (i.e., any input/output device can be switched to either computer). Also, there were two options on the method of switching: (1) automatically under program control, or (2) manually by local device switches and remotely from a central control area. Implementation schedule constraints, programming considerations, and availability of "off-the-shelf" hardware were also considered. In the final analysis, manual switching was decided upon as best meeting the various design criteria and schedule constraints.

Following is a description of the user device switching assemblies as implemented in the Mark IIIA IBM 360/75 computer configuration (see *Section B,* R. A. Stiver).

2. CRT Display Station Switch

Figure 1 is a block diagram showing the function of the CRT display station switch. The switch provides for the switching of 32 CRT display stations between the A and B computers through a multiplexer and Model II display controller. The controller is capable of driving 16 Model II CRT display stations; consequently, two display controllers are required per computer system. The switch is easily expandable to accommodate 64 display stations, some of which are equipped with keyboards for making inquiries, data entry, and updating; the other stations are used simply for data display and are therefore without keyboards. Relays having 12 poles are used for switching; to make the switch flexible in handling any number of both types of CRT displays, the relays are made as if all CRT displays had keyboards.

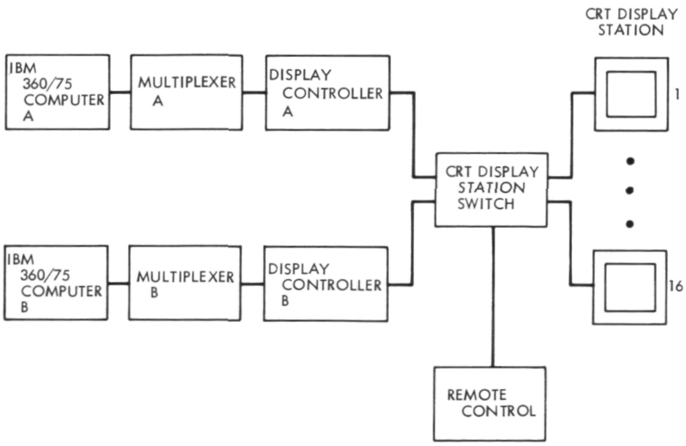

Fig. 1. CRT display station switch

3. CRT Display Station Remote Control

The CRT display station switch is provided with remote control located in the data processing control area. Consequently, each CRT display station is switchable between the A and B computers from either the local switch or remote control console. Of course, in order to be switchable from the remote console, a display station must be put in remote (RMT) at the local switch. A typical CRT display station switching schematic, along with its remote control, is shown in Fig. 2. When the local switch is put on RMT, an indicator light comes on in the remote panel to inform the operator that the selection of computer A or B, for the CRT display station, is now possible. The A computer, through the display controller, is connected to the normally closed contacts of the relay, and the normally open contacts are connected to the B computer. The switching, consequently, is made to the B computer when the relay is energized.

4. IBM 2914-1 Switch

Switching of the line printer and card reader between the A and B computers is accomplished through the IBM 2914 Model 1 switch, which receives data from a selector subchannel, as shown in Fig. 3. The switch, a solid-state device, is modular in design with a matrix configuration of 2×4. The first digit in the switch nomenclature refers to the number of computer channel interfaces and the second refers to the number of control unit interfaces. A

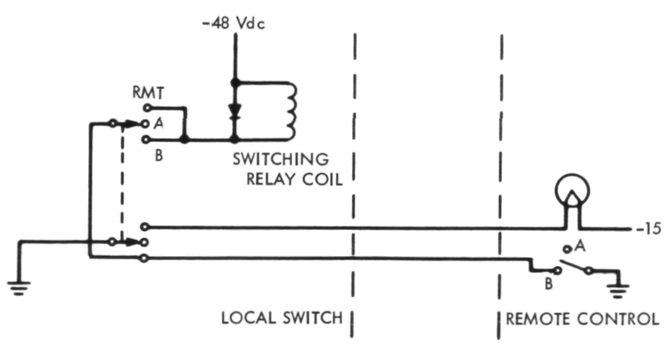

Fig. 2. Typical CRT display station local and remote switching

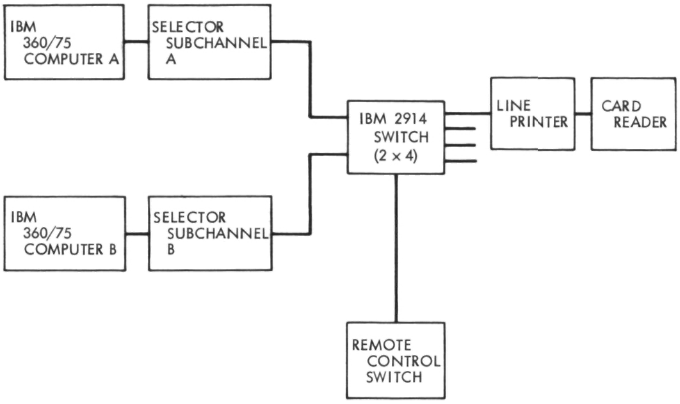

Fig. 3. Line printer and card reader switch

supervisory plug board organized into a matrix representing the switch configuration of channel interfaces and control unit interfaces is located on the control panel. A pin inserted in the node of the matrix would make it possible for a signal transfer between the channel interface and the control unit interface. The control panel also contains a rotary switch for each of the control unit interfaces to enable the operator to manually make the computer selection. The rotary switch can be set to RMT to enable the remote console operator to make the computer selection for any input/output device attached to the control unit interface.

5. Line Printer and Card Reader Remote Control Switching

The remote control station for the line printer and card reader consists of a light indicator and a switch, just as in the case of the CRT display station remote control. The indicator light, when on, would inform the remote console operator that it is possible to make a computer selection for the input/output station. The RMT signal of the 2914-1 switch is used for this purpose after being conditioned and amplified. The switch enables the operator to make the actual computer selection.

D. Thrust Collar Survey (DSS 14), *C. C. Lundy*

This article describes the installation of 24 monuments in the radial bearing thrust collar at DSS 14. The monuments form a net of surveyed points, from which the circularity of the radial bearing runner can be measured.

In the 210-ft-diam antennas, radial loads of a few hundred tons exist between the rotating alidade and the fixed thrust collar. The thrust collar resists these loads (partly preload, partly caused by wind) and also defines the axis of rotation in azimuth. A drawing of this part of the antenna is included as Fig. 1. The thrust collar is concrete, 4 ft thick, belted with steel. The steel forms two concentric rings, an inner hoop 4½ in. thick and 20 in. high, covered by a hardened wear strip 1⅜ in. thick.

The rotating alidade assembly has three trucks, each made with two rollers which bear on the wear strip. Each truck has a preload of about 400,000 lb. This preload insures that, when the antenna is operating, the wind will never force the alidade off center more than a few thousandths of an inch, limited to the elastic bending of the structures.

Should the wear strip depart from its nominal figure of a vertical cylinder, the preload will vary from the desired force, wear will increase, the shape of the alidade may be changed, and the axis of rotation may be displaced significantly. As built, DSS 14 had no provision to measure how accurately cylindrical the wear strip is. The need for precise measurements led the JPL Antenna Engineering Group to add the necessary capability of surveying the wear strip.

The central axis of the antenna is isolated from the thrust collar by the instrument tower and cable wrap-up. There is no way to install a sweep template and no line of sight. Even conventional triangulation is impractical because of these obstructions. It was decided that 24 monuments should be installed in the concrete thrust collar, equally spaced and at a fixed radius from a central pivot. From these 24 known locations, the survey could be extended to the wear strip.

For 35 ft above the ground, the instrument tower is a concrete foundation. Above 35 ft, it is made of ⅜-in.-thick steel. At the junction between steel and concrete, there is a concrete shelf around the inside about 4 ft wide. The top of the concrete in the instrument tower is about level with the top of the thrust collar. Downward, it is 72 ft to the floor of the tower, 33 ft underground. A work platform was made of steel grating, suspended about 40 in. below the concrete shelf. The opening was spanned by a 10-in. steel channel. This work is shown in Fig. 1. In the middle of the channel, a standard antenna engineering theodolite adaptor was installed.

A portable drill press with a magnetic base was brought into the tower and used to drill 24 pairs of holes through the steel tower. A pair of holes consists of a gage bar hole 3.70 in. over the concrete and a sight hole at 10.90 in. All holes are 1½ in. in diameter. The theodolite was used to lay out all the holes equally spaced in azimuth at 15-deg intervals.

The swivel of the theodolite adaptor is fitted with a removable gage bar. At the swivel end, the gage is rigidly fixed when pinned to the swivel, but can be uncoupled to move from one hole to another. In practice, an instrument man remained in the tower to use the theodolite and to connect and disconnect the gage bar. A second man, stationed on the thrust collar, handled the gage bar and did all marking. The gage bar weighs only about 4 lb.

Permanent bronze monuments were set at 24 equally spaced intervals in the thrust collar as a primary net of survey points. The location for each monument was determined by using the gage bar to establish a uniform radius and the theodolite to set the 24 angles. Figure 2 is a photograph of the two ends of the gage bar. The bar in front has a tapered nose that was ground to a precise fit with a hole in the swivel. A hole for a tapered pin is seen in the end. Figure 2 also shows the outer end of the gage bar. There are three leveling screws to adjust the height and slope of the base. The man at the theodolite directs his partner to set the target to exactly the same height each time. In each case, the target is an inch or more above the concrete.

Figure 2 shows a rectangular tower at the left end of the platform, topped by a cylindrical assembly. This tower carries a pair of linear ball bushings with their axis exactly vertical when the platform is leveled. These bushings guide a variety of punches from the floating target to the physical surface. One of the punches is in place in the figure.

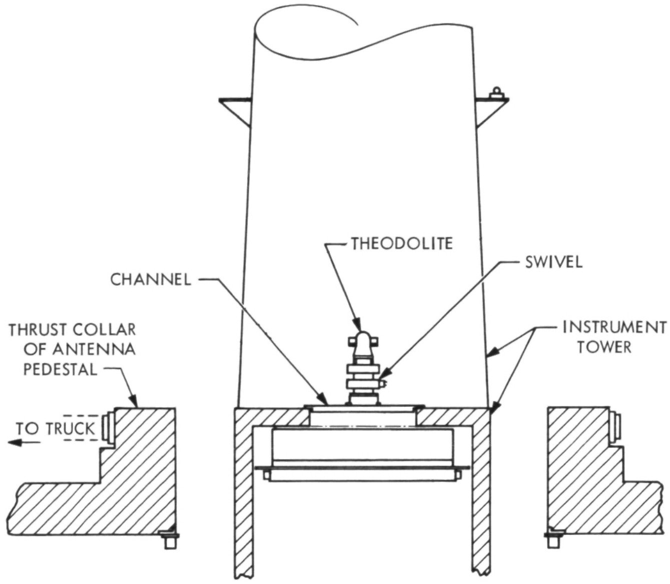

Fig. 1. Thrust collar and work platform of 210-ft-diam antenna

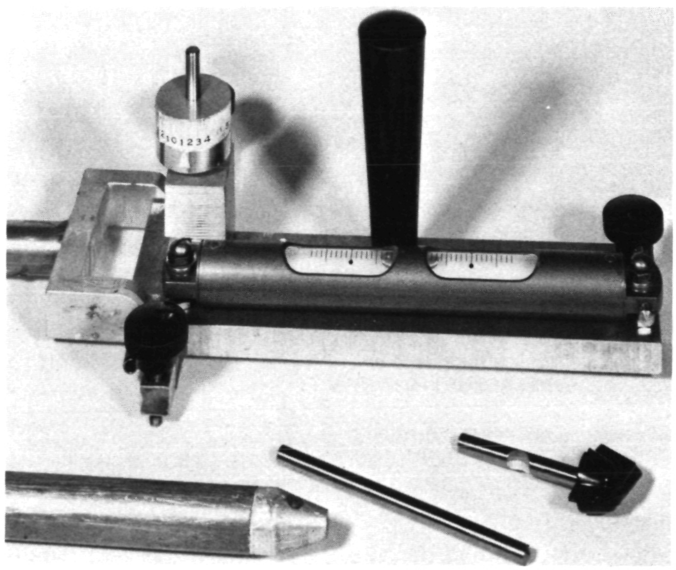

Fig. 2. Gage bar

In the foreground, there is a short rod with a black pointer knob. The middle of the rod is cut back to the midline, and carries a target pattern whose center is the aiming point. When the rod is inserted in the platform, the pattern is visible from the theodolite. It is the task of the man at the outer end to adjust the platform horizontally and vertically until the pattern is centered in the line of sight. He then levels the platform and locates the monument mark exactly beneath the target.

The first punch was used only to prick into the concrete. At each point marked, a hole was drilled to accommodate a bronze monument with its top surface an eighth of an inch below the surface. The monuments were grouted into the thrust collar and time was allowed for the grout to cure.

The same gage bar was used to mark the monuments. A punch with a flat polished tip was first used. This is the long punch shown in Fig. 2. It produced a glossy dent in the monument about 0.06 in. in diameter and 0.005 in. deep. This is easy to see against the smooth dull background. This punch was withdrawn and a punch with a tiny needle point dropped in. It makes a mark 0.005 in. in diameter in the center of the dent. The center of this 0.005-in. mark is our reference point. Figure 2 shows the needle-pointed punch in the platform.

The gage bar is made of steel. A temperature change of 1°F causes a change in length of about 0.001 in. To permit small corrections in the length of the gage bar as the temperature changes, the needle point of the final punch is offset 0.005 in. from the centerline. It carries a dial and guide pin so it can be set to a total correction range of 0.010 in. During the final survey, the temperature of the gage bar was monitored and all lengths rectified as the temperature changed.

By this means, a family of points at a uniform radius and equal angular spacing was established. The chordal distance, monument to monument, was next measured all around the collar. The average of these 24 dimensions divided by twice the sine of 7.5 deg gave us the radius from the vertical axis of the theodolite. The chords can be measured more accurately than the radius, since the center of rotation of the swivel is not accessible.

The chordal gage is a steel tube fitted at each end with a traversing microscope. One end of the gage is shown in Fig. 3. The microscope, the small black tube standing vertically, magnifies about 50 times. In the photograph, the gage is shown on a 72-in. scale, which is used as a field standard for calibration. The scale was compared in the JPL inspection office against their length standard, and over the range used it reads 0.0014 in. too short.

Each end of the gage has a micrometer spindle controlling the travel of the microscope. Two men worked together, each setting the microscope over a punch mark and reading the micrometer. The distance from mark to mark is the sum of the two micrometer readings and a fixed length determined at calibration.

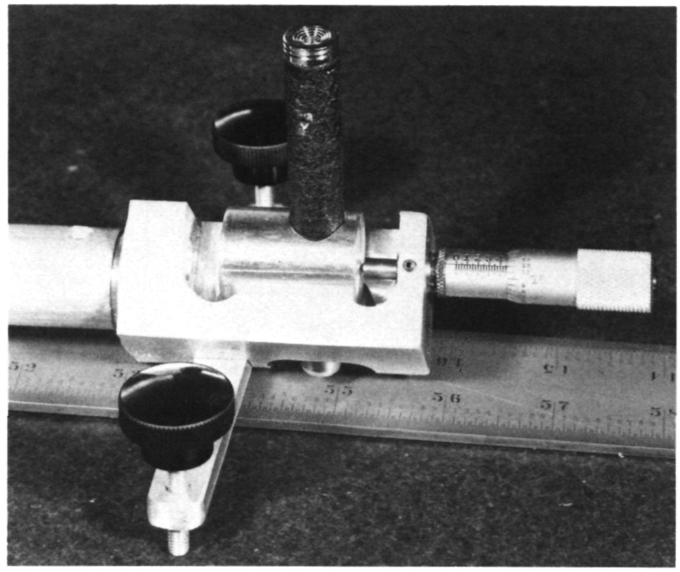

Fig. 3. Chordal gage

The gage was calibrated at the work site by comparison with the 72-in. scale. Both were kept at the same temperature. The average temperature of the gage was noted while measuring the 24 chords. When the temperature in Fahrenheit degrees was T, the readings were corrected by adding 0.00028 in. $(T - 68°\text{F})$ to the average chord length. This was combined with the constant 0.0014-in. correction noted above.

With 24 monuments at known locations, we are ready to extend our survey to the wear strip. The tool used is shown in Fig. 4. A microscope at the left is set precisely over an index point of a monument. The bar carrying the microscope is set radially by sighting to a gage bar hole in the instrument tower. The bar is leveled tangentially with a circular level and radially with a 10-s level. When this is done, the tips of the two dial indicators lie one above the other in a plane that includes the central axis of our survey and the index mark of the monument. One dial indicator touches the wear strip near its top, the other touches 9 in. lower. This gage was made so the distance from the axis of the microscope to the tip of the dial indicator is 11.5000 in. plus the indicator reading.

A setting fixture that can be carried to the work area is shown in Fig. 5, with the wear strip gage on it. The fixture is placed on a carefully leveled base and the 10-s level zeroed. A Talyvel electronic level was used as a standard when this photograph was made. The vertical arm carrying the indicators is made accurately vertical in the plane normal to the picture, using in this case a

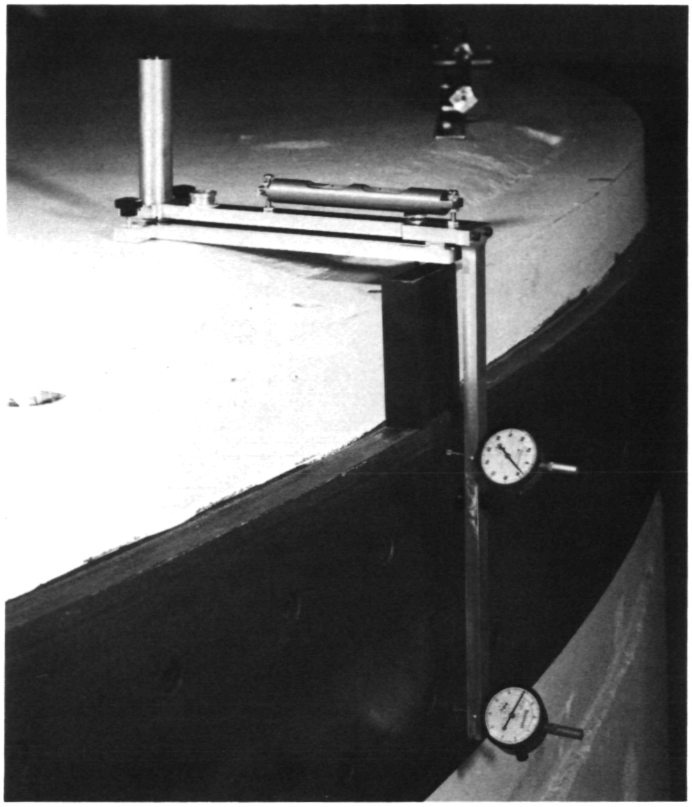

Fig. 4. Tooling used to survey wear strip

gunner's quadrant. The microscope is aligned on a reference carried by the small shelf at the left. From this reference to the right edge of the fixture, the horizontal distance was determined in the JPL inspection shop to be 12.0300 in. The dial indicators are both set to 0.5300 while the gage is on the fixture. Both the gage and fixture are made of aluminum, so there is no significant

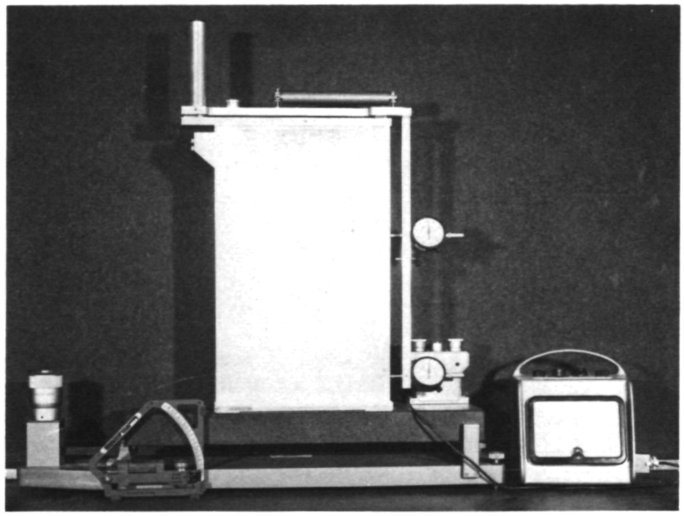

Fig. 5. Setting fixture

error if they are kept at the same temperature during setting and checking. Measurements on the antenna are affected, and the readings reported are corrected for the temperature difference between the inspection room and the antenna. In this case, the correction is 0.00014 in. $(T - 68°F)$.

At each of the 24 monuments, we center the cross-hair of the microscope over the 0.005 index mark of the monument and level the base carefully. We record the two dial readings.

The distance from the center of the antenna to each point measured is the radius of the monuments plus 11.500 plus the dial reading, including of course the temperature corrections mentioned above.

E. Hydrostatic Bearing Runner Level Reference,

G. Gale and H. Phillips

This article describes a method used to survey a 70-ft-diam circle, which is used as an elevation reference for surveying the 210-ft-diam antenna hydrostatic bearing runner at DSS 14. The surface surveyed, and then used as an intermediate height reference, is the top of the azimuth drive bull gear, which is set on the antenna concrete pedestal. The center of the circle is shielded from the reference circle so that conventional optical methods are not applicable. The method described gives a probable error in elevation of less than 0.001 in.

To assure adequate oil film thickness between the bearing pads and the runner surface of the hydrostatic bearing, the runner surface must be flat to within approximately 0.001 in./ft. Shims are placed under the runner surface to force it into the necessary flatness. It is impossible to make direct flatness measurements along the runner surface because the runner is covered and under about 10 in. of oil. Therefore, the top surface of the azimuth drive bull gear is used as an intermediate height reference since it is readily accessible and is independent of changes in the hydrostatic bearing runner height as the runner is shimmed into place.

A groove was machined into the top surface around the gear as a step toward preparing its surface as a reference. When the groove was machined, the only way to support the milling head was to hang it on the beam connecting two of the hydrostatic bearing pads. The height of the groove, therefore, reflects changes in the height of the hydrostatic bearing runner surface (Fig. 1).

There are three steps used in the determination of the deviations. The first step is a careful level survey of the reference groove at 10° intervals. Bollinger, Paine, and Valencia (SPS 37-54, Vol. II, pp. 58–62) described the method for measuring accurately the relative heights at 10° intervals around the reference groove. The second step is to determine the groove height at 3⅓° intervals between the 10° points and thus establish the mean pad height (socket height) at the 3⅓° points (Fig. 2). Finally, the third step is to establish the heights at the ½° intervals by using a cubic fit of the socket height as an interpolation. Shims are placed under the hydrostatic bearing runner at each ½° interval around the bearing; therefore, the deviations of the height of the bull gear reference groove from a true level reference plane must also be determined for each ½°.

A two-channel brush recorder Mark 280 series with a 1-MΩ input impedance was used for the records. The gain of each channel was adjusted so that 1 minor chart division was equivalent to 0.0005 in., and the chart could be easily read to the nearest ½ division or 0.00025 in. (Fig. 3). Calibration was made by placing the probes

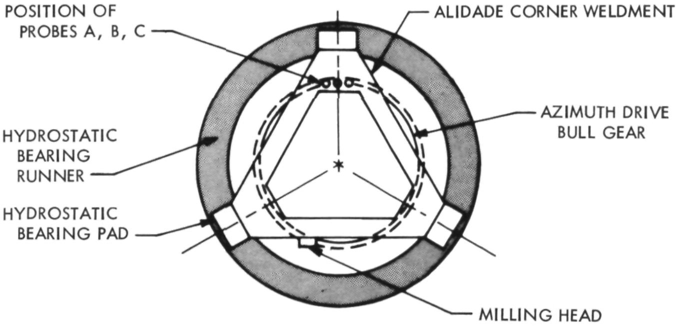

Fig. 1. Plan view of 210-ft-diam antenna azimuth drive and hydrostatic bearing

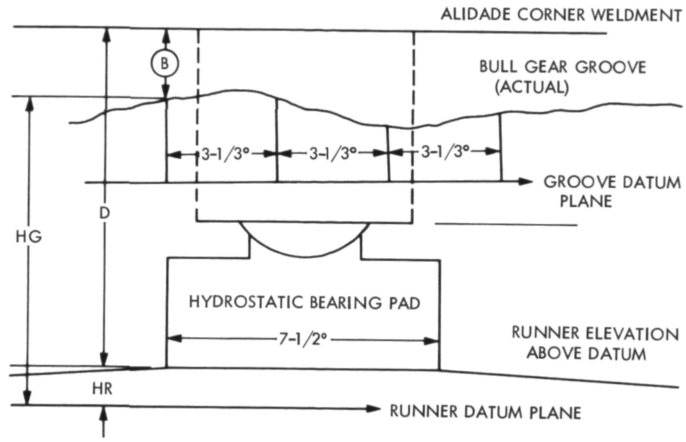

Fig. 2. Side view of corner weldment, runner, and bull gear

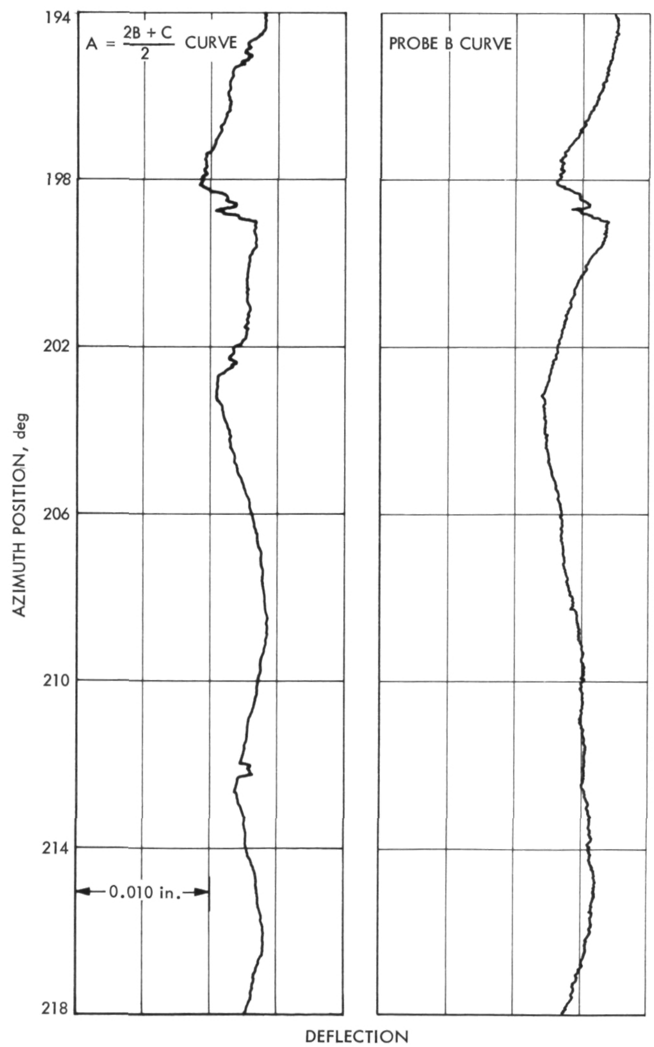

Fig. 3. Recorder trace showing deflection vs antenna azimuth position

into a special micrometer calibrating block in which the probe can be displaced by known amounts to an accuracy of better than 0.0001 in.

The order of magnitude of the errors in the readings are:

10° data	0.0003 in.
Probe error	0.000016 in.
Zero set	0.0003 in.
Scale set	0.0003 in.
Chart reading	0.0003 in.

The rms error is 0.0006 in., and the probable error for each point is

$$\frac{0.6745}{(\sqrt{n-1})^{1/2}} \times 0.0006 = \text{approximately } 0.0002 \text{ in.}$$

Thus, the probe error per point of the ½° heights, as computed, can be considered as ± 0.0002 in.

The 10° data are used directly to establish the absolute or hard data points. However, there are local deviations between the 10° intervals which require a more detailed survey. This was done by suspending a bar from the corner weldment supported by the rear hydrostatic bearing pad to carry three linear transducer probes which extend to the reference groove in the top surface of the bull gear (see Figs. 1, 4, and 5).

These probes are to indicate change in distance between the top of the bull gear and the hydrostatic bearing runner surface as the antenna is rotated in azimuth.

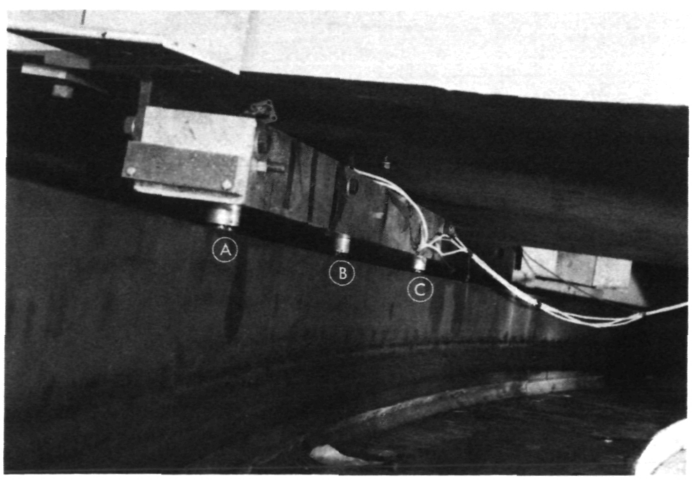

Fig. 4. Placement of 3⅓° bar to carry linear transducer probes to surface of bull gear

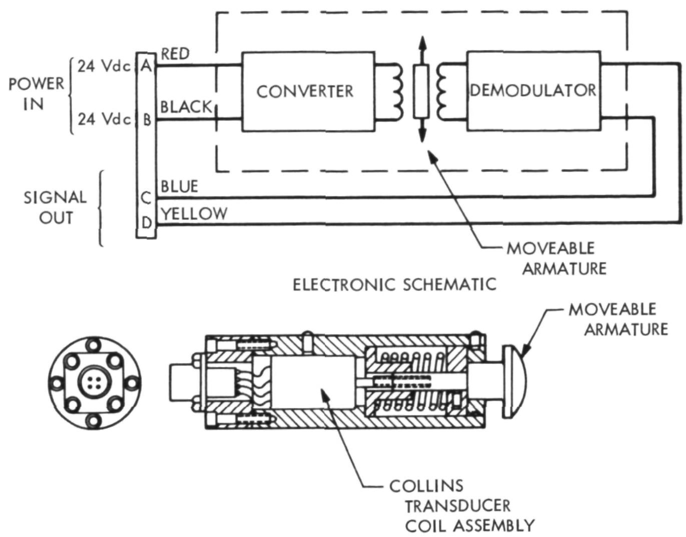

Fig. 5. Linear transducer probe

The three probes are located to span 3⅓° along the reference groove. The assumption is made that all deviations of the groove from the true plan plane have the configuration of a circle. The outputs of the three probes located in the 3⅓° bar are connected to indicate the curvature of the reference groove surface area directly under the bar (Fig. 6):

$$\frac{A - 2B + C}{2}$$

The curvature signal so derived was recorded continuously on the two-channel recorder as the antenna was rotated 360° in azimuth (Fig. 3). Azimuth marks are printed along the edge of the strip chart to synchronize the data with angular position.

By using the 10° data, the curvature data, and the mean pad or socket height (the data from Probe B which was recorded simultaneously with the curvature data), the groove height or deviations from a horizontal datum plan can be computed.

With reference to Fig. 6, the following input data are known:

(1) H_1 and H_4, which are points taken from the 10° data.

(2) Δ_1, Δ_2, Δ_3, etc., where $\Delta_n = \dfrac{A - 2B + C}{2}$ is taken from curvature data.

(3) B, which is taken from the recorder trace of Probe B.

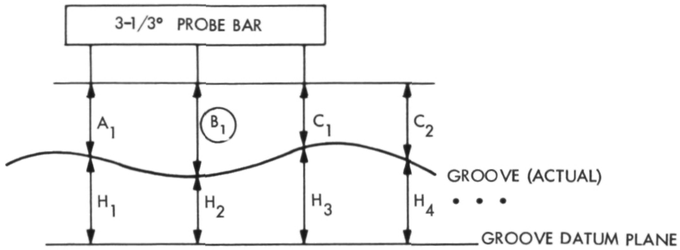

Fig. 6. Groove datum reference

By arbitrarily placing the groove datum plane below the reference groove, the height of the groove can be expressed as $H_1 = -A_1$, $H_2 = -B_1$, $H_3 = -C_1$, etc, and the curvature of the runner between Probes A and C can be expressed as

$$\Delta_1 = \frac{A_1 - 2B_1 + C}{2}$$

and can be taken from the curvature data. The curvature can also be written as

$$\Delta_1 = \frac{H_1 + 2H_2 - H_3}{2}$$

using $H_1 = -A$, etc, and the curvature 3⅓° further along the groove can be expressed as

$$\Delta_2 = \frac{B_1 - 2C_1 + C_2}{2} \text{ or } = \frac{-H_2 + 2H_3 - H_4}{2}, \text{ etc}$$

By rewriting the equations for Δ_1 and Δ_2,

$$H_1 = 2H_2 - H_3 - 2\Delta_1$$

$$H_2 = 2H_3 - H_4 - 2\Delta_2$$

$$H_3 = 2H_2 - H_1 - 2\Delta_1$$

$$H_4 = 2H_3 - H_2 - 2\Delta_2$$

H_2 can be rewritten in terms of H_1 and H_4 by substituting the equation for H_3 in the equation for H_4 and solving for H_2.

$$H_4 = 2\,(2H_2 - H_1 - 2\Delta_1) - H_2 - 2\Delta_2$$

Thus,

$$H_2 = \frac{2H_1 + H_4 + 4\Delta_1 + 2\Delta_2}{3}$$

By a similar substitution,

$$H_3 = \frac{2H_4 + H_1 + 2\Delta_1 + 4\Delta_2}{3}$$

H_1, H_2, H_3, and H_4 have now been determined by using only the 10° data and the curvature data.

The elevation of the groove at ½° intervals can now be obtained from the Probe B curve which was recorded simultaneously with the curvature data. With reference to Fig. 2, the signal from the probe at B includes changes in the runner elevation above the reference level datum plane in addition to the changes in the groove elevation. The height of the groove can be expressed as

$$HG = HR + D - B$$

where HR represents the runner height and D is the fixed mechanical distance between the pad surface and the alidade corner weldment and can be ignored. The Probe B signal can then be expressed as

$$B + HG - HR$$

Because the bearing pad spans approximately 7½° along the runner, localized changes in the runner surface are averaged out, and HR can be considered as a smooth curve through the 3⅓° points. Therefore, the Probe B data can be forced to fit the 3⅓° groove elevation points and the data can be interpolated between these points as a cubic function, or

$$H\theta = a\theta^3 + b\theta^2 + c\theta + d$$

around the bull gear reference groove.

$$(H_1 - H_2), (H_2 - H_3), (H_3 - H_4) + \cdots$$

and computed for each ½° interval between

The linear transducer probes used in the 3⅓° bar are made with a Collins SS-202 element in an aluminum housing (Fig. 5). The element is a differential transformer type, with a built-in converter and a phase-sensitive demodulator, which delivers a dc output voltage directly proportional to the displacement of the core piece. A spring-loaded button coupled to the core piece is used to track the groove in the bull gear. Repeated tests of this probe assembly have shown a repeatability of 0.000016 in. when the unit is carefully utilized. The electrical output of the transducers is approximately 200 mA per 0.001-in. displacement of the core piece and should look into an impedance greater than 20 kΩ.

F. Switched-Carrier Experiments, *R. B. Kolbly*

A previous article (SPS 37-65, Vol. II, pp. 81–84) describes initial single-carrier experiments where a single 66-MHz carrier is switched. Spectrum results are shown.

In order to investigate intermodulation distortion, experiments with two carriers were made. The 66-MHz diode switch previously described failed to perform in a satisfactory manner due to excessive capacitance of the diode when in the OFF mode. The resultant leakage, combined with nonlinear diode operation, resulted in intermodulation products at -22 dB being generated within the 66-MHz diode switch. A solution to the problem is to increase the isolation of the diode switch, possibly by adding shunt diodes. However, in the interest of expediting the experiment, the switching of two carriers was accomplished at S-band using readily available PIN-diode modulators. Filters and isolators are used to prevent interaction between units. This equipment, illustrated in Fig. 1, showed no evidence of interaction.

Using frequencies of 2115.0000 and 2115.699846 MHz as test frequencies in the equipment (Fig. 1), the third-order intermodulation products will occur at

$$f_{im} = 2f_1 - f_2 \text{ and } 2f_2 - f_1$$

These correspond to 2114.300154 and 2116.39962 MHz. Table 1 lists the switching and distortion products in the vicinity of the two carriers.

Figure 2 is the spectrum at the output of the klystron with the 2115.0000-MHz carrier only switched. Figure 3 shows the spectrum with the 2115.6998-MHz carrier only, and Fig. 4 shows the spectrum with both carriers switched. The third-order intermodulation products are approximately 50 dB down and most likely attributable to imperfect phase adjustment of the switching waveforms to the RF switches, resulting in an overlap period when both carriers are on simultaneously. Work is proceeding on a switching waveform generator with control over the time and phase of each switch voltage.

Table 1. Switching and distortion products
($f_1 = 2115.0000$ MHz, $f_2 = 2115.6998$ MHz, $f_{switch} = 0.50000$ MHz)

Frequency, MHz	Source
2114.199846	Third switching sideband of f_2
2114.300154	Third-order intermodulation product (IM), $2f_1 - f_2$
2114.500000	First switching sideband of f_1
2114.699846	Second switching sideband of f_2
2115.000000	Fundamental f_1
2115.199846	First switching sideband of f_2
2115.500000	First switching sideband of f_1
2115.699846	Fundamental f_2
2116.000000	Second switching sideband of f_1
2116.199846	First switching sideband of f_2
2116.399692	Third-order intermodulation product (IM), $2f_2 - f_1$
2116.500000	Third switching sideband of f_1

As a comparison to the switched carrier techniques, the two carriers were simultaneously run through the klystron and intermodulation levels noted. Figure 5 shows intermodulation products under different power output levels.

This investigation will continue with the following experiments:

(1) Development of a refined 66-MHz switch with independent control of each channel.

(2) Investigation of spurious and modulation products in the output of the klystron in the DSIF receive band (2290–2300 MHz).

(3) Measurement of RF modulation envelopes to evaluate pulse distortion in the multipliers and klystrons.

From the results of these experiments, the feasibility of using this system to support dual carrier commitments will be determined.

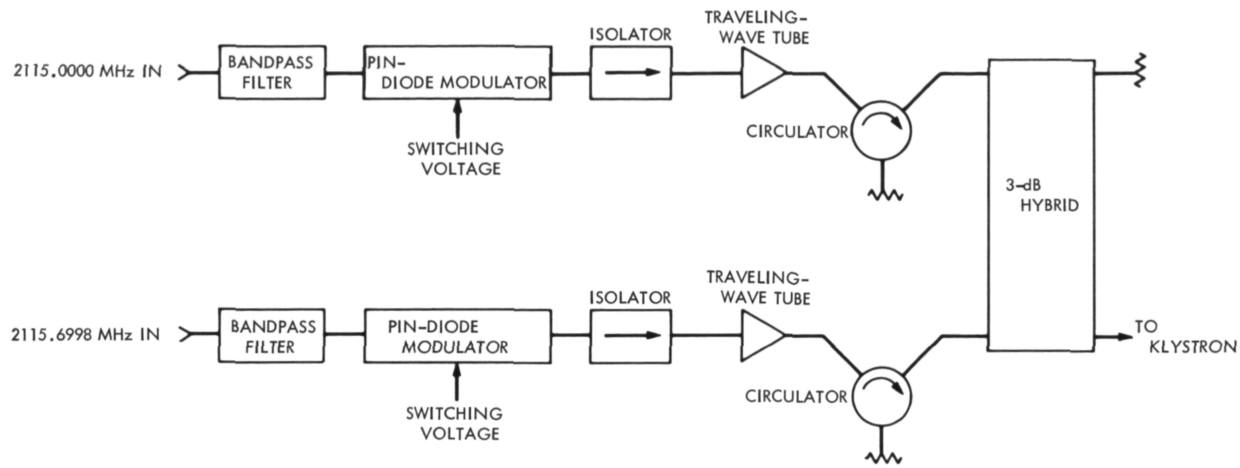

Fig. 1. S-Band carrier switching equipment

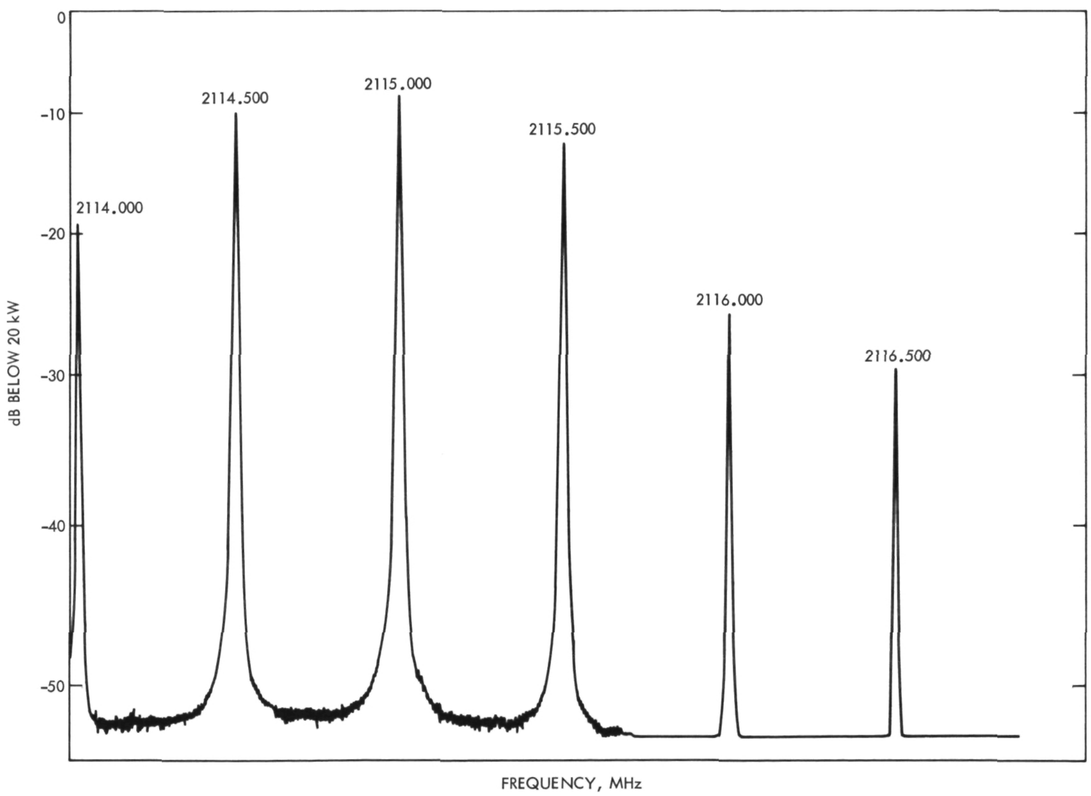

Fig. 2. Spectrum at output of klystron with 2115.0000-MHz carrier only switched

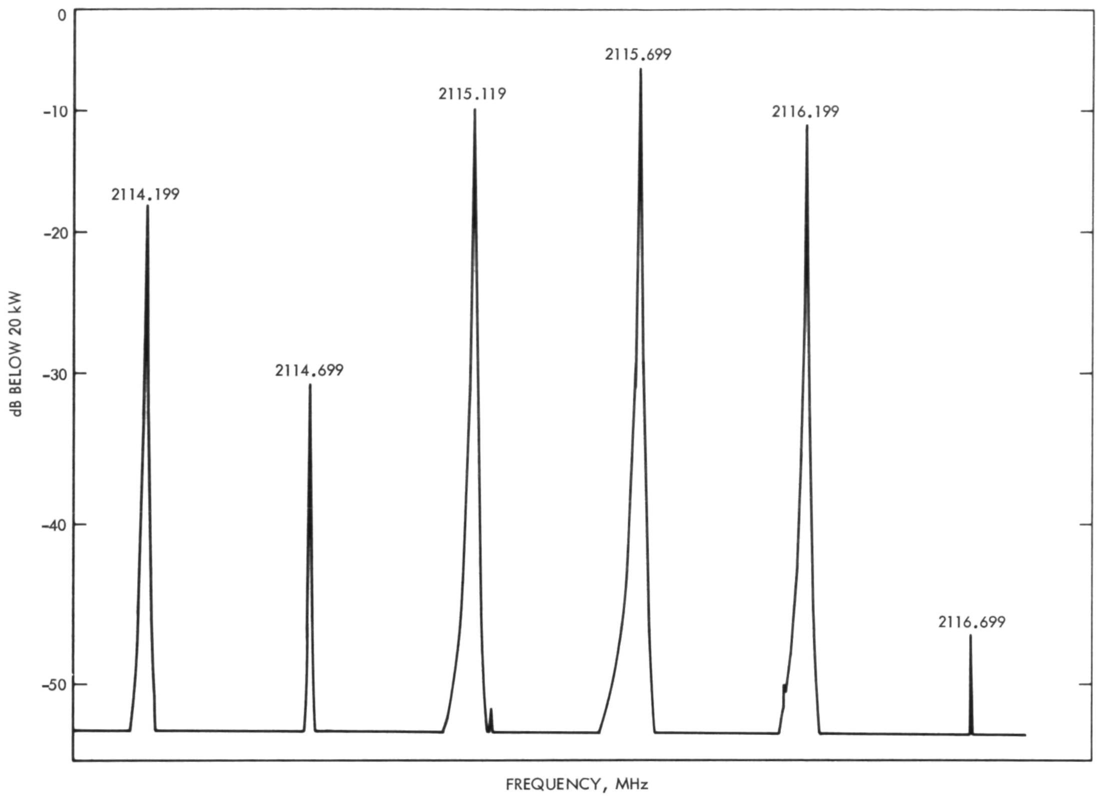

Fig. 3. Spectrum at output of klystron with 2115.6998-MHz carrier only switched

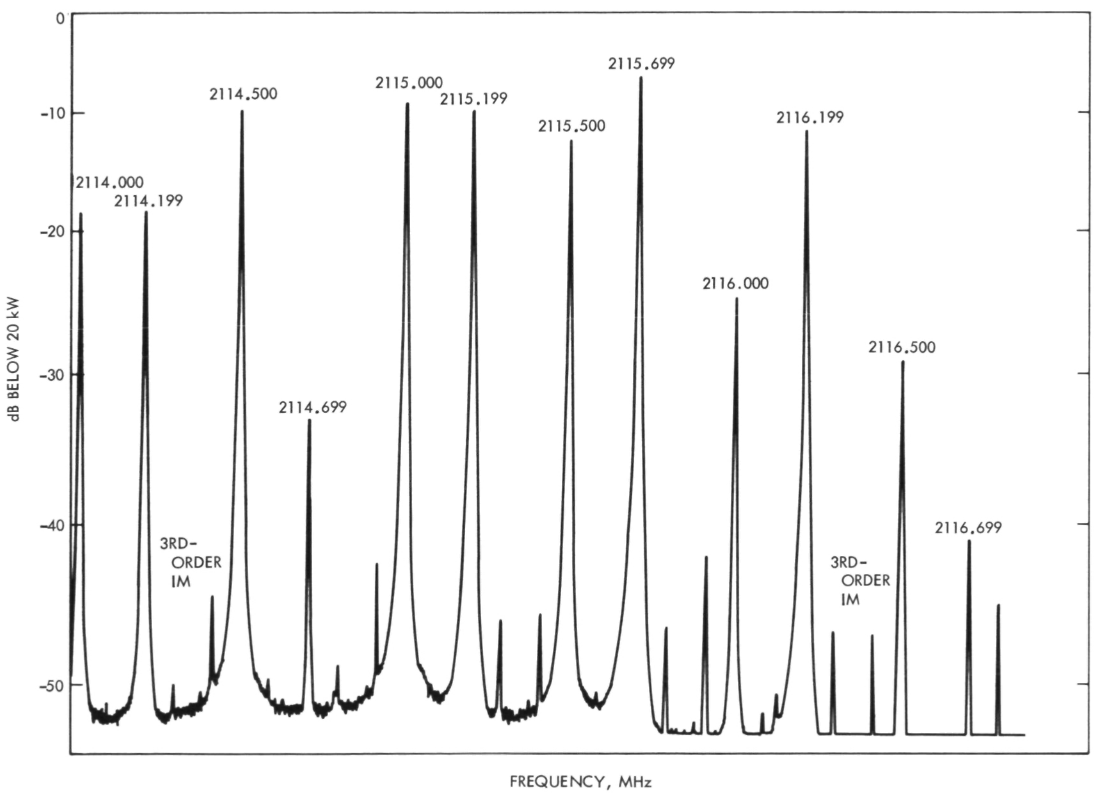

Fig. 4. Spectrum at output of klystron with both carriers switched

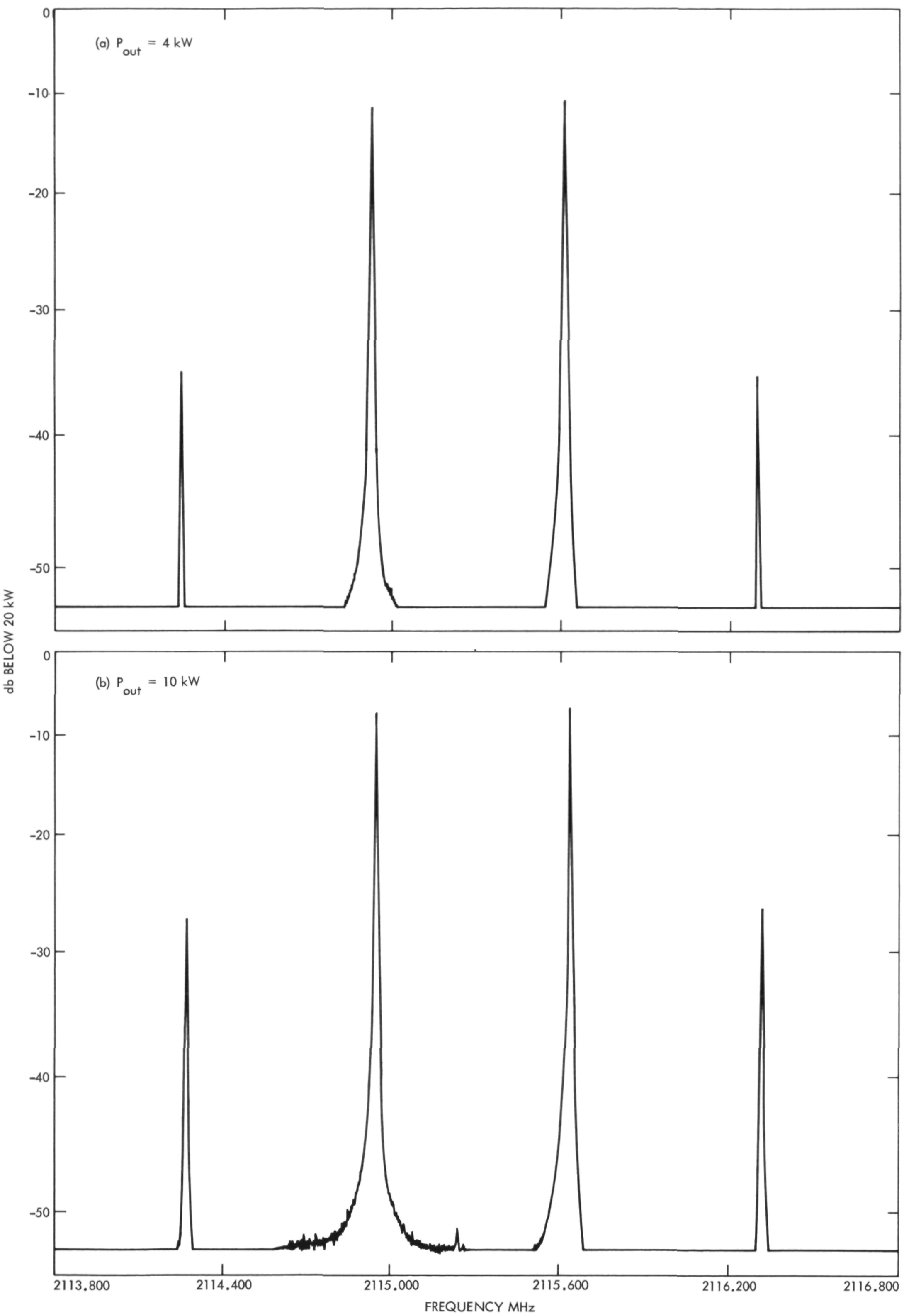

Fig. 5. Intermodulation products under different power output (P_{out}) levels

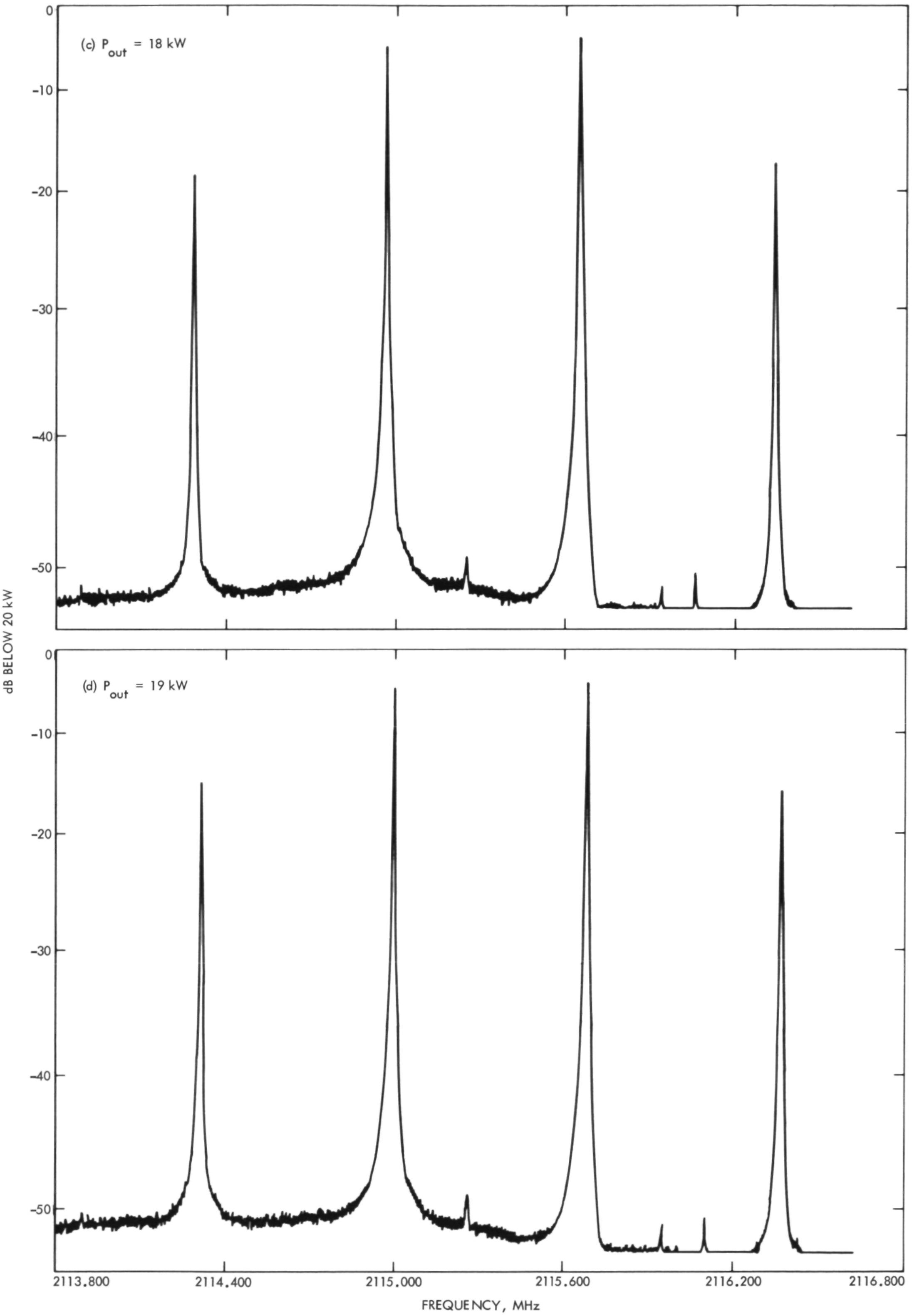
(c) P_{out} = 18 kW
(d) P_{out} = 19 kW
dB BELOW 20 kW
0
-10
-20
-30
-40
-50
2113.800
2114.400
2115.000
2115.600
2116.200
2116.800
FREQUENCY, MHz

Fig. 5. (contd)

G. DSS 13 Operations, *E. B. Jackson*

1. Experiments

During the period August 16 through October 15, 1970, DSS 13 continued clock synchronization transmissions to DSSs 14, 41, 42, and 51. Routine pulsar observations (24 h per week) continued along with planetary radar activities, both mono- and bi-static, with the planets Mercury and Venus as targets. Spectra collected included both crossed and normal polarization, total spectrum, and ranging.

2. Program Development

Development of the Ephemeris Offset Program continued with most of the effort being devoted to analyzing the available and desired system parameters with a minimum (one track per week) of antenna time being required. This program is expected to be completed by December 31, 1970.

3. Major Maintenance

Failure of the 450-kW 2388-MHz amplifier klystron forced conversion of the recently installed 100-kW 2215-MHz transmitter to operate at 2388 MHz by means of a klystron substitution. This enabled continuation of the Venus ranging experiments until increasingly urgent signs of impending bearing failure forced shutdown of the 1.2-MW 400-Hz motor generator.

Main bearing replacement was effected in the generator portion of the motor generator set in 10-days time, although detailed manufacturer's instructions and special bearing removal tools were not available. The removed bearings were carefully examined and the bearing which had been generating the increasingly high level of noise was discovered to have a crack in the surface of the inner race. This failure, illustrated in Fig. 1, is quite similar to failures which are known to be caused by excessive static load, particularly as a result of shipment on railroad cars with suspension improperly matched to the load. The resulting acceleration loading due to roadbed shock and "shunting" activities quite often results in localized hardening of the bearing and race with consequent early failure. This particular machine had accumulated only approximately 10,000 h of operation before the bearings were replaced to avoid the consequences of possible catastrophic failure.

4. Implementation of Fire Program

The FIRE-X program, which provides additional fire protection to the Goldstone stations, is well underway at DSS 13 and the Microwave Test Facility. AT DSS 13, carpet floor tiles and non-fire resistant wall and ceiling tiles were replaced in building G-51 and sprinklers were installed in buildings G-51 and G-53. Addition of smoke detectors in the tunnel between the 85-ft antenna and building G-53A will aid in early fire detection in that area. A network of fire hydrants was provided around DSS 13 and the Microwave Test Facility. To provide sufficient water for the fire hydrants, a 750-gpm pump house, automatically activated by the pressure drop caused by opening a hydrant, is being constructed at DSS 13.

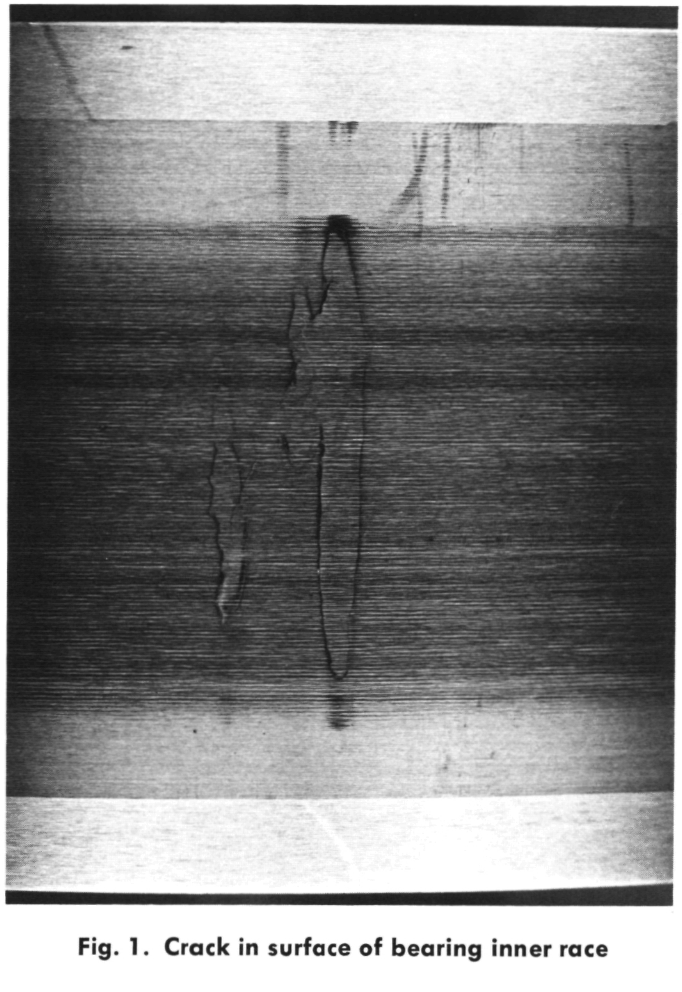

Fig. 1. Crack in surface of bearing inner race

VII. SFOF Development

DEVELOPMENT AND IMPLEMENTATION

A. Functional Design of the Space Flight Operations Facility for the 1970–1972 Era,

H. S. Simon

1. Introduction

The Space Flight Operations Facility (SFOF) will be required to provide test and flight support for the following projects in the 1970 through 1972 Mark IIIA era:

(1) *Mariner* Mars 1971.

(2) *Pioneer F*.

(3) *Pioneer G* (test only).

The SFOF will also provide flight support for the following on-going projects:

(1) *Mariner* Mars 1969.

(2) *Pioneers VI* through *IX*.

In addition, the SFOF will generate and transmit antenna predicts for future manned *Apollo* missions.

The SFOF is comprised of five systems: Central Processing, Telemetry, Tracking, Command, and Monitor and Operations Control. These systems are *functional* entities which mutually share the hardware and software of the SFOF. Hardware and software are *physically* partitioned into groupings called subsystems. One level below the subsystem are assemblies. An assembly is defined as a number of subassemblies or parts grouped together in order to perform a discrete function within a subsystem.

This article describes the functional design of the SFOF to the subsystem level and its interfaces with the Ground Communications Facility (GCF) and the Scientific Computing Facility (SCF). A generalized block diagram of the SFOF Mark IIIA configuration and its interfaces with the GCF and SCF is shown in Fig. 1. The configuration provides the capabilities that are necessary to satisfy the processing and display requirements for the DSN Command, Telemetry, Tracking, and Monitor and Operations Control Systems.

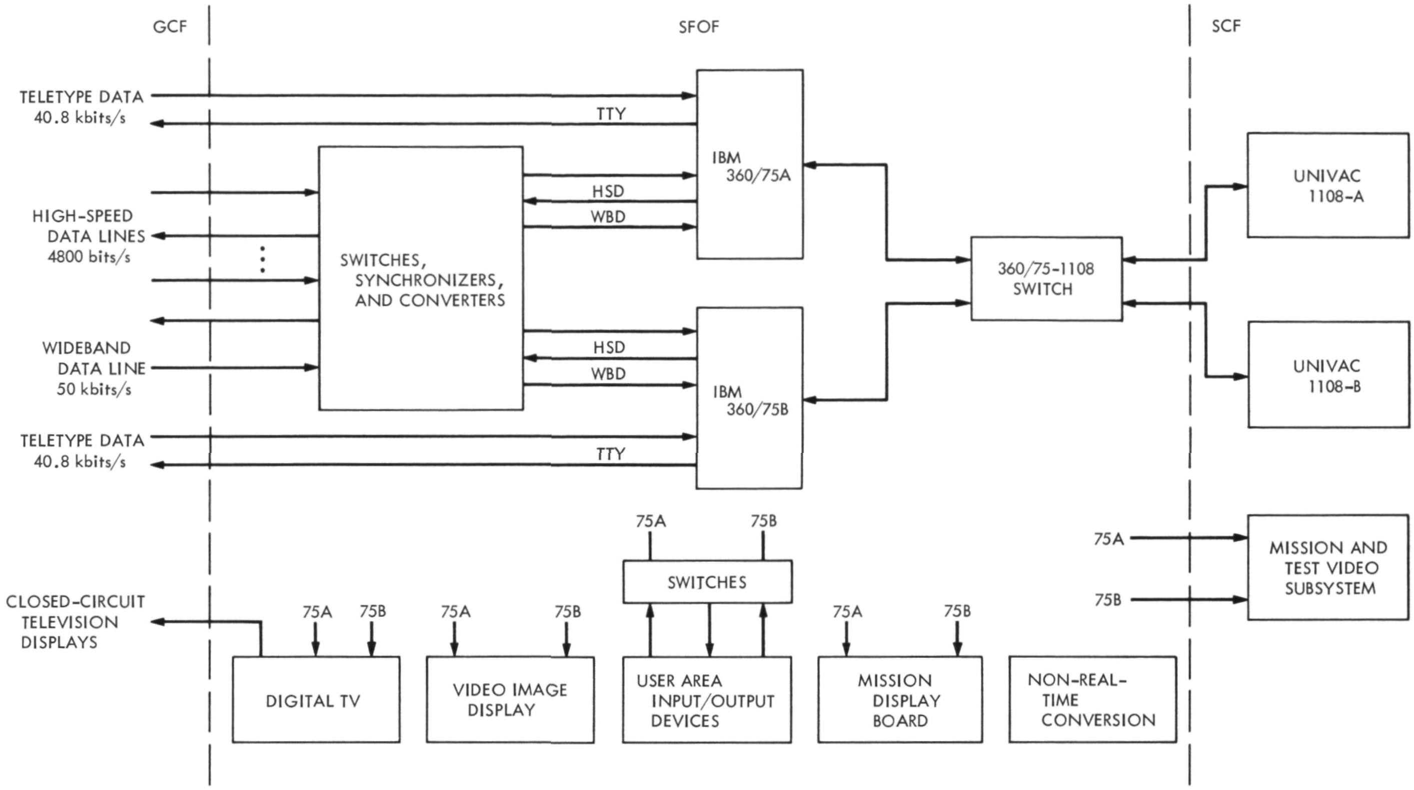

Fig. 1. Generalized block diagram of the SFOF Mark IIIA configuration (1970–1972 era)

2. SFOF Mark IIIA Configuration

Significant capabilities are provided with the Mark IIIA configuration that were not available with the SFOF Mark II configuration. These include the following:

(1) The transmission of data over outbound high-speed data lines (HSDLs).

(2) Reception of wideband data (WBD).

(3) The processing and display of high-rate telemetry data.

(4) Incorporation of a multi-channel digital television assembly (see SPS 37-65, Vol. II, pp. 86–91).

(5) Interface with the SCF to implement the transfer of orbital and trajectory data between programs in the IBM 360/75 and UNIVAC 1108 computers.

(6) Uninterrupted power supply to guard against critical period power outages.

(7) Redesign of the physical plant to provide expanded capability for DSN and project users.

3. SFOF Subsystems

The SFOF consists of five hardware subsystems as shown in Fig. 2:

(1) Computation.

(2) Memory and auxiliary storage.

(3) Real-time input/output (I/O) interface.

(4) User terminal and display.

(5) Non-real-time conversion.

Additionally, there are six software subsystems. These are:

(1) Master control and user interface software.

(2) SFOF telemetry and command software.

(3) SFOF tracking software.

(4) SFOF monitor and operations control software.

(5) Orbit software.

(6) User software integration.

Power, air conditioning, and space allocation in the SFOF are provided by the technical facilities subsystem.

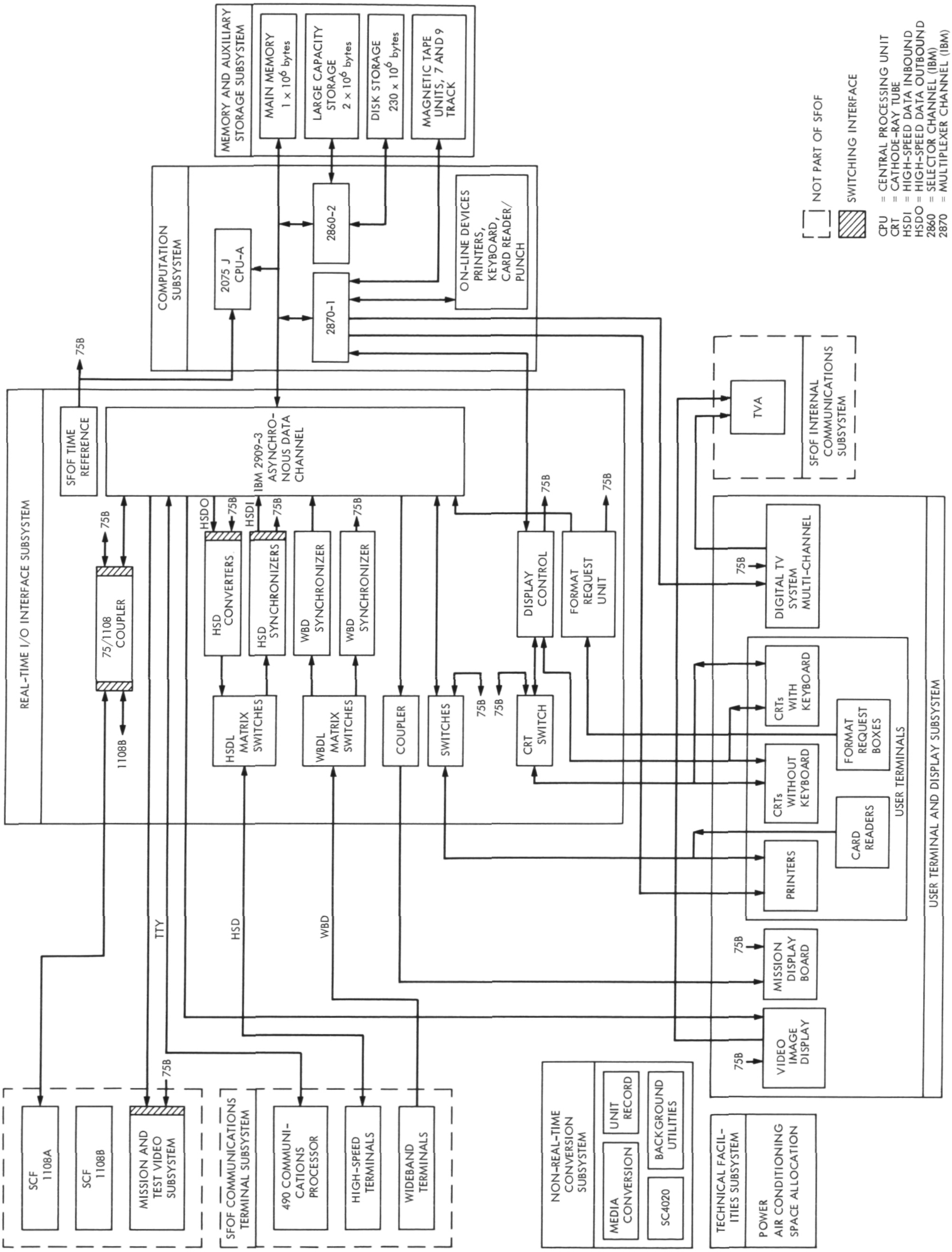

Fig. 2. SFOF hardware subsystems

The software subsystems, presently being integrated into the facility, will not be described in this article.

4. SFOF Hardware Subsystems

As of October 1, 1970 the hardware subsystems were installed in the SFOF enabling the software subsystems to proceed with program checkout and integration. Concurrently, non-real-time background jobs can be processed utilizing this configuration. The following is a brief description of the hardware subsystems.

a. Computation subsystem. This subsystem contains the central processing units, selector, and multiplexer channels and a group of peripheral input/output devices that are used for computation support and system control. Refer to Stiver, *Chapter VI-B*, this volume, for more detail on this subsystem.

b. Memory and auxiliary storage subsystem. This subsystem contains all storage assemblies, including main memory, large capacity storage (LCS), disk files, and magnetic tape units. These elements provide storage for real-time data streams, software subsystem programs, application programs, system and master data records and system diagnostics. Refer to Stiver, *Chapter VI-B*, this volume, for more detail on this subsystem.

c. Real-time I/O interface subsystem. This subsystem contains the assemblies that are necessary to satisfy the real-time processing and display requirements during the periods of mission support. Refer to Stiver, *Chapter VI-B*, this volume, for more detail on this subsystem.

d. User terminal and display subsystem. This subsystem contains display and message entry assemblies that are required by the DSN and projects for mission support. Output data can be displayed on a multichannel digital TV (DTV) system with hard copy, line printers, cathode-ray tube (CRT) devices and a four-section mission display board. User messages can be entered via card readers or keyboard devices. This subsystem also provides the capability to display video imagery data.

e. Non-real-time conversion subsystem. This subsystem contains the assemblies that provide the following capabilities:

(1) Media conversion center.

  (a) Provide conversion for paper tape to/from digital magnetic tape.

  (b) Provide conversion for analog magnetic tape to digital magnetic tape.

  (c) Provide printer copy from paper tape and digital magnetic tape.

  (d) Provide quality check of *Pioneer* analog data.

(2) Microfilm printer and plotter (SC4020). Provides microfilm records and hard copy plots, graphs, and prints.

(3) Unit record equipment. Includes card sorters, collaters, reproducers, interpreters, keypunches, and card listers.

(4) Background utilities. Will be run on the IBM 360/75 computer.

5. SFOF Interfaces With the GCF

The following interfaces exist between the SFOF and GCF subsystems (refer to Fig. 2):

(1) Real-time I/O interface and SFOF communications terminal.

  (a) Teletype data is transferred, serially, between the UNIVAC 490 communications processor and IBM 2909 subchannels at a 40,800-bit/s rate.

  (b) High-speed data (HSD) is transferred from data terminals in the GCF, over HSD lines, to HSD synchronizers in the SFOF at a 4800-bit/s rate.

  (c) High-speed data is transferred from HSD converters in the SFOF, over HSD lines, to data terminals in the GCF at a 4800-bit/s rate.

  (d) Wideband data is transferred from data terminals in the GCF, over WBD lines, to WBD synchronizers in the SFOF at a 50,000-bit/s rate.

(2) User terminal and display and SFOF internal communications. Data from the output of the multi-channel, digital TV system and the video image display assembly (see following article by Diem, *Section B*) is transferred to the television assembly for display over the closed-circuit TV network.

6. SFOF Interfaces With the SCF

An electrical interface can be enabled between the IBM 360/75 computer in the SFOF and the UNIVAC 1108 computer in the SCF. Data is transferred between the two computers, serially, at a nominal rate of 50,000 bits/s.

Video data is transferred from the output of two 2909 GPO (general-purpose output) subchannels to the film recorders in the mission and test video subsystem in 32-bit word transfers.

7. Conclusion

The development of the SFOF hardware and software subsystems for the 1970–1972 era will provide new capabilities for mission support that were not available with the Mark II configuration.

B. Video Image Display Assembly, *W. Diem*

1. Introduction

With the advent of imaging devices on most unmanned exploratory space probes, the DSN has undertaken development of a multiple-mission capability for the reconstruction, display, and printing of tonal pictures in the Space Flight Operations Facility (SFOF). The basic objectives are to support mission operations with video displays and hard-copy prints for real-time validation and preliminary analysis of spacecraft pictures.

This capability is being developed as an integrated set of hardware and software because it involves a closely related group of functions and a common technology. The software will be incorporated into the Central Processing System (CPS).[1] The hardware, called the Video Image Display (VID) Assembly, will be installed in the SFOF as part of the user terminal and display subsystem.[2] When completed, the VID Assembly will expand the functional capability of the High-Rate Telemetry System to include display and rapid access prints of spacecraft pictures. The VID displays and prints will be used in real-time and near-real-time for studying the topographic features, dynamic characteristics, and atmospheres of the planets and for the selection and certification of landing sites.

[1]The CPS is discussed by Stiver in *Chapter VI-B*, this volume.

[2]Additional information on the user terminal and display subsystem is given by Simon in the previous article, *Section A*.

2. Capabilities

Review of space flight operations support requirements and the capabilities of existing JPL video ground data handling facilities disclosed the need for four basic capabilities. These capabilities are depicted in Fig. 1 and described below.

a. Operational prints. High-quality operational prints including the spacecraft image, alphanumeric data, and histogram plots will be used by the experiment and science teams for preliminary measurements and analysis involved in making near-real-time decisions.

Initially two printers will be provided in the user area. Each will be a self-service unit with the capability of printing any image that is displayed on any VID Assembly display channel. The prints will contain the full spacecraft image at full resolution plus alphanumeric data and histogram plots. The printers will produce 8- by 8-in. semi-archival positive opaque prints with a resolution of 1536 by 1536 elements and 32 discernible shades of gray. Sixty-four shades will be recorded to eliminate quantization contouring. Pincushion distortion will be non-existent and geometric errors and spatial jitter will be greatly reduced compared with existing cathode-ray tube (CRT) film recorders. In order to accommodate the needs of future missions, the VID Assembly will be expandable to handle up to 32 printers.

Two 16-shade grayscales will be recorded adjacent to the right side of the image. The grayscale nearest the image will be output from the CPS and will reflect any

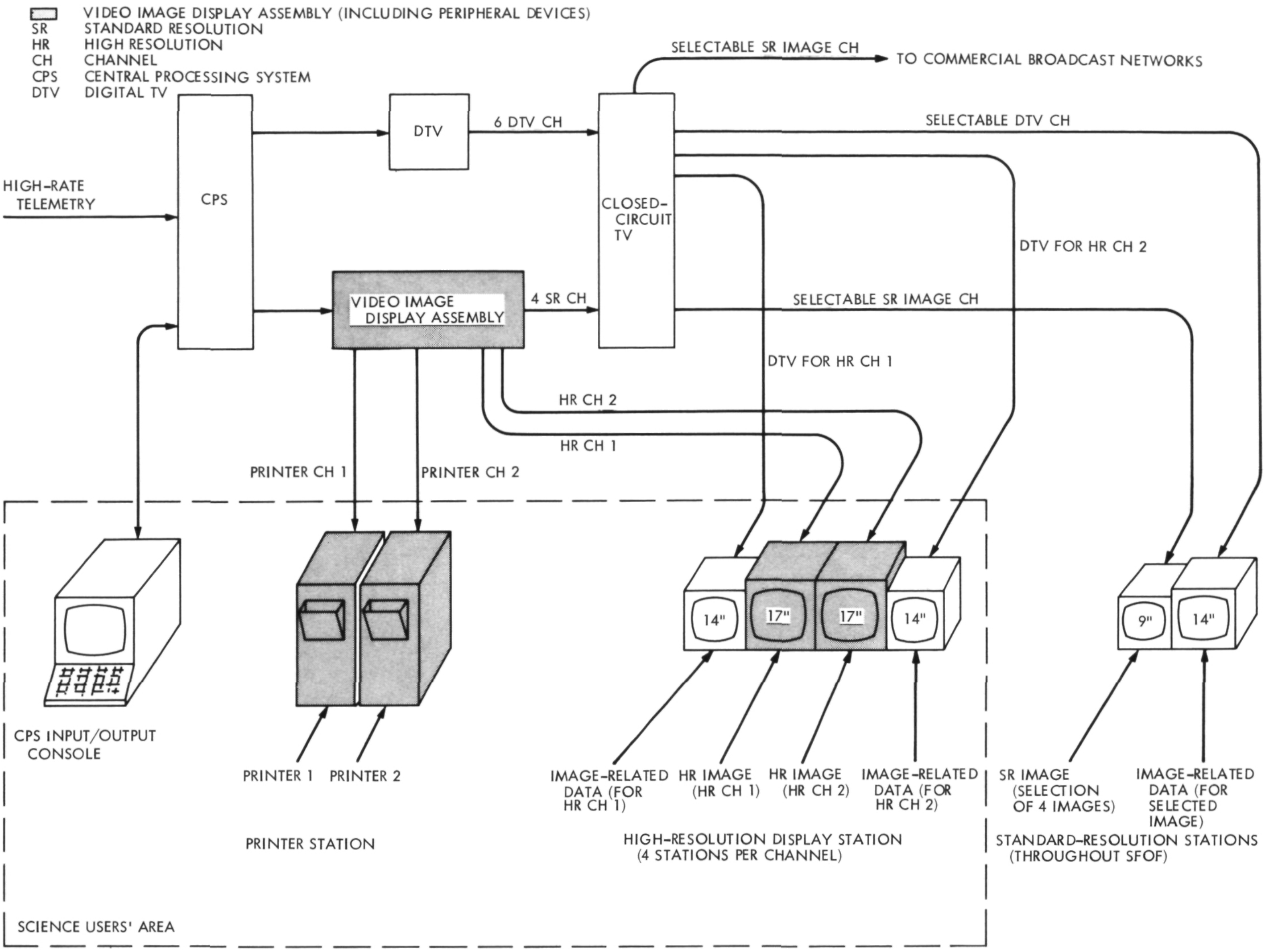

Fig. 1. Video image display functional diagram

contrast enhancement performed on the image. The other grayscale will be a reference grayscale produced in the VID. If the image is not enhanced, the two grayscales will be identical and will appear as one grayscale of twice the width. However, if the intensity values of the image are modified, the CPS grayscale will likewise be modified and the enhancement will be immediately obvious by comparing the two grayscales.

The printer will record at a rate of six scan lines per second (s) and will record a full 1536- by 1536-element print in 4.8 min. Normally a print will be recorded in less time because most missions will not require the full-print format. For example, a complete *Mariner* Mars 1971 print can be recorded in 2.75 min. Therefore, each printer can produce two prints for each image received from a *Mariner* Mars 1971 spacecraft. One of these prints might contain a raw image, and the other an enhanced image.

Likewise, if the Venus–Mercury spacecraft were to transmit an 832- by 700-pixel image each 42 s, five VID printers would be capable of printing each frame received. The VID can sequentially assign printers in a rotary fashion and multiplex the data to concurrently record on all printers. If required, additional printers could be added to handle enhanced images. The VID Assembly can be expanded to concurrently record 32 different images.

b. High-resolution display. High-resolution display of the spacecraft pictures on 17-in. TV monitors will enable the experiment and science teams to make real-time decisions based on the spacecraft pictures. The high-resolution monitors will display 832 elements per line and 800 lines. They will provide 32 discernible shades of gray with equal resolution of shades over the dynamic range. Six bits per pixel image data will be converted to 64-level video to eliminate quantization contouring. In addition to the image, a 16-shade reference grayscale will be displayed to the right of the image. Geometric error will be held to 2%. Dynamic focus and gamma correction will be provided. To provide maximum picture definition, digital signals will be fed to the monitors; the conversion to analog video will be performed at each individual monitor. The VID will be capable of updating the entire display in 5 s. The basic VID Assembly will include two high-resolution channels with capability for expansion to eight channels.

c. Standard-resolution display. Display of the spacecraft images will be made via SFOF closed-circuit television (CCTV) for distribution to mission operations personnel and the commercial broadcast networks. This will be standard 525-line analog video with a display format of 640 elements per line and 480 active lines. The design goal is to display 16 discernible shades of gray.

Due to the limited format of the standard-resolution display, the VID will provide the capability to display the full image at reduced resolution and to display any selected section of the image at full resolution.

Update will require 5 s. The capability will exist for non-destructive overlay of alphanumeric characters on the displayed image. The basic VID Assembly will contain 4 standard-resolution display channels with the capability for expansion to 16 channels.

d. Image-related data display. Alphanumeric identification data and histogram plots associated with the image are required for the user to identify and analyze the picture data. As mentioned previously, this information will be provided on the operational prints along with the image. This same information will be provided to the users of both the high-resolution and standard-resolution displays by the SFOF digital television (DTV) assembly via closed-circuit television.

3. Modes of Operation

The VID Assembly will be capable of operating in an automatic on-line mode under CPS control, in a manual off-line mode for maintenance, and in a combined on-line/off-line mode. This combined mode will provide the capability to manually test one or more faulty devices, displays, or print channels without interfering with other channels operating under CPS control.

In this mode the CPS will control which VID devices may be manually accessed from the VID display diagnostic unit. Manual inputs will be inhibited from affecting the operation of other devices and the outputs of other channels.

In the automatic mode, the CPS will compute and edit the image and image identification data from the high-rate telemetry data received from a DSIF tracking station. The CPS will compute the intensity histogram, format and output the image and image-related data, and store the data in a disk file for further processing. At the option of the user, the CPS will either output the image data to the VID for display as it is being received, or output the complete image immediately following receipt of the last image line. If the user requests contrast enhancement, the CPS will recall the image from the disk file, perform a contrast stretch, and output the enhanced image to the VID for display.

4. Concluding Remarks

The VID Assembly is being designed to meet the picture display needs of future missions through the next decade, including multiple-mission operation. It will provide high-quality tonal image displays and operational prints for real-time validation and preliminary analysis of spacecraft pictures in support of scientific investigations of the planets.

C. Discernibility of CRT Gray Shades, *J. J. Volkoff*

1. Introduction

To just discern the luminances of two gray-shade objects displayed on a cathode-ray tube (CRT) monitor, a certain minimum contrast between the two gray shades is required. Since contrast is a function of the gray-shade luminances, an experiment was performed to determine the luminances at which shades of gray produced on a CRT monitor are discerned. The results are presented as the required luminance difference between the gray shades as a function of the luminance of the brighter shade. These results were measured at a just-discernible criteria.

Photon noise generated in a CRT system causes an increase in the contrast required for discernibility. The results of this experiment shall be used to substantiate the formulations obtained from a study of photon noise generated in CRT systems. These formulations shall be applied in establishing the requirements for and evaluating the performance of the SFOF Video Image Display Assembly CRT displays. These results shall also be used to establish the minimum dynamic range requirements for the SFOF user terminal and display subsystem/digital television assembly graphics mode.

2. Physical Description

The gray-shade discernment experiment was performed with a CRT monitor, a signal generator, and a photometer in the SFOF. This equipment and its related equipment are described in Table 1.

Table 1. Equipment description

Equipment	Description
Monitor	Conrac Type 14BDP4 Serial No. 7008
Test signal generator	Telechrome Model 3508 Manufactured by Telemet Co., Ametyville, N.Y.
Photometer	Gamma Scientific Inc. Model 700 log-linear
Calibration lamp source	Gamma Scientific Inc. Model 220 standard Serial No. 152
Calibration Lamp	Gamma Scientific Inc. Model 220-1 luminance standard head 100:2 ft-L Color temperature 2854°K Serial No. 152
Light sensor	Gamma Scientific Inc. Model 700-1, fiber optics tube-bundle with general-purpose photomultiplier head Serial No. 767

Two adjacent vertical gray shades were generated on the monitor in a masked display zone of 4-in. square. This zone was selected such that the highest uniformity of luminance over the entire area of each shade was obtained. The luminance level along the horizontal direction of each shade was reasonably uniform. However, the maximum to minimum luminance levels of each shade along the vertical direction were within 6% of each other. The luminance for each shade decreased toward the lower and upper edges of the raster. This variation in luminance was a function of raster position along the vertical direction as shown in Fig. 1. Since there was this correspondence of luminance variation for each shade along the vertical direction, the difference of luminance between each shade along the vertical direction held to within ±3%. This variation was not discernible.

The viewing distance was 10 ft resulting in a visual angle of 57 min per shade. The uniform scan lines on

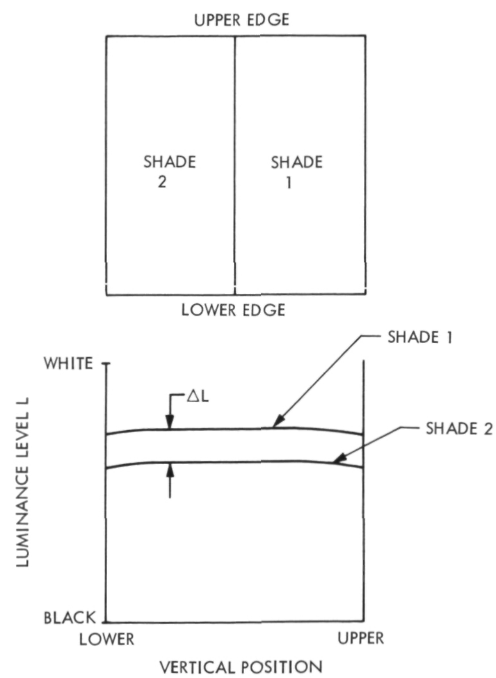

Fig. 1. Luminance as a function of vertical position of the test object

the CRT were not distinguishable from this viewing distance. Viewing of the test object was performed in a dark environment. All observers had approximately 20/20 visual capability.

Shade brightness was modulated by means of brightness and contrast controls. A potentiometer was installed in series with the contrast control to facilitate a refinement of the contrast modulation between the two adjacent shades. Calibration checks and adjustments of the photometer were periodically made during the experiment to insure accurate luminance measurements.

3. Procedure

During the experiment, procedures were exercised to insure reliability in establishing the measurement of the degree of contrast required to discern gray shades. The procedures also included fatigue, accommodation, acuity, and adaptability considerations of the observer.

At a given luminance, both shades were initially set at the same luminance and then the luminance of one of the shades was decreased until the observer was just able to discern the shades. This process was repeated a number of times to establish a representative reading and an appraisal of the level of discernment.

All tests began at a high luminance level (nominally 100 ft-L). The luminance levels were sequentially decreased toward the lowest luminance level measured and then sequentially increased toward the high luminance level. This procedure provided a means by which a hysteresis pattern may be established. No definite pattern of hysteresis was found since the data randomly fell about a mean line for each observer regardless of increasing or decreasing luminance order. The luminance levels displayed were varied over three orders of magnitude.

4. Results

The difference in luminance ΔL between the shades required to discern the existence of two shades as a function of the luminance of the brighter shade L_b is shown in Fig. 2. This curve represents an average of 180 measurements made on five observers. It is estimated that the curve represents a discernment level such that the shades were discerned for over 95% of the time.

It was found that these experimental results substantiated the preliminary results obtained from a CRT gray-shade discernment rationale. This rationale includes photon noise generated in a CRT system.

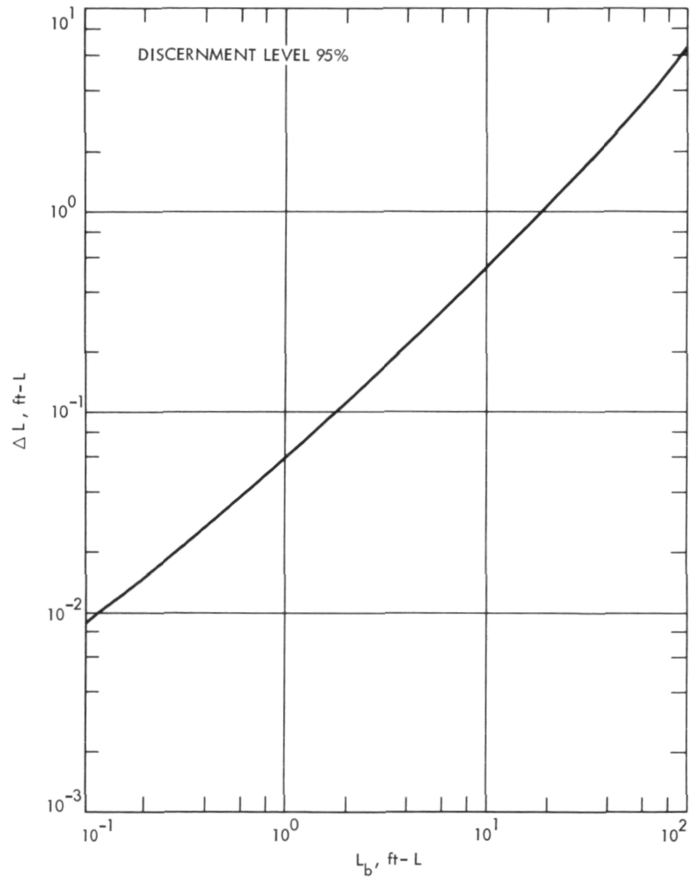

Fig. 2. Difference of luminance ΔL to discern gray shades vs luminance of the brighter shade of test object L_b

VIII. GCF Development

DEVELOPMENT AND IMPLEMENTATION

A. Ground Communications Facility Functional Design for 1971–1972, *J. P. McClure*

1. Introduction

The Ground Communications Facility (GCF) provides the ground communications capability required by the DSN for the conduct of space flight operations. This capability changes in an evolutionary manner to meet the constantly changing (generally increasing) communications requirements of the DSN.

This article discusses the general design of the GCF for the 1971–1972 era. The majority of the implementations required for this new capability will be completed by the end of 1970.

The GCF consists of four systems: voice, high-speed data (HSD), teletype, and wideband data (WBD). Though each system provides a distinctly different capability, the systems share some terminal equipment and transmission circuits.

2. Transmission Capability

The principal transmission capability of the 1971–1972 GCF is shown in Fig. 1. This capability provides one voice, one high-speed data, and four teletype circuits between the Space Flight Operations Facility (SFOF) and the majority of the Deep Space Instrumentation Facility (DSIF) stations. Other locations have varying capability depending on their requirements. A significant difference from the past is the wideband 50-kbit/s transmission capability between the SFOF and DSS 14, the Compatibility Test Area (CTA 21), and Cape Kennedy Hangar AO.[1] A heavy quantity of voice circuits are provided between the SFOF and DSS 71 and Hangar AO in support of launch and near-earth phases of the forthcoming missions. New circuits also radiate out from the SFOF to both Ames Research Center (ARC) and Laboratory for Atmospheric and Space Physics (LASP), Boulder, Colorado.

The majority of the GCF's transmission capability is furnished by NASA Communications (NASCOM) from a pool of circuits which it uses to satisfy all of NASA's long-haul tracking network communications requirements. The communications capability of the GCF ebbs and flows as requirements change and is seldom constant from day to day. The capability shown in Fig. 1 represents the circuit quantities used for terminal equipment design purposes. Though circuit quantities may

[1]The SFOF/Cape Kennedy Hangar AO circuit is a temporary capability installed specifically for *Mariner* Mars 1971 support.

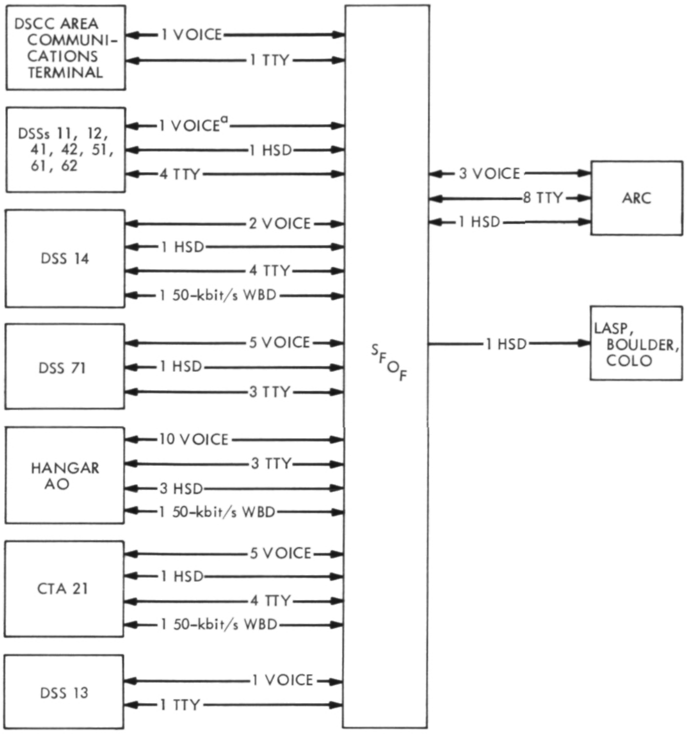

[a]DSSs 41 AND 42 WILL SHARE A SINGLE VOICE CIRCUIT DURING NON-CRITICAL PERIODS.

DSSs 51, 61 AND 62 WILL SHARE A SINGLE VOICE CIRCUIT DURING NON-CRITICAL PERIODS.

Fig. 1. Ground Communications Facility 1971–1972 principal transmission capability

change quickly, the highly specialized terminal equipment is permanently installed and has a relatively lengthy development and implementation cycle.

The transmission capability shown in Fig. 1 is not exhaustive. The GCF provides many circuits on the Laboratory and to other locations too numerous to realistically depict herein.

3. Voice System

The GCF Voice System for the 1971–1972 era will be little changed from the present system. Additional voice circuits will be provided between the SFOF and Hangar AO/DSS 71 for short-term launch requirements. Otherwise the transmission capability will remain substantially static. The SFOF internal voice communications subsystem will continue to provide a total of 72 conference networks; however, this assembly will be expanded to include the *Pioneer F* Mission Support area to be located in the new Systems Development Laboratory building which is now under construction. Additionally the entire Systems Development Laboratory building will be covered with operational public address service.

At most DSSs the tactical intercom (TIC) will remain in service in its current configuration. Additional TIC stations will be added at DSSs 42/43 and 61/63 in support of the new 210-ft-diam antennas.

4. High-Speed System

A general configuration of the GCF 1971–1972 High-Speed System (HSS) is indicated on Fig. 2. Station capabilities shown on the left of this figure will be provided at all DSIF locations except DSS 13. The HSS will provide one 4800-bit/s full-duplex high-speed data circuit between each of the equipped stations and the SFOF. This circuit will support all DSS–SFOF HSS traffic. All stations will be provided with backup terminal equipment for reliability purposes.

In terms of changes, the outbound (SFOF to DSS) direction of transmission has been activated and the data rate per circuit has been increased from 2400 to 4800 bits/s. The standardized block size used on all of these circuits has been increased from 600 to 1200 bits per block.

In all cases, two or more data sources will time-share a single 4800-bit/s circuit. The sharing will be accomplished and controlled by the block multiplexer (BMXR) which permits each source to transmit blocks in accordance with its priority. At the stations, a new block demultiplexer (BDXR) deletes the BMXR-generated filler blocks and routes each received data block to the appropriate destination(s) based on the routing instructions contained in the data block header.

The encoders generate and attach an error detection polynominal code to each block. This code is detected by the decoder and compared against the body of the block, thus permitting detection of any transmission errors. At the SFOF, incoming blocks containing detected errors are counted. This error information is processed and used to drive a televised display.

At the SFOF, all received data are parallel-routed (broadcast) to the Central Processing System 360/75 computers, the Simulation Center, and, when applicable, to project-dependent facilities such as the Mission Test Computer (MTC) and special-purpose hardware.

The High-Speed System will have an end-to-end (DSIF–SFOF) long-term uncorrected error rate of 3×10^{-5} or lower. The one-way transmission time delay will usually not exceed 1.0 s; however, this figure may be exceeded if the transmitting computer has a low priority.

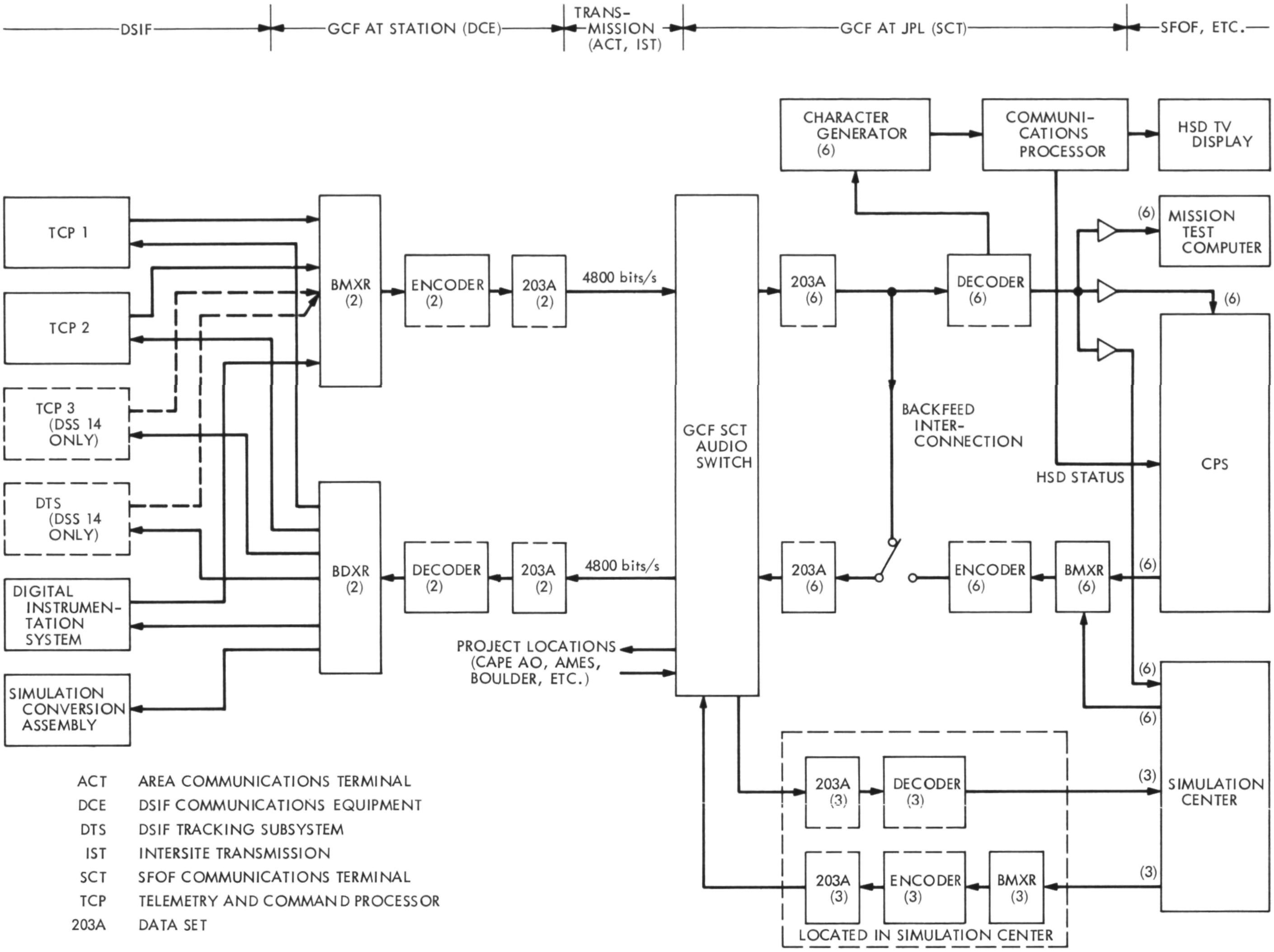

Fig. 2. Ground Communications Facility 1971–1972 High-Speed Data System 4800-bit/s capabilities

5. Teletype System

The Teletype System will remain essentially unchanged from the 1969 version. All teletype will operate at 100 words per minute.

Teletype will be the prime transmission medium for tracking data, predictions, operational plain language messages, and conferences. Teletype will be backup for the transmission of telemetry, command, and monitor data. In future designs, efforts will be made to decrease teletype usage, since it is quite slow in comparison with current data rates.

The GCF Teletype System will continue to be widely used within the SFOF for the output of Central Processing System (CPS) data. In this role the teletype machines are used as low-speed data printers driven by the GCF Communications Processor.

6. Wideband System

The new Wideband System capabilities to be provided by the GCF are shown in Fig. 3 (also see SPS 37-65, Vol. II, pp. 102–103). Full-duplex 50-kbit/s circuits permitting simultaneous transmission in both directions will be provided between the SFOF and DSS 14, CTA 21, and (temporarily) Cape Kennedy Hangar AO. The inbound direction (to the SFOF) will be used for the transmission of multiplexed video data, while the outbound direction will carry simulated data to the stations during tests and verifications.

As in other cases, switching capability in the basement of the SFOF permits full flexibility of interconnection

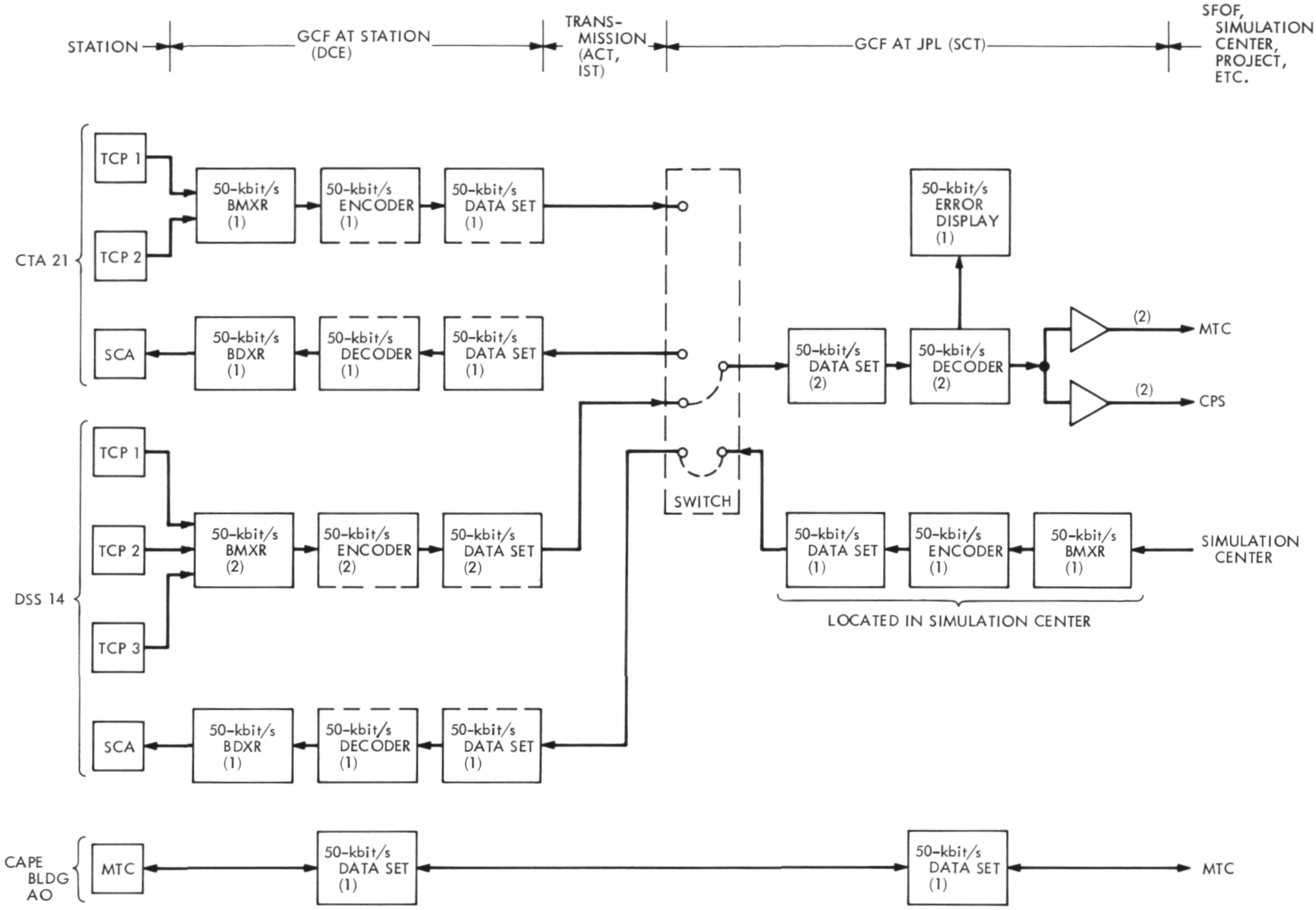

Fig. 3. 1971–1972 Wideband System 50-kbit/s capability

between CTA 21, DSS 14, and SFOF circuits. The Cape Kennedy Building AO/SFOF circuit, which is specifically installed in support of *Mariner* Mars 1971, will be direct routed.

Permanent portions of the Wideband System will use a standard 1200-bit block format with the same header and error detection code used for high-speed data. The wideband block multiplexers and encoders/decoders will perform the same functions as in high speed. The wideband demultiplexer, however, is used purely to remove filler data from the synchronous stream prior to passing this information on to the station Simulation Conversion Assembly (SCA).

7. West Coast Switch

In support of NASCOM, the GCF provides and operates a West Coast switching center for voice, teletype, and high-speed data circuits. Permanent circuits radiating out from Pasadena to many NASA/contractor locations are switched, on a scheduled basis, to long-haul trunks extending to the NASCOM Central Switch at the Goddard Space Flight Center in Greenbelt, Maryland.

This West Coast switching permits a relatively few cross-country trunk circuits to satisfy the needs of numerous individual users in the western U.S. The West Coast Switch handles a continuously growing proportion of NASCOM's western U.S. circuits.

8. Reliability

In the 1971–1972 era, each traffic path through the end-to-end GCF will have a critical period long-term design availability of not less than 0.99 during any scheduled usage period, measured after data flow is established. The critical period mean time to repair will not exceed 15 min.

B. High-Speed System Design Mark IIIA,

D. Nightingale

1. Introduction

A new design of the Ground Communications Facility (GCF) High-Speed System became a clear requirement during the development of DSN systems planning for the capability to support the *Mariner* Mars 1971 and *Pioneer F* and *G* projects. Several constraints and tradeoffs were considered in finalizing the design for which new items of hardware were required. The implementation was carefully controlled since much of the activity had to be dovetailed into the upgrade of the High-Speed System of the NASA Global Communications Network (NASCOM). The GCF accomplished its task of providing the required design and implementation by the fourth quarter of CY 1970.

2. Design Requirements

High-speed communication channels became the prime medium for the transfer of data between the Deep Space Instrumentation Facility (DSIF) stations and the Space Flight Operations Facility (SFOF) as a result of the multi-mission concept of the DSN. The increase in high-speed traffic load consisting of command, telemetry, operations control and monitor data, and to a lesser extent, tracking data, proved to be in excess of the existing GCF capacity per station of 2400 bits/s. Furthermore, the amount of traffic to be sent to the DSIF stations required that an automatic message switching device be provided to deliver the data to the appropriate station computer. The requirements of the DSN Simulation System placed additional traffic loads in order to exercise the station equipment performance via the Simulation Conversion Assembly (SCA). The total requirements for both directions of transmission could be handled by 4800-bit/s full-duplex capability.

3. Design Considerations

During the early part of CY 1969, a study was made to determine the advantages of providing a single 4800-bit/s channel from each station to the SFOF as compared with increasing the existing single 2400-bit/s channel to two in order to achieve the required 4800-bit/s station capacity. Both arrangements were technically feasible, because higher rate data sets were becoming available while past experience at the 2400-bit rate demonstrated efficient performance in support of *Mariner* Mars 1969. (See SPS 37-57, Vol. II, pp. 127–130.)

The study considered that NASCOM was planning to change all existing 205B data sets (2400 bits/s) for a higher rate version, probably a 203 (4800 bits/s) although the precise schedule was somewhat uncertain. The preliminary requirements for flight projects in the 1973 era indicated that further increases in high-speed data (HSD) traffic were becoming more certain. However, the time factor to accomplish the necessary engineering and implementation placed a severe constraint upon a new design as compared to an increase in existing capability. Finally, from an economic standpoint it was determined that both solutions presented about the same cost initially, that is to say up to and including *Mariner* Mars 1971 orbit phase. Thereafter the line costs alone heavily outweighed all others so that the change to 4800 bits/s seemed more logical.

Some consideration was given to upgrading the *Mariner* Mars 1971 prime support stations only while the uncertainty of guaranteed deliveries of the new data sets would necessitate a firm fall-back plan to the two 2400-bit channel configuration.

Finally in the event that conversion to single 4800-bit/s channel capability was selected, engineering work-around configurations would have to be developed so that continued support of *Pioneers VI* through *IX* and extended *Mariner* Mars 1969 could be provided at 2400 bits/s at the SFOF during the installation and checkout of the new equipment.

By October 1969, the decision was made to convert the GCF High-Speed System to 4800-bit/s data sets and to implement the associated hardware, training, installation, and documentation to accomplish all the required tasks.

4. Final Design

Figure 1 illustrates the functional block diagram that was the basis for the design. In general, this design provided increased capabilities to permit:

(1) Upgrade of the data rate from 2400 to 4800 bits/s by replacing 205B data sets with 203A data sets.

(2) Addition of block multiplexers (BMXR) at the SFOF Communications Terminal (SCT) for outbound block synchronous data transmission.

(3) The establishment of a new interface with the Mission Test Computer (MTC) for *Mariner* Mars 1971 mission-dependent data processing.

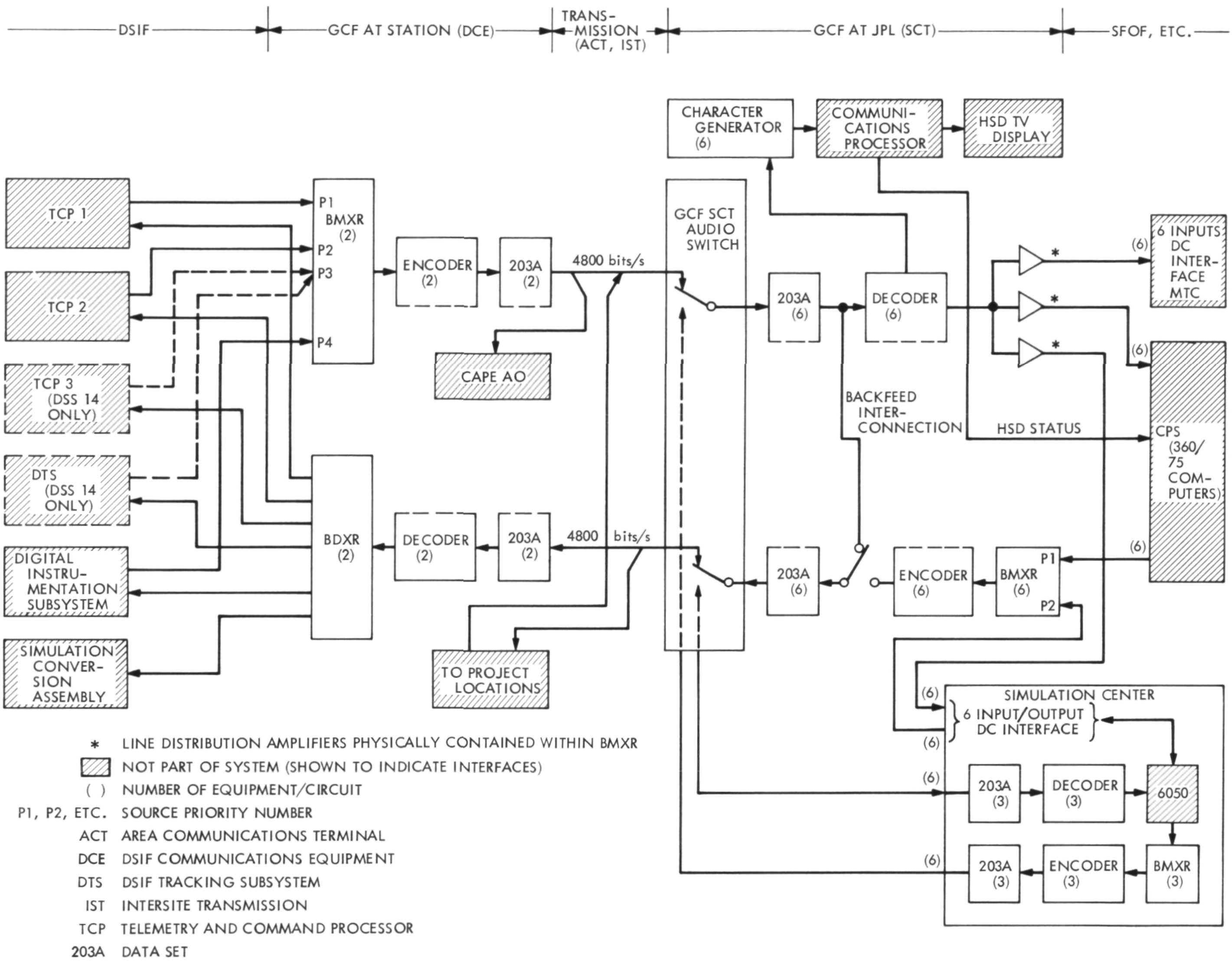

Fig. 1. High-Speed System functional block diagram

(4) The expansion of the interface with the DSN Simulation Center (SIMCEN) to meet increased Simulation System requirements for both outbound and inbound data transmissions.

(5) The addition of block demultiplexers (BDXR) on both prime and backup channels at the Compatibility Test Area (CTA 21) and at each DSIF station except DSS 13, to automatically distribute the received data blocks to the correct station computer.

Some additional modifications were also made to existing hardware to accommodate the higher data rate of 4800 bits/s. The operation of each hardware unit is described in detail in the following article (Evans, *Section C*) and in SPS 37-57, Vol. II, pp. 127–130.

The implementation schedule was keyed to the delivery of 203A data sets from the NASCOM since it was clearly necessary for extensive changes to be made to regeneration installations in the NASCOM Switching Centers at Madrid, Spain, at Canberra, Australia, and at Goddard Space Flight Center. The block demultiplexers were designed and procured, installation instructions were written so that station personnel could carry out the necessary changes, and operating procedures were prepared.

As a parallel effort, two test programs were developed to enable comprehensive checkout of the system to be made on a station-by-station basis. These programs provided a source of known high-speed data blocks, formatted in accordance with DSN-GCF standards and transmitted from an SDS 920 computer at the station or from the 360/75 computer at the SFOF. At the same time, the programs at each end analyzed the incoming data blocks, providing performance and error rate data from which the expected operational system performance could be determined.

5. Conclusions

In summary, the design of the GCF High-Speed System will provide the following capabilities:

(1) One full-period full-duplex 4800-bit/s high-speed circuit between each DSIF station and the SFOF with a limit of six simultaneous data streams at the SCT. Each circuit is shared by the DSN Command, Telemetry, Monitor and Operational Control Systems (with special provision for tracking data at DSS 14).

(2) Block synchronous transmission is provided by the use of block multiplexers which use filler blocks to insure continuous block generation.

(3) Error detection on an end-to-end basis at block rate is provided by using error detection encoders and decoders.

(4) Block demultiplexing is provided at each DSIF station to direct block formatted messages to any or all of the station computers by reading a discrete segment of each block header.

(5) Access to the system from the DSN Simulation Center is provided at both audio and digital levels in order that the SIMCEN may appear at the SCT as a simulated station or may multiplex outbound data with commands generated by the SFOF Central Processing System (CPS).

(6) All inbound traffic to the SFOF is fed to the MTC for *Mariner* Mars 1971 mission-dependent data processing.

Early tests indicate that the performance of the system is in accordance with specifications; however, the actual circuit error rates have not yet been established. By mid-November 1970, all prime *Mariner* Mars 1971 support stations will be ready to support DSN system tests. Within the following four months, the remaining DSIF stations will complete their installation and acceptance checkout testing to bring the total system into full operational use.

C. High-Speed Data Block Demultiplexer,

R. H. Evans

1. Introduction

The block demultiplexer (BDXR) will become an integrated part of the Deep Space Station Communications Equipment Subsystem (DCES) High-Speed Data Assembly (HSDA) for the 1971–1972 configuration of the High-Speed Data System (HSS).[1] The BDXR will be used in the DCES HSDA to interconnect the receiving circuit of one high-speed data (HSD) channel to a maximum of six on-station computers (OSCs). Preprogrammed instructions within the BDXR will permit transfer of only those data blocks addressed to one (or more) of the OSCs. Each OSC will receive only its own data and, consequently, will not have to accept and examine all received data blocks.

The existing DCES HSDA (1968 upgrade) provides for the indiscriminate transfer of *all* receive data, including filler blocks, from the one HSD channel to a maximum of four OSCs. This broadcasting of all received data has not been a problem as the DSN is only equipped to send data to the stations from the simulation subsystem. High-speed data have been sent to the stations only during simulations and GCF HSS error rate test exercises. The station telemetry and command processors (TCPs) were not equipped with a GCF receive data interface.

The new DSN reconfiguration presently being implemented (for multiple-mission telemetry, command, and

[1]For related articles, see McClure, *Section A*, and Nightingale, *Section B*, in this chapter.

simulation, and additional increased utilization of the GCF HSS for Operations Control and Monitor Systems data flow), coupled with the increased HSD rate (from 2.4 to 4.8 kbits/s), would impose prohibitively heavy machine loading for the receive data function of all OSCs, particularly the TCPs which will service the DSN Command and Telemetry Systems.

The BDXR examines the user dependent type (UDT) code bits 52 to 58 in each block header and routes only those blocks addressed to the specific OSC(s). Thus, the HSS hardware function of transferring data blocks from source to sink is precisely performed, and data sink machine loading is not burdened beyond that of processing data intended for its use.

The BDXR was developed basically for use in the DCES HSDA. Both the prime and backup HSD channels in each DCES HSDA will be equipped with the new BDXRs.

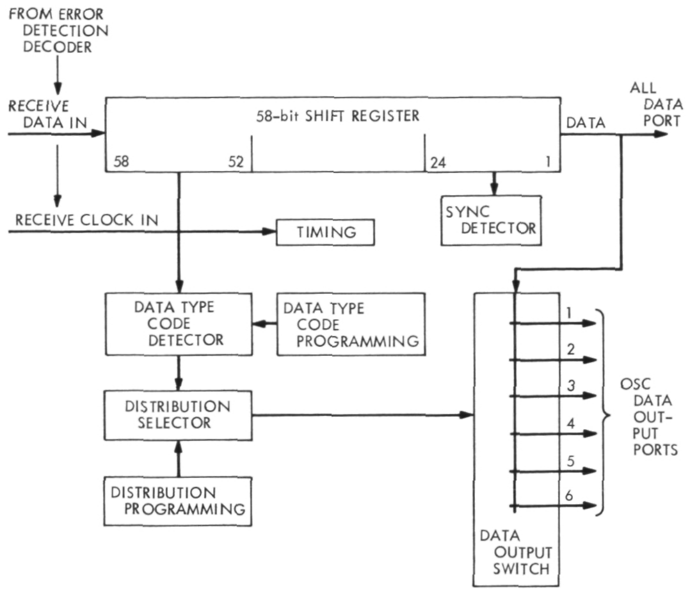

Fig. 1. Block demultiplexer functional block diagram

2. Functional Description

A block diagram depicting the primary functions of the BDXR is shown in Fig. 1. Each data block is delayed only long enough to determine its intended destination and to turn the data-block-detected (DBD) signal on one bit time before starting transfer of data.

Receive data enters the BDXR from the error detection decoder in addition to the serial clock receive (SCR) signal and the signal ground lead. The data enters the BDXR serially and is shifted through a 58-bit shift register. When the 24-bit sync word which begins each block has been shifted into register stages 1 through 24, the sync detector recognizes the sync word and starts the block timer. Simultaneously, the 7-bit UDT code is in register stages 52 to 58. The BDXR UDT code identification matrix and the OSC distribution matrix are preprogrammed with the desired distribution for the various data types expected. The data type code detector determines the user data type. The distribution program for the data type sets up the data output switch for transfer of the data block out to any subset or to all of six ports in a serial bit stream to interfaced OSCs. At the beginning of the next block, the sync detector looks for another sync word at the expected time.

The BDXR goes into lock mode (block synchronized timing) when an error-free sync word is detected. Lock is maintained as long as any one of the four consecutive 6-bit quarters of each succeeding block sync word is error-free.

The programmable UDT code matrix board is limited to 10 assigned UDT codes. One UDT code is used to identify filler blocks which when received illuminate a front panel lamp and provide a visual indication of proper BDXR function. The other nine UDT codes can be programmed as desired.

The BDXR also provides an *all data* port through which all data are transferred for testing or monitoring functions.

Additional significant monitor signals available are:

(1) No match signal indicating a block sync word was detected but the UDT code did not match a preprogrammed code.

(2) BDXR test/operate switch position indicator signal lead.

(3) BDXR block size switch position indicator signal lead.

(4) BDXR alarm indicator signal leads.

A BDXR patch and test panel is provided with each pair of BDXRs. All data control and signal leads for the six OSC ports and the all data port are made available via this panel for patch and test functions.

The BDXR is designed to operate up to a minimum of 50 kbits/s and after prototype testing was selected for use in the DCES Wideband Data Assemblies now being developed.

D. Wideband Digital Data System Terminal Configuration, *R. Hanselman*

1. Introduction

This article describes the specific configuration of each terminal used in the Deep Space Network Ground Communications Facility Wideband Digital Data System. This article is an amplification of a previous article reported by McClure in SPS 37-65, Vol. II, pp. 102–103.

The Deep Space Network (DSN) Ground Communications Facility (GCF) 50-kbit/s (synchronous) digital data terminals have been implemented for real-time transmission of the *Mariner* Mars 1971 spacecraft video information, during the spacecraft's planetary encounter, from the DSN Mars tracking station (DSS 14) at Goldstone, California, to the DSN Space Flight Operations Facility (SFOF) located in Pasadena. The transmission path utilizes existing microwave links between the two locations. In addition to the DSS 14/SFOF link, a second circuit connects the SFOF with the Compatibility Test Area (CTA 21) located approximately 2000 ft from the SFOF in JPL Building 125.

The 50-kbit system will also serve as a prototype for the DSN GCF Mark III configuration wherein 50-kbit data will be returned from the overseas 210-ft-diam antennas located in Australia and Spain.

2. Definition of the GCF Wideband System

The GCF Wideband System (WBS) includes all wideband equipment and facilities (both analog and digital), such as microwave, closed-circuit television, and telemetry between Deep Space Stations (DSSs). For this article only that equipment required for the 50-kbit data portion will be discussed.

3. Configuration of Wideband System (Data Portion)

a. DSS 14 to SFOF. The DSS 14 50-kbit terminal is equipped with two independent full-duplex (FDX) digital circuits. The second FDX circuit is a backup to the first. Both FDX circuits are connected full time to the SFOF via two microwave links. The first link is between DSS 14 and the Echo Site Area Communications Terminal (ACT), also located at Goldstone, approximately 12 miles distant. The second link is between the Echo ACT and the SFOF. The Goldstone/SFOF microwave link is actually a system of back-to-back links, five in all, and is a leased service from the Western Union Company.

Switching at DSS 14 allows any of three transmitting sources within the station to time-share, on a block basis, either of the two outbound circuits. This is accomplished by the use of block multiplexers (BMXRs). The BMXR output is in turn fed to an error detection encoder prior to conditioning by the outbound data set. Figure 1 shows the DSS 14 outbound configuration in functional form.

At the SFOF both microwave circuits from DSS 14 are converted back to digital form and are sensed with an error-detection decoder for a dynamic display of the circuit quality. Switching in the SFOF Communications Center allows either circuit to be fed to DSN computers and the Mission Test Computer (MTC) over redundant parallel circuits, isolated with digital line drivers. Figure 2 shows this arrangement in functional block form.

Demultiplexing of 1200-bit blocks takes place in the computers in the SFOF.

b. SFOF to DSS 14. Other than test signals, the SFOF Communications Terminal does not have the capability to transmit wideband data to DSS 14.

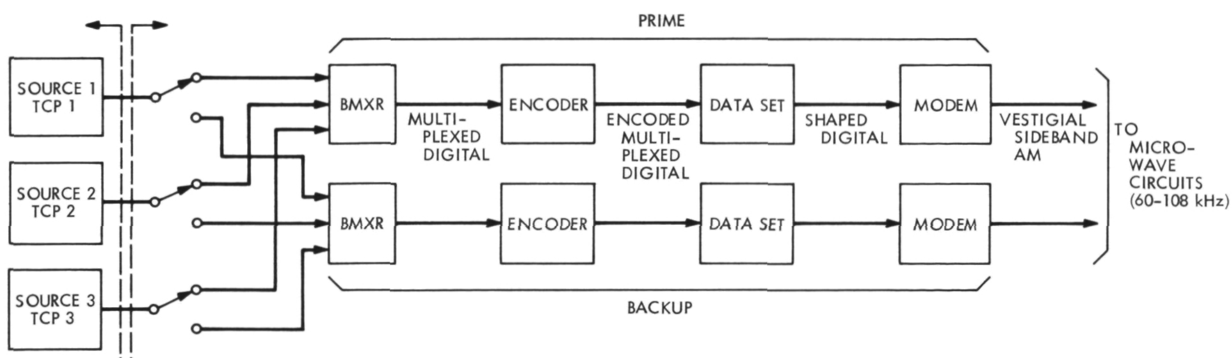

Fig. 1. DSS 14 outbound functional block diagram

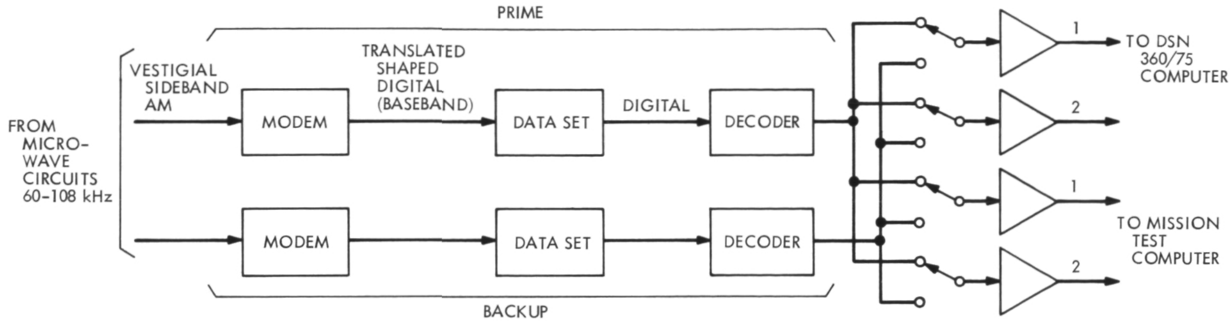

Fig. 2. SFOF Communications Terminal receiving from DSS 14 functional block diagram

The DSN Simulation Center (SIMCEN), located in the SFOF, is the source of outbound data to DSS 14 and passes through the SFOF Communications Terminal as a shaped digital signal (baseband). In the SFOF Communications Terminal the baseband signal is patched to either of two send modems connected to two outbound microwave circuits.

The Simulation Center Wideband Terminal consists of identical equipment as the *prime* group of transmitting equipment at DSS 14, with the exception of the modem (translator). This equipment essentially consists of a BMXR, an encoder, and a data set. Although the Simulation Center has only one source of outbound data (an EMR 6050 computer), a BMXR is used in this terminal to produce *filler* data to the outbound circuit when the SIMCEN computer is not transmitting. Filler data, in GCF 1200-bit block form, is required to keep the DSS 14 50-kbit receiving equipment in sync, even though simulation data are not being transmitted.

At DSS 14, the destination for the simulation data is the Simulation Conversion Assembly (SCA) computer. A block demultiplexer (BDXR) is used to feed this computer. The primary function of the BDXR in this application is to prevent filler data, generated by the Simulation Center Block Multiplexer, from entering the SCA computer. The receiving equipment at DSS 14 consists of redundant modems, data sets, decoders, and a single BDXR, switchable to either the prime or backup decoders. Figure 3 shows this arrangement in functional block form.

c. CTA 21 to SFOF. The CTA 21 Wideband Terminal, consisting of a single full-duplex 50-kbit circuit and equipment group, transmits to the SFOF 360/75 and MTC computers and receives from the Simulation Center EMR 6050 computer via the SFOF Communications Center. Additional capability in the SFOF Communications Center enables CTA 21 to transmit to DSS 14 and vice versa. Figure 4 shows this arrangement in functional block form.

d. SFOF to CTA 21. The destination for 50-kbit data to CTA 21 is the SCA computer. A similar arrangement to that of DSS 14 is provided. The modem is not required between the SFOF Simulation Center and CTA 21. The backup circuit and equipment is not required at CTA 21. Thus, simulation data (or filler data) is generated at the SFOF Simulation Center and is transmitted to CTA 21,

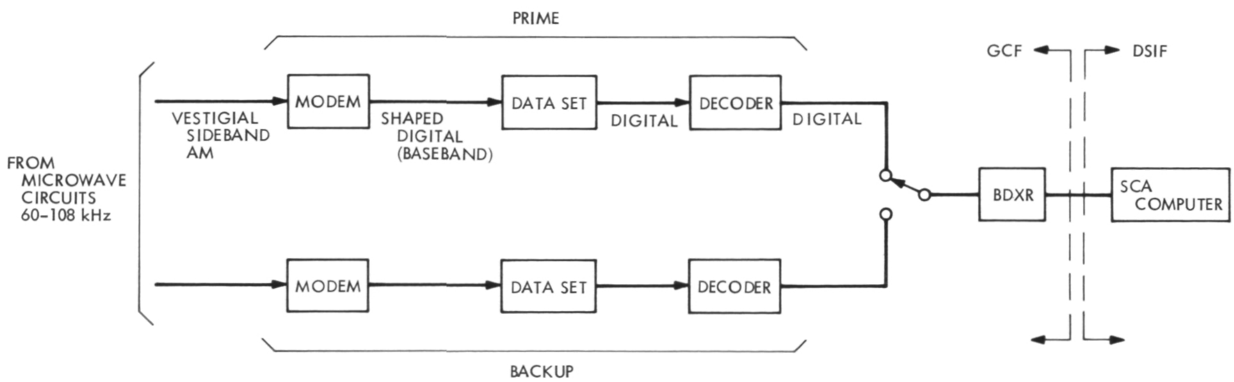

Fig. 3. DSS 14 receiving functional block diagram

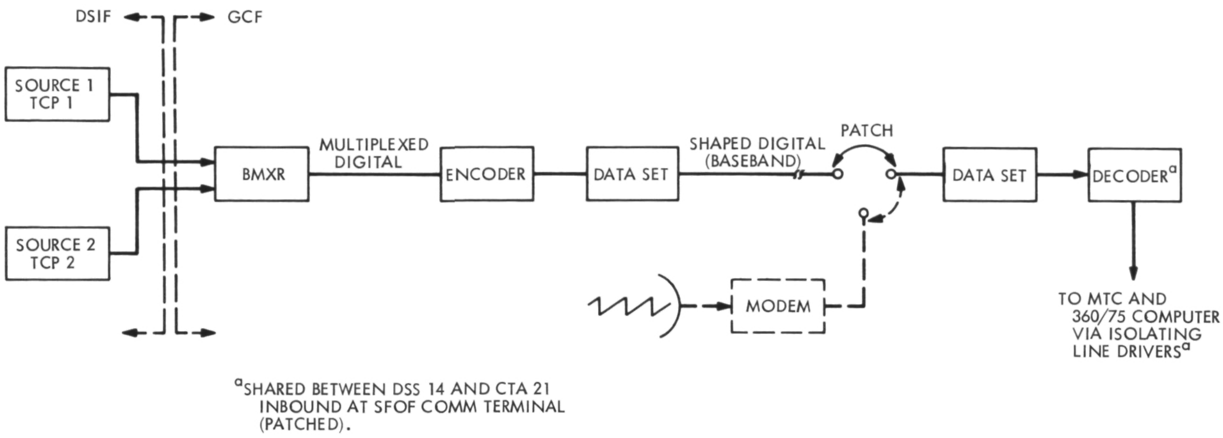

Fig. 4. CTA 21 to SFOF functional block diagram

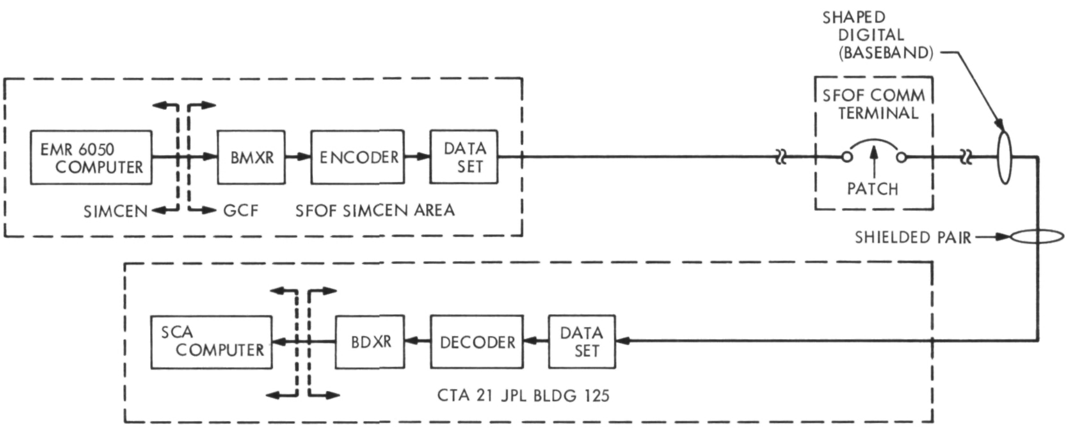

Fig. 5. SFOF to CTA 21 functional block diagram

as a baseband signal, via a patch in the SFOF Communications Center. The receiving equipment at CTA 21 consists of a data set, decoder, and BDXR functionally arranged as shown in Fig. 5.

e. Goldstone Echo site Area Communications Terminal. The Goldstone Area Communications Terminal (ACT) is located at the Goldstone Echo site and, among other functions, serves as a hub for all intra-site microwave links. It is at this station that the Western Union SFOF/Goldstone microwave terminal is located, as well as the GCF microwave link to the DSS 14 210-ft antenna. This station serves as a regenerative repeater (REGEN) point for both full-duplex circuits between DSS 14 and the SFOF. Error detection encoders and decoders are not employed in this arrangement. The REGEN assembly consists of back-to-back modem/data set groups interconnected at their digital interface to form a 50-kbit regenerated signal in both directions for both the prime and backup circuits. Figure 6 shows the ACT 50-kbit REGEN in functional form.

4. Equipment Used for the Wideband System (Data Portion)

a. Encoder, decoder, BMXR. The error detection encoders, decoders, and BMXRs utilized in the Wideband System are identical to equipment previously developed for and currently in use in the GCF High-Speed System. This equipment is manufactured by Monitor Displays of Fort Washington, Pa. Identical encoders and decoders are also used throughout the NASCOM High-Speed System.

b. Block demultiplexer. The BDXR is JPL-designed equipment and was designed for the GCF High-Speed System. It is used in the Wideband System without modification.

c. Data set and modem. The *data set* is used to convert the 50-kbit digital signal to a form suitable for transmission over a standard unloaded twisted pair. The signal transmitted to the line is a polar digital signal with

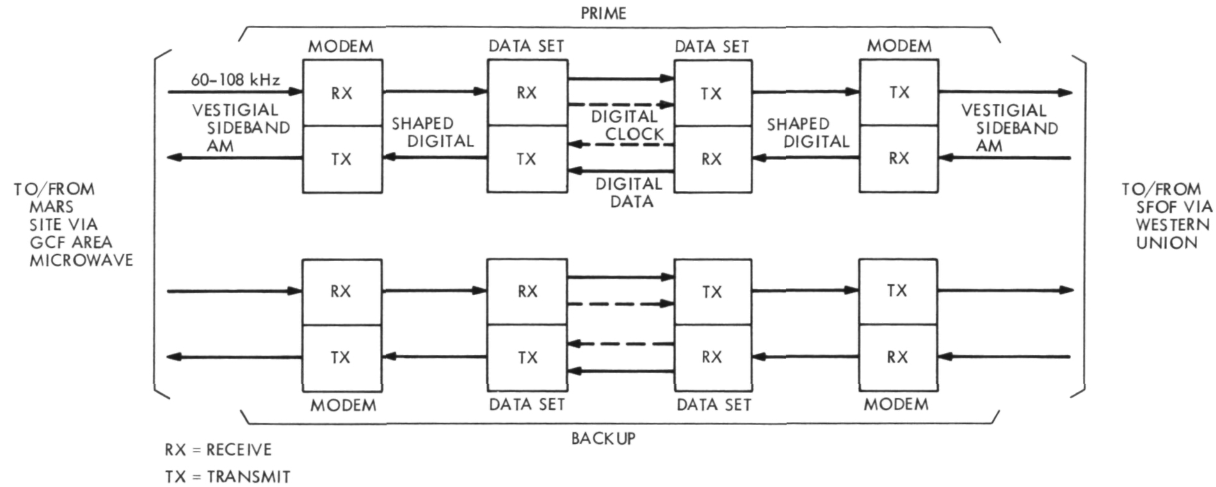

Fig. 6. Area Communications Terminal 50-kbit REGEN functional block diagram

the dc component removed. Through filtering in the data set, the line signal is limited to occupy a 2- to 44-kHz spectrum. The *modem* (modulator–demodulator) is used to convert the signal produced by the data set (baseband) to a vestigial sideband (VSB) AM signal that occupies the 60- to 108-kHz portion of the spectrum. It is this VSB signal that is placed on a microwave system via a voice multiplex at the "group" level, replacing 12 standard 4-kHz voice circuits.

Both the data set (TDM 401) and the modem (TDM 420) are a standard product of the General Electric Co., modified for cabinet-mount by JPL.

d. Wideband Conversion and Switching Assembly. The encoder, decoder, BMXR, and BDXR, mentioned in *a* and *b*, above, operate at the digital interface at a polar 6-Vdc level per EIA specification RS-232C. The data set and user digital interface operate in a neutral "current mode" over coaxial transmission lines. The Wideband Conversion and Switching Assembly (WCSA) was designed by JPL to convert between the two logic levels, "current" and RS-232. A secondary function of the WCSA provides for switching between the two 50-kbit circuits (at the DSSs) and switchable parallel drivers to the SFOF computers (in the SFOF Communications Terminal). The WSCAs were built under contract by Raytheon Computer in Santa Ana, Calif., and utilize Raytheon's standard logic card line.

5. Western Union Microwave Modifications

For the data portion of the 1971–1972 Wideband System, minor modifications were made by Western Union to their General Electric TCS-600 voice multiplex. The modifications included the relocation of 12 channels of 4-kHz voice circuits from group 2 to group 5 and the deletion of a 96-kHz analog circuit which occupied both groups 4 and 5. Thus, 2 new group-width (48 kHz) FDX circuits were made available in the basic supergroup (240 kHz) for the wideband VSB signals. The current allocation of the 50-kbit VSB signals is group 4 (prime) and group 2 (backup). No conditioning of the group circuits has yet been provided by Western Union.

6. Reliability

It is anticipated that the DSS 14/SFOF 50-kbit system will operate with a long term block error rate of 3×10^{-5} or better.

E. Communications Control Group Assembly Voice Data Switching Equipment, *D. W. Passell*

1. Introduction

The transmission, monitoring, control, and distribution of voice and/or data audio frequencies (300–3000 Hz) are accomplished within the Deep Space Network (DSN) through several interconnected Ground Communications Facility (GCF) subsystems and assemblies. This article describes the purpose, interfaces, development and status, and configuration of the Communications Control Group Assembly (CCGA) voice data switching equipment. The CCGA is part of the GCF Deep Space Station Communications Equipment Subsystem (DCES) and functions as a component of the GCF Voice, High-Speed, and Teletype (Goldstone only) Systems as described by McClure in *Section A* of this chapter.

2. Purpose of CCGA

Coordination of DSN operations between Deep Space Stations (DSSs) and the Space Flight Operations Facility (SFOF) requires standardized transmission interfaces for the distribution of voice messages. There is also a requirement to receive and transmit audio frequencies originating in High-Speed Data Assembly (HSDA) equipment with minimum noise and distortion. At the Goldstone DSSs, teletype data is placed on audio frequency carriers and transmitted from the DSS to the Area Communications Terminal (ACT) and thence to the SFOF. There is also provision for transmission in the reverse direction.

The CCGA must terminate receive circuits coming into the DSS from landlines or microwave equipment, amplify the signal on these circuits to a standard level, and then provide for multiple distribution to other GCF assemblies within the DSS. At the same time signal levels must be adjusted to be compatible with other GCF assemblies. Additional data originating within the DSS must be sent to the CCGA, the signal level amplified to a standard level, and then transmitted out of the DSS at a level compatible with external circuits.

The CCGA also provides an operator with a means to locally monitor and access the circuits for preoperational checkout. Other than preoperational checkout, no operator intervention is required unless there is a circuit failure. Quick emergency substitution of failed circuits is provided by line patching. For standardization, CCGA units at all sites are operationally identical.

3. Interface With GCF Assemblies

Figure 1 shows the voice data path from the CCGA to other GCF assemblies at the DSS. Figure 2 shows the voice data path from the CCGA to the SFOF.

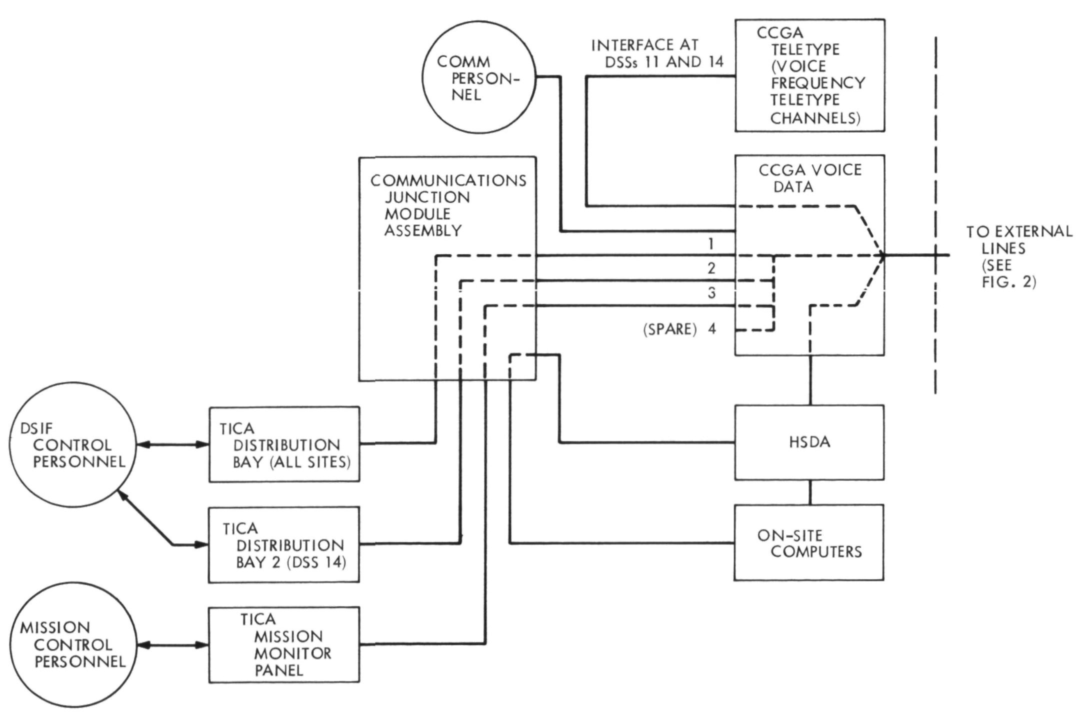

Fig. 1. GCF DCES voice data flow

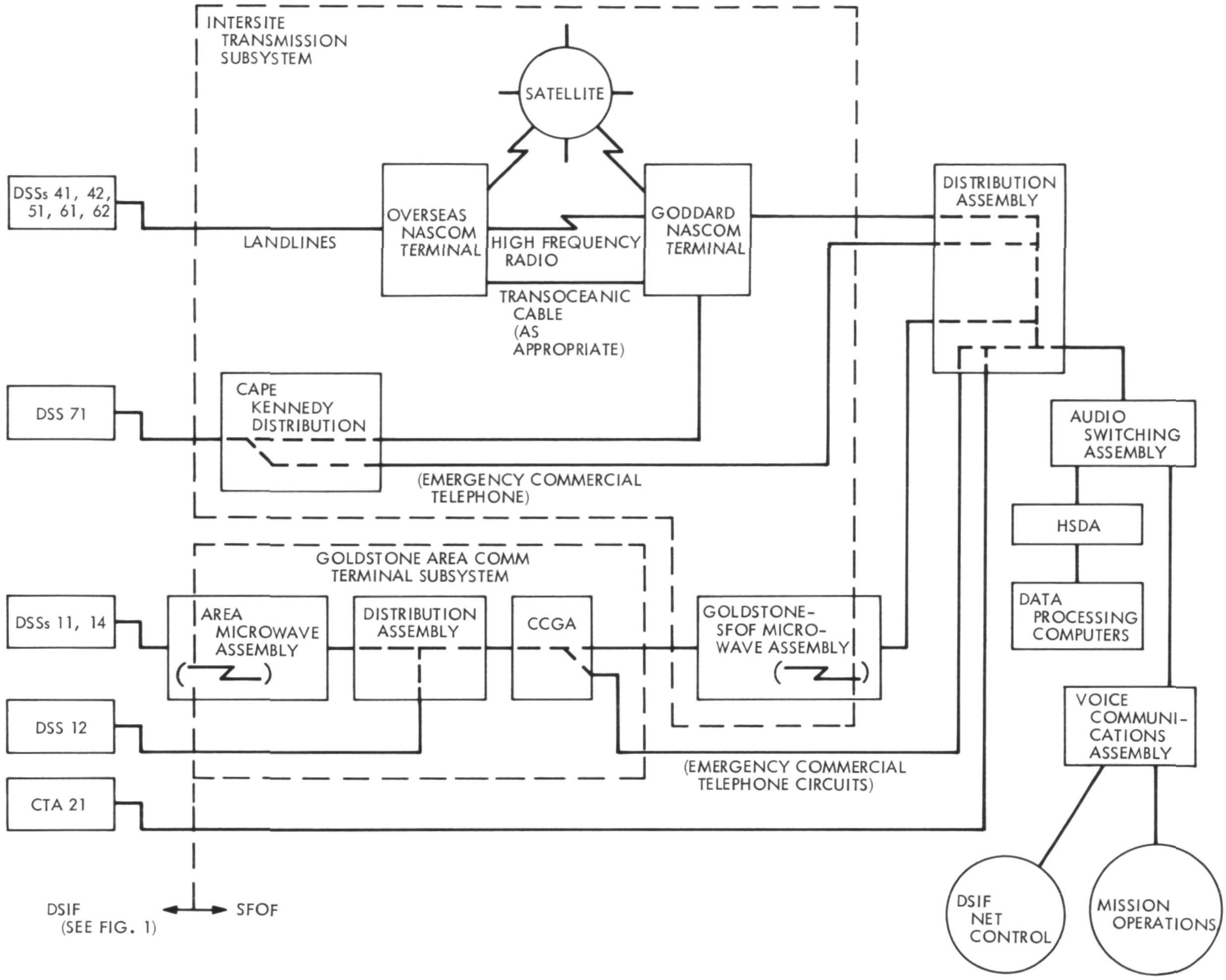

Fig. 2. Voice data flow from GCF DCES to SFOF Communications Terminal

At overseas sites and DSS 71 (Cape Kennedy), the CCGA interfaces with landlines which pass through NASCOM facilities to the SFOF. At Goldstone the CCGA interfaces with Area Microwave Assembly equipment and data is passed to the SFOF via the Goldstone–SFOF Microwave Assembly. The CCGA in the Compatibility Test Area (CTA 21) interfaces with lines which go directly to the SFOF.

4. Development and Status of the CCGA

Along with other systems and assemblies of the Ground Communications Facility, the Communications Control Group Assembly has undergone evolutionary development. Development is evolutionary because service must be maintained for current operations simultaneously with upgrading the overall facility to meet ever increasing requirements of data volume and data rates. Originally the CCGA was designed in 1966. Prior to that time its functions were performed by a variety of equipments meeting local communications requirements. Multimission commitments of the DSN have dictated standardization of the communications configurations at all of the tracking stations. This standardization was achieved at all 10 DSSs in 1969 when the CCGA equipment became operational. Even so, redesign of the assembly and upgrading of hardware components have been accomplished by JPL Ground Communications Facility development engineering.

This redesign has taken a modular approach so that upgrading would not interfere with current service. Completely connectorized hardware has replaced the solder terminal board approach of the original design. Circuit distribution capabilities have been expanded.

Using late developments in solid-state amplifiers, a four-wire, six-way bridge was designed. This bridge is a plug-in module occupying half the space required by commercial units which provides zero loss of signal while eliminating many external amplifiers, high isolation between input and output of the same circuit, and high stability.

5. Operational Features

The CCGA has the capability to terminate, amplify, and distribute external four-wire voice data lines via the six-way bridge to up to four on-site Tactical Intercommunications Assembly (TICA) equipments (Fig. 1). All lines may be monitored simultaneously at the CCGA. A telephone handset or headset may be connected to any line for setup and troubleshooting by communications operators. A dial telephone connection is provided which either permits the operator to use handset or headset over a commercial telephone circuit or permits the telephone circuit to be substituted for one of the four-wire lines in case of emergency.

Signalling transmitters and receivers are provided in the CCGA. The receivers respond to a modulated tone, sent from the distant NASCOM terminal, to operate a bell and flashing lamp. The transmitter sends a modulated tone to the NASCOM terminal.

Two additional external four-wire lines may be connected to the CCGA. These appear on jacks with no further distribution except at DSSs 11 and 14. At these sites a cable between the voice data CCGA and the teletype (TTY) CCGA continues these lines into tone keyer and converter shelves where the conversion of teletype signals to and from audio carriers takes place. Provision on a jack panel is made for 10 four-wire tie lines to the High-Speed Data Assembly (HSDA) audio bay. This provides flexibility in connecting HSDA data sets to external lines at the CCGA. The four-wire six-way bridges are bypassed on the line used for high-speed data. Blown fuse alarms, power supply status monitoring, and 24 Vdc required by some types of TICA equipment are provided by the CCGA TTY equipment. In all other respects the voice data equipment operates independently.

6. Physical Details

The CCGA voice data equipment consists of assemblies installed in a standard DSIF equipment rack (82 in. high $\times$ 24 in. wide $\times$ 28 in. deep with 19-in. panel width), and is the third bay of the complete CCGA (bays 1 and 2 are TTY). Each assembly contains plug-in modules. Assemblies have connectors and may be individually removed or added to change the capability of the equipment up to eight external lines, excluding audio TTY. Interassembly connections are accomplished through cables to a junction box.

7. Conclusion

As designed the Communications Control Group Assembly voice data switching equipment provides a flexible, serviceable, and reliable means for controlling, monitoring, transmitting, and distributing voice and/or data in the audio frequency band (300–3000 Hz).

IX. DSIF Development

DEVELOPMENT AND IMPLEMENTATION

A. DSS Upgrades for *Mariner Mars 1971*,

T. L. Burns

1. Introduction

During mid-July 1970, and through December 1970, the DSSs committed to the *Mariner* Mars 1971 Project (DSSs 12, 14, 41, 51, 61, and 71) have undergone or are scheduled to undergo reconfiguration in preparation for the *Mariner* Mars 1971 Project. At present, DSSs 12, 51, and 71 have successfully completed reconfiguration and have returned to normal tracking; DSSs 41 and 61 are completing system tests and will return to the normal tracking mode in November. DSS 14 is scheduled for reconfiguration during November and December, but due to heavy tracking commitments will not be "off-line" during this period. All implementations will be accomplished on a noninterference basis. The reconfiguration consists of block upgrades of subsystems and rearrangement of the control and communications rooms to provide space for new cabinets of equipment to improve operator and maintenance efficiency, and to perform major maintenance of older equipments. The work performed on each subsystem is described in this article.

2. Receiver–Exciter

The receiver–exciter (RCV) was updated for *Mariner* Mars 1971 with modifications to existing subcarrier demodulator assemblies (SDAs) and the addition of SDA cabinets. The basic RCV was modified with multi-mission command updates and test transmitters were added.

3. Digital Instrumentation Subsystem

The digital instrumentation subsystem (DIS) was expanded to accommodate high-speed data (HSD) equipment and CRT display in the station monitor consoles.

4. Antenna Mechanical

The antenna mechanical update was accomplished outside of the reconfiguration period. The surveillance TV installation was scheduled during this period; however, due to vendor problems and test installation and verification at Goldstone DSCC, delays have been experienced. Therefore, implementations have been rescheduled at the various DSSs to be performed on a non-interference basis.

5. Servo-Control-Antenna

The four servo-control antenna "low-boy" equipment cabinets were combined into one full-height cabinet.

6. Station Monitor Console

The station monitor console (SMC) was updated to include the CRT display and keyboard. This was installed in the SMC for use by the station director to permit him to address the computer, call up the specific formats, and display parameters of interest.

7. Telemetry Command Data Handling

The telemetry command data handling was updated to include the telemetry command processor modification for *Mariner* Mars 1971, and to add symbol synchronizer assemblies, block decoder assemblies, command modulator assemblies, and simulation conversion assemblies, which provide the multi-mission telemetry and multi-mission command increased capability.

8. Communications

The communications junction module was updated in conjunction with the HSD assembly.

9. Control Room Arrangements

The control rooms at each DSS were reconfigured to group equipment functions and types were put together as much as possible, which permits greater operator and maintenance efficiency and provides additional floor space for the new equipments.

10. Testing

At the completion of reconfiguration, each DSS has been subjected to a series of configuration verification and system performance tests, and has tracked a *Pioneer* spacecraft to verify proper functioning of all equipments.

B. Block IV Receiver–Exciter Development,

H. Donnelly, A. C. Shallbetter, and R. E. Weller

1. Introduction

The Block IV receiver–exciter is being developed to provide tracking capabilities required for 1973 and beyond. A prototype unit at DSS 14 will support the S- and X-band experiments of the *Mariner* Venus–Mercury 1973 probe on an R&D basis. For the *Viking* Orbiter 1975 and subsequent projects, it is now planned to provide a limited number of operational units at the 210-ft-diam antenna DSS subnet, DSS 71, and CTA 21.

The increased capabilities of the Block IV over the Block III subsystem are as follows:

(1) Improved single-pass phase and modulation delay stability.

(2) Increased receiver sensitivity.

(3) Increased modulation bandwidth.

(4) Programmable oscillators for exciter and receiver.

(5) S- and X-band operation.

(6) Automatic control capability.

(7) More efficient packaging.

(8) Increased reliability.

To incorporate all of these improvements into the Block III subsystem would have required a major redesign effort; therefore, developing the Block IV subsystem appeared to be the more practical approach.

2. Description

a. General. The Block IV receiver–exciter can operate coherently in both the S and X frequency bands (Fig. 1) in the following modes:

Mode	Transmit	Receive	Coherent ratio
1	S-band	S-band	240/221
2	S-band	S-band and X-band	240/221 880/221
3	X-band	X-band	27/23

No project requirement exists at the present time for mode 3 configuration. The subsystem is being designed so that the mode 3 capability can be added.

Both the S- and X-band receivers have a 100 MHz operating range capability; however, the full band is not always utilized. When operating in mode 2, it is necessary to have two receivers associated with each exciter: one at S-band and one at X-band. Likewise, for full flexibility, each exciter requires two doppler extractors and three translators so that any one of the three modes of operation can be selected. To provide this flexibility, the Block IV receiver–exciter subsystem is being packaged into two separate assemblies: (1) an exciter assembly containing the exciter, doppler extractors, and

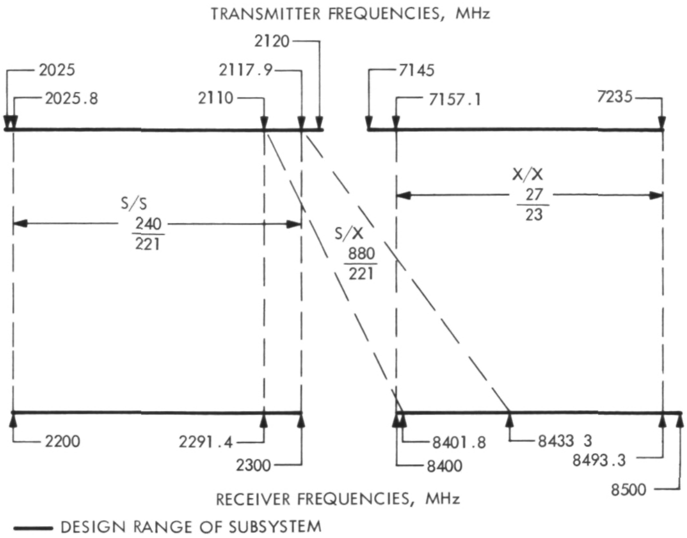

Fig. 1. Block IV operating frequencies

translators and (2) a receiver assembly. A switch assembly will select the combination of receivers and exciters necessary for the mode of operation.

b. Receiver. The Block IV receiver is a quadruple conversion superheterodyne phase-locked receiver capable of either S- or X-band operation. Figure 2 shows a basic block diagram of the receiver.

The incoming signal is converted to a first intermediate frequency (IF) of 325 MHz, which makes an IF output with greater than 100 MHz instantaneous bandwidth available to accommodate any future telemetry or radio science experiment requirements. The 325 MHz first IF is then mixed down to a second IF of 55 MHz, where a non-gain-controlled output is made available for noise temperature measurements or radio science experiments. The signal is then coherently automatic gain controlled (AGCd) to provide three constant signal level outputs at 55 MHz. These outputs exhibit a greater than 30 MHz instantaneous bandwidth to accommodate high-rate telemetry as well as future X-band ranging. The 55 MHz IF frequency was chosen over the 50 MHz IF of the Block III subsystem to avoid harmonically related IFs (i.e., 50 MHz first IF and 10 MHz second IF as in the Block III subsystem). The 55 MHz IF is mixed with a 45 MHz reference to generate a third IF frequency of 10 MHz. Eight outputs, compatible with the present Block IIIC specifications but with greater bandwidth and linearity, are available for telemetry and ranging. A fourth IF of 100 kHz is obtained by mixing the 10 MHz signal with a 10.1 MHz reference. This low-frequency last IF allows narrower predetection filters to be obtained more easily and with greater stability.

The local oscillator (LO) multiplier chains have been designed to utilize the greatest amount of S-band hardware to mechanize the X-band. In addition, the multiplier factors have been chosen to minimize mixer intermodulation frequencies in the IF passbands. Except for the first LO, all reference frequencies are coherently generated from the DSS frequency standard for maximum subsystem stability. In addition, broadband untuned IF amplifiers and multipliers have been used to improve phase and group delay stability.

The Block IV subsystem employs programmed oscillators in the exciter and receiver to provide automatic control of both transmitted and received frequencies. This allows programming of the doppler to reduce tracking loop stress and provides frequency agility. The details of the operation and mechanization of the programmed oscillators are discussed in *Section D* of this chapter.

Another unique feature of the Block IV subsystem is an open-loop automatic acquisition technique that utilizes the programmed oscillator for frequency sweeping and a zerobeat detector to indicate signal acquisition. This technique is described in SPS 37-65, Vol. II, pp. 107–116.

The phase-locked loop has two modes of operation: wide-band and narrow-band. In the wide-band mode, the voltage-controlled oscillator (VCO) range is the same as the present Block III subsystem and the loop has approximately the same characteristics. In the narrow-band mode, a more stable narrow-range VCO is employed, reducing the tracking range by a factor of 10. In this mode, it is necessary to program the oscillator if a large doppler shift occurs during the pass. Some of the major receiver parameters are listed in Table 1.

As noted from Table 1, loop bandwidths have been selected on a 5-dB incremental basis. The values selected are being reviewed to assure that the receiver provides adequate performance for all known project requirements.

c. Exciter. The exciter assembly contains the exciter, doppler extractors, and translators. Figure 3 shows a simplified functional block diagram of the exciter assembly. The modules and associated microwave hardware enclosed by the dashed line are temperature-stabilized to obtain the desired doppler stability.

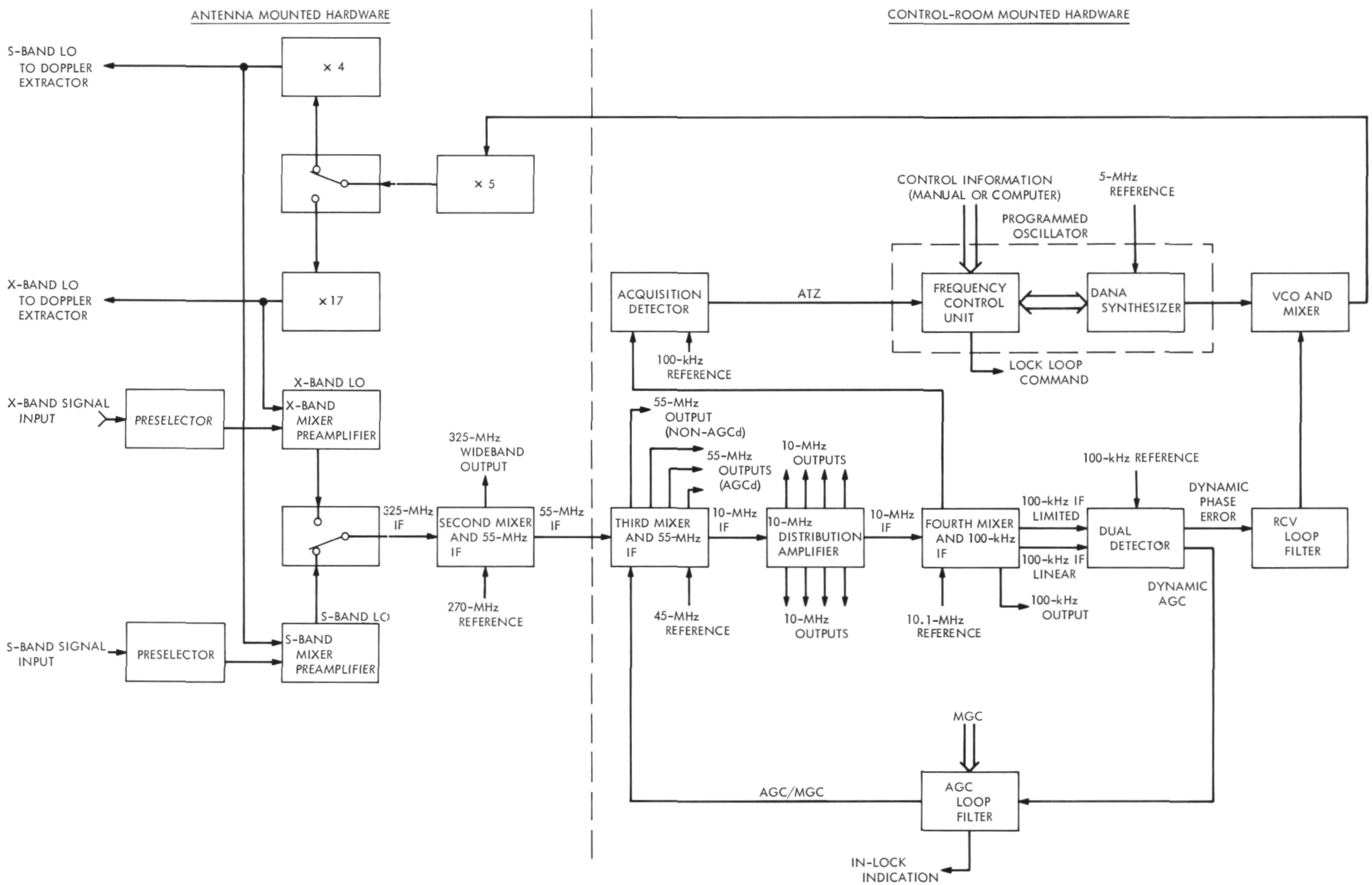

Fig. 2. Basic receiver block diagram

Table 1. Receiver characteristics

Characteristic	Specified limits: S-band	Specified limits: X-band
Input frequency range	2200–2300 MHz	8400–8500 MHz
Input impedance	50 Ω nominal	50 Ω nominal
Noise figure	6.5 dB maximum at input of preselector	11 dB maximum at input of preselector

Bandwidth (BW) parameters: Mode	BW position	S-band: Predetector BW, kHz	S-band: Noise BW — $2\beta_{LO}$, Hz	X-band: Predetector BW, kHz	X-band: Noise BW — $2\beta_{LO}$, Hz
Narrow	1	0.200	1	N/A	N/A
	2	0.200	3	0.2	3
	3	2.0	10	2.0	10
	4	2.0	30	2.0	30
Wide	1	2.0	10	N/A	N/A
	2	2.0	30	2.0	30
	3	20.0	100	20.0	100
	4	20.0	300	20.0	300

Receiver sensitivity (threshold level = 1 rad rms noise error at phase-locked loop output): Mode	BW position	Noise BW — $2\beta_{LO}$, Hz ($\pm 10\%$)	Nominal signal suppression factor α_0	Minimum threshold sensitivity, dBmW: S-band	Minimum threshold sensitivity, dBmW: X-band
Narrow	1	1	0.0625	−167.3	N/A
	2	3	0.1079	−162.5	−158.0
	3	10	0.0625	−157.3	−152.8
	4	30	0.1079	−152.5	−148.0
Wide	1	10	0.0625	−157.3	N/A
	2	30	0.1079	−152.5	−148.0
	3	100	0.0625	−147.3	−143.8
	4	300	0.1079	−142.5	−138.0

Table 1 (contd)

Characteristic	Specified limits			
Carrier tracking loop	S-band		X-band	
Phase detector gain (K_d)	87 mV/deg		87 mV/deg	
VCO sensitivity (K_{VCO})				
Narrow mode	192 Hz/V		192 Hz/V	
Wide mode	1920 Hz/V		1920 Hz/V	
Multiplication factors (K_m)	20		85	
Loop filter gain (g)	4		4	
Threshold loop gain (G_o) $G_o = K_d K_{VCO} K_m g \alpha_0$ s^{-1}	Nominal threshold loop gain		Nominal threshold loop gain	
Mode / Loop BW, Hz				
Narrow 1	3.01×10^4		N/A	
3	5.19×10^4		2.21×10^5	
10	3.01×10^4		1.28×10^5	
30	5.13×10^4		2.21×10^5	
Wide 10	3.01×10^5		N/A	
30	5.19×10^5		2.21×10^6	
100	3.01×10^5		1.28×10^6	
300	5.19×10^5		2.21×10^6	
Automatic gain control (AGC) loop (receiver employs a coherent type AGC)				
Receiver IF gain	15 dB/V nominal			
Coherent amplitude detector gain	0.018 V/dB nominal			
Loop filter dc gain	−500 nominal			
Loop gain	135 nominal			
Receiver signal level dynamic control angle				
Narrow mode	−80 to −167 dBmW			
Wide mode	−80 to −157 dBmW			
AGC loop filter time constant (τ) AGC bandwidth	τ, sec		Nominal frequency response (−3 dB) at −100 dBmW (strong signal), Hz	
Narrow	400		0.0138	
Medium	40		0.138	
Wide	4		1.38	
IF signal outputs Frequency, MHz	Bandwidth (at −1 dB), MHz	Nominal level	Number of outputs	Nominal impedance, Ω
325	100	35 dB gain above input (non-AGCd)	1	50
55	30	−65 dBmW	3	50
55	60	20 dB gain above input (non-AGCd)	1	50
10	6	−55 dBmW	7	50

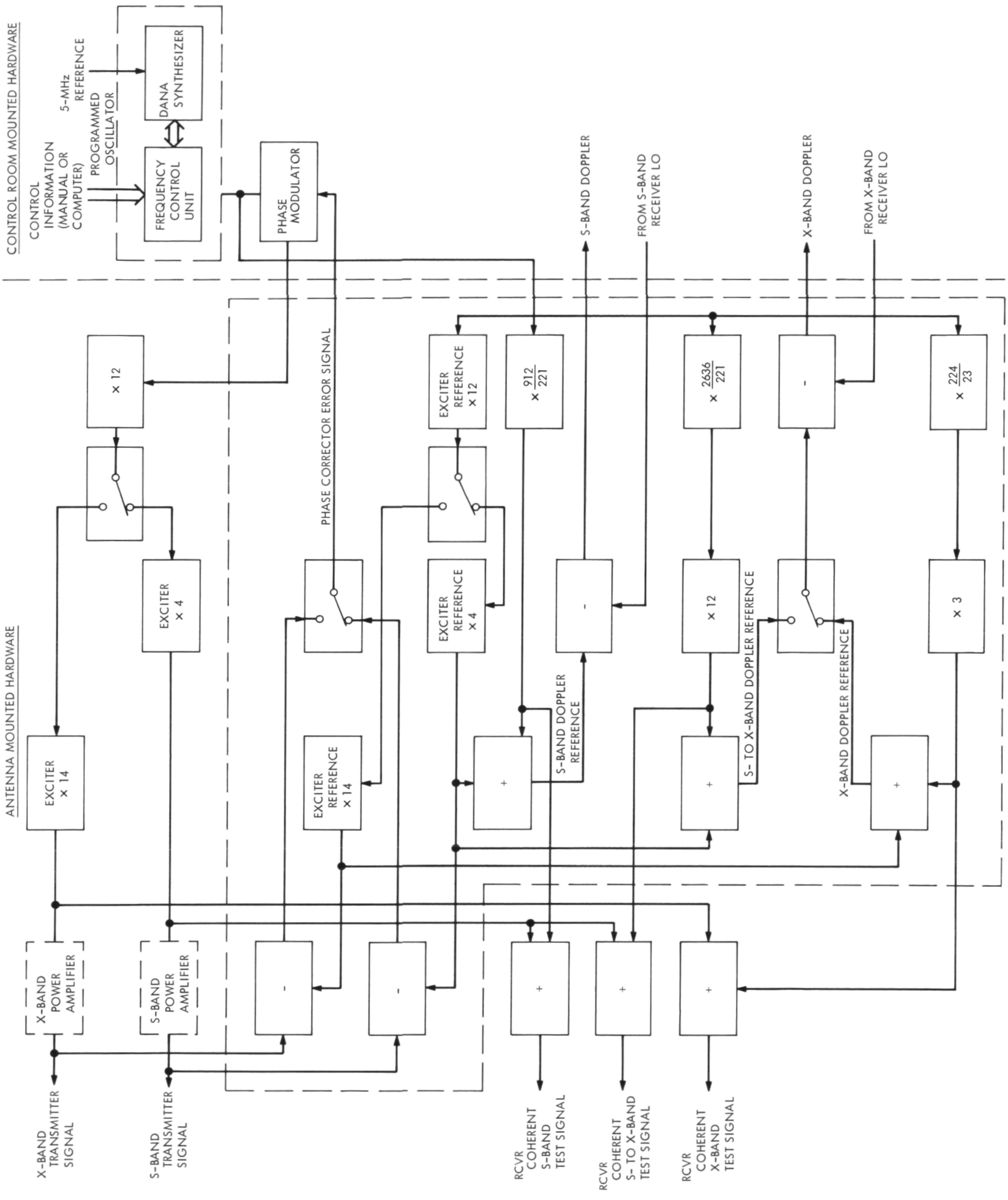

Fig. 3. Exciter assembly simplified functional block diagram

One outstanding feature of the exciter and doppler extractor is the inclusion of an exciter reference multiplier chain. This chain is a low-level ultra-stable multiplier that provides a stable reference to which the exciter or the klystron amplifier output may be phase locked to provide maximum long-term phase stability of the transmitted signal. In addition, the exciter reference multiplier, when mixed with the output of the appropriate frequency shifter, provides the translated exciter frequency as a reference to the doppler extractor. Mixing this signal with the receiver LO yields a representation of the true S- or X-band doppler for further processing. This technique of extracting the doppler at S- and X-band allows the carrier tracking loop to track out any drift in the receiver LO multiplier chain so that these drifts do not appear in the doppler output. This feature is very important in maintaining long-term doppler stability. By inspection of Fig. 3, it can be seen that with the exciter transmitting at S-band, doppler can be extracted from one receiver operating at S-band and another receiver operating at X-band in the S/X mode. When the exciter is transmitting at X-band, doppler is extracted only at X-band from one receiver.

The detector used to provide an error signal for the transmitter phase control can also serve as a modulation confirmation detector. The exciter or klystron amplifier output is also combined with the three frequency shifters to provide a test signal for the receiver. The main characteristics of the exciter assembly are shown in Table 2. The phase stability, both long- and short-term, and the modulation delay stability (Table 2) represent the total for the combined exciter and receiver assemblies.

d. Automatic control. The Block IV receiver–exciter is an automated subsystem wherein all tracking functions (i.e., receiver–exciter frequencies, acquisition, configuration, etc.) may be controlled by a digital computer. If desired, control may be accomplished manually by actuating a manual override switch on the control console.

e. Packaging.

General. The following paragraphs describe the packaging of the engineering model. Some compromises were made in the fabrication of the engineering model and the prototype will not necessarily be identical to it. These differences occur primarily in two areas: (1) combining the receiver–exciter into one assembly and (2) mounting of all equipment into one cabinet for the control room and one for the antenna. The basic design, however, will be used in the fabrication of the prototype.

As stated before, the Block IV receiver–exciter engineering model is contained in two standard DSIF equipment cabinets (one located in the control room and the other located on the antenna structure). The control room cabinet contains the low-frequency portions of the receiver, exciter, programmed oscillators, and the necessary equipment and interfaces to control the receiver–exciter. The antenna-mounted cabinet contains the exciter and reference exciter multipliers, modulation confirmation detectors, receiver local-oscillator multipliers, receiver first and second mixers, doppler extractor, and the coherent receiver test-signal translators.

Control room cabinet. The equipment contained in the control room cabinet is shown in Fig. 4. The receiver

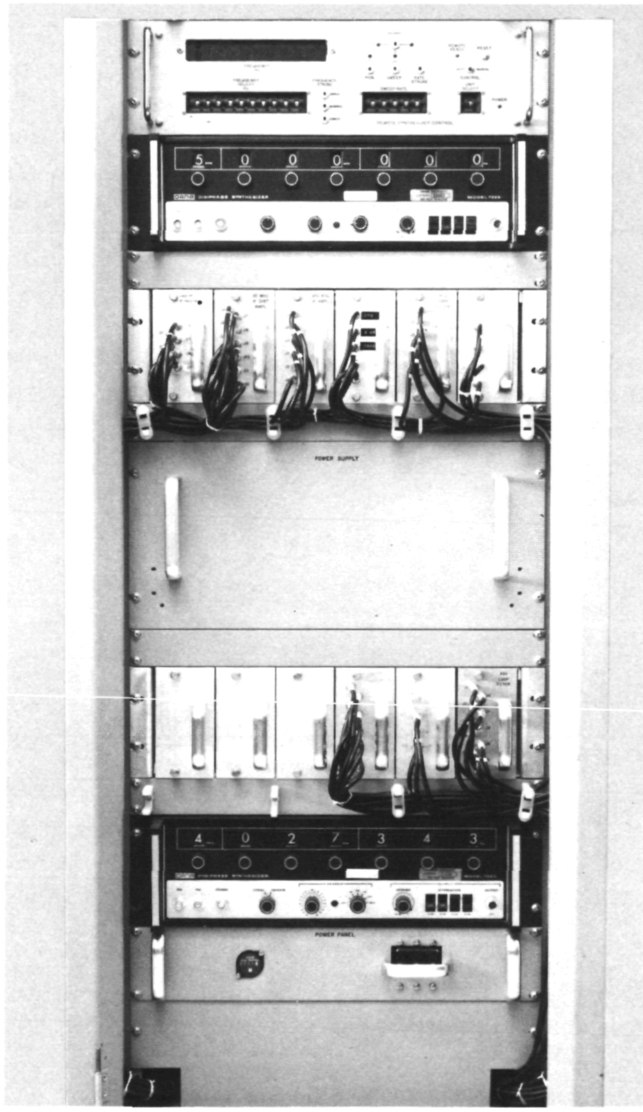

Fig. 4. Control room cabinet front view

Table 2. Exciter characteristics

Characteristic	Specified limits S-band	Specified limits X-band
Signal exciter		
Frequency range	2025 to 2120 MHz	7145 to 7235 MHz
Frequency stability	Same as station standard	Same as station standard
Output power level	+24 dBmW minimum	+18 dBmW minimum
Modulation		
Number of input channels	4	4
Sensitivity	3.0 rad peak, 1.0 V peak	3.0 rad peak, 1.0 V peak
Linearity	±1.0%	±1.0%
Frequency response		
±1%	dc to 100 kHz	dc to 100 kHz
±2%	100 kHz to 1.0 MHz	100 kHz to 1.0 MHz
−3 dB	10 MHz minimum	10 MHz minimum
Modulation delay stability (12 h)	0.4 m rms maximum	0.4 m rms maximum
Input impedance	50 Ω resistive with VSWR ≤ 1.10:1	50 Ω resistive with VSWR ≤ 1.10:1
Sense	Positive modulation voltage shall produce a phase advance of the carrier	Positive modulation voltage shall produce a phase advance of the carrier
Doppler extractor		
Frequency bias	1.0 MHz	To be determined
Frequency range	±1.0 MHz	±3.0 MHz
Velocity vector		
Towards receiver	Decreasing frequency	Decreasing frequency
Away from receiver	Increasing frequency	Increasing frequency
Power level output	+14 dBmW ±1.0 dB	+14 dBmW ±1.0 dB
Output impedance	VSWR ≤ 1.2:1 relative to 50 Ω	VSWR ≤ 1.2:1 relative to 50 Ω
Phase stability		
Long term (12 h)	550 deg rms maximum (0.1 m)	1700 deg rms maximum (0.1 m)
Short term		
Wideband	8 deg rms maximum ($2\beta_{LO}$ = 12 Hz)	8 deg rms maximum ($2\beta_{LO}$ = 48 Hz)
Narrowband	11 deg rms maximum ($2\beta_{LO}$ = 1 Hz)	11 deg rms maximum ($2\beta_{LO}$ = 3 Hz)

synthesizer remote control and the receiver Dana frequency synthesizer, which it controls, are shown at the top of the cabinet. Below the receiver frequency synthesizer are two RF module cage assemblies separated by a power supply drawer. Below the bottom cage assembly is the exciter Dana frequency synthesizer. The subsystem power panel is located at the bottom of the cabinet.

The circuitry for the low-frequency portion of the receiver–exciter is contained in RF modules that plug into the cabinet-mounted cage assemblies as discussed in SPS 37-59, Vol. II, pp. 90–93. The cabinet mounting rails are set 2-in. back from the front of the cabinet to recess all panel-mounted equipment and allow room for the front-panel coaxial cable connection, and also allow the coaxial cables to be run in the available recessed area. The blank panels above and below each cage assembly are to provide a surface for coaxial cables and clamps, a surface for the location of RF module reference designation, and an air space between assemblies for proper ventilation.

The power supply drawer contains two sets of power supplies necessary for the RF modules. One set of power supplies is used for the upper cage assembly and one set for the lower cage assembly so as to obtain the best possible regulation by minimizing the lead lengths between the power supply remote sensing point and the RF modules.

A rear view of one of the cage assemblies and the associated terminal boards is shown in Fig. 5. The front of the first terminal board plate is for the module control function while the back is for the sense or tell-tale functions. The second terminal board plate is for power-supply distribution to each RF module. Figure 6 shows the front plate hinged down to allow access to the sense and power supply terminal boards. The power supply terminal board plate also is hinged to gain access to the RF module/cage power connector.

The interface for the cabinet is at the bottom and is made up of four interface plates. The engineering model uses one plate for AC voltage distribution and one plate for the receiver–exciter. Two plates are blank and could be used for any future equipment. Modifications or additions to the system can be easily accomplished without disassembling the entire cabinet.

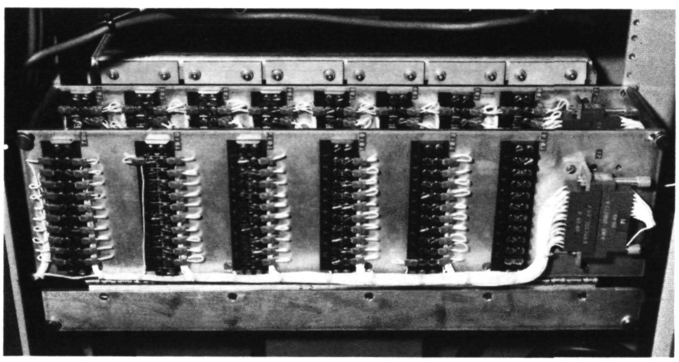

Fig. 5. Control room cabinet rear view

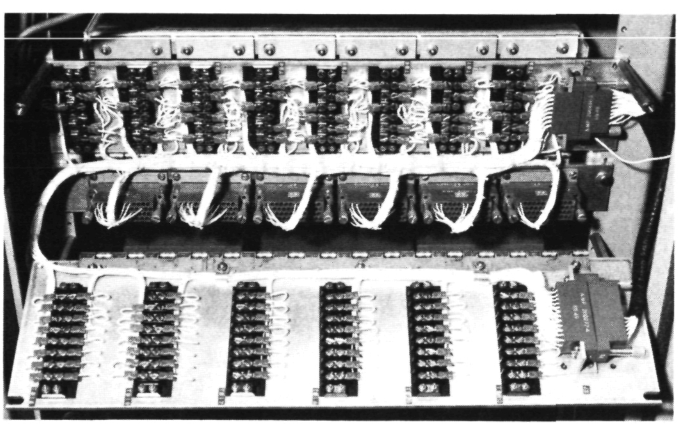

Fig. 6. Control room cabinet front panel open (rear view)

Antenna-mounted cabinet. The antenna-mounted cabinet contains the following drawer assemblies: exciter, coherent reference receiver test signal translator, doppler extractor, and the receiver. Each drawer contains RF modules, associated microwave equipment, and power supplies necessary for the equipment in the drawer. A typical layout and construction is shown by the top and bottom views of the exciter drawer (Figs. 7 and 8, respectively).

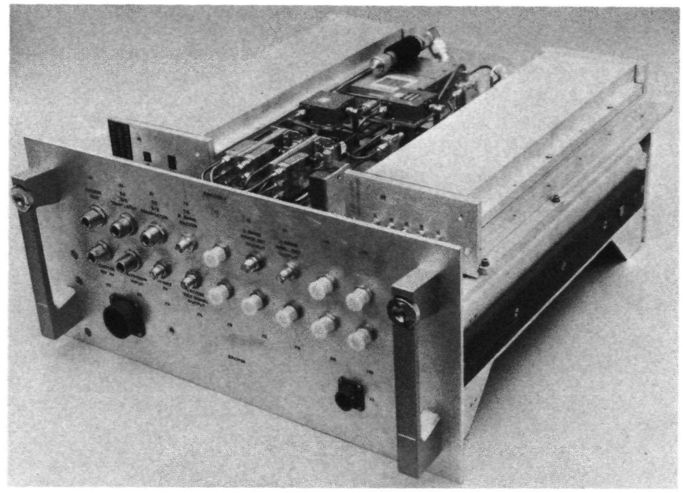

Fig. 7. Exciter drawer assembly top view

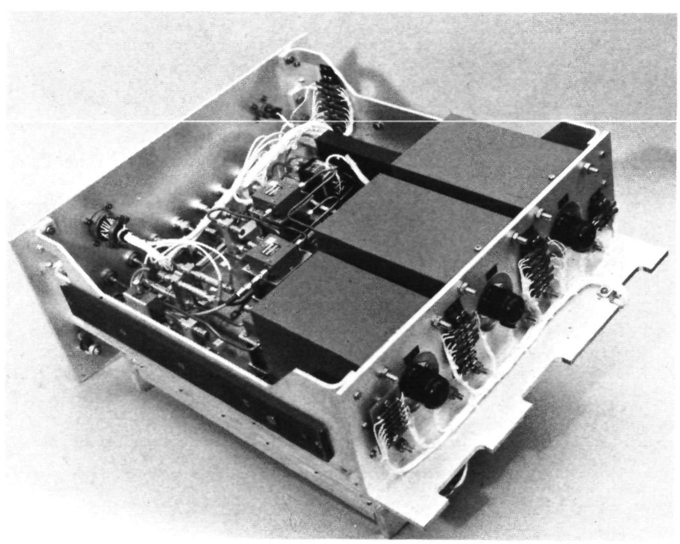

Fig. 8. Exciter drawer assembly bottom view

The RF modules use the same type of chassis used in the control room, but these modules are mounted directly to the drawer for increased temperature stability. The power supplies, the same type as used in the control room equipment, are also mounted for best temperature stability. A front panel cabinet fan is mounted at the bottom of the cabinet for air circulation. The cabinet front mounting rails are recessed 3 in. to allow room for the front panel coaxial connectors and permit the cables to be run in the available recessed area.

3. Performance

A manually-controlled Block IV receiver–exciter engineering model operating at S-band with automatic acquisition capability has been developed and evaluated, during a 2-mo period, at DSS 13 while tracking *Pioneer* and *Mariner* probes. This engineering model has now been returned to the Ground Radio Development laboratory for a detailed testing program that will collect data on pertinent subsystem parameters and characteristics. In addition, development will extend into the areas of automatic control, X-band capability, and improvements in the present S-band design.

While at DSS 13, several spacecraft, including *Mariners VI* and *VII* and *Pioneers VI, VIII,* and *IX,* were automatically acquired and tracked at signal levels ranging from -168 dBmW to -174 dBmW in a 3-Hz loop bandwidth. The *Mariners VI* and *VII* spacecraft were also automatically acquired and tracked in a 1-Hz loop noise bandwidth. Subsystem threshold tests have indicated that the receiver VCO phase jitter caused no noticeable degradation in receiver performance in loop bandwidths down to 1 Hz.

C. Development of Techniques for Mark III Implementation, *R. C. Coffin*

1. Introduction

In response to the Deep Space Development Plan, there have been a number of design developments pertinent to the DSN. The nature of these developments span the range of work being done by the JPL Telecommunications Division. Some of the work encompasses new techniques in packaging, in circuitry development, and in the area of computer-control concepts. The ranging demodulator assembly, which is currently being built, will employ these techniques.

2. Packaging

A new packaging concept, shown in Fig. 1, has been developed. It was designed to be compatible with the Mark III packaging module designed for the Block IV receiver/exciter subsystem (SPS 37-59, Vol. II, pp. 90–95). Careful liaison has been maintained to insure that the two developments are as completely compatible as possible. The two modules use the same power plug and coaxial interface and will plug into the same cage assembly.

The differences between these two modules arise from the fact that this module is designed under the constraint that preventing RF leakage is of paramount importance. A number of design techniques were employed to achieve that result. The module is machined from one piece of aluminum to which a front panel and two side covers are attached. Machining from a single block of material allows the designer to employ compartment-type construction to minimize intercircuit RF leakage. DC power is supplied to the module circuitry through a shielded RF filtered compartment located at the rear of the "cold" side of the module (Fig. 1a). Also, on the "cold" side of the module is an area used for distribution of power, signal, and control. RF integrity is maintained by the use of shielded coaxial cables for signals and feedthrough filtering for control and power lines.

The RF "hot" side of the module (Fig. 1b) will use container-type construction to prevent circuit-to-circuit leakage. Leakage to the exterior of the module is controlled by machining the surface mating the cover plate to the module chassis flat to within 0.001 in. on the average. In addition, the module may be plated with gold to form a relatively soft, highly conductive, mating surface. Screws every 1.5 in. help to prevent warping of

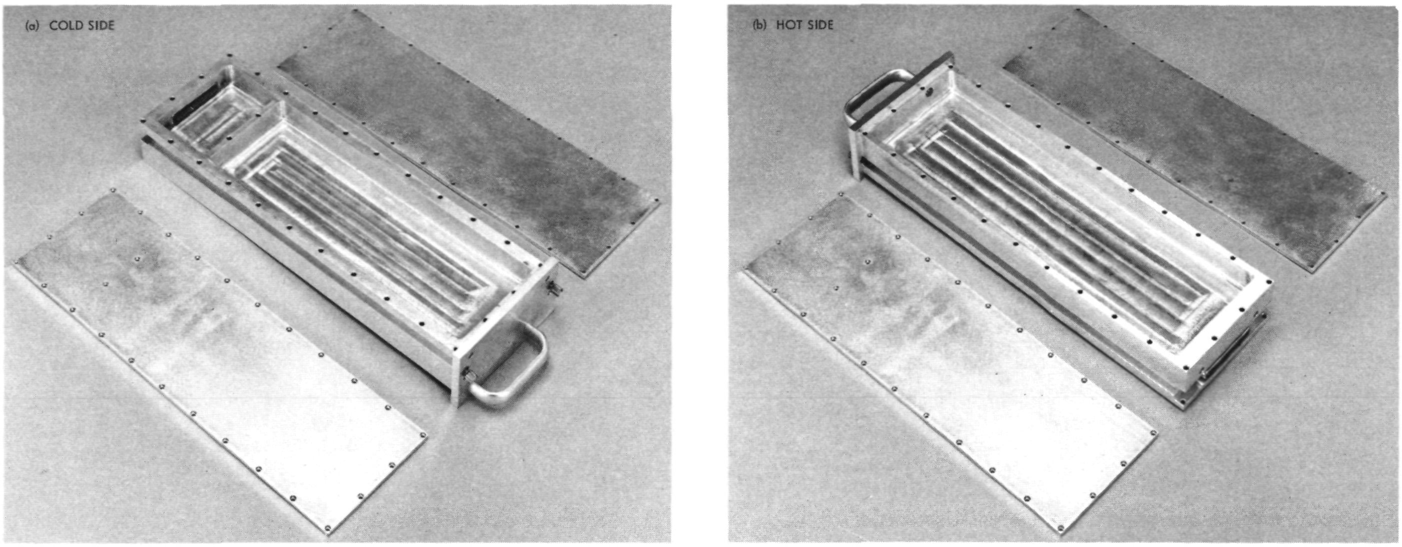

Fig. 1. RF "cold" and "hot" sides of solid Mark III packaging module

the coverplates and to insure proper mating of the two surfaces. All screw holes are through holes, which permit proper removal of machining filings and allow easy access of the plating solutions. The screw thread dimensions are oversize so that retapping of plated holes will be unnecessary.

3. Circuitry

Mark III performance characteristics indicate that systems and subsystems of the future must be controlled, maintained, and calibrated automatically. Circuitry must be designed that will allow for computer control. Two functions that are prevalent in receiver-type equipment are phase control and signal level control.

For each of these functions, there are several possible techniques for circuit design. Phase control might be achieved by stepping motor control of a resistance–capacitance or goniometer-type phase shifter. It is also possible, with the advent of high-speed logic elements, to build a digital phase shifter (SPS 37-58, Vol. II, pp. 121–122, and SPS 37-61, Vol. II, pp. 100–102). Another computer-controllable phase shifter, not previously reported, has been developed. This new phase shifter operates under control of an analog voltage. It has a linear control characteristic of 72 deg/V. A functional diagram of this phase shifter is shown in Fig. 2. The phase characteristic of a mixer is used as a standard in a feedback system that linearizes the phase shift of an analog voltage-controlled phase shifter. To minimize the nonlinearities of the S-curve of the mixer, only one-fourth of its characteristic is used. This is accomplished by dividing the input and output by 4 before applying them

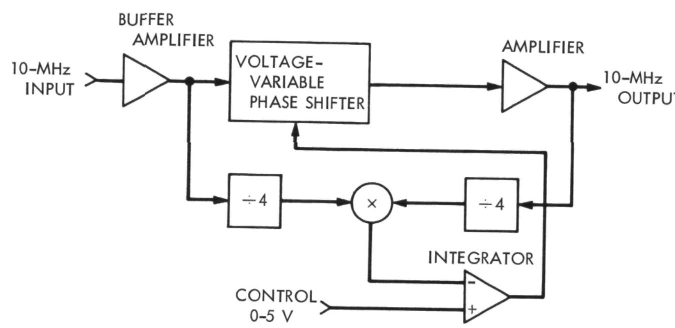

Fig. 2. Analog phase shifter functional diagram

to the mixer. Tests indicate that the control is linear to within a degree and that over a ±10-deg temperature range the control characteristic is 72 deg/V ± 2%. A control range of greater than 360 deg is readily available. Using this technique, it should be relatively easy to build linear analog phase shifters at any IF frequency.

Signal level control is being approached on two fronts, attenuators and automatic gain control (AGC) amplifiers. Several commercially available attenuators have been purchased and tested. At least one of these was active, and tests show that the state-of-the-art is sufficient to make it possible to buy computer-controllable attenuators that have a dynamic range of greater than 50 dB with a phase variation over that range of less than 2 deg. It should be pointed out, however, that if the attenuator is to be used to maintain a constant output (as in AGC applications), is should be tested in that fashion. It has also been found that some of the commercially available switched T-pad type of attenuators lose signal during switching.

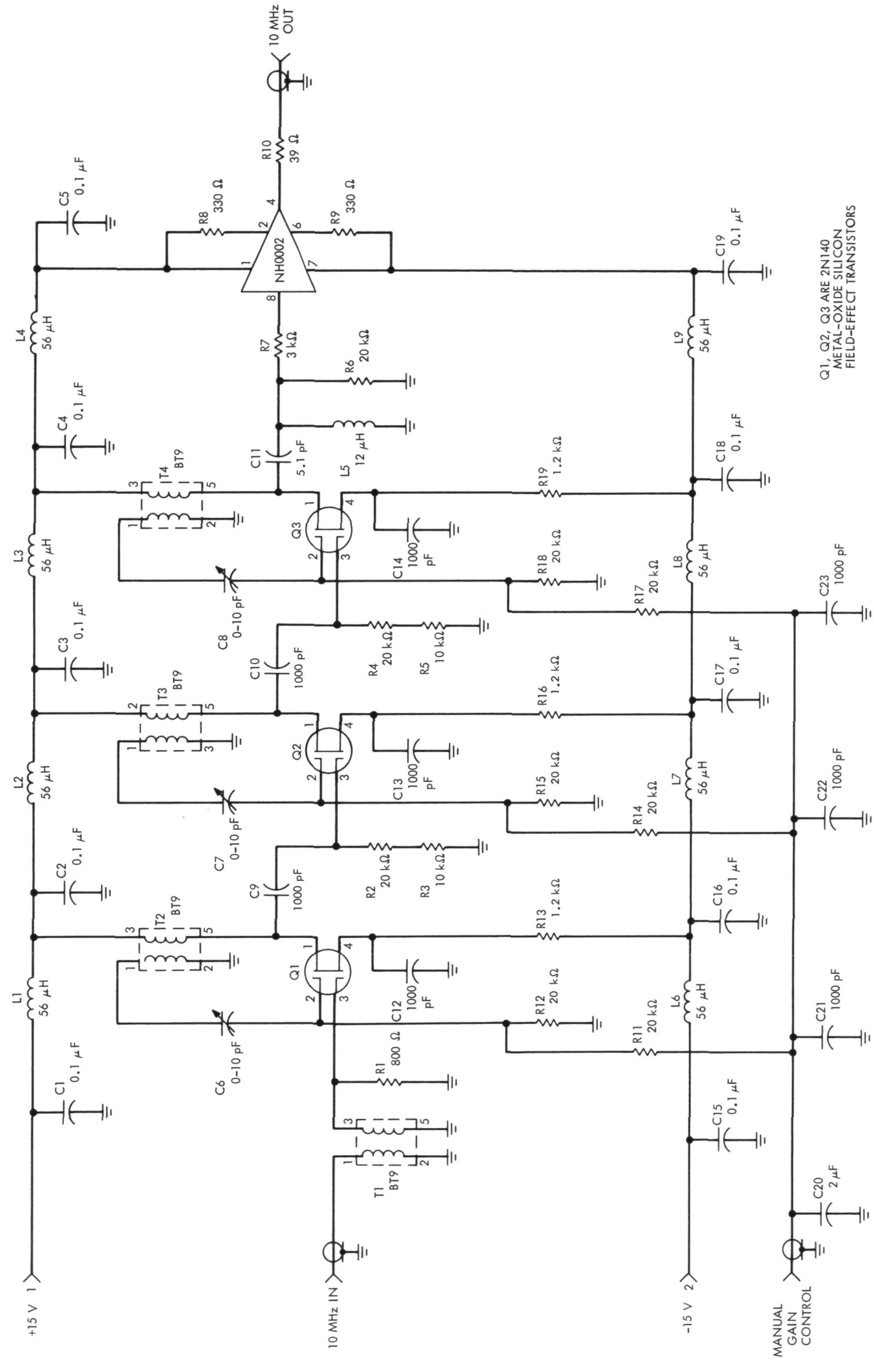

Fig. 3. Low phase-shift AGC amplifier

Using a neutralizing technique and dual-gate metal-oxide-silicon field-effect transistors, an improved AGC amplifier has been built. The circuit diagram is shown in Fig. 3. A wideband transformer and adjustable trimmer capacitor are used to neutralize the control gate-to-drain capacitance. The AGC amplifier characteristics are shown in Table 1. This technique has good possibilities with respect to phase stability, but there remains a problem of gain stabilization versus temperature.

Table 1. AGC amplifier characteristics

Characteristic	Value or type
Gain, dB	0 to 50
Phase shift (fixed output; 0–50-dB gain), deg	±0.3
Noise figure (50-dB gain), dB	9
Input impedance, Ω	50 ± 5
Control characteristic	Nonlinear (approximately logarithmic, 0 to 8 V)
Temperature characteristic (gain), °C/dB	6

4. Computer concepts

The third aspect of the Mark III development work being done is that of computer concepts. In automating a given system, it is tempting to use the computer to perform the operations in the same order, same manner, and with the same regularity that they are currently being done. However, a more appropriate approach is to re-evaluate, from a designer's standpoint, the impact of the era of automatic control. For instance, when designing a phase shifter that will be controlled by man, it is necessary to simplify the interface to the extent that little, if any, calculation is required to determine correct adjustment. When operated by a computer, however, there is a trade-off available to the designer by which he can take advantage of the machine's ability to perform mathematical or logical operations to determine the control setting.

Another facet to be taken into account when designing computer-controlled hardware is the matter of time. A computer, when controlling a particular system or subsystem, can perform many more operations per unit time than is possible by an operator. This has possible ramifications on the design of the circuitry in that the designer may want to provide more monitor points or functions to be observed.

In general, then, for Mark III development there has been a re-examination of the circuitry and procedures in light of the fact that the systems of the future will be controlled, monitored, and calibrated by machine.

D. Programmed Oscillator Development, *M. R. Wick*

1. Introduction

Programmed oscillators have been under development over the past several years for use in deep space communications, radar astronomy, and, most recently, in the time-synchronization transmitter of the DSN. With a programmed oscillator in the ground receiver to track the doppler, the loop stress can be reduced and the degradation of the communication link resulting from loop stress minimized. The same technique can be applied to the spacecraft receiver. However, to simplify the spacecraft system, the frequency of the ground transmitter is programmed to minimize the stress in the spacecraft receiver.

The first programmed oscillator (Model I) was built in 1960–1961 for use in the radar exploration of Venus in 1961 (Ref. 1) and was manually controlled. Since that time extensive developments have occurred (Ref. 2).[1] The Model V programmed oscillator currently in use

[1]SPS 37-18, Vol. III, pp. 32–38; SPS 37-30, Vol. III, pp. 69–71, 84–86; SPS 37-32, Vol. III, pp. 36–44; SPS 37-36, Vol. III, pp. 54–63; SPS 37-39, Vol. III, pp. 71–77; SPS 37-43, Vol. III, pp. 92–106.

controls the search oscillator in one of the decades of a Hewlett-Packard 5100A/5110A synthesizer (SPS 37-39, Vol. III, pp. 71–77) by means of a digital loop. A Model V programmed oscillator is presently installed at DSS 14 in the S-band experimental receiver and is controlled by an SDS 920 computer. Another Model V programmed oscillator is installed at DSS 13 for time-synchronization X-band transmissions and is controlled by an SDS 910 computer (SPS 37-43, Vol. III, pp. 92–106).

The frequency range of the Model V design is limited to the decade range of the search oscillator being controlled. To obtain the short-term stability required for use in narrow-band receiver loops, the synthesizer search oscillator control is limited to the tens decade, a total frequency range of 100 Hz at the programmed oscillator output frequency (SPS 37-39, Vol. III, pp. 71–77).

Since the present Model V programmed oscillator does not simultaneously provide both the frequency range and short-term stability required by the DSN for tracking deep space probes, other techniques are being investigated. The present technique under development and described in this article is based on the use of the Dana Laboratory Model 7020-103 digiphase synthesizer (Ref. 3). Preliminary measurements of short-term stability demonstrated the capability of operation with this synthesizer in very narrow-loop noise bandwidths. Also, the Dana synthesizer programmable frequency range is not restricted to any particular decade. It appears that the Dana synthesizer can be programmed over expected doppler frequency ranges and still possess adequate short-term stability necessary for operation in narrow bandwidths.

2. Dana Digiphase Synthesizer

The Dana synthesizer is a fixed frequency synthesizer. The Dana synthesizer contains a digital loop controlled by inserting, either locally by means of the frequency selection knobs on the front panel or remotely, a binary-coded decimal (BCD) signal for the number in each decade from the unit Hz to the MHz decade. The basic technique used in the synthesizer is a digital loop (Fig. 1) which contains a divide by N in the feedback path. Phase lock occurs when f_{VCO}/N exactly equals the reference frequency,

$$\frac{f_{VCO}}{N} = f_{REF}$$

where f_{VCO} is the voltage-controlled oscillator frequency and f_{REF} is the reference frequency. To obtain the 1-Hz

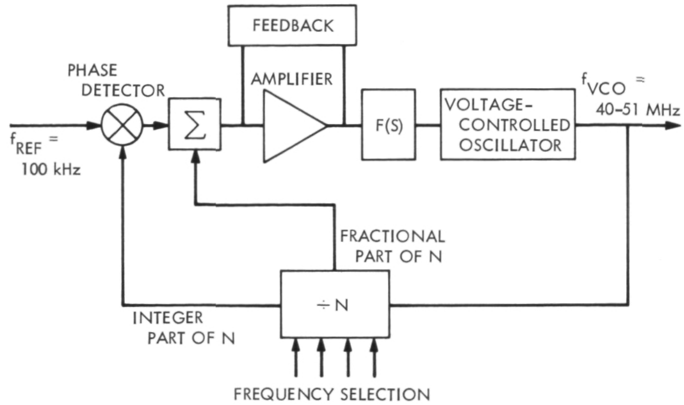

Fig. 1. Dana Laboratory digiphase synthesizer block diagram

resolution of the synthesizer available in the local mode, fractional values of divider N are required. A unique method of accomplishing fractional division by N is used. This method will not be discussed in detail in this article; however, a brief description follows. The output signal of the VCO, f_{VCO}, is divided by the integer part of N and compared with f_{REF} in the phase detector. The error signal appearing at the output of the flip-flop detector is a linear saw tooth at the difference frequency. The fractional cycle portion of the divide by N is converted into an analog quantity scaled exactly to oppose the value in the flip-flop phase detector, and summed together with the output of the phase detector. Under these circumstances, the output of the summing junction is nulled and the loop sees no phase error.

In the local control mode of operation, the Dana synthesizer is limited to fixed frequency applications with 1-Hz resolution. Much more capability can be obtained in the remote control mode, and this article describes the development of one control technique to obtain this additional capability.

3. Remote Control Development

The remote control development effort to extend the capabilities of the synthesizer covers the following areas:

(1) Increase in frequency resolution to fractional Hz.

(2) Capability of changing frequency in a controlled manner without phase transients.

(3) Capability of computer control.

a. Fractional Hz control. The digital logic circuitry in the Dana synthesizer contains an accumulator which tabulates at each clock cycle the input BCD numbers inserted into the decades. The tabulation of these numbers actually represents the accumulation of phase increments. A 3-μs computing interval is used during each clock cycle to sample the input BCD numbers (Fig. 2), during which time the phase accumulator increments. With the 100-kHz clock signal, each digit in the unit decade then represents an accumulation of 10^{-5} cycles of phase each 10 μs. If the input BCD number is constant, the accumulation of phase is linear and a fixed frequency output is obtained with 1-Hz resolution. However, the input BCD number can be changed if this change is synchronized with the clock (Fig. 2). The ability to change the input BCD number in the remote control mode provides the capability of fractional Hz resolution.

Figure 3 illustrates the method used for externally entering the BCD codes into the synthesizer decades when operating in the remote mode. The front panel manual selector switches are disabled and the BCD numbers are read into the synthesizer from the frequency control register. For a constant frequency output, the numbers in the registers are fixed. To provide partial Hz resolution, it is necessary to have the capability of changing the BCD number in the Hz decade. The reason for this can be illustrated in an example. If the BCD number read into the Hz decade is increased by one for 1 clock cycle each 100 clock cycles, then the average increase in frequency over the whole number value is

$$\frac{100}{100{,}000}\ \text{Hz or } 0.001\ \text{Hz}$$

To accomplish incremental changes in the BCD input numbers, the external frequency control registers consist of UP/DOWN counters. The BCD number in the frequency control register can then be incremented up or down by the application of pulses from the fractional Hz control. Decimal rate multipliers (DRMs) are used in the fractional Hz control to generate the controlled pulses for interpolation between integer values of the synthesizer output frequency. DRMs produce output pulse rates which are a programmed fraction of the applied input rate. The program input is a BCD code over the selection range of 0 to 9. Figure 4 is a circuit design of a DRM using J-K flip-flops (F/F). Design of the DRM stages used in the engineering model is illustrated with reference to a logic truth table (Table 1) and related timing diagram (Fig. 5).

Table 1 illustrates the sequential states S assumed by the flip-flops 1, 2, 3, 4 as the input clock rate (R_{in}) advances. Outputs A, B, C, and D are derived from logic

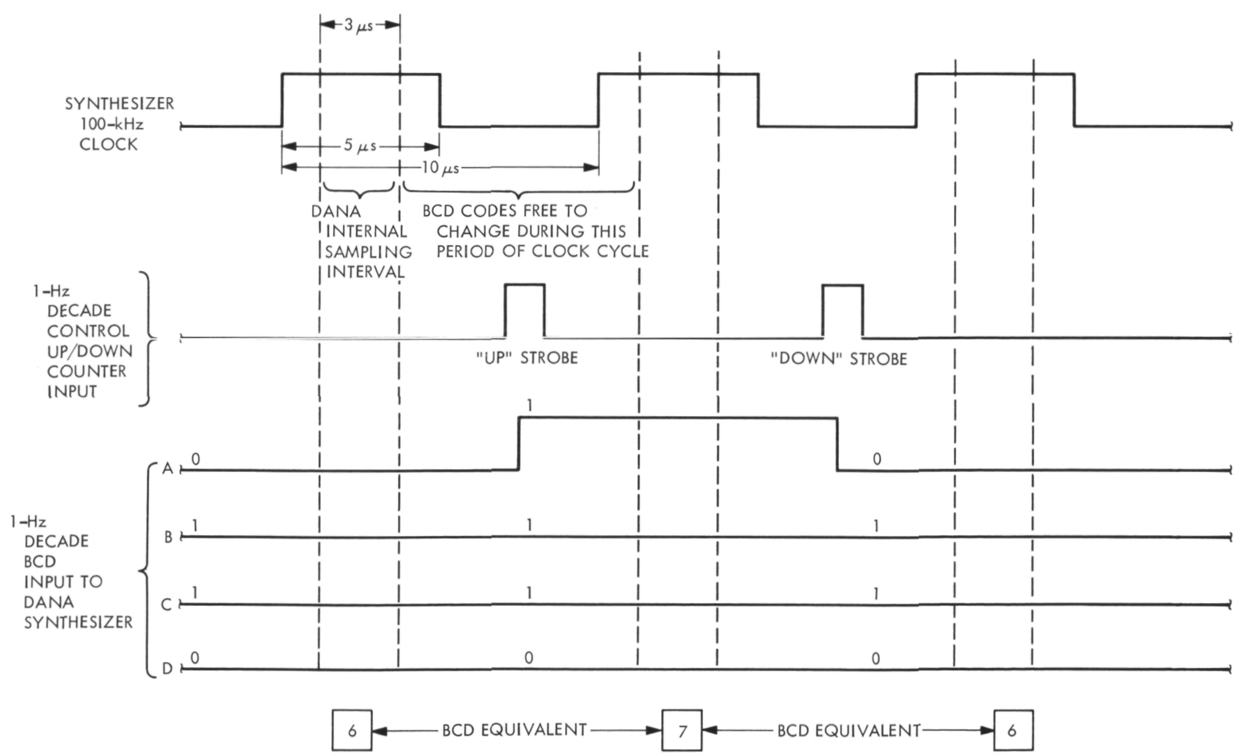

Fig. 2. Remote control (1-Hz decade)

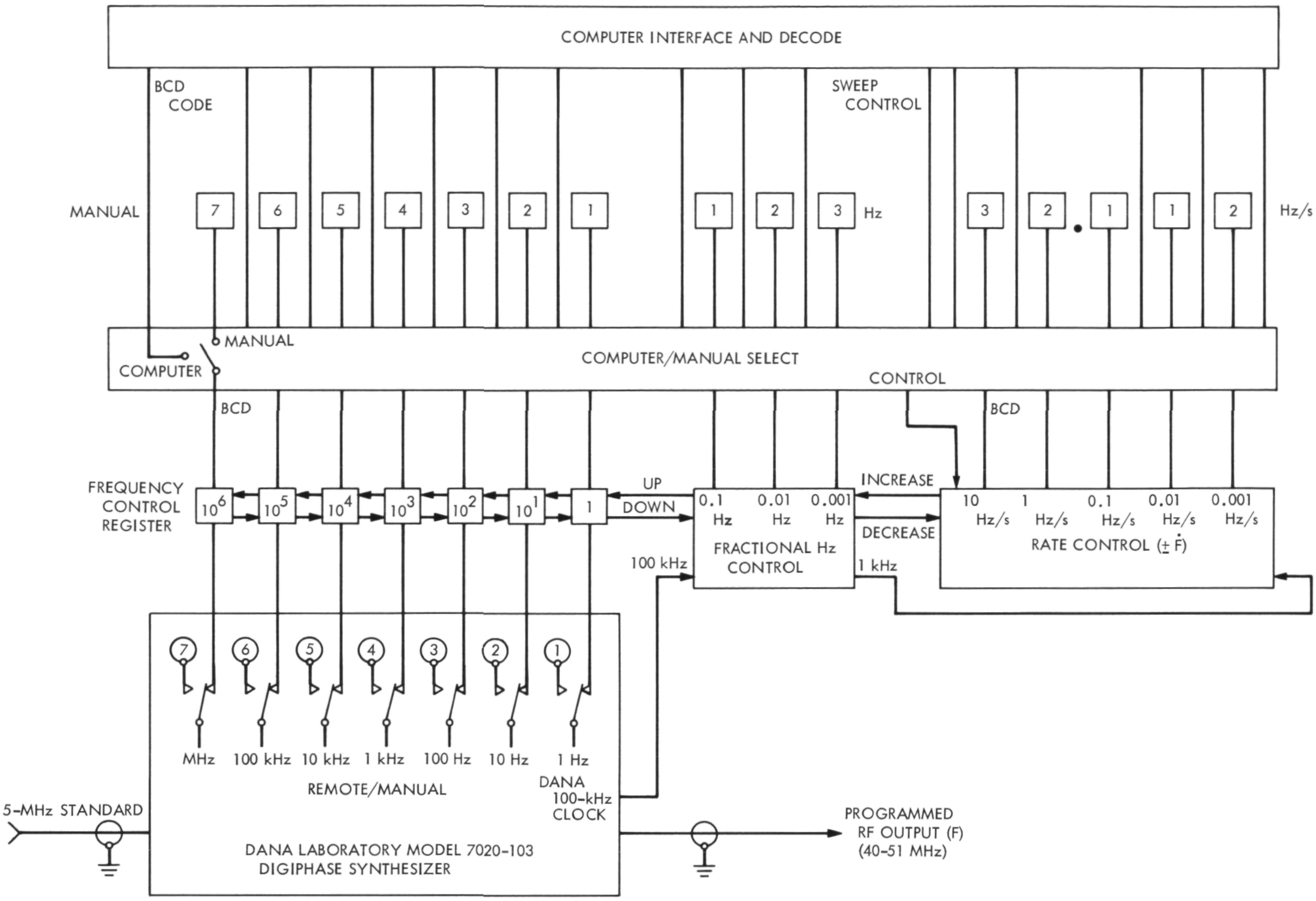

Fig. 3. Digital control block diagram

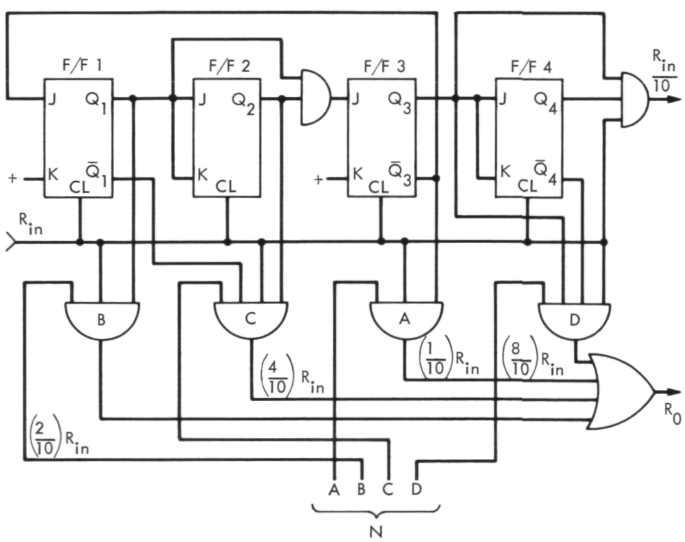

Fig. 4. Decimal rate multiplier and waveforms

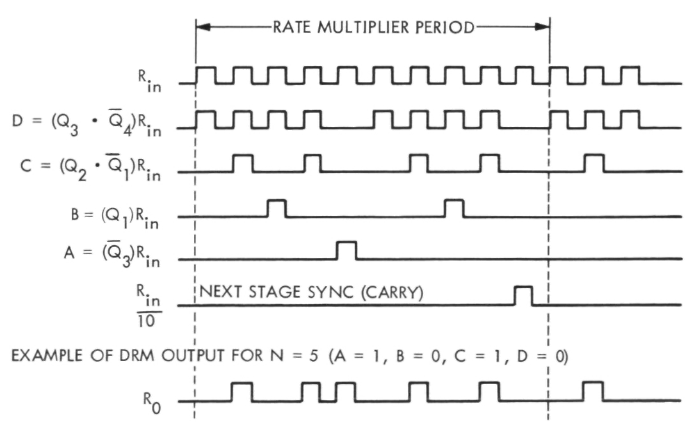

Fig. 5. Timing diagram

Table 1. Logic truth table

Input clock	S	4 3 2 1	D	C	B	A
0	a	0 0 0 0	1			
1	b	0 0 0 1	1	1		
2	c	0 0 1 0	1		1	
3	d	0 0 1 1	1	1		
4	e	0 1 0 0				1
5	f	1 0 0 0	1			
6	g	1 0 0 1	1	1		
7	h	1 0 1 0	1		1	
8	i	1 0 1 1	1	1		
9	j	1 1 0 0				

gates enabled by corresponding inputs to produce serial pulse trains, as shown in the timing diagram (Fig. 5). The output follows the logical equation

$$\sum = A\left(\frac{1}{10}\right)R_{in} + B\left(\frac{2}{10}\right)R_{in} + C\left(\frac{4}{10}\right)R_{in} + D\left(\frac{8}{10}\right)R_{in}$$

The effect is to produce an indicated multiplication of the input number N and the input rate

$$R_{in}\left[\sum = R_{in}\left(\frac{N}{10}\right)\right]$$

where N is the decimal equivalent of the BCD code. The BCD code selects a combination of the A, B, C, D waveforms of the timing diagram such as the example given for $N = 5$. The resultant output is a serial pulse train of rates from 1/10 to 9/10 R_{in}.

Figure 6 shows three stages cascaded to produce a pulse train with from 1/1000 to 999/1000 R_{in}. This provides fractional Hz control with millihertz resolution. To evaluate this technique of fractional Hz control, an engineering model similar to Fig. 6 with millihertz resolution has been designed.

b. Frequency rate control. Frequency rate control is included in the engineering model digital control to provide the capability of tracking doppler and also to provide a linear frequency sweep for acquisition. Doppler tracking can be accomplished by a series of linear approximations, so whether we are concerned with doppler tracking or acquisition, what is required is the capability

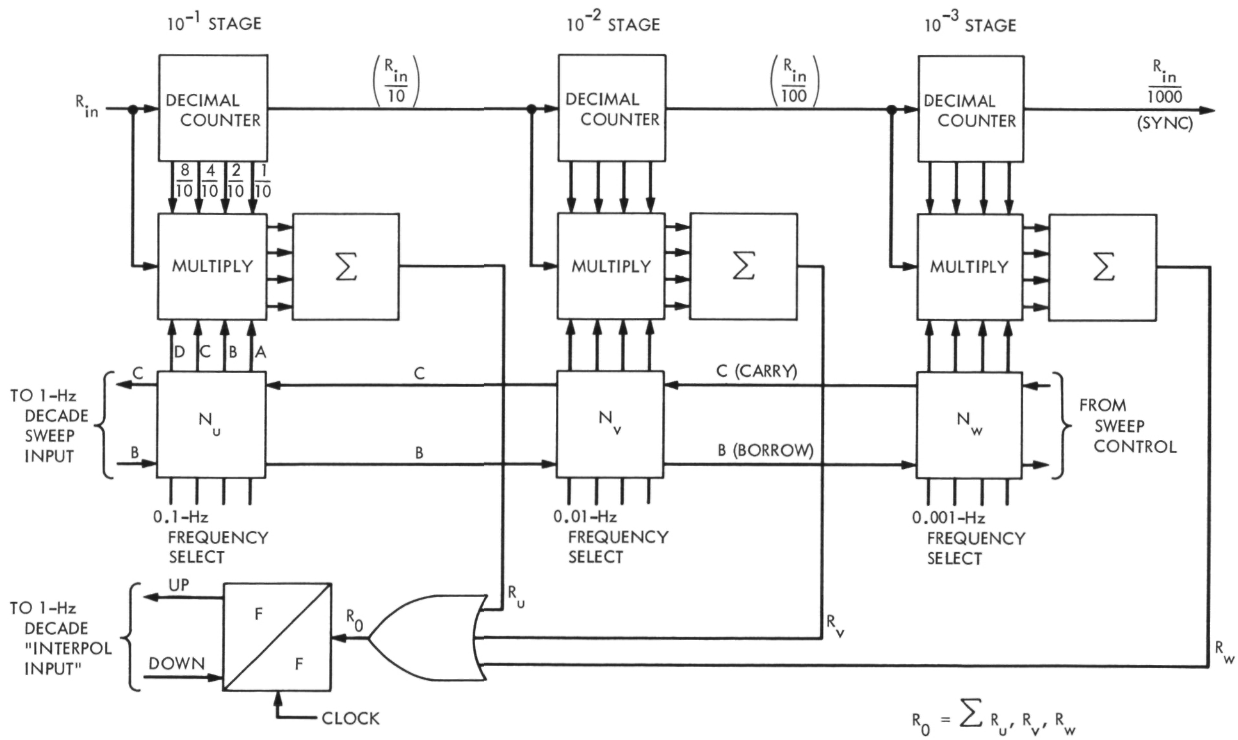

Fig. 6. Three-stage decimal rate multiplier

of selecting a frequency rate for a prescribed time period. The DRM technique is also used for generating the pulses to provide linear frequency ramps. The output pulses from the rate control are used to increment the fractional Hz control. The rate control is synchronized with the fractional Hz control to assure that the output frequency represents the programmed frequency.

Since DRMs produce unevenly spaced pulses, it is necessary to assure that the BCD numbers are not incremented until a complete cycle has elapsed. For example, with millihertz resolution, the complete cycle time is 1000 pulses of the clock or

$$\frac{1{,}000}{100{,}000} = 0.01 \text{ sec}$$

The frequency cannot be changed, therefore, more often than 0.01 s and must be synchronized to a multiple of 0.01 s.

The engineering model (Fig. 7) being evaluated provides step changes of 1 millihertz over the range of 0.001 to 99.999 Hz/s at the synthesizer output. The control unit provides for the selection of the following:

(1) Nominal frequency (F_{nom}).

(2) Sweep rate (F).

(3) Sweep polarity ($+/-F$).

(4) Sweep limits (F_{min} and F_{max}).

c. Computer control. The digital control is being designed to interface with the computer in the primary mode of operation. A manual mode will also be available to control the synthesizer during the time a computer is not available.

4. Future Development

An engineering model of the digital control for the Dana digiphase synthesizer was used successfully in automatic acquisition experiments at DSS 13 as part of the Block IV engineering model receiver/exciter subsystem. Acquisition was initiated by the station SDS 910 computer. Phase stability measurements indicate no inherent instabilities in loop performance due to the digital control while operating in a 1-Hz loop bandwidth. Software is currently being developed for doppler tracking capability using the engineering model digital control.

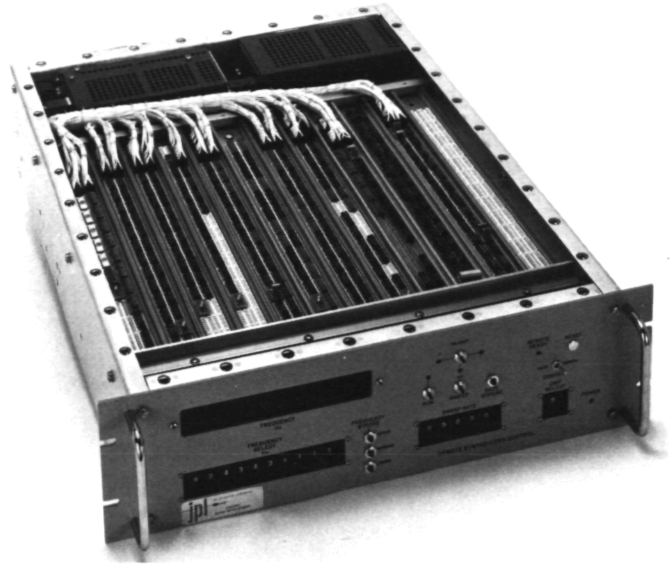

Fig. 7. Digital control (engineering model)

The present control is adequate for tracking doppler in order to reduce loop stress in the receiver. However, to obtain more accurate doppler while programming the exciter, increased resolution is desirable. This capability can be added to the existing external fractional Hz control. However, Dana is developing for JPL fractional Hz resolution to 10^{-6} Hz within the synthesizer. The external control to be developed for use with this unit will then require only frequency rate control.

References

1. Golomb, S. W., Stevens, R., and Victor, W. K., *Radar Exploration of Venus: Goldstone Observatory Report for March–May 1961*, Technical Report 32-132. Jet Propulsion Laboratory, Pasadena, Calif., Aug. 31, 1961.

2. Thompson, G. D., Jr., and Sydnor, R. L., "Programmed Oscillators for Doppler Radar Systems," *Frequency*, Vol. 4, No. 4, pp. 22–29, Jul.–Aug. 1966.

3. Gillette, G. C., "The Digiphase Synthesizer," *Frequency Technology*, Vol. 7, No. 8, Aug. 1969.

E. High-Speed Data/Wide-Band Data Input/Output Assembly, *R. Wengert, L. DeGennaro, and J. McInnis*

1. Introduction

An introductory description of the high-speed data/wide-band data input/output assembly (HSD/WBD I/O assembly) was given in SPS 37-63, Vol. II, pp. 75–77. The current article includes an update of the description to incorporate equipment changes and the results of DSS installation and testing.

The HSD/WBD I/O assembly provides the interface and logic required for the bidirectional transfer of high-speed (4.8 kbits/s) and wide-band (50 kbits/s) information between the telemetry and command processor (TCP) computer and the HSD/WBD equipment in the GCF system.

The former TCP high-speed data interface equipment provided a 2.4 kbits/s unbuffered send-only capability. Because of the unbuffered output, the increased data rates imposed severe time constraints on the operational software of the TCP's XDS 920 computer. The buffered input/output of the new HSD/WBD I/O assembly removes the time constraint, allowing more computer freedom to perform other operations.

The new equipment provides a full duplex capability in either the high-speed or wide-band data operation modes. To maintain standardization throughout the network, each DSS will be provided with identical equipment: one assembly for each TCP and digital instrumentation system (DIS) computer.

2. Description

The HSD/WBD I/O assembly provides: (1) interface logic to convert the logic level differences between the TCP computer and the GCF system, (2) buffered inputs and outputs, (3) uninterrupted transfer of blocks of stored data from the computer, and (4) uninterrupted transfer of command information blocks to the computer.

Data of two types, high-speed and wide-band, may be transferred between the TCP computer and the GCF equipment. For all operations, the logic within the HSD/WBD I/O assembly is the same, i.e., positive voltage level for a logical 1 and ground for a logical 0. In the high-speed data mode, the GCF interface logic levels are −6 V for a logic 1 and +6 V for a logic 0. Hence, bipolar logic levels are used for the high-speed data mode. In the wide-band data mode, the GCF interface provides current mode logic, i.e., less than 5 mA of current is a logic 1 and greater than 23 mA of current is a logic 0.

The HSD/WBD I/O assembly operates under program control of the TCP computer. The data transfer rate to and from the GCF equipment is controlled by the GCF timing signal: 2.4 or 4.8 kbits/s for high-speed data and 50 kbits/s for wide-band data transmission. Panel-mounted indicator lights provide operational status information and panel switches allow the selection of word length, data type, test-clock rate, equipment unit number, and allowable bit error in the sync word of each data block.

3. Operational Characteristics

The equipment is capable of sending and receiving data either independently or simultaneously. Word lengths of 16 or 24 bits may be selected for transfer. Initial reset of the entire unit is performed by execution of an energize output M (EOM) instruction. This action places the send section in the standby, or ready to start new transmission mode, and the receive section in the search mode, sampling all information on the receiver data line from the GCF, searching for a data block sync word.

Hence, the HSD/WBD I/O equipment can be divided into two sections, the send section and the receive section. A functional block diagram of the send section is shown in Fig. 1. Preparation for transmission of a data

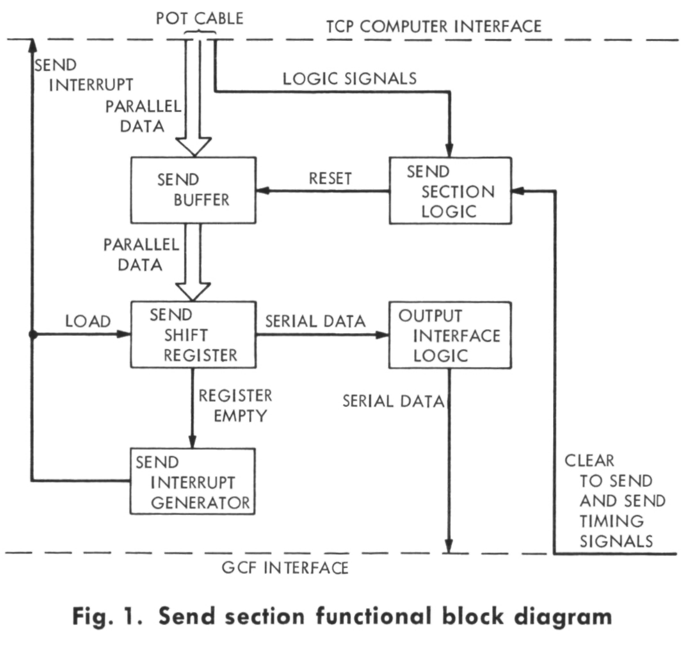

Fig. 1. Send section functional block diagram

block from the computer may be started by executing a skip-if-not-set (SKS) instruction (37637), which tests the readiness of the GCF equipment. If ready, an EOM (75577) parallel output (POT) sequence is performed, which sets the marker bit flip-flop and causes a parallel transfer of a word from the TCP computer into the send buffer unit. The transfer (or buffer load) pulse and the send shift register being empty initiates an interrupt signal to the TCP computer requesting another data word. This interrupt signal also initiates the "request to send" signal to the data modem and transfers the word stored in the send buffer to the send shift register. A "clear to send" signal from the data modem and the next modem clock pulse enables data to be serially shifted from the send shift register to the data modem. Each time the marker bit (which had been set to 1 in the last stage of the send shift register) is transferred out of the shift register, another interrupt signal is sent to the computer requesting another data word. The interrupt signal is again used to transfer the data word that was waiting in the buffer to the send shift register. This process is repeated until the last data word is transferred from the computer.

Immediately after the last word is transferred to the send buffer, an EOM (37637) instruction is issued. This instruction resets the interrupt enable circuit, disabling transmission of additional interrupts to the computer. When the last data word has been shifted out of the send shift register, the request to send signal is disabled, returning the send section to a ready to start new transmission mode.

A functional block diagram of the receive section is shown in Fig. 2. The data, from the data modem, is serially gated into the receive shift register at the modem clock rate. Until the sync word is detected, a bit is also placed into the 24-bit sync detector and end-of-word register at modem clock time and shifted through this register at a 2M-bit/s rate between modem clock pulses.

As this bit is shifted through the register, a bit for bit comparison is made with the word present in the receive shift register and the wired sync word in the sync detector. When the sync word is present in the receive shift register, it matches the wired sync word in the sync detector; this match produces a "sync-detected" pulse from the word detector. The "sync-detected" pulse is used to switch the receive section from the search mode into the sync mode. The "sync-detected" pulse is also used to: (1) initiate a computer interrupt signal (indicating a word is ready to be transferred to the computer), (2) command a transfer of data from the receive shift register to the receive output buffer register, and (3) reset the sync detector register.

The modem continues to send data to the receive shift register at the modem clock rate, after the sync word is

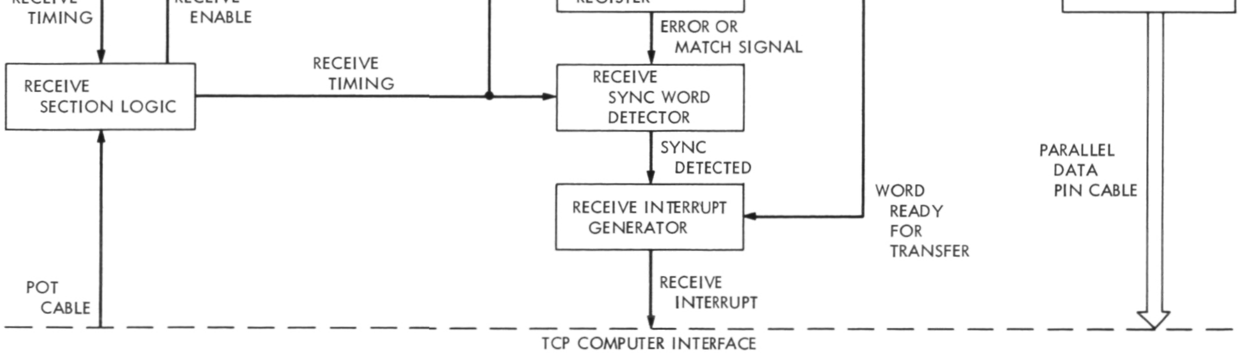

Fig. 2. Receive section functional block diagram

detected. Every word time (normally 24-bit times), another word is transferred to the receive output buffer and another receive interrupt is sent to the TCP. The computer always responds to the interrupt signal by accepting the data from the receive buffer register with an EOM (77717) parallel input (PIN) instruction. The computer then resets the receive buffer with an end-of-PIN signal (Rti) before the receive shift register is ready to transfer another word to the receive buffer. When the receive register is filled again, another computer interrupt signal is generated to indicate a transfer is ready again (a full buffer). The process of receiving modem data in the receive shift register, transferring of data to the receive buffer, and transferring of the data word to the computer is repeated until the computer has acknowledged receipt of a full data block. It then responds with an EOM (37717) instruction, which returns the receive section to the search mode.

The HSD/WBD I/O assembly also can be operated in a test mode. A functional block diagram of the unit operating in the test mode is shown in Fig. 3. Note that the system is now operating in closed-loop form, i.e., data from the computer are transferred in parallel to the send section, which serially transfers the data to the receive section, which in turn parallel transfers the data back to the TCP computer. The equipment is placed in the test mode by an EOM (77637) instruction from the computer. While in this mode, the send section is connected to the receive section and they operate in the

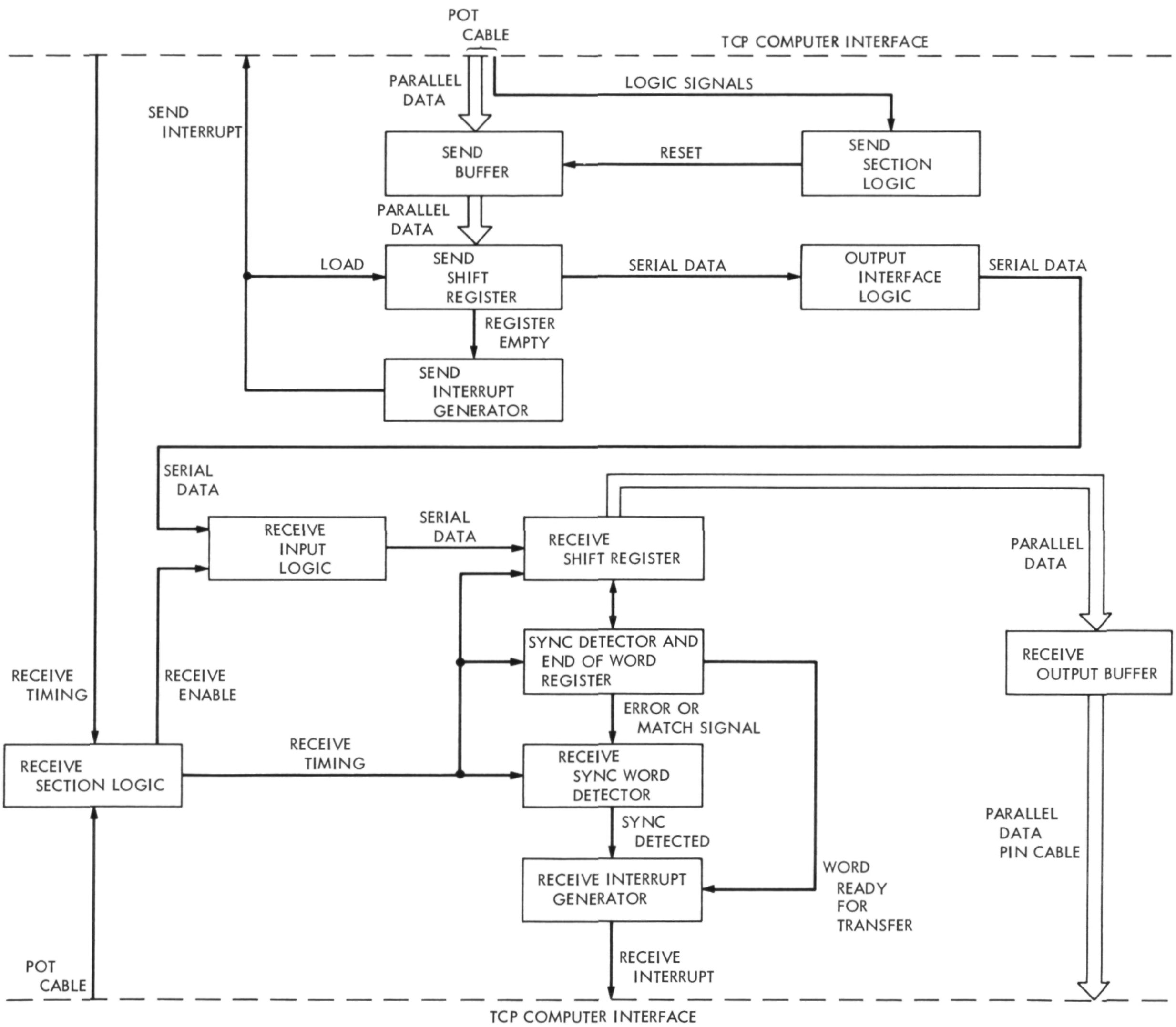

Fig. 3. Test mode functional block diagram

same manner as during normal operation, with these exceptions:

(1) The interface with the modem is interrupted.

(2) A test clock is used for the data clock.

(3) The send data are returned to the computer through the receive section to verify the transfer of the data words through the entire assembly.

The installation of the HSD/WBD I/O equipment now allows the bidirectional transfer of information between the TCP computer and the GCF high-speed and wide-band data systems.

4. Station Implementation

The design of the HSD/WBD I/O assembly was frozen for production purposes, at a time when several deficiencies were still unresolved. Specifically, these included implementation of a 16-bit word-length operating mode and several minor problems. None of the known deficiencies are such as to prevent installation checkout and all are subject to relatively easy field retrofit correction.

Sixteen complete HSD/WBD I/O assemblies have been shipped, twelve for TCP installation at DSSs 12, 41, 42, 51, 62, and four for DIS installation at DSSs 41, 51, 62, and 71.

In the meantime, a field modification to correct the known minor deficiencies has been designed and validated, and a retrofit modification kit is being assembled. Once the retrofit kits are available, it is planned to modify all future HSD/WBD I/O assemblies prior to shipment. Retrofit kits will be sent to all sites whose I/O assemblies have already been shipped.

A second modification to implement the 16-bit word-length operating mode has been designed and is undergoing evaluation and validation testing. Retrofit modification kits for this purpose will probably be available in approximately one month. I/O assemblies, which have not been shipped prior to availability of the 16-bit mode retrofit kits, will have this kit installed at JPL, in addition to the first modification described above. All other HSD/WBD I/O assemblies will be modified on-site.

Experimental HSD/WBD I/O assemblies at CTA 21, which already include the first retrofit modification, have been functioning perfectly in the 24-bit word-length operating mode for approximately one month.

The only residual HSD/WBD I/O assembly unknown is the WBD operating mode, which has not been validated due to lack of an operational wide-band data communications modem. This modem equipment is currently under installation at CTA 21. It is anticipated that validation of the HSD/WBD I/O assembly WBD mode can begin shortly after the modem installation is complete, yielding final results within approximately one month. Inasmuch as the HSD/WBD I/O assembly currently operates correctly in its internal test mode, no serious difficulty in interfacing with the wide-band data modem is anticipated.

F. Post-Detection Recorder Evaluation,

J. P. Buffington

In SPS 37-58, pp. 127–129, it was shown that the primary source of data degradation in the telemetry recording subsystem (baseband) is time displacement error (TDE). We define TDE as the timing error variations between the capstan servo reference oscillator and the events recorded on the data track adjacent to the reference track in the same head stack on the recorder. It is conveniently measured by recording the capstan reference oscillator on both the reference track and the data track simultaneously and then observing the output of the data track, on playback, on an oscilloscope which is triggered from the reference oscillator. This test setup is shown in block diagram in Fig. 1.

It is possible to make a record of this observation with an oscilloscope camera, using a slight under exposure for 5 or 10 s, and then to read the total peak-to-peak value of TDE from the cumulative exposure; in this way, a single tape can be used to evaluate machines which are physically remote from each other. To solve the problem of non-real-time data processing of the recorded baseband telemetry data, a reference tape was accordingly generated, using a standard FR-1400 Ampex recorder. The tape was carried to those vendors that

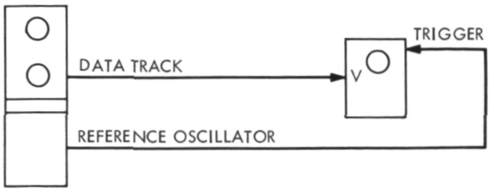

Fig. 1. Test setup to measure TDE

make recorders which have low time base error; their machines were evaluated and the evaluations were documented by means of the oscilloscope camera, using the test setup shown in Fig. 1.

The Ampex FR-2000, a new machine, was found to have the lowest TDE; when measured in the test setup of Fig. 1, a TDE of 200 ns at 60 in./s was observed and photographed. At the conclusion of the vendor TDE tests, an FR-2000 recorder was borrowed from the vendor for pragmatic tests at the JPL Compatibility Test Area.

The tests were conducted by using both a high-rate (259 kHz) and a low-rate (24 kHz) subcarrier, and were divided in two sections:

(1) Recording and reproducing on the FR-2000.

(2) Using the FR-1400 as an acquisition machine (record only) and the FR-2000 as a reduction machine (reproduce only).

All tests were conducted by using bit rates and symbol rates appropriate to the respective subcarriers, and by using the subcarrier demodulator assembly (SDA) loop filter in the recommended position for the specified subcarrier. No flutter or speed compensation techniques external to the tape recorder were used. The ST/N_0 was printed out in real time during the recordings, using the 10-MHz SDA real-time input for reference; and immediately after each recording, the ST/N_0 was printed out for the baseband receiver output connected directly to the up-converter input on the SDA for a real-time baseband ST/N_0 calibration. This is useful in determining how much of the ST/N_0 degradation should be charged to the recording process, and how much should be charged to the baseband conversion process.

Initially, tests were made at high signal-to-noise ratios (18.6 dB) for the high-rate subcarrier, to establish the capability of the SDA to lock at lower tape speeds. The ability of the SDA to lock at 30 ips, and even 15 ips, demonstrates considerable systems design margin in TDE, since TDE increases approximately inversely with tape speed.

The other tests were conducted at ST/N_0 figures (3.9 dB for the high-rate subcarrier and 7 dB for the low-rate subcarrier) which are estimated to be the worst case for *Mariner* Mars 1971. Results of the tests are given in Table 1.

As might be expected, the best results were obtained by using the FR-1400 for recording the data and by reproducing the data on the FR-2000. This is evidently because the record process takes place in an "open loop" condition with regard to tape speed control, and the relatively high mass of the FR-1400 capstan exerts a stabilizing influence on the tape speed in the record mode. In the reproduce mode, the superior capstan servo gain and bandwidth of the FR-2000 serve to optimize the TDE. This experimental evidence sustains the writer's conclusion that, to a good approximation, all TDE should be charged to the reproduce process.

Table 1. Recorder test results

Subcarrier rate, kHz	Tape speed, ips	Real-time ST/N_0 (10 MHz), dB	Real-time ST/N_0 (baseband), dB	ST/N_0 (reproduced), dB	Recorder loss, dB	Recorder + conversion loss, dB
FR-2000 (acquisition and reduction)						
259	60	18.6	—	16.6	—	2
259	30	18.6	—	15.0	—	3.6
259	15	18.6	—	8.0	—	10.6
259	60	3.9	3.5	2.6	0.9	1.3
259	30	3.9	3.5	1.86	1.64	2.04
24	15	7.15	5.8	5.54	0.26	1.51
FR-1400 (acquisition) and FR-2000 (reduction)						
259	60	3.9	3.5	2.6	0.9	1.3
24	15	7.15	5.8	5.8	—	1.35

G. Tau Ranging Subsystem Rebuild, *R. W. Tappan*

1. Introduction

The pseudonoise planetary ranging equipment was designed and installed at DSS 14 as part of the celestial mechanics experiment of the *Mariner* Venus 1967 mission (SPS 37-42, Vol. III, pp. 52–56, and SPS 37-50, Vol. II, pp. 54–69). The equipment consisted of two racks of analog equipment, one rack of digital equipment, and an SDS 920 computer. It was used again in support of the *Mariner* Mars 1969 mission from launch through Mars encounter. At this time, the signal level dropped below the threshold of the equipment, which was then returned to JPL where it was rebuilt to improve its operational and performance characteristics.

The objectives of this rebuilding effort were:

(1) To improve measurement accuracy and long-term stability.

(2) To automate the checkout and calibration procedures.

(3) To improve the operational capabilities of the software.

(4) To improve maintainability.

These objectives were met by redesigning the analog and digital hardware to eliminate sources of inaccuracy and drift, by reprogramming the computer to provide the checkout and operational characteristics desired, and by providing the spares necessary for adequate maintenance.

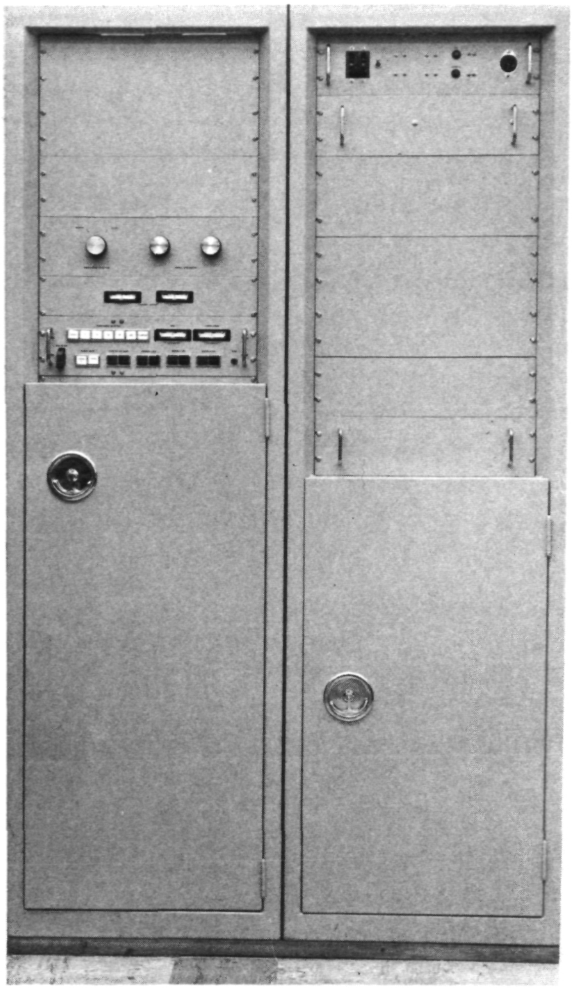

Fig. 1. Tau ranging subsystem

Figure 1 is a photograph of the rebuilt tau ranging subsystem, and Fig. 2 shows the functional interaction of the components of the rebuilt tau ranging subsystem. Several significant changes were made:

(1) The receiver coder switch loop was removed, and the digital correlators and the correlator switching assembly were added to enable synchronization of the transmitter and receiver coders.

(2) A precision frequency synthesizer was designed to drive the transmitter coder and the clock doppler detector (SPS 37-63, Vol. II, pp. 42–44).

(3) The maximum frequency of the UHF doppler counter was increased to 100 kHz.

(4) The computer was reprogrammed to automate the calibration and alignment procedure, to measure and compensate for unavoidable drifts in the hardware, and to perform extensive error checking as an aid to hardware troubleshooting.

2. Digital Hardware

The digital hardware was repackaged into card cages and installed in one standard DSIF digital rack. Signal input and output buffering was added where required by the length of interconnect wiring.

The main functional blocks of the ranging subsystem are as follows:

(1) Transmitter and receiver code generators.

(2) Receiver code output control.

(3) One-second interrupt and timing.

(4) Clock doppler counter.

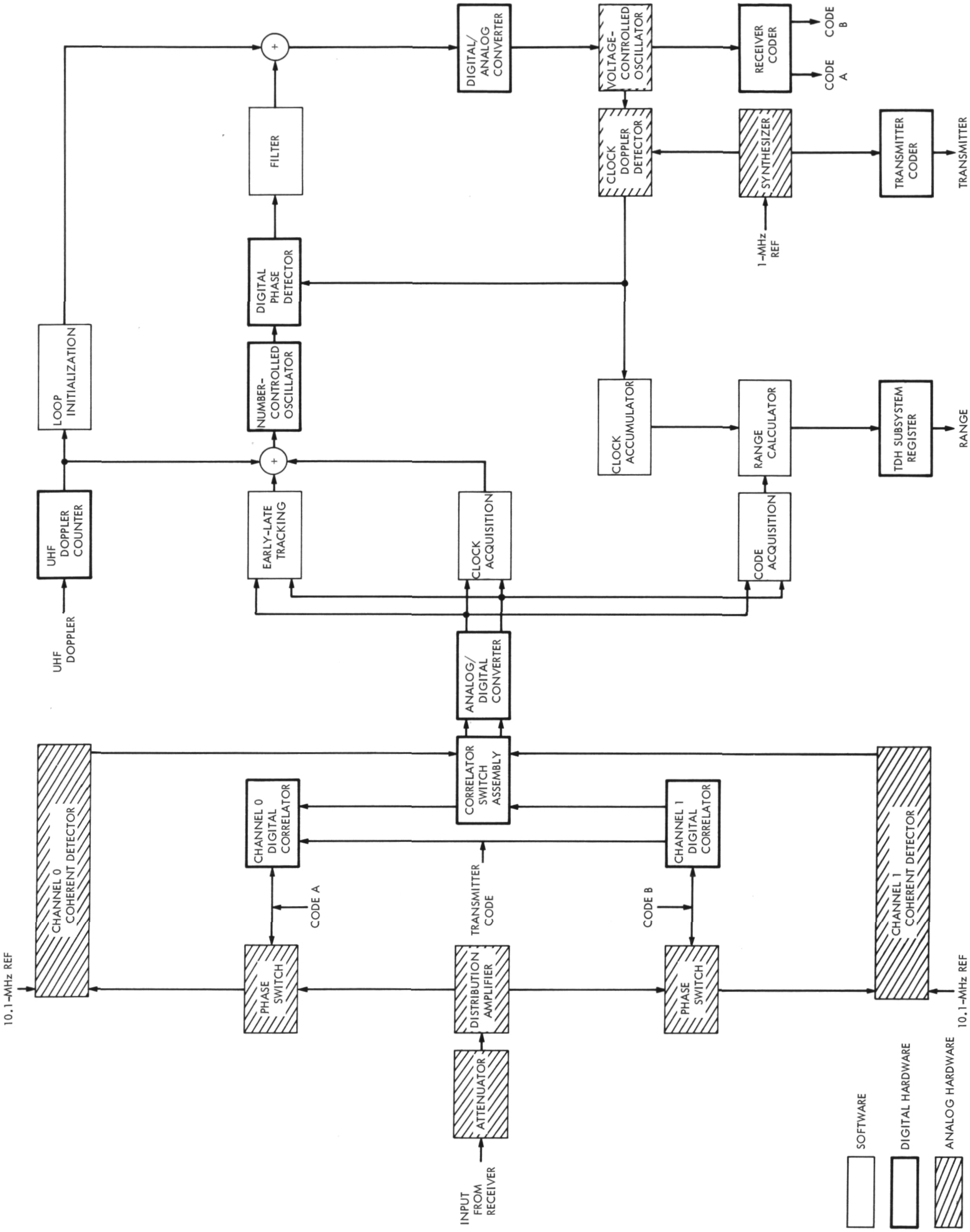

Fig. 2. Tau ranging subsystem block diagram

(5) Fractional cycle counter.

(6) Number-controlled oscillator.

(7) Computer interface.

(8) Digital phase detector.

(9) UHF doppler counter.

(10) Range data output register.

(11) Correlator switching assembly.

Blocks 1 through 6 were unchanged except for the additional signal buffering required by the longer interconnect harness. SPS 37-50, Vol. II, pp. 54–61, explains the operation of these blocks.

a. Computer interface. The computer interface was changed to provide digital input buffering, command energize output M (EOM) decoding, and output gating in a central location. The EOM decoding structure was changed for compatibility with the telemetry and command processor (TCP) EOM structure. This structure permitted only 12 distinct EOMs to be used for ranging. The flag bits (C_0, C_1, and C_2) were used to expand the number of EOMs to the 35 required by the tau ranging subsystem.

b. Digital phase detector. The digital phase detector is a counter that is used to give the time measurement of the phase difference between the number-controlled oscillator (NCO) output and the clock doppler to the nearest 2 μs. The counter was modified so that it is started by the clock doppler pulse and stopped by the NCO. This modification causes the phase detector count to be ready at NCO interrupt time and eliminates the necessity of generating a separate phase detector interrupt to the computer.

c. UHF doppler counter. The UHF doppler counter was redesigned to increase the maximum frequency to 100 kHz. Two full-length counters were installed which alternately count the received signal; one counter (A) counts the signal for one sample period while the other counter (B) remains stationary for readout. During the following sample period, counter B counts while counter A data are read out. All of the cycles of the input signal are counted, using this approach, and an entire sample period is available for data readout.

d. Range data output register. The range data register was changed to convert the data output signals from relay contact closures to logic levels compatible with the tracking data handling (TDH) subsystem. The register is composed of two identical storage registers, each holding one-half of the range word. These registers are loaded with the current range by the computer each time the TDH subsystem requests an updated range.

e. Correlator switching assembly. This assembly switches the channel 0 and 1 inputs of the doppler aid loop between the coherent amplitude detectors in the ranging demodulator assembly and the auxiliary correlators in the digital control assembly. The auxiliary correlators are used to synchronize the receiver and transmitter coder clocks prior to code synchronization, a function performed by the switch loop in previous pseudonoise ranging systems. The correlators are connected directly between the digital outputs of the receiver and transmitter coder clocks. Code synchronization is accomplished as follows: The doppler aid loop input is switched to the auxiliary correlators, the loop locked to the correlator output, and the "clock" component acquired in the normal manner. The receiver coder and transmitter coder clocks are now in phase and the receiver coder is synchronized to the transmitter coder. The doppler aid loop input is then switched to the coherent amplitude detectors and locked to the received signal to begin the ranging acquisition.

3. Conclusions

The rebuilt tau ranging subsystem has been functionally tested and is installed in the control room at DSS 14. It is awaiting final testing with the *Mariner* Mars 1969 spacecraft to demonstrate its capability to support the *Mariner* Mars 1971 mission.

The subsystem has been substantially improved in the digital, analog, and software areas to increase the long-term stability, decrease the signal threshold, and improve operational reliability.

X. DSN Projects and Systems Development

DEVELOPMENT AND IMPLEMENTATION

A. DSN Status Code, *R. B. Rung and L. W. Miller*

1. Introduction

A design goal of the DSN Monitor System and DSN Operations Control System is to provide for automated reporting of DSN status to DSN management and to the individual flight project. The methodology by which this information will be displayed was discussed in SPS 37-61, Vol. II, pp. 147–149. The next step in this design has been accomplished, i.e., defining a summarized format which accurately indicates the current status of the DSN. The information will be derived from the DSN Monitor System and will indicate in a basic format the status, at each facility, of the DSN Command, Telemetry, and Tracking Systems. Data quality will be treated in a manner somewhat analogous to that used for writing the DSN master data records (SPS 37-62, Vol. II, pp. 7–12); however, emphasis is on data flow. This article describes the rationale upon which the display will be based.

2. Deep Space Instrumentation Facility

Within a DSS, there is more than one data flow path for each data type. The status code algorithm automatically selects only that configuration which has been established by DSS personnel as the "critical" data path to monitor. For example, assuming Telemetry and Command Processor (TCP) beta and CMA-2 (Command Modulator Assembly) were attached to the transmitter as the selected command path, this would be the only path monitored for a DSN status display. Correspondingly, the prime receiver, Subcarrier Demodulator Assembly, and TCP (Symbol Synchronizer Assembly and Block Decoder Assembly, if applicable) as selected by station personnel, would be the only equipment monitored for both configuration and performance of the Telemetry System. Tracking System monitoring is based on the paths selected for doppler and ranging.

The status of each system will be displayed on a scale from 9 to 0, with 9 being "perfect" performance with the highest equipment complexity. The next few lower numbers still indicate "perfect" performance, but at a lower level of hardware complexity in use; e.g., in Table 1 the numerical value 8 is based on a logical condition producing good two-way doppler but with the ranging modulation turned *off*. Still lower numbers indicate marginal or defective system performance; again in Table 1, the numerical value 6 indicates that the transmitter is *on*, ranging modulation is *on*, but the ranging receiver is out of lock. Tables 1, 2, and 3 show the numerical assignments for the Tracking, Command, and Telemetry Systems, respectively.

3. Ground Communications Facility

Entry of GCF data into this system is complex, due to the use of time (block) division multiplexing on the high-speed data (HSD) system. It is also complicated by the lack of automated instrumentation on the TTY system. However, that information which the GCF monitor sends to the DSN monitor contains sufficient high-speed data system performance status to provide both error rates and alarms. The Tracking System, being the only prime user of TTY, has established a TTY outage detection program within the Central Processing System (CPS). Therefore, it is possible to develop and display, on the same 9 through 0 scale, the general condition of GCF as a facility for all systems (Table 4).

Table 1. Tracking System

9	Good two-way doppler with ranging
8	Good two-way doppler
7	Good one- or three-way doppler
6	Good two-way doppler with ranging out of lock
5	Not assigned
4	Not assigned
3	Station *on*, transmitter bad
2	Station *on*, receiver out of lock
1	Station *on*, transmitter bad, and receiver out of lock
0	Station scheduled *off*

Table 2. Command System

9	Command modulation *on*, two-way lock
8	Command modulation *on*, receiver out of lock
7	Command modulation *on*, two-way lock (abort last five seconds)
6	Command modulation *on*, receiver out of lock (abort last five seconds)
5	Not assigned
4	Not assigned
3	Not assigned
2	Not assigned
1	System *on* with major system failure
0	Station command, system scheduled *off*

Table 3. Telemetry System

9	System operating OK as selected
8	Not assigned
7	Multiple-channel telemetry, science signal-to-noise ratio (SNR) *alarmed*
6	Multiple-channel telemetry, engineering SNR *alarmed*
5	Single-channel telemetry, SNR *alarmed*
4	Multiple-channel telemetry, science out of lock
3	Multiple-channel telemetry, engineering out of lock
2	Single-channel telemetry out of lock
1	Not assigned
0	System scheduled *off*

4. Space Flight Operations Facility

The Central Processing System in the SFOF will both drive the DSN status display and report partial status on internal processing. The extent to which the CPS can degrade in performance and still provide displays is not currently known. Therefore, the CPS is constrained to provide status display information only as to throughput, i.e., system data record (SDR) generation, common to all systems. Again, the display will be based on a 9 through 0 scale (Table 5), with the perfect state being a 9.

Table 4. GCF conditions

9	Up, good
8	Not assigned
7	Not assigned
6	TTY alarmed
5	HSD alarmed
4	HSD alarmed, TTY alarmed
3	Communications processor (CP) down
2	HSD down
1	System down (HSD and CP/TTY down)
0	Scheduled off

5. Display

The display will take the form:

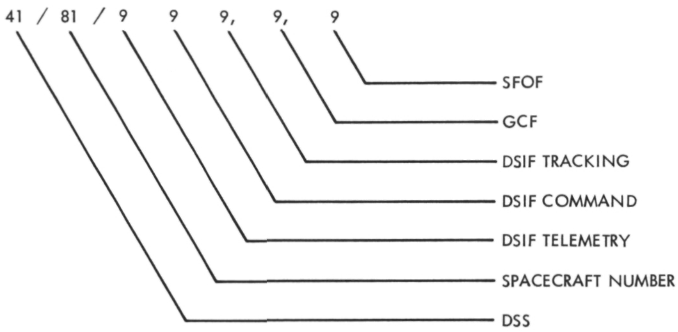

It is fully compatible with the Digital Television System and can be added to existing or planned volatile and printed data displays. It is also compatible with the current projection display system in the DSN Operations Control Area.

Table 5. CPS 360 conditions

9	Up, good, all system data records (SDRs) being written
8	Not assigned
7	Command SDR alarming
6	Telemetry SDR alarming
5	Not assigned
4	Tracking SDR alarming
3	Not assigned
2	Multiple SDRs alarming
1	System in recovery
0	Scheduled off

6. Implementation Status

The algorithms to provide this display have been developed and are in the process of being incorporated in a software requirements document for implementation in the *Mariner* Mars 1971 time period.

B. The DSN User Requirements Forecast,

R. Rubinstein

In March 1970 work was started to implement a data bank for DSN planning and systems engineering. In May the first tabulation of the data called *DSN User Requirements Forecast* was published. Subsequently, changes were made and an updated version was published on September 1, 1970.

One of the major objectives of the DSN is to support present and future Deep Space Missions. This objective can be stated in terms of requirements imposed by the missions on the DSN. The DSN planning and the systems engineering functions are to produce alternatives which will satisfy these requirements and select an optimum solution by some criteria; the main difference between planning and systems engineering being in the direction and granularity of the different conceptual and implementation processes but not in the approach and methods per se. This delineates the relationship of requirements vis-à-vis the planning process. For the planning to be meaningful, the requirements have to be amenable to analysis.

Therefore, the quality of the analysis will depend not only on the goodness of the data (validity, relevance, accuracy) describing the requirements, but also on the appropriateness of their organization. It will now be shown how this was done and the use of the organized data will be illustrated.

Discussions with advanced mission planning and systems engineering personnel in the DSN resulted in the determination of 173 data categories for the deep space missions of the decade 1971–1980. A total of 6900 data words were then obtained in these categories from the DSN managers of the planned projects. The large number of data words resulted from the requirements to list all mission parameters for each distinct mission phase (near-earth, midcourse, cruise, encounter, etc.) It soon became clear that a mechanized data system was necessary, not only because of economic reasons but even more compelling, on grounds of a fast response of the system to changes. This included the ability to quickly:

(1) Accommodate updates (change of data words) and modifications (change in data categories).

(2) Change the format of the tabulated data.

(3) Produce reports on selected data.

The Mark IV File Management System, a proprietary software product of Informatics, Inc., for data processing was selected for implementation. As this system was being used on the Laboratory for other data management functions, its implementation for the DSN involved only incremental costs. The Mark IV System resides in the IBM 360/75 located in the SFOF.

The DSN User Requirements Forecast consists of 17 tables of data together with notes and comments, all computer generated, and has a total of 52 pages. It is an ordered compilation of all project information and is broken down into the following main categories:

(1) Project and Mission.

(2) Telemetry.

(3) Command.

(4) Tracking.

(5) Operations.

(6) Simulation.

Within each category the data are listed sequentially in the order of projects (by launch date) and within each project sequentially in the order of mission phases. Tables 1 and 2 illustrate the type of information that can be extracted from the *Requirements Forecast.* Looking at the telemetry subcarrier characteristics, it becomes evident that a large degree of commonality exists among the characteristics of all missions. Thus, by providing a maximum of two Subcarrier Demodulation Assemblies per Deep Space Station for PCM/PSK/PM modulation with a range of frequencies from 24 to 2000 kHz, and accommodating a range of modulation indices from 11 to 73 deg, a multi-mission capability in the next decade can be established for all missions except for Planetary Explorer Venus 1975. Similarly, a cursory analysis of command characteristics reveals different requirements in terms of subcarrier waveform and modulation type indicating that a multi-mission capability for command subcarriers does not seem practical. A possible solution might consist of asking some projects to change their requirements. While not all data lend themselves to such a simple analysis, the examples nevertheless demonstrate that a judicious representation and ordering of data can be advantageous.

The DSN User Requirements Forecast has been adopted as the single source for project information by all DSN planning and systems engineering personnel. It will be continuously updated and new issues will be published when needed.

Table 1. Telemetry subcarrier characteristics

Mission	Number of simultaneous subcarriers per carrier	Subcarrier frequency, kHz	Waveform	Modulation type	Modulation index, deg
Mariner Mars 1971	2	24	Square	PCM/PSK/PM	12–41
		34.286 or	Square	PCM/PSK/PM	50.5
		259.2	Square	PCM/PSK/PM	65
Pioneer F (1972)	1	32.768	Square	PCM/PSK/PM	51–63
Pioneer G (1973)	1	32.768	Square	PCM/PSK/PM	51–63
Mariner Venus–Mercury 1973	2	*	Square	PCM/PSK/PM	41
		*	Square	PCM/PSK/PM	70
Helios 1974	1	32.768	Square	PCM/PSK/PM	11–72
Planetary Explorer Venus 1975	1 bus	50	Square	PCM/PSK/PM	57
	1 probe	35	Square	PCM/PSK/PM	57
	3 miniprobes with MFSK, no subcarrier				
Helios 1975	1	32.768	Square	PCM/PSK/PM	11–72
Viking 1975 Orbiter	2	24	Square	PCM/PSK/PM	41
		34.286 or	Square	PCM/PSK/PM	11
		259.2	Square	PCM/PSK/PM	65
Viking 1975 Lander	2	23.36	Square	PCM/PSK/PM	25.8–45.8
		144	Square	PCM/PSK/PM	45.8
Grand Tour 1977	2	50	Square	PCM/PSK/PM	11–30
		1000–2000	Square	PCM/PSK/PM	35–73
Grand Tour 1979	2	50	Square	PCM/PSK/PM	11–30
		1000–2000	Square	PCM/PSK/PM	35–73

MFSK = M-ary frequency-shift keying
PCM = pulse-code modulation
PSK = phase-shift keying
PM = phase modulation
* = unknown at present

Table 2. Command characteristics

Mission	Subcarrier waveform	Subcarrier frequency, Hz	Modulation type	Modulation index, deg	Bit rate, bits/s
Mariner Mars 1971	Square	255	PSK–2 channels	36.4	1
				33.8	
Pioneer F (1972)	Sine	128–204.8	FSK	51–63	1
Pioneer G (1973)	Sine	128–204.8	FSK	51–63	1
Mariner Venus–Mercury 1973	Sine	*	PSK–2 channels	*	1
Helios 1974	Square	512	PSK–1 channel	*	1–4
Planetary Explorer Venus 1975	Not applicable	1000	8-level MFSK	57	1–100
Helios 1975	Square	512	PSK–1 channel	*	1–4
Viking 1975	Sine	500	PSK–1 channel	47.6	4
	Sine	656	PSK–1 channel	47.6	4
Grand Tour 1977	Square		PSK–1 channel	56.7	4–64
Grand Tour 1979	Square		PSK–1 channel	56.7	4–64

MFSK = M-ary frequency-shift keying
FSK = frequency-shift keying
PSK = phase-shift keying
* = unknown at present

XI. DSN Operations

OPERATIONS AND FACILITIES

A. DSN Command System Analysis Group,

W. G. Stinnett

1. Introduction

The key characteristic of the 1971 era DSN Command System is centralized control at the Space Flight Operations Facility (SFOF). Command System data are generated at the SFOF, transmitted via high-speed data lines (HSDL) by the Ground Communications Facility (GCF), and received by the Telemetry and Command Processor (TCP) at the Deep Space Station (DSS). System status and alarm information is returned via the same HSDL.

Figure 1 is a simplified functional diagram of the DSN Command System. Command data and system instruction data originate at the SFOF and are transmitted by high-speed data (HSD) messages to the DSS. The messages are returned to the SFOF where a bit-by-bit comparison is accomplished. Failure to verify initiates automatic re-transmission of the message until a successful verification is accomplished. Prior to actual spacecraft commanding, the DSN sends the appropriate mission configuration message, and the standards and limits message to the DSS. The mission configuration message sets the appropriate values in the TCP to allow proper computer control of the Command Modulator Assembly (CMA). The standards and limits message includes alarm warning conditions and command abort conditions for symbol rate, subcarrier frequencies, and also sets the exciter frequency. After the configuration and standards and limits are set, the DSN sends a test command to the DSS to verify that the system is operational. At the conclusion of this test, the project may enter command data into the system. Storage of commands in the TCP, sequence of transmission, and time of command transmission to the spacecraft are controlled by project inputs into the system at the SFOF. Data may be recalled from the TCP at any time to verify the contents of command storage. Alarms and status information are generated by the TCP when the standards and limits are violated or when conditions do not meet pre-defined standard conditions. The alarm and status information are transmitted to the SFOF via HSD. Successful command transmission to the spacecraft or an attempt at transmission results in an HSD confirmation or abort message to the SFOF.

"PAGE MISSING FROM AVAILABLE VERSION"

As a backup to the prime operational mode described above, all system input data can be manually typed into the TCP at the DSS in case of HSDL failure. Voice and teletype communications between the SFOF and DSS provide for data transmission, verification, confirmation, and system status.

Digital magnetic tape records of the HSD messages described above exist in the DSN Command System. The TCP records all inbound and outbound HSD messages and this record is defined as the Original Data Record (ODR). Likewise, the SFOF Central Processing System (CPS) records all inbound and outbound HSD messages on what is defined as the System Data Record (SDR). The SDR is utilized to construct the DSN Command System Master Data Record (MDR).

2. Functions of the DSN Command System Analysis Group

The functions accomplished by the DSN Command System Analysis Group can be divided into *real-time* and *non-real-time* tasks. Real-time tasks include: monitor and analyze the performance of the DSN Command System, maintain interface with the DSN Operations Control Team, maintain appropriate operations and performance logs, validate the contents of the DSN Command System Data Record (SDR), and ensure generation of the DSN Command System Master Data Record. Non-real-time tasks include: supervise and support real-time functions, accomplish second-level performance analysis, and maintain performance and historical records.

a. Real-time functions. The real-time Command System Analyst is a member of the Network Analysis Team (NAT), and occupies an operational position in the SFOF. In addition to providing operational data for input into the Command System, the analyst is required to establish a technical interface with project and DSN Operations Control Team members. He is responsible for reporting Command System status on a regular basis and upon request. Digital television displays, character printer displays, line printer displays, voice communication circuits, and an input/output device are available for accomplishing the real-time functions.

The analyst is responsible for monitoring and analyzing the operational performance of the DSN Command System. Prior to DSS acquisition of the spacecraft, the analyst will ensure that the proper configuration and standards and limits data are available for transmission to the TCP. There exists multiple-command processors in the SFOF CPS to support multiple-TCP activity. These command processors must be initialized and allocated for use prior to HSD transmission. The analyst will monitor the activity and allocation of these processors. The analyst maintains knowledge of the HSD circuit status by monitoring the results of configuration, standards and limits, and test command message transmission to the DSS. Throughout the station's track the analyst monitors the HSD transmission verification loop, DSS Command System status, SDR logging status, command configuration results, and HSDL status.

The analyst maintains an interface with the DSN Operations Control Team. He ensures that the proper configuration and standards and limits messages are transmitted to the TCP by operations personnel. He reports test command transmission results to the DSN Operations chief. On a regular basis, or upon request, the analyst reports system status. The analyst identifies and reports system anomalies to appropriate operations personnel. At the conclusion of the station's track, the analyst determines if data outages exist on the SDR. He will request recall of command data from the TCP ODR to fill the data gaps.

For real-time and off-line analyses, the analyst will maintain appropriate operational logs. In most cases, the logs are generated automatically by the system and include records of: system alarms, commands entered into the system, commands confirmed/aborted, and command system instructions. In addition to the logs defined above, the analyst maintains logs of appropriate performance parameters and system test results.

At the conclusion of a station's track, the analyst makes appropriate entries into the system with an input/output device to accomplish validation of the contents of the SDR. The results of this validation allow determination of data outages and the corresponding data recall requirements. If data recall from the TCP ODR is necessary, the analyst ensures that merge of the recall data on the SDR is accomplished successfully.

The DSN is required to deliver a Master Data Record to the project, 24 hours after a station's track. The analyst ensures that extraction of data from the SDR is accomplished to generate the MDR. The analyst verifies that the contents meet DSN and project-negotiated requirements. Supplementary documentation accompanies the MDR when it is transferred to the project and the analyst collects this required documentation.

b. Non-real-time functions. The non-real-time functions of the group include: assistance in DSN Command System upgrade, supervision and support of real-time functions, accomplishment of second-level analysis of the Command System, and maintenance of performance and historical records.

The Command System Analysis Group is a principal user of the DSN Command System. As a user, the group assists in Command System upgrade. Operational requirements, hardware requirements, and software requirements are documented for use by the system planning and design engineers. The group assists in system upgrade testing by documenting appropriate procedures, manning operational positions, and documenting test results. In addition to the pre-implementation functions listed above, the group provides system operational performance results to the design engineers for future use in system upgrade.

One of the major tasks of non-real-time personnel is supervision and support of real-time functions. The DSN Command System is scheduled for use by the project for spacecraft commanding. Real-time personnel are scheduled for an operational position based upon Command System activity. The non-real-time personnel will generate appropriate configuration and standards and limits card files for use by the DSN Command System. In addition to the day-to-day scheduling of personnel and file generation, the non-real-time personnel will ensure the proper training of real-time personnel and will maintain current real-time operations and analysis procedures.

Detailed performance analysis of the DSN Command System is accomplished by the group. This analysis provides a measure of the support provided by the DSN Command System to a given project. The analysis data are also utilized as feedback information to system design engineers and also as an aid to improving operational procedures. The group is tasked to document appropriate analysis results, maintain performance logs, and maintain documented records of data package transfers and location.

XII. DSIF Operations

OPERATIONS AND FACILITIES

A. Radio Science Support, *T. Sato, L. Skjerve, and D. Spitzmesser*

1. RAES Panel Activities

The Radio Astronomy Experiment Selection (RAES) Panel has favorably evaluated one of the three proposals that were submitted during the last reporting period (SPS 37-65, Vol. II, pp. 132–133). Table 1 gives a general summary of this new experiment. Also, two new proposals have been received. These will be forwarded to the Panel for review by November 1, 1970.

2. Radio Science Operations

Since September 1, 1970, two radio science experiments, previously approved by the RAES Panel, have been conducted at DSN facilities.

a. Test of general relativity by VLBI techniques. During the first two weeks of October 1970, a team of experimenters, with members from the Goddard Space Flight Center (GSFC), the Jet Propulsion Laboratory (JPL), and the Massachusetts Institute of Technology (MIT), conducted an experiment designed to test the theory of general relativity. The objective was to measure, by the use of very long baseline interferometer (VLBI) techniques, the apparent change of angular separation between two radio sources, 3C273 and 3C279, near the solar occultation of the latter. This is an annual event and occurs in early October.[1]

The interferometer consisted of two fully steerable parabolic antennas, operating at 7840 MHz (3.8 cm), located on an east–west transcontinental baseline. The West Coast terminal was the DSN 210-ft antenna facility (DSS 14) located at Goldstone, California, while the East Coast terminal was the 120-ft MIT–Haystack facility located near Tyngsbord, Massachusetts. The block diagram of the configuration employed at DSS 14 is

[1]In October 1969, two experimental teams attempted similar experiments utilizing short baselines. One utilized DSN facilities at Goldstone (SPS 37-60, Vol. II, pp. 170–173, and Ref. 1), while the other team utilized the facilities of the Owens Valley Radio Observatory (Ref. 2).

Table 1. Summary of recently approved experiments

Experimenter	Affiliation	Objective	Comments
Dr. J. Broderick Dr. B. Clark Dr. M. Cohen Dr. D. Jauncey Dr. K. Kellermann	National Radio Astronomy Observatory National Radio Astronomy Observatory California Institute of Technology Cornell National Radio Astronomy Observatory	To determine structure of 50 extragalactic radio sources	Will use various baselines by employing NRAO 140-ft facility and selected DSN 85-ft facilities. First observation scheduled for Nov. 23, 1970

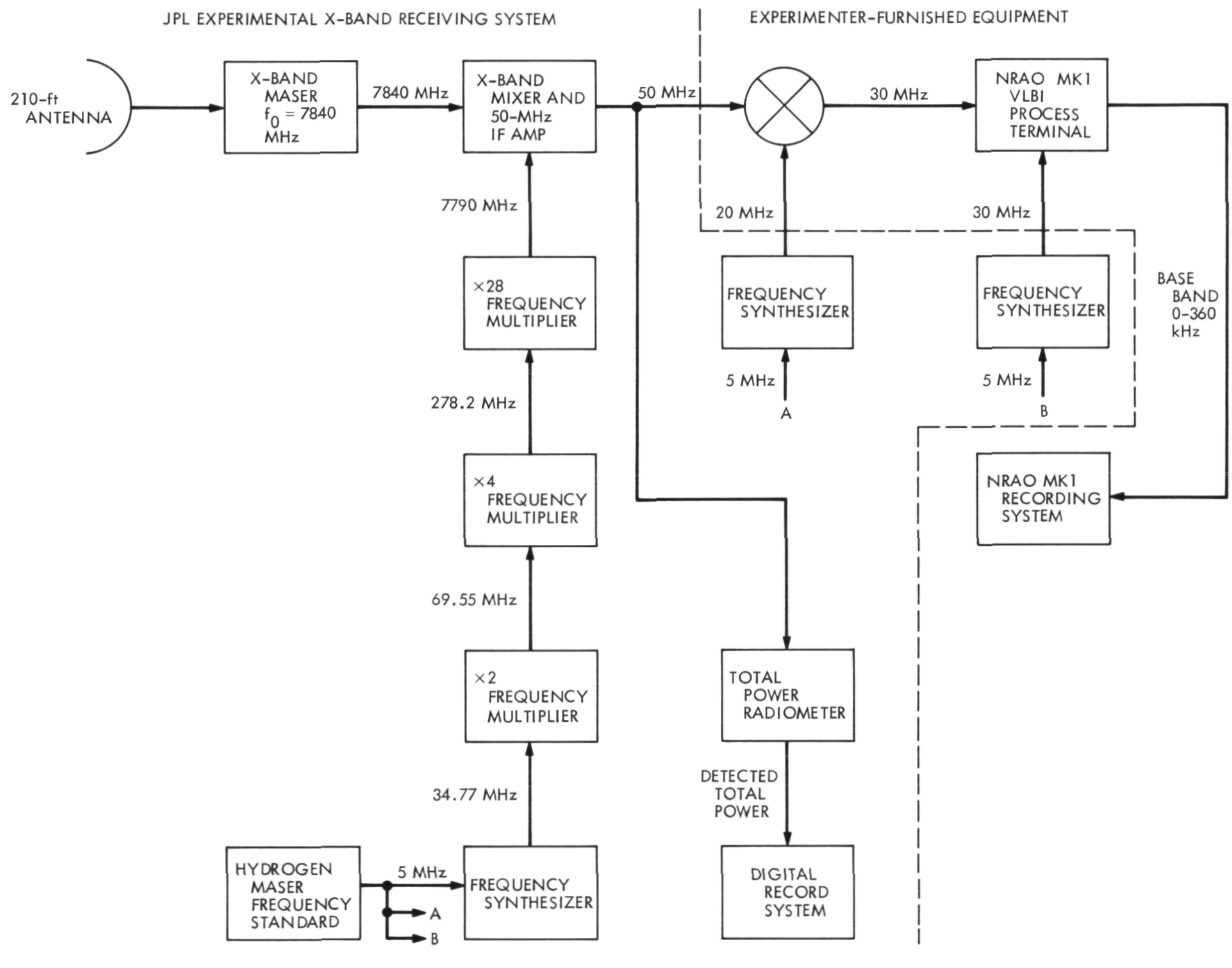

Fig. 1. DSS 14 configuration for X-band general relativity experiment

shown in Fig. 1. At both terminals, all local oscillator frequencies were coherently synthesized from hydrogen maser frequency standards, while the data were processed and recorded by standard National Radio Astronomy Observatory (NRAO) Mark I VLBI terminal equipment.

The experimental observations took place from 16:00 to 21:00 UT during the period October 1–6, 1970 and from 15:00 to 20:00 UT during October 10–15, 1970. The observational format was to observe 3C273 for 50 s, allow 70 s to switch sources, then observe 3C279 for 110 s and then switch back to 3C273.

At this writing, the data obtained during the October 1–6, 1970 observations have been partially processed on the IBM 360 computer located at GSFC. Fringes were obtained on both sources on the first five days; however, definitive results must await complete data processing.

b. Pulsar polarization study. In 1968 and 1969, Dr. R. D. Ekers and Dr. A. T. Moffet of the Owens Valley Radio Observatory utilized the facilities at DSS 14 to study polarization characteristics of five pulsating radio sources at 2295 MHz (Ref. 3). The installation of a polarization diversity S-band (PDS) feed cone at DSS 14 in September 1970 enabled further polarization studies by the remaining member of the team, Dr. A. T. Moffet; these were conducted from 00:00 to 13:00 UT on October 7, 1970.

The PDS cone is equipped with a dual-polarized feed system, and the independent orthogonal outputs may be fed to separate low-noise S-band receivers. The outputs of the receivers, which were proportional to the amplitudes of the two orthogonal components of the received signal, were fed to an experimenter-supplied polarization detector. The output of the polarization detector provides four base band signals which are linear combinations of the four Stokes parameters. These signals may then be used to completely define the polarization of the received pulses. The output of the detector is fed to a four-channel signal averager for final processing and display.

During the observation several pulsating radio sources were observed and the data obtained are being processed by the experimenter.

References

1. Muhleman, D. O., et al., "Radio Interferometric Test of the General Relativistic Light Bending Near the Sun," *Phys. Rev. Lett.*, Vol. 24, No. 24, pp. 1377–1380, June 15, 1970.
2. Seielstad, G. A., et al., "Measurement of the Deflection 9.602 GHz Radiation from 3C279 in the Solar Gravitational Field," *Phys. Rev. Lett.*, Vol. 24, No. 24, pp. 1373–1376, June 15, 1970.
3. Ekers, R. D., and Moffet, A. T., "Polarization of Pulsating Radio Sources," *Astrophys. J.*, Vol. 158, No. 1, Part 2, pp. 61–68, Oct. 1969.

XIII. Facility Engineering

OPERATIONS AND FACILITIES

A. DSS 61/63 Facility Modifications and Construction, *R. Casperson, G. Kroll, and L. Kushner*

1. Introduction

DSS 61/63 is in process of becoming an 85-ft-diam/210-ft-diam antenna complex (Fig. 1). This article describes the facility modifications and construction necessary to accomplish this reconfiguration.

The primary tasks are:

(1) Modify the operations and engineering building.

(2) Modify and extend the utilities support building (power plant).

(3) Modify and extend the water and sewerage systems.

(4) Modify and extend the electrical generation and distribution systems.

(5) Modify the site grading, paving, and drainage configuration.

(6) Convert the dormitory building into a maintenance facility.

(7) Construct the RF protection and utility tunnel.

(8) Install fire protection and safety equipment.

(9) Modify and extend the NASCOM building.

(10) Construct the high-power transmitter support facilities.

(11) Construct the antenna pedestal and alidade building and associated facilities.

All of the tasks, except task 11, are being accomplished through the U.S. Navy, Officer in Charge of Construction, Naval Facilities Engineering Command, Madrid, Spain. Task 11 is included in the Collins Radio Company, Richardson, Texas, contract for the fabrication, construction, and testing of a 210-ft-diam antenna at DSS 63.

In general, the facility modification tasks provide the space, weather protection, heating, lighting, ventilation,

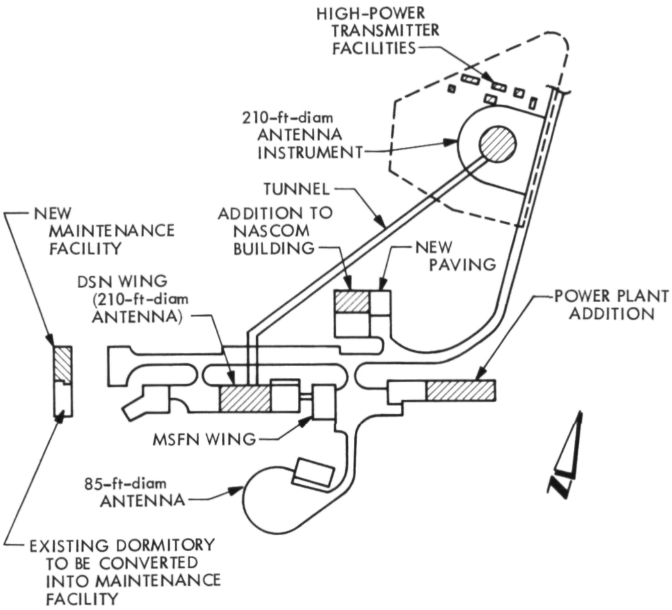

Fig. 1. Plot plan for DSS 61/63 complex

air conditioning, power, water, sewerage, fire protection, safety, and access to support the equipment and personnel necessary to operate the 85-ft-diam/210-ft-diam antenna complex.

2. Task 1

The operations and engineering building is being modified (Fig. 2) to increase the DSN control room size to 3600 ft², increase the plenum size to 3600 ft², replace the fixed floor with a modular removable floor, increase the air conditioning capacity to meet the 1973 to 1975 era electronic load cooling requirements, increase the electrical power distribution system, and provide access from the tunnel to the operational areas of the building.

3. Task 2

The utilities support building (power plant, Fig. 3) is being enlarged to accept six 750-kW engine-generator

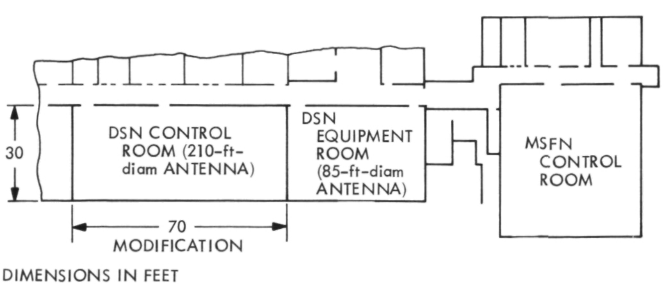

Fig. 2. Operations and engineering building plan

sets and associated controls, switchgear, transformer fuel storage and distribution, batteries, etc.

The reconfigured power plant will include a control console for automating of power generating equipment and for load sharing and synchronizing of standby units. An annunciator status panel is being provided. A 1500-kW load bank is to be permanently installed so that power generating equipment can be tested during normal plant operations without interference.

4. Task 3

The estimated maximum water usage for the complex is 300,000 gal per month with a maximum daily usage of 15,000 gal. The existing two wells are to be augmented with a third well to increase the present minimum flow of 12,000 gal per day. Storage capacity will be increased from 50,000 to 100,000 gal. At all times, 50,000 gal will be held in reserve for fire protection purposes. The water distribution system, including fire mains and hydrants, will be extended to all new facilities.

The sewerage collection system will be extended and rerouted as necessary to support all new and modified facilities. No additional disposal or treatment equipment or construction is required.

5. Task 4

It is planned initially to install four 750-kW engine generator sets to support the new 210-ft-diam antenna through the 1973 era. Two additional units will be installed to support the high-power transmitter when it is implemented in the 1975 era.

The 85-ft-diam antenna power plant capacity will be modified to reduce the standby capacity. The 85-ft-diam antenna units and the 210-ft-diam antenna units operate at different voltages; transformers and switching will be provided to permit mutual support.

The power plants will have two basic types of diesel engines: 12 cylinder engines for driving the 350- and 500-kW generators, and 16 cylinder engines for driving the 750-kW generators. The engines are of the same configuration and manufacture. Spare parts and engine operational procedures are common to both types.

Power loads for the complex were developed (Table 1), utilizing actual power demands from the existing 210-ft-diam antenna station at DSS 14, from the existing

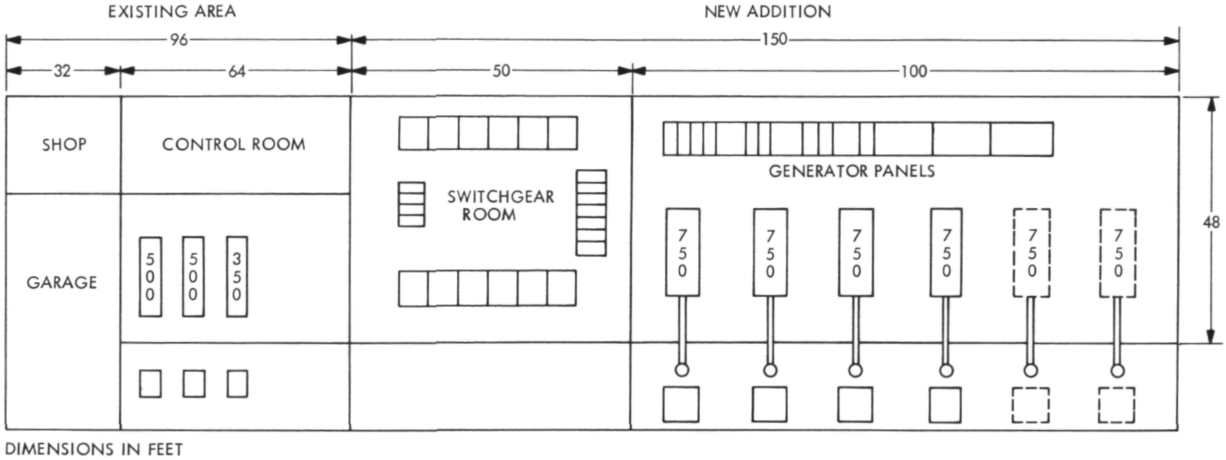

Fig. 3. Utilities support building (power plant) plan

85-ft-diam antenna station at DSS 61, and from projections of requirements of additional planned equipments.

The configuration for the electrical generation and distribution systems (Table 2) is based on the DSN power philosophy which requires enough generator capacity to supply the maximum demand plus one spare of the largest unit in ready standby and one spare of the largest unit assumed down for routine maintenance.

The existing power distribution system will be enlarged and extended as necessary to integrate the existing system with the new and to provide power to all modified and new facilities. Spare duct capacity will be provided for future growth requirements. Power for the 210-ft-diam antenna system will be distributed at 2400 V, as it is at DSS 14.

Table 1. Power requirements

Power function	1973 load, kW	1975 load, kW
Electronics/communications	425	475
Antenna drive	500	500
Power plant auxiliary	75	150
Transmitter	100	1650
Station support	1575	1525

Table 2. Engine-generator units required

Generator function	1973 units	1975 units
Operational	1 350-kW	1 350-kW
	2 500-kW	2 500-kW
	2 750-kW	4 750-kW
Standby	1 750 kW	1 750 kW
In maintenance	1 750-kW	1 750-kW

6. Task 5

To accommodate the considerable site changes caused by constructing the 210-ft-diam antenna pedestal and apron and by extending the utility building and the access and RF protection tunnel, the site storm drainage system is being redesigned.

On-site access roads will match existing construction. Additional paving will be placed to and around the 210-ft-diam antenna, and on the south side of the utility building. Twelve additional parking places will be provided adjacent to the 210-ft-diam antenna.

The existing off-site access roads are considered adequate. No changes are currently considered since no significant increase in operations traffic is anticipated. No landscaping is currently planned.

7. Task 6

An additional 1500 ft^2 is being added to the dormitory building and the building is being modified to provide a 4500-ft^2 maintenance facility for the complex. This facility will contain a TTY maintenance shop, a shipping, receiving and storage area, a module maintenance laboratory, a dc and low-frequency standards laboratory, a microwave standards laboratory, in instrument maintenance laboratory, and two offices.

8. **Task 7**

A RF-shielded personnel access tunnel is to be provided to the 210-ft-diam antenna pedestal. This access will be a walk-through type, ventilated, drained, and well lighted. Signal and power cables between the pedestal and operations building will be routed through the tunnel via wall-mounted cable trays. This tunnel will originate in the operations building basement.

9. **Task 8**

Fire protection and safety modifications will be made in all existing and new buildings. Sensing devices, sprinkler systems, fire water distribution systems, hydrants, fire water storage, and fire resistant construction will be provided.

10. **Task 9**

The NASCOM building extension (Fig. 4) consists of construction of a 3000-ft^2 addition, modifications of service utilities, a new heating and air conditioning system for the new and existing sections, and the installation of an uninterruptible power supply to serve the facility electronic bus.

11. **Task 10**

To support the high-power transmitter in the 1975 era, additional facilities are planned. These include a vault-type building to house the high-power transmitter rectifier and concrete foundations for a 60- to 400-Hz motor-generator set, high-voltage switchgear, a substation, motor-generator controllers, and a cooling tower with auxiliary piping and pumping. The electrical distribution system will also be extended.

A 1200-gal water storage tank is to be installed underground as part of a closed-circuit distilled water cooling system. Trenches will be provided for interface piping, conduits, and cables between transmitter facilities units and from the units to the vault and the 210-ft-diam antenna pedestal.

12. **Task 11**

The concrete and fabricated steel portions of the antenna pedestal, the instrument tower, the pump house, the alidade building, the instrument tower windshield,

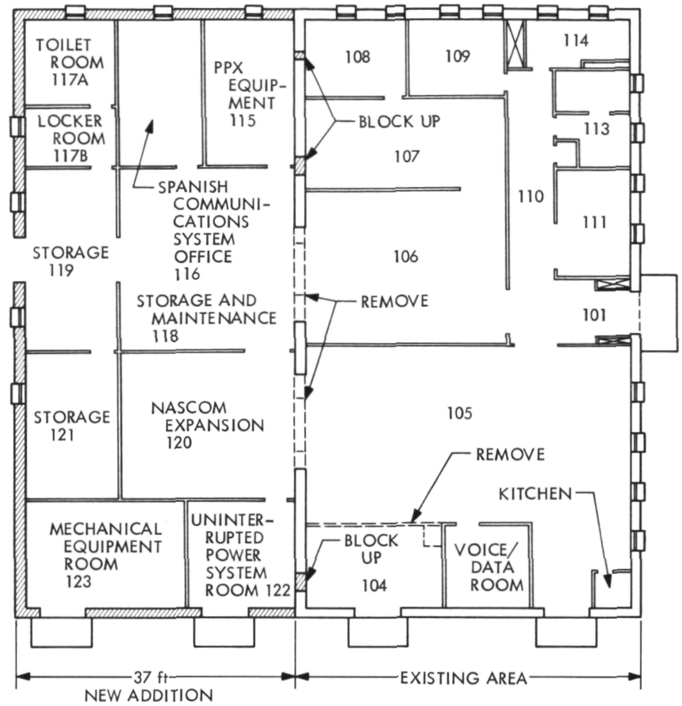

Fig. 4. NASCOM building plan

and the astrodome will be constructed (Fig. 5). Also provided will be the utilities within the 210-ft-diam antenna instrument, including electrical power distribution, water supply, heating, ventilating, air conditioning, sewerage plumbing, cable wrapup, and a coolant system.

13. **Status of Tasks**

Tasks 1 through 9 are currently under design contract with architectural and engineering firms in Madrid, Spain. The 30% design review has been accomplished; the 90% design review will be accomplished in January. Construction is scheduled to begin in early 1971.

Task 10 will not be started until installation of the high-power transmitter. This task has not been firmly scheduled, but will probably be completed for 1975 operations.

Design was completed on task 11 prior to contract. Construction is in progress. At present, excavation for the instrument tower and pedestal foundations is in progress. First concrete placement will occur in late November 1970.

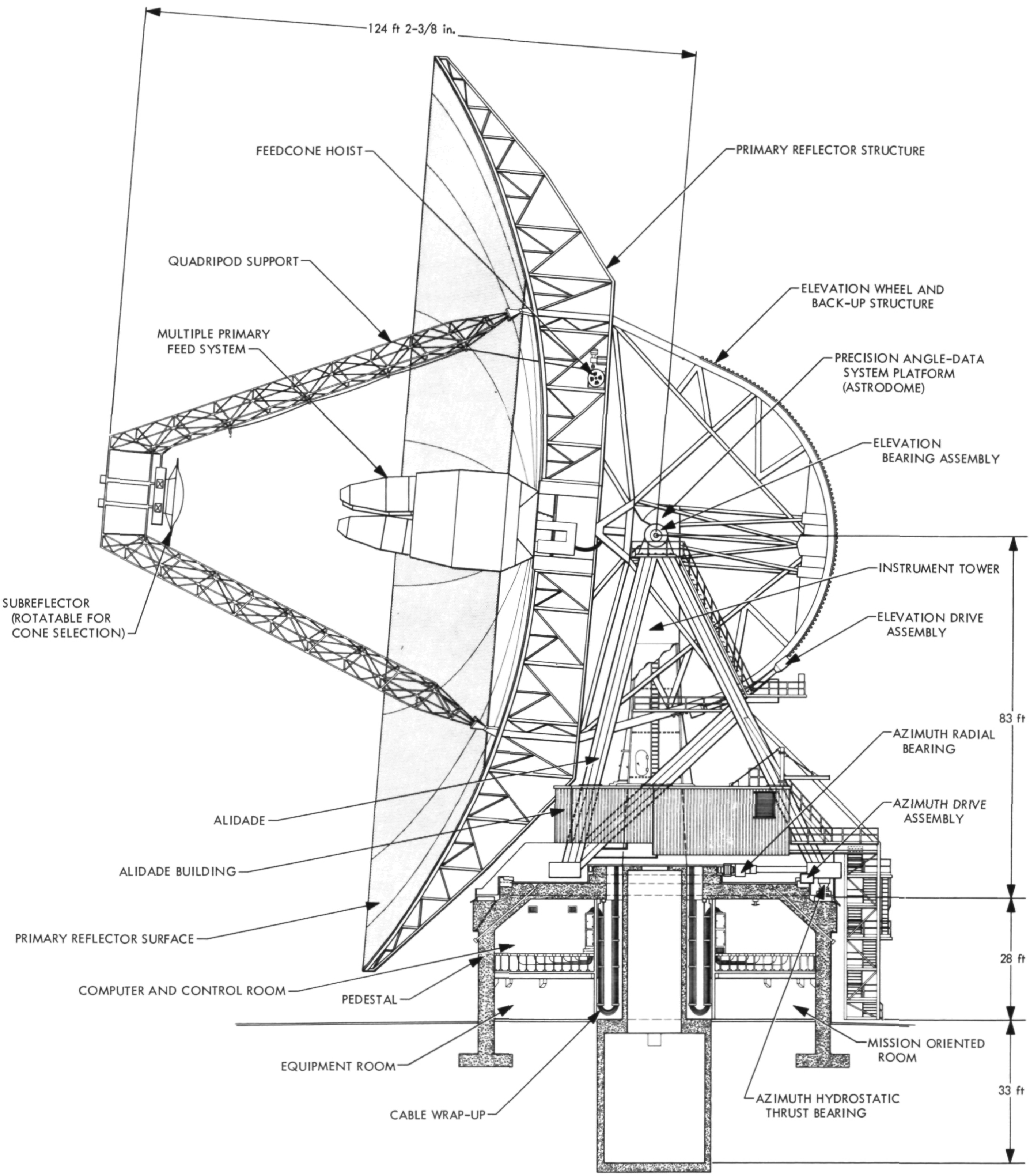

Fig. 5. Side elevation and section of 210-ft-diam antenna

B. 85-ft-diam Antenna Tracking Station Power Plant Reconfiguration, *L. H. Kushner*

Ever since the initial planning for implementation of the first DSIF 85-ft-diam antenna tracking station, approximately 15 years ago, a continuous on-going engineering task has been to provide the necessary on-site power generating service required to operate and maintain existing and new tracking stations. Continual growth of station technical facilities, electronics, and transmitter equipment has necessitated similar generated power plant growth to maintain a high degree of power quality and reliability.

The DSIF 85-ft-diam antenna tracking stations scheduled for power plant reconfiguration are located as follows (DSS 42 configuration already meets requirements):

Goldstone, California	DSS 11 DSS 12
Australia	DSS 41 DSS 42
South Africa	DSS 51
Spain	DSS 61 DSS 62

Reconfiguration of these 85-ft-diam antenna tracking stations will standardize types of power generating equipment capable of supporting known station loads forecast to the 1975 era. Existing equipment will be modified in place where feasible. Surplus equipment at one station that conforms to standard configuration will be utilized by relocation, where required, to another station. The equipment selected for the standard configuration was based on an evolution of equipment experience within the known proven framework of the latest state of the art. The major components of power generating equipment involved in the reconfiguration are engine-generator units and generator control panels.

The DSIF generated power philosophy applicable to size and number of engine-generator units is as follows:

(1) On-line units number and size are to provide for total maximum station demand load.

(2) Back-up unit is sized for largest on-line unit.

(3) Spare unit is available for down unit due to maintenance and service sized for largest on-line unit.

Considering this philosophy and the known forecast of station loads, the following size and allocation of engine-generator units are obtained:

One 350-kW unit	Electronics equipment load
One 500-kW unit	Utility equipment load
One 500-kW unit	Back-up
One 500-kW unit	Spare for maintenance and service

The resulting power plant standard configuration requires one 350-kW and three 500-kW engine-generator units. Experience has demonstrated that the engine prime mover (Caterpiller D-398) can be utilized for both 350-kW and 500-kW units, the difference being that the 350-kW-unit speed is 900 rpm and the 500-kW-unit speed is 1200 rpm. Utilizing the same engine for both generators

Table 1. Tasks required for power plant reconfiguration (one 350-kW and three 500-kW engine-generator units)

DSS	Task
11	Relocate from DSS 41 and install two engines and one 350-kW generator Procure and install one 500-kW generator Procure and install two engine-generator base skid mountings
12	Construct new power plant building Modify and install new generator control panel already purchased Relocate from DSS 41 and install four engines Relocate from DSS 41 and install one 350-kW generator Procure and install three 500-kW generators
41	Construct new power plant building Procure and install generator control panel Procure and install one 350-kW and three 500-kW engine-generator units
42	None required
51	Procure and install generator control panel Procure and install three 500-kW engine-generator units
61	Modify existing generator control panel Procure and install one 500-kW engine-generator unit
62	Procure and install generator control panel Procure and install two 500-kW engine-generator units

is an economical advantage in regard to spare parts, documentation, maintenance, and operation.

The tasks required for power plant reconfiguration at each DSS concerning procurement, modification, relocation of existing equipment, and installation are given in Table 1. DSS 42 and 61 are located on the same site as a 210-ft-diam advanced antenna station in complexes DSS 42/43 and DSS 61/63. Back-up power is provided from the power plant at the complex.

Completion of the power plant reconfiguration of the 85-ft-diam antenna tracking stations is scheduled for November 1972, when final work is completed at DSS 12.

Subject Index

Subject Index (contd)

NASA — JPL — Coml., L.A., Calif.